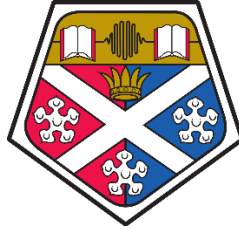


Resorcinol-Formaldehyde/Titania (RFTi) Gel Composites for Wastewater Treatment



Anam Anwar Ali Safri

Department of Chemical and Process Engineering
University of Strathclyde

This dissertation is submitted for the degree of
Doctor of Philosophy

April 2023

Declaration

This thesis is the result of the author's original research. It has been composed by the author and has not been previously submitted for examination which has led to the award of a degree.

The copyright of this thesis belongs to the author under the terms of the United Kingdom Copyright Acts as qualified by University of Strathclyde Regulation 3.50. Due acknowledgement must always be made of the use of any material contained in, or derived from, this thesis.

Anam Safri

April 2023

Acknowledgements

The completion of this PhD project would not have been possible without the support and encouragement I received from many people during my journey. Firstly, I would like to extend my deepest gratitude to my supervisor, Prof Ashleigh Fletcher, for accepting me into her group and allowing me to pursue the research ideas I had. I consider myself extremely fortunate to have had this opportunity to conduct my PhD research under her supervision, and it is hard to express in words how grateful I am for her continuous guidance and support, not only in academia, but also in my personal life. There were several occasions when I believed that I had no way out, but one conversation with her always cleared out the matter. I cannot thank her enough for her patience and confidence in me and for being available whenever I needed her.

I would like to thank Dr. Claudia and Dr. Vitor for their help with the equipment in the laboratory and senior group members, Maryam, Martin, and Elisha, for providing me with experimental guidance, as well as other colleagues, particularly Wenhan and John. I would also like to thank the lab technicians, especially Ian Airdrie, for providing equipment-related support and teaching.

I am grateful for the personal support I have received from my family, my husband's family, and my closest friends. In particular, I would like to thank my father for giving me wings, believing in me, inspiring me, and supporting me in so many ways; my mother for her prayers, support, and guidance; my sister for keeping me sane, and my niece Sophia, for being a source of happiness. Finally, I want to give special thanks to my husband, Salman, for endlessly supporting me, being there for me through thick and thin, believing in me, and constantly reminding me of my capabilities to achieve more.

Abstract

Increasing levels of water pollution, together with the appearance of emerging pollutants, necessitates the development of efficient new techniques for water remediation. Conventionally, adsorption and environmental catalysis can effectively respond to this demand, and these methods can be enhanced by developing new materials and processes to deliver on the needs of an increasingly industrialised society. A combination of adsorption and photodegradation has been proven effective in targeting a wide range of pollutants, and research into materials development pertinent to the integration of both processes is ongoing.

Previous studies have recognised the synergistic effects of carbon and Titanium (IV) oxide or Titania in various applications. Within water remediation, carbon has been utilised in several forms, such as activated carbon, graphene, carbon nanotubes, and fullerenes, for integration with TiO_2 . This work focuses on employing a new type of organic carbon gel, which are carbon nanospheres, to host TiO_2 photocatalysts. This organic carbon gel is derived from a sol-gel process via polycondensation of resorcinol-formaldehyde (RF), yielding unique properties that are ideal for use as an adsorbent for water treatment. TiO_2 was successfully incorporated into the RF matrix during the polycondensation reaction of RF, to produce a chemically crosslinked, stable structure. The integration of carbon and TiO_2 improves the photocatalytic activity by several means: (i) modification of the electronic structure of TiO_2 to lower its band gap for visible-light absorption, (ii) reduction of the recombination rate, and (iii) facilitation of pollutant adsorption. The highly porous carbon gel, with a large surface area, facilitated dispersion of TiO_2 , enhancing pollutant adsorption. The chemical complexes formed between both phases increase the number of active sites, and interactions between the pollutant and disinfectant, while the carbon phase facilitates charge transfer and minimises the recombination of charge carriers on the TiO_2 surface. These combined properties make the composite materials efficient materials for adsorption-photodegradation remediation of contaminated water.

The relative composition of RF and TiO_2 phase in an integrated material is crucial in determining the ultimate adsorption-photodegradation performance; therefore, a suite of RFTi gels was synthesised, moving from pure RF to pure TiO_2 in 10% steps, to

understand the structure-property relationship, and its impact on the final application, as well as to determine the optimal composition. Extensive analysis of the materials was conducted to determine their textural, chemical, thermal, and optical properties. Firstly, the compositional analysis validated the experimentally deposited theoretical compositions of both phases. The analysis of the results demonstrated the composition-dependent properties of RFTi. The micrographs showed a homogenous distribution of TiO_2 in the three-dimensional porous RF network for samples up to 30% TiO_2 , beyond which TiO_2 tended to start aggregating. The surface area analysis was in agreement with the micrographs, demonstrating that the aggregates blocked the pores of the RF network, resulting in a decrease in surface area and poor textural properties. Furthermore, the optical properties revealed that the electronic structure of TiO_2 was successfully modified, with a narrowed bandgap observed and a shift of the absorption edge to the visible region of the electromagnetic spectrum; hence, the material was capable of activation upon visible light irradiation. RFTi30 and RFTi40 (30% and 40% TiO_2 in RF) showed the lowest bandgaps with broadened UV-Vis spectra covering almost the entire visible region.

Characterisation of the materials was followed by application tests performed against a model pollutant dye, methylene blue (MB). The experimentally obtained data for the adsorption capacity for MB reduction correlated with the physiochemical properties of the respective samples. The equilibrium adsorption data were extensively studied to elucidate adsorbent-adsorbate interactions by applying kinetic and isotherm models to the adsorption data, and most of the samples showed a combination of physisorption and chemisorption phenomena. The effect of temperature showed that the reactions were thermodynamically feasible, and temperature-dependent adsorption depended on the nature of the RFTi sample. The synergy of RF and TiO_2 was corroborated by an observed enhancement in dye reduction upon visible light irradiation, demonstrating > 95% dye reduction for RFTi30 and RFTi40, owing to their optimal physiochemical and optical properties. The antimicrobial performance, evaluated against the reduction of indicator microorganisms (total and faecal coliform and *Escherichia coli*) was in agreement with the results obtained through adsorption analysis, with no bacterial colonies found after treatment. The synthesised sample was

reusable for four repeated cycles without significant loss of performance, as demonstrated for RFTi30.

This work not only highlights the potential of RFTi gels for water remediation applications, but also proposes the possibility of their application in various other fields such as thermoelectric applications.

Contents

Chapter 1: Introduction.....	1
1.1 Water Treatment Processes	3
1.1.1 Physical Processes.....	3
1.1.2 Chemical Processes	6
1.1.3 Biological Processes.....	7
1.2 Limitations of Treatment Processes	8
1.3 Selected Treatment Methods	8
1.3.1 Adsorption Method.....	9
1.3.2 Photodegradation Method.....	19
Chapter 2: Literature Informed Development of New Composite Materials	31
2.1 Porous Carbon Gels.....	32
2.1.1 Previously Developed Porous Carbon Modified Titania.....	35
2.2 Development of New Carbon-Titania Xerogels	38
2.3 Aims and Objectives	44
2.4 Summary	46
Chapter 3: Synthesis and Characterisation of RFTi Composites	47
3.1 Methodology	47
3.1.1 Sol-Gel Procedure	48
3.1.2 Solvent Exchange	49
3.1.3 Vacuum Drying	50
3.2 Materials Characterisation Techniques, Application and Theory	51
3.3 Field Emission Scanning Electron Microscopy	52
3.3.1 Imaging of Non-Conductive Samples	55
3.3.2 Sample Preparation and Analysis.....	56
3.4 Adsorption analysis	57
3.4.1 Adsorption Process.....	57

3.4.2	Adsorption Isotherm Features.....	58
3.4.3	Surface Area Measurement.....	66
3.4.4	Pore Size Distribution	67
3.4.5	Nitrogen Adsorption Analysis of Synthesised Samples	68
3.5	Point of Zero Charge.....	70
3.5.1	Experimental Procedure to Measure Point of Zero Charge	70
3.6	Thermal Analysis	70
3.6.1	Thermal Analysis Procedure	73
3.7	Spectroscopic Analysis.....	73
3.7.1	Fourier Transform Infrared Spectroscopy	74
3.7.2	UV-Vis Spectroscopy	76
3.8	Application Tests	81
3.8.1	Evaluation of Concentration an Adsorption Measurement.....	81
3.8.2	Antimicrobial Analysis	82
3.8.3	Membrane Filtration Procedure	85
3.9	Summary	86
Chapter 4: Characterisation and Analysis of Materials		87
4.1	Morphological Analysis	87
4.2	Surface Area and Pore size Analysis	93
4.3	Fourier Transform Infrared Spectroscopy.....	101
4.4	UV-Vis Spectroscopy	103
4.4.1	UV-Vis Analysis of RF Gels	103
4.4.2	UV-Vis Analysis of RFTi Gels	106
4.5	Compositional and Thermal Analysis	111
4.6	Summary	122
Chapter 5: Adsorption Performance.....		123
5.1	Experimental Analysis of Adsorption Capacity	124

5.2 Modelling of Experimental Adsorption Processes	131
5.2.1 Adsorption Kinetics	132
5.2.2 Adsorption Isotherms	143
5.3 Effect of Temperature on Adsorption and Thermodynamics	152
5.4 Adsorption Potential	162
5.5 Summary	164
Chapter 6: Photodegradation Studies	165
6.1 Photodegradation Performance.....	165
6.2 Kinetics of Photocatalytic Activity	170
6.3 Summary.....	175
Chapter 7: Antimicrobial Analysis	177
7.1 Mechanism.....	177
7.2 Results and Discussion.....	179
7.3 Summary	185
Chapter 8: Conclusions	186
Chapter 9: Future Work	191
Appendices	213
Appendix A- Experimental.....	214
Appendix B- EDX Analysis	215
Appendix C- X-Ray Diffraction Patterns.....	217
Appendix D- Experimental Evaluation of Point of Zero Charge.....	218
Appendix E- Van't Hoff's Plots.....	221
Appendix F- Antimicrobial Activity.....	222
Appendix G- Error Analysis.....	224
Appendix H- Publications	225

List of Abbreviations

BET	Brunauer-Emmett-Teller
BJH	Barrett-Joyner-Halenda
C_0	Initial concentration of solution
C_e	Equilibrium concentration of solution
CFU	Coliform forming unit
DSC	Differential scanning calorimetry
DTA	Differential thermal gravimetric analysis
E_a	Activation energy
E_g	Band gap
FESEM	Field Emission Scanning electron microscopy
FTIR	Fourier transform infrared spectroscopy
HOMO	Highest occupied molecular orbital
IPD	Intra-particle diffusion
K_L	Langmuir constant
K_s	Sips isotherm constant
LUMO	Lowest unoccupied molecular orbital
MF	Membrane filtration
n_F	Adsorption favourability parameter
N_s	Sips heterogeneity factor
PCA	Photocatalytic activity
PFO	Pseudo-first order
PSO	Pseudo-second order
P_{zc}	Point of zero charge

q_e	Equilibrium adsorption capacity
q_t	Concentration of solution at given time
R^2	Correlation coefficient
RFTi	Resorcinol-Formaldehyde and Titania
R_L	Separation factor
ROS	Reactive oxide species
SBET	BET surface area
TGA	Thermal gravimetric analysis
TiO_2	Titania or Titanium (IV) oxide

Chapter 1: Introduction

Water covers approximately 70% of the Earth's surface, and many people assume that it will remain an abundant resource. However, freshwater for domestic and agricultural use is incredibly rare, and two-thirds of freshwater is unavailable for our use. The rising demand for and scarcity of decontaminated water sources have become a global concern, mainly because of population growth, industrial development, and prolonged droughts. Inadequate access to clean water is, hence, causing a major impact on social and economic development. The World Health Organisation reports that, globally, one in three people lacks access to clean drinking water, approximately 850 billion are facing a shortage of potable water, and two billion people use a contaminated drinking water source, consequently suffering from water-borne infections, including diarrhoea, typhoid, hepatitis A, cholera dysentery, and polio [1, 2]. Every year, approximately 500,000 deaths are caused by diarrhoea from water contamination by infestation or inadequate management of industrial, urban, and agricultural wastes, and 2017, 220 million individuals need preventive treatments for schistosomiasis (a chronic acute disease caused by parasitic worms within infested waters). Dengue fever is another disease of concern, caused by insects that breed in waters that are not properly managed. Lack of, inadequate, or unmanaged water and sanitation services have caused preventable health risks, especially in healthcare facilities where there is an additional risk of diseases and infections.

To prevent the worsening of clean water scarcity, the development of sophisticated, affordable, and high-efficiency wastewater treatment technologies is desirable. One of the most appealing solutions is to reuse rural and refined municipal wastewater recovered from agricultural and industrial treatment plants. However, the recycling of these wastewaters is typically paired with the occurrence of suspended particles, bacteria that pose a health risk, and miscible refractory complexes that are expensive to treat. Additionally, the impact of existing pollutants has given rise to emerging pollutants which are persistent and becoming increasingly common. Surface water contamination by emerging pollutants is increasing owing to excessive pesticide use, pharmaceutical discharge, and improper wastewater treatment [3]. Exposure to emerging pollutants can occur through ingestion, inhalation, and skin contact. Therefore, as recommended by the European Environmental Agency, emerging pollutants need to be carefully monitored because they are less biodegradable and,

hence, may be more toxic. The most significant environmental consequences of emerging pollutants are bioaccumulation, persistence, toxicity, endocrine disruption potential, and carcinogenic and mutagenic effects [4]. Some emerging pollutants that cause endocrine disruption, hormone disruption, foetal deformity, and DNA damage can be detrimental to humans and aquatic organisms. In the light of the global freshwater crisis, there is a serious need for sustainable water use thus it may be useful to think along the lines to 'reduce, reuse, and recycle' so that water is available for future generations and non-human needs as well.

Conventional water treatment methods are designed to remove solids, organic compounds, and microbes. These methods include mechanical separation, chlorination, chemical and biological treatment, coagulation-flocculation, oxidation, granular sand or activated carbon filtration, and disinfection. These methods require massive land area for wastewater treatment plants, recycled water is below standard to be consumed, nitrification processes are interrupted by temperature fluctuations in tanks; generation of a large amount of sludge that is disposed of off-site; system cannot efficiently respond to seasonal or long term changes of wastewater composition, processes are inefficient to reduce a wide spectrum of organic and inorganic contaminants and regeneration of a material requires further treatment of the generated solid waste; due to these issues, conventional methods are ineffective.

Owing to rapid urbanisation and industrialisation, improvements in these processes are necessary since conventional treatment methods are not designed to target emerging pollutants [5]. This predicament is exacerbated by the escalating impacts on the water supplies because of increasing population, depreciation of groundwater sources, and knowledge of new emerging pollutants. Thus, the new laws and standards require stringent concentration limits. The elimination of specific emerging pollutants from raw water requires advanced water treatment methods associated with the consumption of energy and chemicals, leading to expensive treatment procedures which may impact the environment. As discussed by Rodil *et al.* [6], the following criteria must be considered in the case of the implementation of advanced treatment and technologies: (i) a wide range of targeted pollutants, treatment efficacy, and simple post-treatment removal mechanism, (ii) ease of implementation and system that requires minimal maintenance, (iii) eco-friendly and socially acceptable, and (iv)

inexpensive. The following sections discuss existing promising (as regards removal efficiency) advanced wastewater treatment technologies for emerging pollutants

1.1 Water Treatment Processes

Ongoing developments are being made to develop innovative wastewater treatment methods that meet the standards for clean water. Nevertheless, complete eradication of pollutants using existing methods remains a challenge. The various wastewater treatment methods reported in the literature can be broadly classified into physical, chemical, and biological methods, which are selected based on the type and concentration of pollutants and their cost-effectiveness. Treatment processes which require high maintenance, complicated installation, prolonged processing duration, less output, and the generation of harmful by-products after treatment are less considered for large-scale applications. Therefore, it is important to develop alternative treatment systems to eliminate or completely disintegrate pollutants.

1.1.1 Physical Processes

Physical wastewater treatment processes are based on the mass transfer of pollutants. Requiring fewer protocols to operate the system, physical processes are simple, flexible, and reproducible. These processes include adsorption, membrane filtration, and coagulation–flocculation. Among these, adsorption is attracting considerable interest.

Adsorption processes

Adsorption is one of the most promising advanced water treatment methods that is effective if the adsorbent has a high surface area and porosity, and is accessible and sufficiently available. Possessing exceptional qualities, such as low energy consumption, ease of use, and scalability, adsorption can play an important role in the removal of pollutants. All these factors are associated with the reversibility of adsorbents for regeneration and reuse. In this regard, the specific surface area plays a crucial role because it impacts the time of adsorption and the kinetics to establish adsorption equilibrium. Therefore, adsorption capacity is one of the primary measures that must be evaluated for adsorbates. Adsorption of porous materials is a mass transfer process that involves the adherence and accumulation of molecules, ions, or

atoms (these surface-assimilated species are called adsorbates) onto a solid surface (adsorbent). Generally, adsorption occurs in three successive steps: (i) transfer of the adsorbate to the boundary layer of an adsorbent, (ii) pore diffusion, and (iii) adsorption of the solute species. The adsorption rate depends on the adsorbent, adsorbate, and media in which adsorption takes place [7]. The adsorption capacity depends on the properties of the material, including its surface chemistry, surface area, pore size distribution (consisting of macropores, mesopores, and micropores), and operating parameters, including the contact time, initial concentration, temperature and pH. The maximum adsorption capacity of an adsorbent is determined by adsorption isotherms which are constructed by plotting the maximum adsorption capacity versus the concentration of the solution at equilibrium (in the case of aqueous systems) [8]. The most commonly applied adsorption isotherm models for studying pollutant removal are the Langmuir and Freundlich isotherm models [9].

The adsorption capacity of materials can be improved using nanomaterials to engineer nanoadsorbents with the required features to attain effective adsorption properties and target a wide range of pollutants [10]. Additionally, most adsorbents are recyclable; hence, reuse makes them cost-effective. Examples of engineered nanoadsorbents reported in the literature include carbon materials such as carbon composites, carbon nanotubes, graphene and carbon derived from other sources, such as polymer-derived porous carbons; other materials including biosorbents, metal oxides, magnetic composites, alloys with superparamagnetic properties; and core shell particles made from alumina, silica, and titania [11-13].

Several investigations have demonstrated that adsorption using activated carbon is a promising technique for pollutant removal from surface water because of its high surface area and porosity, low cost, nontoxicity, and high efficiency. In addition, the high adsorption efficiency of silica has been demonstrated owing to its mesoporosity, large surface area, and catalytic applications. It has also been used as a support material [14]. Titania-based adsorbents are appealing because of their tuneable electronic structure [15]. The adsorption of the dye onto titania occurs via electrostatic interactions between the sulfonic groups and hydroxyl groups. More recently, porous nanomaterials, such as titania [16], zinc oxide [17], iron oxide [18], and their

composites have attracted interest owing to their large surface area, chemical stability, non-toxicity, uniform pore structure, and catalytic properties.

Membrane filtration

Water treatment using membrane processes efficiently removes a wide variety of organic and inorganic pollutants in addition to solid particulate matter from surface water through permeable materials that can separate pollutants through a semipermeable membrane, while retaining the concentrate at membrane's surface. These membranes are prepared from various materials that provide specific properties, such as surface area, pore size, and surface charge, which target and retain specific pollutants [19]. A wide range of polymers, polymer blends, metals, ceramics, and hybrid membranes can be employed for this purpose [20]. Various membrane procedures [21-23] may be used to produce drinking water, and the processes, depending on the driving force for separation, are classified as (i) pressure-driven processes which include micro, ultra, and nanofiltration, and reverse osmosis; (ii) electric potential gradient which includes electrolysis; and (ii) concentration gradient which involves forward osmosis .

The process type and membrane material are selected depending on water treatment requirements, influent quality, targeted pollutants, and their concentrations [5]. The risk of membrane fouling and clogging depends on the membrane material and type and concentration of pollutants. Therefore, several cleaning methods such as flushing or chemical treatment have been employed [24]. The advantages of using membrane processes are the simplicity of operation, adaptability to existing treatment procedures, modular design, low energy usage and minimal chemical requirements. The most appropriate membrane processes for the elimination of emerging pollutants are attributed to their small pore sizes, and include reverse osmosis, ultrafiltration, and nanofiltration. Electrodialysis was used to treat seawater using ion-exchange membranes. Furthermore, these systems can be applied in combination to enhance the efficacy [25]. A disadvantage of membrane processes is that contaminants are transported into concentrate streams rather than eliminated, thereby requiring further treatment and disposal of the concentrate.

Coagulation/flocculation processes

Coagulation/flocculation processes involves destabilisation of dyes in solution media to form agglomerates and floccules. While flocculation involves destabilisation of suspended particulates that join to form aggregated floccules which further grow into large agglomerates to sediment due to gravity. This technique uses coagulants including lime, aluminium sulphate and ferric chloride to bind dye particles through electrostatic interactions, and sorption results in the reduction of dissolved matter and suspended and colloidal particles via coagulation/flocculation. This process is generally efficient for the removal or decolourisation of dispersed pollutant dyes; however, it is ineffective for the reduction of reactive dyes [26].

1.1.2 Chemical Processes

Essentially, chemical processes include advanced oxidation processes which are based on the release of hydroxyl radicals ($\text{HO}\cdot$), one of the most powerful oxidants that may be employed for the removal/disintegration of pollutants for diverse applications, such as pretreatment of raw water, drinking water treatment, and wastewater treatment [27]. Many pathways exist to produce $\text{HO}\cdot$, allowing appropriate advanced oxidation processes to be selected based on the characteristics of wastewater and targeted pollutants [28]. This process is categorised by considering methods to produce $\text{HO}\cdot$ into chemical, electrochemical and photochemical processes, with combinations of advanced oxidation and other processes being frequently used [21]. Advanced oxidation processes can be homogeneous or heterogeneous, depending on their interactions with the reactant. The removal efficiency of pollutants in homogeneous processes is determined by the interactions of chemical reagents with target molecules, in heterogeneous processes, reactant and product adsorption and desorption at the active sites of the catalyst surface are crucial. Metal-supported catalysts, semiconductors, or carbon-based composites incorporated with materials such as tungsten (VI) oxide (WO_3), titanium dioxide (TiO_2), copper (I) oxide (Cu_2O), zinc oxide (ZnO), and composite materials are utilised in heterogeneous processes [29, 30].

To date, the application of advanced oxidation processes to treat wastewater is limited to the laboratory scale. The major problems pertaining to the utilisation of advanced

oxidation processes for pollutant removal from contaminated water are associated with (i) low pollutant concentrations, (ii) incomplete mineralisation of the targeted species generating reaction intermediates, and (iii) relatively high process costs for large-scale installations. The most common catalysts or radical generator systems for advanced oxidation processes are Fenton reagent (hydrogen peroxide with iron species), ozone/UV light, hydrogen peroxide/UV, hydrogen oxide/ozone, and UV/photocatalyst or solar irradiation.

1.1.3 Biological Processes

Microorganisms disintegrate organic dyes through aerobic–anaerobic cycles. Anaerobic biofilm reactors with different carriers were connected to an aerobic reactor system, and the creation of aromatic amines resulted in the decolourisation of dyes under anaerobic conditions. Hence, a combined aerobic and anaerobic system could be an effective method for water decontamination. A variety of microorganisms, such as bacteria, algae, and fungi, can break down the wide spectrum of dyes found in textile effluents. Compared with physical and chemical methods, biological methods for treating textile wastewater have advantages including environmental friendliness, cost effectiveness, production of less sludge, production of non-hazardous metabolites, and requirement of less dilution. The efficacy of biological methods for pollutant degradation depends on the enzyme activity and adaptability of microbes. Consequently, several microbes and enzymes have been separately tested for dye degradation. An intriguing aspect of biological treatment methods is the isolation of active bacteria and their application in degradation.

However, these biological techniques have several limitations. Several dyes are toxic to aerobic organisms and produce rising sludge (due to denitrification or anaerobic biological activity) and bulking sludge (due to excessive growth of bacteria). Consequently, biological methods that involve the aerobic route have proven to be inadequate for the decomposition of dyes, particularly azo dyes. Additionally, it requires aeration, a larger area, and a longer hydraulic retention time (the average duration of wastewater in a bioreactor). The treatment takes a longer time owing to the slow growth and acclimatisation of anaerobic microorganisms.

1.2 Limitations of Treatment Processes

Generally, conventional water treatment methods do not completely remove contaminants, treatment costs are time-consuming, and alternative secondary pollutant techniques are required to improve the quality of water. Physical methods such as membrane filtration are efficient at high concentrations and are suitable for several pollutants, including suspended particles, dyes, and mineral ions. However, it incurs high operating costs owing to membrane clogging, which necessitates constant maintenance. Although advanced oxidation processes are efficient, they are restricted to the lab scale owing to high energy requirements; however, they are not economical to be put into practice for large-scale applications. Although coagulation/flocculation is a straightforward process, handling large sludge volumes is a challenge and increases the cost of the process. On the other hand, chemical methods involve several approaches related to the production of oxidants which target pollutants. Although the treatment process using oxidants is simple and effective, the method is generally limited to the laboratory scale, and fulfilling the energy demands is a time consuming and challenging procedure.

1.3 Selected Treatment Methods

The unique characteristics of each treatment method might be beneficial in one manner but limiting in another. The treatment techniques that have high installation and operating costs, protracted processing time, limited output, and the release of toxic by-products following treatment are insufficient for industrial purposes. Therefore, it is essential to design an alternate treatment method capable of eliminating pollutants completely.

Considering the wide range of pollutants, including emerging pollutants, several water treatment processes can be employed separately or in combination with other advanced wastewater treatment techniques. The effectiveness of a process depends on the properties of the contaminated water being tested, material employed in the process, and operational parameters of the water treatment system. Hence, removal efficiency can be articulated based on these criteria. Comprehensive study on the efficiency of independent processes, such as advanced oxidation processes,

adsorption using activated carbon and other carbon-based materials, reverse osmosis, and nanofiltration, has been reviewed previously [31, 32]. Similarly, combined treatment methods, such as adsorption using powdered activated carbon combined with ozonation [32, 33], UV/hydrogen peroxide and UV/hydrogen peroxide/ozonation [33], and fusion of ceramic microfiltration and ion exchange [34], have demonstrated significant pollutant degradation. Additionally, nanomaterials for advanced wastewater treatment processes, such as nanocarbon employed independently for adsorption or integrated into membranes, have shown synergistic effects for photodegradation or chemical decomposition of pollutants. However, these systems are more expensive than conventional water-treatment processes, particularly for the eradication of emerging pollutants.

After examining several advanced water treatment techniques, it was determined that a unified adsorption and photodegradation process could broaden the application potential for widespread use in the water treatment sector. Adsorption is a simple, efficient, and cost-effective approach; however, it does not completely degrade pollutants and, hence, cannot be applied alone. In contrast, assistive photodegradation techniques have the potential to completely degrade pollutants into harmless substances, owing to their ability to produce hydroxyl radicals or reactive oxide species. Therefore, an integrated adsorption-photodegradation process may widen the application efficacy for widespread use.

1.3.1 Adsorption Method

Adsorption is a process in which molecules, ions, or atoms (adsorptive) adhere to and accumulate on a solid surface (adsorbent), without being transferred to another phase. In terms of water treatment, the adsorption of porous materials is a mass transfer process that involves the accumulation of pollutants on the adsorbent surface to remove a wide spectrum of compounds, including micropollutants, non-degradable organic compounds from industrial wastewater, and a few metals. Sorption (a phenomenon in which both adsorption and absorption can occur individually or simultaneously) can be used to remove chemicals and pollutants, whereby different materials adsorb different pollutants reliant on the nature of the material, leaving the output clean. As mentioned earlier, a high surface area and porous material facilitate

pollutant access, the features of which are defined according to the material's ability to interact with the external media. Figure 1.1 shows the adsorption onto a typical porous carbon material. Pores of different sizes are generally classified as macropores (> 50 nm), mesopores (2-50 nm), and micropores (< 2 nm) [35]. As shown in the Figure 1.1, the molecules diffused into the porous carbon matrix, where pores of different sizes allowed the entrance of contaminants and facilitated adsorption on the internal surface of the porous structure.

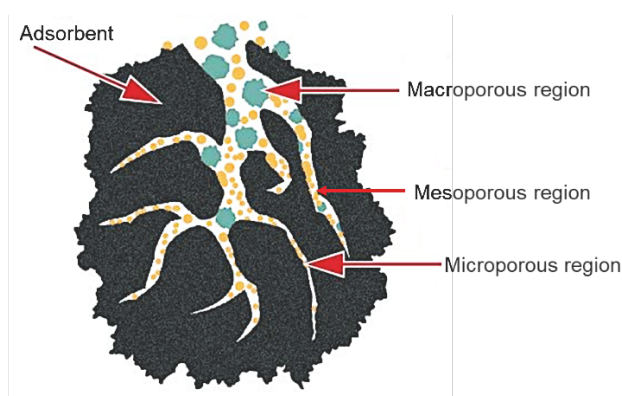


Figure 1.1 Schematic representation of the interaction of pores with molecules present in external media showing its diffusion dependence on different pore sizes (adapted from [36]).

Adsorption is classified into two types, physisorption and chemisorption, based on the interactions between the adsorbate and the adsorbent surface. Physisorption is a surface adsorption phenomenon primarily due to the diffusion of pollutants into the network of porous materials, and subsequent interaction at the interface may occur through van der Waals forces, hydrogen bonding, or hydrophobic interactions (π - π interactions). The reaction is reversible, and the adsorbate can be easily desorbed from the surface. In contrast, chemisorption involves chemical bonding via a reaction between the adsorbent interface and adsorbate. These reactions are due to electrostatic interactions, complexation, and strong covalent binding and are usually not fully reversible. Physisorption is faster than chemisorption and usually forms a multilayer on the adsorbent surface, whereas chemisorption normally forms a monolayer. In contrast to physisorption, chemisorption typically occurs at extremely high temperatures. In terms of defining thermodynamic parameters, physisorption is characterised by decrease in free energy and entropy, and thus is an exothermic phenomenon (enthalpy 2-20 kJ mol⁻¹) occurring rapidly at lower temperature. Whereas

chemisorption increases with an increase in temperature to a certain point where it starts to decrease the enthalpy ($20\text{-}400\text{ kJ mol}^{-1}$) [37, 38].

The adsorption of pollutants from the aqueous phase can be regulated by a phase transfer process which depends on adsorbate-adsorbent interactions under different microenvironmental conditions. Several parameters are crucial in the adsorption process, including the net surface charge of the adsorbate, nature of the adsorbent, mechanism of adsorption, and viscosity of the liquid phase. There is an ongoing development to enhance the adsorption capacity for the removal of a wide spectrum of contaminants by investigating the impact of these factors on the adsorption mechanism. Since the adsorption capacity depends on the nature of pollutant, and the adsorbent and adsorption mechanism should be suitably devised based on the physiochemical properties of adsorbate under provided optimum conditions.

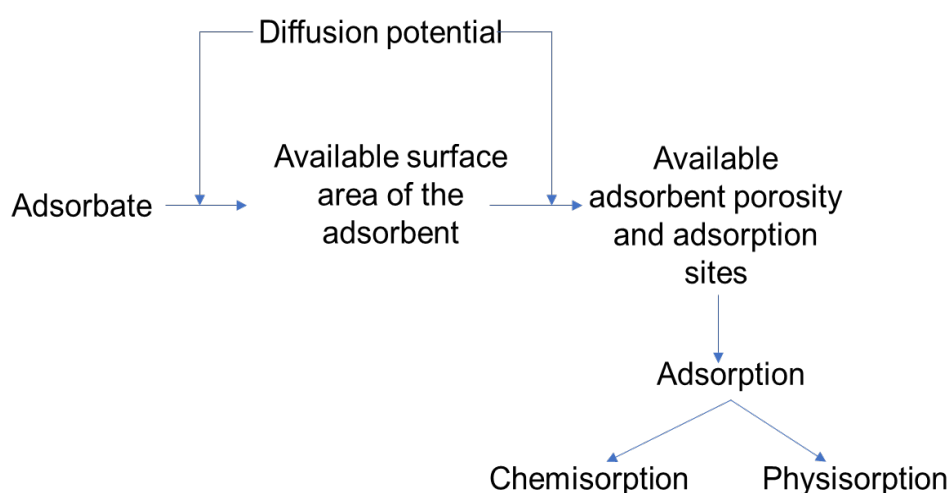


Figure 1.2 Adsorption process pathway.

The adsorption of pollutants including heavy metals and dyes occurs in three steps: (i) migration of pollutant species to the surface, (ii) dissociation of the complex aqueous structure of pollutants, and (iii) surface complexation [39]. Figure 1.2 shows the general pathway of an adsorption process. The adsorbate diffuses on the external surface of the adsorbent because of the diffusion potential characterised by the adsorbate concentrations and surface area of the adsorbent. The adsorbate then diffuses in the available pores or active sites of the adsorbent and the active sites are

occupied by physisorption or chemisorption depending on the surface functional moieties of the adsorbent and adsorbate.

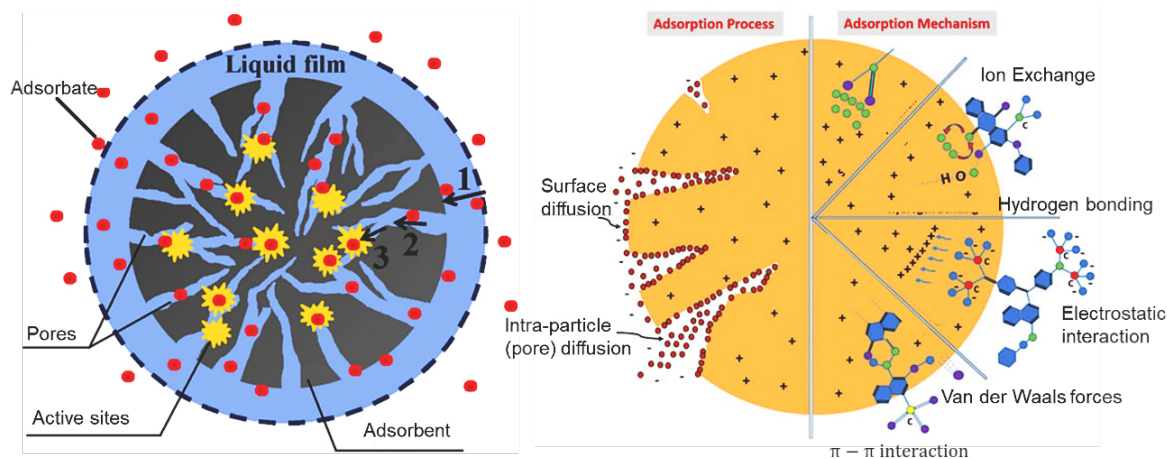


Figure 1.3 Illustrations of mass transfer steps labelled (left) (1) external diffusion (2) internal diffusion and (3) adsorption on active sites (right) showing possible adsorbent and adsorbate binding mechanisms [40].

Gulipalli *et al.* [41] explained that the adsorption process takes place either in one or multiple steps including external diffusion, internal/pore diffusion, and adsorption on the active sites/pores. The adsorption mechanism consists of three basic phases, as illustrated in Figure 1.3 (potential surface interactions of methylene blue dye molecules are illustrated as an example): first, the mass transfer of contaminants occurs on the surface of the porous material (or adsorbent); then, the contaminants diffuse into the pores of the adsorbent (internal diffusion occurs particularly for a porous material), and finally, the contaminants bind to the adsorbent bound by the surface reaction.

Adsorption equilibria

Considering the adsorption data at equilibrium under the given conditions, adsorption isotherm models are used to interpret the interaction mechanism of adsorption at a constant temperature. Based on literature, various adsorption isotherm models were used to explain the adsorption mechanism by evaluating the adsorption model parameters to predict the adsorption data at equilibrium. All isotherm model equations relate the amount of adsorption to the concentration of the adsorbent at a constant temperature.

The equilibrium adsorption can be identified by monolayer and multilayer adsorption dependent on the textural and surface properties of the adsorbent and its interactions with the adsorbate which can be predicted by adsorption isotherm models. Based on previous reports, the adsorption equilibrium for the elimination of contaminants such as heavy metal, dyes and pesticides is best interpreted by Langmuir and Freundlich isotherm models [6], organics best fit to Langmuir, Freundlich, and Redlich Peterson [42]; for dyes and heavy metals, the removal is best explained by the Langmuir, Freundlich, Harkin Jura, Toth, and Sips models [8]. Several factors should be evaluated before selecting the most suitable isotherm model for the equilibrium data, including: (i) there should be a good fit between the equilibrium data and the isotherm function, (ii) the isotherm function must be thermodynamically plausible, and (iii) in an ideal case, analytical determination of capacity from concentration should be feasible.

Adsorption kinetics

The adsorption kinetics study provides information on the adsorption rate, adsorbent performance, and mass-transfer processes. Understanding adsorption kinetics is critical for designing adsorption systems hence various kinetic models of which most commonly applied include pseudo-first order, pseudo-second order and Elovich models have been developed to interpret the kinetics of adsorption. Additionally, an intra-particle diffusion model maybe applied to gain an understanding of the mass transfer or external diffusion processes.

Based on literature, the pseudo-first-order model approximates the conditions of (i) the initial stage of adsorption, (ii) the adsorbent material has few active sites, and (iii) the adsorbate concentration is high. The pseudo-second-order model corresponds to the conditions of (i) at the final phase of adsorption, (ii) the adsorbent has numerous active sites, and (iii) the adsorbate concentration is high. The Elovich model is commonly applied to interpret the chemisorption of an adsorbate onto a solid. The basic assumptions of these models are (i) an increase in the activation energy with adsorption time, and (ii) a heterogeneous adsorbent surface. The mass transfer process which occurs in three phases: film diffusion, surface diffusion, and diffusion through pores, can be studied using external diffusion models [43]. This implies that the adsorbate diffusion in the outer liquid film in the vicinity of the adsorbent is the

slowest step. To determine the rate-controlling step, the most convenient and commonly applied model has been proposed by Weber and Morris [40].

Adsorption thermodynamics

A thorough investigation of adsorption thermodynamics, in combination with adsorption kinetics, is imperative. Quantifiable thermodynamic parameters including the temperature equilibrium constant and their non-measurable equivalents, such as Gibbs free energy change, enthalpy, and entropy, are highly essential parameters that are commonly used for evaluating and predicting adsorption process mechanisms. These parameters are required to predict the spontaneity and feasibility of adsorption processes; therefore, the experimentally determined equilibrium adsorption data were used to evaluate the thermodynamic parameters, including the Gibbs free energy (ΔG), change in enthalpy (ΔH), change in entropy (ΔS), activation energy (E_a), and adsorption potential (A) [44]. This is explained in detail in Chapter 6.

1.3.1.1 Types of Adsorbents

Low-cost adsorbents

Low-cost adsorbents are useful mainly because of their cost-effectiveness, and a wide range of them can be used to decontaminate wastewater without producing by-products. Different types of low-cost adsorbents have been developed from natural, industrial, and agricultural sources.

There are several naturally present materials that have the characteristics of adsorbents and, therefore, have been effectively utilised to eradicate organic and inorganic pollutants from wastewater. A few examples mentioned in a review by Lin *et al.* [45] include natural adsorbents, such as zeolites, which are tetrahedral aluminosilicates connected with oxygen atoms and have shown 65% pollutant removal performance. Biopolymers such as chitosan and chitin have been reported to produce fibres with adsorbent properties, biodegradability, and enhanced strength comparable to that of activated carbon. Inorganic adsorbents, such as clay minerals, can adsorb pollutants owing to their negatively charged layers and colloidal properties which can effectively adsorb cations and organic pollutants [46] but show limited adsorption towards anions.

A few clay materials adsorb anionic pollutants based on electrostatic interactions; however, this process is complicated. In addition, untreated clay effectively eliminates ionic dyes and several additives [47]. Non-regenerable materials, such as wood, are employed as adsorbents owing to their hierarchical porous structure composed of cellulose polymers embedded in a porous matrix. Several plants with bark and wood, such as Eucalyptus bark, have been reported to remove dyes without pretreatment [48]. Several other plants, such as lotus leaves, pine needles, neem leaves, and cactus leaves, are reported to eliminate dyes such as methylene blue and chromium under optimum conditions [49].

Agricultural waste, another category of low-cost adsorbents, is mainly obtained from fruit and vegetable peels and can be modified to enhance its adsorption properties for pollutant removal. The adsorbent features are ascribed to the structure and characteristics of these materials, which are composed of lignin and cellulose structures, and the polymeric chains with specific functional moieties that promote the elimination of pollutants from contaminated water. Prior to being applied as an adsorbent for water remediation, the natural form of agricultural waste was pulverised until the desired particle size was achieved. Furthermore, these wastes have been reported to produce granular activated carbon from fruit shells. A study reported the use of rice husks chemically controlled with urea to obtain activated carbon for the removal of nitrate from wastewater [49, 50]. Citric acid modified rice husk has also been reported to remove metal ions from wastewater [51].

The by-products of industrial waste can be reused as adsorbents which would otherwise cause environmental pollution. Examples of such wastes include fly ash which contains high amounts of alumina and silica and has a porous surface with non-uniform shaped particles, making them effective adsorbents [52]. Red mud, an effluent from the aluminium industry, is highly porous with dense surface features, and neutralised red mud was an appropriate adsorbent for removing arsenic and dyes from wastewater [53]. Another example is bagasse fly ash waste from sugar industries, which has been reported to remove zinc and toxic species from aqueous systems [54].

Metal oxide nanoadsorbents

The application of nanotechnology in water remediation has been an intriguing topic because nanoscale materials have adaptable properties, owing to their small size and high surface-to-volume ratio. Briefly, the surface area of a material increases by reducing the particle size; hence, the properties of a material appear to be different from those at the macroscale. With regard to water remediation, nanomaterials or nanoparticles have been successfully applied as nanoadsorbents for the removal of a wide range of organic and inorganic pollutants. The following sections discuss nanoadsorbents and their characteristics, which have shown significant pollutant removal efficiency from wastewater.

Several metal oxide nanoadsorbents and their composites have been reported for the eradication of organic and inorganic pollutants from contaminated water. According to the literature, magnetic nanoparticles, including iron oxide and its compounds, have potential applications in the adsorption and removal of arsenic, heavy metals, toxic, and azo dyes. Magnetic adsorbents, particularly iron oxide and its derivatives, exhibit excellent physicochemical properties for adsorption and removal of pollutants. Additionally, they are nontoxic, reusable, easy to synthesise, and can be conveniently separated after removal by applying an external magnetic field. This makes the treatment process cost-effective because advanced methods are not required for the removal of adsorbents from the treatment system. Other commonly used metal oxide nanoadsorbents include cupric oxide (CuO) which has been reported to remove arsenic from water, function well in the presence of other competing ions, and can be regenerated and reused. For the removal of certain pollutants such as arsenic, the operating pH of the system does not have to be regulated, making it simple to use. Zinc oxide (ZnO) is another nanoadsorbent that is easy to operate because of its nontoxicity, stability, and effective performance in the pH range 6-6.8. Titanium dioxide (TiO₂) or titania nanoparticles are widely employed as nanoadsorbents because of their low cost, chemical stability, anti-corrosive properties, photooxidation power, and high affinity for the removal of metals and dyes. In addition, metal oxide composites have been synthesised to obtain a synergistic effect between metal oxides and adsorbent properties. Examples include combinations of iron-manganese (Fe-Mn), iron-cerium (Fe-Ce), iron-zirconium (Fe-Zr), iron-chromium (Fe-Cr), iron-copper (Fe-

Cu), titanium-cerium (Ti-Ce), titanium-iron (Ti-Fe) and manganese-cobalt (Mn-Co). The enhanced adsorption capacities of bimetal oxides, including Mn_3O_4 , $MnFe_2O$, and Fe_3O_4 , as well as composites of magnetic nanoparticles, such as $CoFe_2O_4$ and $MnFe_2O_4$, have been reported as effective nanoadsorbents because of their paramagnetic nature, and because they can be easily separated using a magnetic field after adsorption [55]. In addition, magnetic oxide nanoparticles were combined with graphene oxide to form magnetite-reduced graphene oxide composites which have shown enhanced adsorption properties due to surface complexation and the pH controlled surface properties were beneficial for removal of a wide range of pollutants [56].

Carbon-based adsorbents

Carbon-based materials with well-developed pore structures, commonly known as activated carbon (AC), are made from a variety of rich carbonaceous materials. Possessing large surface area and porosity, AC is a versatile material owing to its diverse spectrum of surface functional moieties. The main functional groups responsible for pollutant uptake include carbonyl, carboxyl, phenol, and quinones in addition to others. The nature of the carbon surface can be modified by adding or replacing the desired functionalities to target specific pollutants, generally achieved by activation and chemical, thermal, oxidative, and non-oxidative treatments. Generally, the activation step follows the surface modification steps of AC. The efficacy of AC as an adsorbent for various contaminants is widely recognised. AC is known to be significantly more effective than inorganic adsorbents in eliminating organic pollutants. AC is a widely used commercial adsorbent for the removal of a wide variety of pollutants owing to its distinguishable properties such as high surface area, porosity, and tuneable surface functionalisation. Recently, the removal of high concentrations of contaminants using AC has gained attention. The mesoporous structure of activated carbon and its composites has encapsulating properties, making it a suitable adsorbent for the removal of heavy metals, dyes, and toxic pollutants. Yao *et al.* [57] reported an iron oxide/AC composite with a high surface area, excellent chemical stability throughout the pH range, and reusability, which corroborated the enhanced adsorption for the removal of arsenic.

Carbon nanotubes (CNTs) were discovered in 1991 by Iijima [58], since then CNTs have been employed in a variety of applications because of their large surface area and modifiable chemical and physical characteristics. The structure of CNTs can be classified based into single walled and multiwalled CNTs, based on number of walls and their diameters. The active sites present in the internal and external structures of CNTs enhance their adsorption capacity and, therefore, have been widely reported for the removal of heavy metals from contaminated water [59]. Likewise, three-dimensional graphene has a high surface area, homogenous structure, hydrophobic surface, chemical and structural stability, and reusability; therefore, it is a reliable candidate for the adsorption of pollutants from polluted water. Additionally, derivatives of graphene, graphene oxide, and reduced graphene oxide have functional groups such as hydroxyl, carboxyl, carbonyl, and epoxide groups suitable for enhanced adsorption of pollutants.

1.3.1.2 Limitations of Adsorption Method

The majority of nanoadsorbents are available in the form of fine powders which are not suitable for large-scale applications. Because of their smaller particle size, nanoadsorbents can only be applied to fixed bed columns in granular form or supported on a large porous matrix such as activated carbon, polymers, or the base material of a nanoadsorbent. Nevertheless, the selection of an appropriate supporting material is challenging. For example, in the case of metal oxide nanoadsorbents, it is difficult to obtain spherical beads of suitable size for practical applications; therefore, the use of supporting materials is beneficial. Another study reported composite gels as nanoparticle supports owing to their high porosity, interconnected pore network, and thermal and mechanical stability. Besides providing support, these composite gels participate in the adsorption of pollutants, thereby enhancing the pollutant eradication process. Additionally, various polymers and grafted polymers such as polyacrylamide or chitosan grafted polyacrylamide has been found advantageous support material for the treatment of wastewater containing mixed ions [60].

After adsorption treatment, the separation of the adsorbent is challenging. Several methods have been described for the separation of nanoadsorbents after equilibrium is established during the adsorption process, including centrifugation, filtration, and

magnetic separation. Most commonly, separation through centrifugation has been found to be an effective method for the preparation of nonmagnetic nanoadsorbents. In addition, the adsorbent may be exhausted after the adsorption process; hence, adsorbent regeneration to restore the adsorption capacity is crucial for economic viability. Several desorption methods, such as adjustment of pH and temperature, have been proposed to recover the adsorption capacity of adsorbents [61].

Adsorption is an extensively used technique for the removal of pollutants. Currently, the focus has shifted to low-cost modified adsorbents with economic viability and enhanced adsorption characteristics. Significant efforts have been made to enhance the porosity, textural characteristics, and adsorbent specific surface area to develop a new class of nanomaterials with better adsorption efficacy. The assets and liabilities of this approach are unclear for industrial applications. Despite these improvements, there is still a need to produce adsorbents whose performance spans a wide range of contaminants, especially on a large scale, for water remediation, as the pollutants are not completely eliminated or destroyed.

1.3.2 Photodegradation Method

Utilising a light source for the degradation (photodegradation) of contaminants in water sources has recently been a successful strategy to alleviate many of the constraints that researchers confront. Photodegradation is a photocatalytic process which involves the following mechanisms: (i) diffusion of contaminants, such as dyes and other organic molecules, from the aqueous phase to the surface material which absorbs photons (photocatalyst); (ii) adsorption of pollutants on the surface of the photocatalyst; (iii) oxidation of adsorbed pollutants with reactive oxide species; and (iv) desorption of products. Compared to adsorption methods that use adsorption mechanisms to eliminate pollutants, pollutants in photocatalysis degrade during redox reactions in the presence of a photocatalyst and in this regard, this section explains the mechanisms and types of photodegradation approaches. When a semiconductor photocatalyst is irradiated under suitable light and the material absorbs photons, the electrons present in the valence band are excited and transferred to the conduction band, leaving holes in the valence band. These photoexcited electron hole pairs have tendency to recombine and dissipate off energy as heat or migrate to the surface of

the photocatalyst where they can participate in a series of reactions to generate reactive oxide species (ROS) and pollutants degrade efficiently when they come in direct contact with ROS.

It is well known that semiconductor photocatalysis is one of the most extensively applied technologies to address global environmental challenges by means of environmentally friendly materials and renewable energy sources, such as solar energy [62]. When photogenerated electron and hole pairs transfer to the surface of a photocatalyst they partake in several reactions, as shown in Figure 1.4.

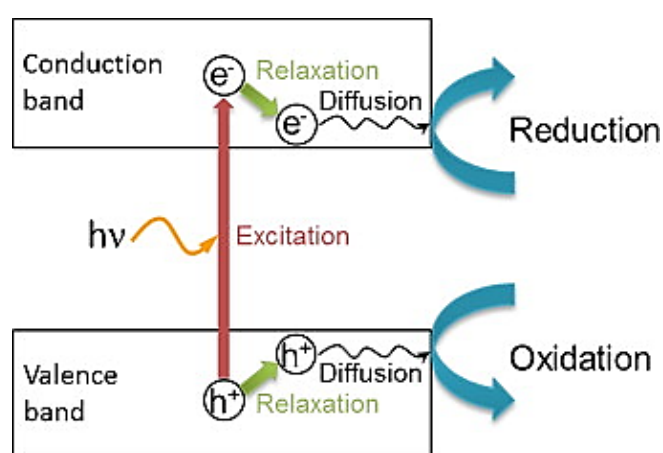


Figure 1.4 Schematic drawing of the formation of photogenerated charge carriers (hole/electron pairs) upon absorption UV light [63].

Electrons can participate in reduction, while holes can participate in oxidation reactions. These photoexcited electrons can be transferred to oxygen molecules that are adsorbed on the surface of a photocatalyst or present in its proximity. These O_2 molecules accept electrons in the conduction band of the photocatalyst and convert them into superoxide anions which are highly active for any kind of redox reaction and further participate in the degradation of pollutants, including dyes and microbes, into harmless by-products, such as CO_2 and H_2O . The photogenerated holes are also used to oxidise water molecules adsorbed on a photocatalyst surface which can be converted into hydroxyl radicals by donating electron into the holes present in valence band and thus can be converted into powerful oxidising agent to degrade pollutants .

Semiconductor metal oxides including tungsten trioxide [64], titanium dioxide [16], zinc oxide [65], manganese oxide [66], tin (IV) oxide [67] and heterostructures including combination of zinc oxide/copper (II) oxide [68], titanium dioxide/zinc oxide [69],

copper (I) sulphide/tungsten trioxide [70], titanium dioxide/tungsten trioxide/zinc oxide [71], copper (I) sulphide/tungsten trioxide/tin (IV) oxide, copper (II) oxide/zinc oxide/tungsten trioxide [72] have been widely studied and probed as suitable photocatalyst for wastewater remediation. Nonetheless, employing these photocatalytic materials for large-scale applications is a challenge, mainly because of their restricted wavelength absorption spectrum and the recombination of electron/hole pairs. To comply with the engineering requirements, the efficiency of TiO₂ solar photocatalysts must be enhanced. Furthermore, the durability and cost efficiency of these materials must be carefully addressed. Hence, identifying and designing novel semiconductor materials that are economical, stable, and effective are challenging.

1.3.2.1 Titania Photocatalysis

For water treatment applications, the conversion of solar energy to chemical energy refers to the generation of oxidative species which disintegrate the chemical structures of pollutants. In 1972, Fujishima and Honda [73] used solar energy and photocatalysis to produce hydrogen through water splitting, and research began to surge. Since then, photocatalytic materials have been extensively explored for solar-to-chemical energy conversion to obtain hydrogen [74, 75] and hydrocarbons [76] and for the removal of pollutants and microbes [77, 78]. One of several photocatalysts, titania, has been extensively studied and used in several industrial applications owing to its low cost, chemical stability, non-toxicity, anticorrosive properties, strong oxidising and decomposition abilities, and responsiveness to UV-Vis light. Titania semiconductor is known to absorb UV light and produce photogenerated charge carriers which separate in the conduction and valence band and is the principle of its photocatalytic activity [16]. Figure 1.5 shows the reaction pathway of the photocatalytic degradation of pollutants by ROS (OH•, HOO•, H₂O₂) present in the vicinity of titania.

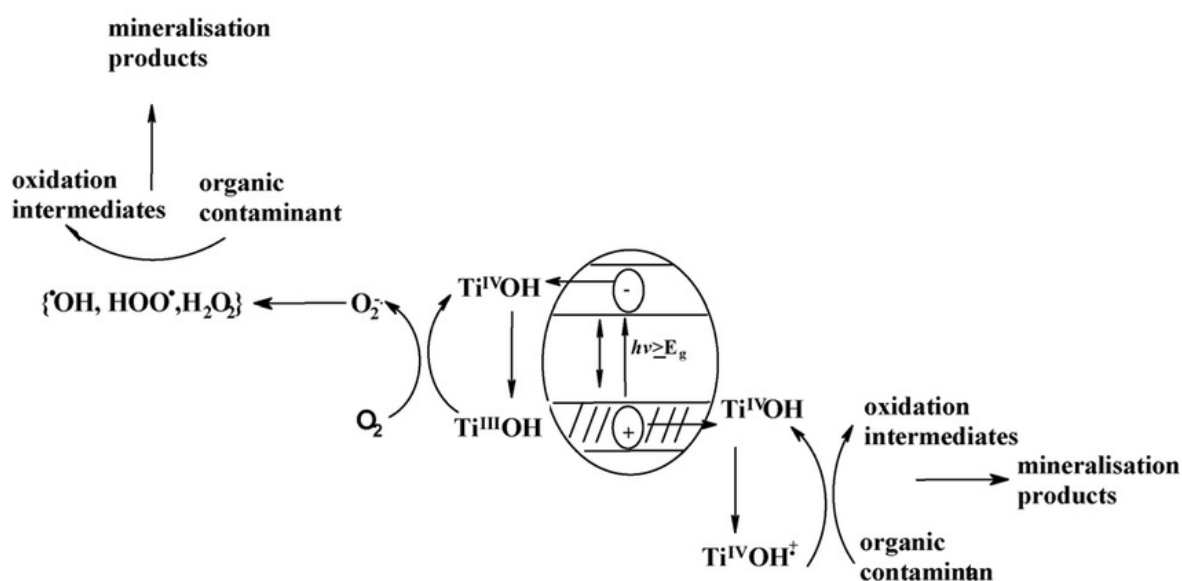


Figure 1.5 Reaction pathway of the photocatalytic degradation of pollutants by photogenerated reactive oxide species [63].

In addition to its excellent photocatalytic and oxidative properties, the superhydrophilic nature of titania facilitates pollutant interactions owing to its ability to change its chemical conformation upon UV irradiation, as evidenced by the evaluation of contact angles $< 5^\circ$ in several reports [79]. Another appealing characteristic is the effortless synthesis in the laboratory, allowing the fabrication of titania for desired applications, for example, in the form of spheres, rods, fibres, or 3D interconnected structures. In terms of water treatment applications, physical modification of titania nanoparticles can increase their surface area and adsorption capacity which helps increase their photocatalytic efficacy. Additionally, decreasing the size of titania nanoparticles to several nanometres can reduce the electron/hole recombination rate [80]. Hence, the photogenerated charge carriers effectively participate in the redox reaction and produce hydroxyl radicals.

Generally, titania has three crystalline phases: anatase, rutile, and brookite. Compared to the other two phases, the anatase phase has been proven to exhibit enhanced photocatalytic activity owing to its bandgap and higher surface energy [16]. The commercial photocatalyst titania (P25) is biphasic (a mixture of rutile and anatase). However, for pure phases, it is generally accepted that anatase exhibits higher photocatalytic activity. The photocatalytic properties of titanium dioxide are obtained from the photogenerated charge carriers or electron/hole pairs (e^-/h^+) produced upon

the absorption of photons corresponding to its bandgap (E_g), as illustrated by pathway (1) in Figure 1.6 [63]. The bandgap of titania (anatase phase) is ~ 3.2 eV and the wavelength is below 400 nm which means that UV irradiation is required for photoexcitation to begin. Upon photoactivation, the charge carriers are separated (Figure 1.6, pathway (2)), and the photogenerated h^+ in the valence band diffuse to the titania surface and react with the water molecules adsorbed on the titania surface, resulting in the formation of hydroxyl radicals ($\bullet OH$) through a redox reaction that oxidises organic molecules close to the titania surface. The e^- in the conduction band undergo reduction to generate superoxide radical anions ($O_2^{\bullet -}$) upon reaction with molecular oxygen. These redox reactions are marked in Figure 1.6 as pathways (3) and (4). The photogenerated mechanism of charge carriers by the titania photocatalyst is widely assumed by Equations 1.1 to 1.8 (conduction band (CB), valence band (VB), bandgap (E_g), trapped (TR)) [81].

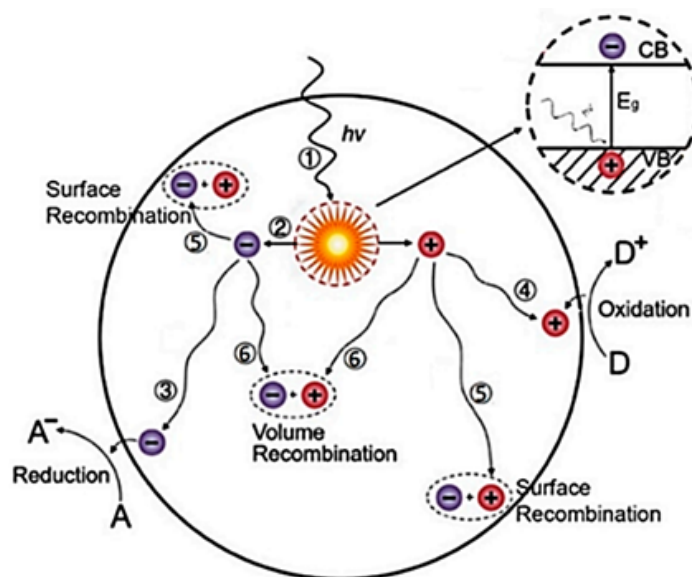
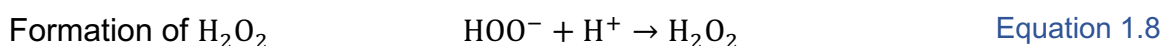
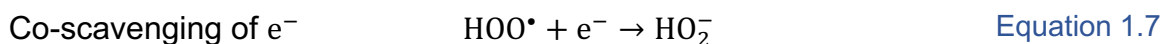
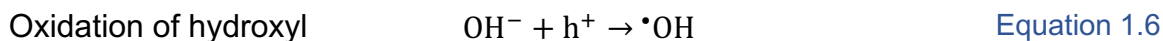
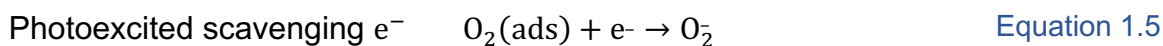
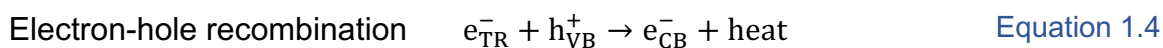


Figure 1.6 Schematic representation of pathways of photogenerated charge carriers in a titania [82].

Photoexcitation	$TiO_2 + hv \rightarrow e^- + h^+$	Equation 1.1
Charge carrier trapping of e^-	$e^-_{CB} \rightarrow e^-_{TR}$	Equation 1.2
Charge carrier trapping of h^+	$h^+_{VB} \rightarrow h^+_{TR}$	Equation 1.3



Photodegradation technique has attracted significant interest during the past decades owing to its efficacy in rapidly degrading and mineralising a wide spectrum of pollutants. However, there are some technical barriers, including a wide bandgap which requires UV light for the activation of titania, low adsorption capacity for certain pollutants, high tendency to aggregate, and difficult recovery after treatment. The following section discusses these limitations and countermeasures in detail.

1.3.2.2 Limitations and Countermeasures of Titania Photocatalyst

Enhancement of visible light absorption

The most important characteristic relevant to the photocatalytic activity of titania is the electronic structure, which governs the absorption of the irradiated photons. Owing to its electronic structure, photocatalytic titania only activates upon solar irradiation, whereas only 5% of UV light falls on Earth; the activation of photocatalytic processes is dormant under the UV-Vis spectrum and its application is limited due to the narrow photocatalytic region ($\lambda < 400 \text{ nm}$). Additionally, the photogenerated charge carriers rapidly recombine, and the electronic band structure is inconsistent with the chemical potential required to initiate redox reactions. In terms of photon absorption, narrow bandgap photocatalysts are more likely to exhibit high absorbance and thus are ideal for effective low-energy photon harvesting. Therefore, the activation of photocatalytic processes under visible light is of great interest because its dormancy under visible light makes it unsuitable for mass processing systems. Engineering the electronic configuration of titania broadens the absorption of photons in the visible region of the electromagnetic spectrum and lower the recombination of photogenerated charge

carriers. Several strategies have been employed to achieve this which mainly involve modification of the bandgap non-metal and metal doping and alloying of different photocatalysts into solid solutions.

Doping with metal is one approach for broadening the absorption edge to the visible region of the electromagnetic spectrum. Titania nanoparticles can be easily substituted or interstitially doped with various cations to generate oxide mixtures. The major parameters include the nature and concentration of the metal dopants and synthesis route. The effect of the dopant on the photocatalytic activity is complicated. The photoexcitation of electrons occurs by photon energy ($h\nu$) from the defect site to the titania conduction band. An advantage of metal doping is the reduced recombination of e^-/h^+ due to enhanced electron trapping (Figure 1.7). For example, doping titania with gold, silver, and platinum has been shown to significantly reduce the recombination rate of photogenerated charge carriers owing to the formation of a Schottky barrier at the titania/metal interface [83, 84]. Hence, improved photocatalytic activity was observed owing to a decrease in charge recombination. In this case, the metal dopant serves as a bridge between the titania surface to store and transport photogenerated electrons shown in Figure 1.7, illustrating dispersion of metal dopant which creates an additional energy level in the bandgap of titania.

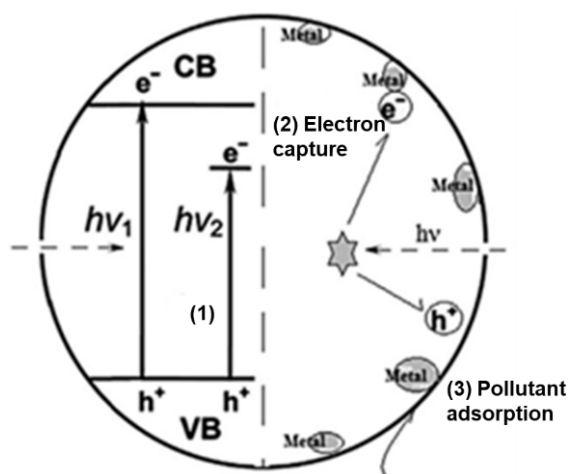


Figure 1.7 Mechanism of metal doped titania photocatalysis (1) band gap narrowing hv_1 and hv_2 are photon energy required for pure titania and for metal doped titania, (2) recombination of electron/hole pair; and (3) adsorption of contaminants. Adapted representation from [85].

Iliev *et al.* [84] showed that doping with silver or platinum significantly enhanced the photodegradation of organic compounds owing to the increased separation of

photogenerated charge carriers and improved rate of the reduction reactions. Several studies have reported the loading of co-catalysts such as platinum, palladium, and nickel oxide on the surface of photocatalysts [86, 87]. The formation of a heterojunction between the photocatalyst and co-catalyst provides an internal electric field which promotes the separation of e^-/h^+ pairs and stimulates the faster charge transfer of photogenerated charge carriers, resulting in improved conductivity, low overpotential, and enhanced photocatalytic activity.

It has been observed that metal doping can also form surface complexes with titania, which may affect its adsorption properties [88]. Additionally, the amount of the dopant plays a crucial role in the ultimate photocatalytic capabilities of titania; thus, an optimum amount of dopant is recommended. Below the optimum concentration, the dopant effectively separates charge carriers, whereas charge recombination increases beyond this concentration [89]. Furthermore, metal doping has certain limitations: large-scale synthesis processes are cost inefficient, and doped titania is thermally unstable [90]. Therefore, the dopant materials are usually substituted by cost-effective transition metals or non-metals.

Non-metal dopants, including carbon, nitrogen, sulphur, phosphorous, and fluorine [91], are more suitable than metal dopants for increasing the photocatalytic activity of titania since their impurity states are close to the valence band; however, they do not act as recombination centres. Many efforts have been made to designing an effective titania doped photocatalysts with extended absorption edge. Among them, nitrogen and carbon doped titania nanoparticles have been discovered to exhibit higher photocatalytic activity when exposed to visible light, while carbon doping has been found to show five times more pollutant degradation than nitrogen doped titania.

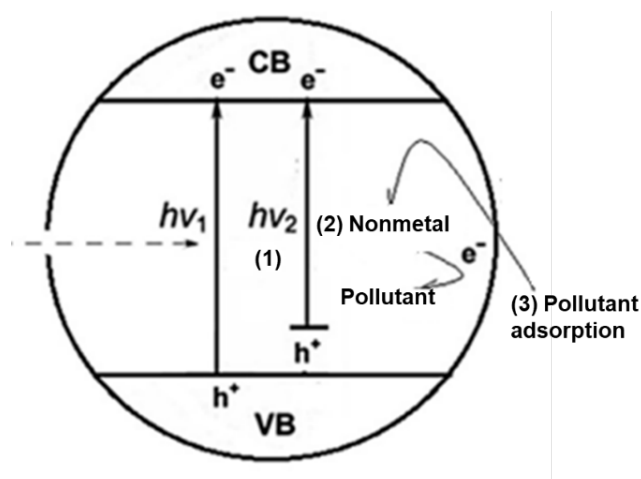


Figure 1.8 Mechanism of non-metal doped titania photocatalysis (1) band gap hv_1 and hv_2 are photon energy required for pure titania and for non-metal doped titania, (2) facilitated transfer of electron/hole pair; and (3) adsorption of contaminants. Adapted representation from [85].

Valentin *et al.* [92] showed that carbon doped titania lattice improve visible light absorption by substituting oxygen sites or entering the interstices of titania, causing introduction of a series of localised occupied states into the band gap of the titania lattice. In addition, carbon doping can improve the conductivity of anatase titania, enhance charge transfer to efficiently generate ROS, stabilise titania, and increase the adsorption of pollutants on the surface of a photocatalyst (Figure 1.8) [93].

Despite enhancement in light absorption by doping with a non-metal, there are some shortcomings: (i) Non-metal doped titania typically results in the creation of oxygen vacancies which can act as recombination centres for photogenerated e^-/h^+ pairs; hence, the overall efficacy of the material is reduced for large-scale applications [94], (ii) the stability of non-metal doped titania gradually deteriorates as the photocatalytic reaction proceeds, and (iii) toxic precursors and high temperatures are required for the synthesis of a stable non-metal doped titania photocatalyst which becomes cost inefficient. Overall, creation of new photocatalysts and the improvement of existing photocatalysts with visible light activity, better surface properties, and high stability are critical for the commercialisation of photocatalytic systems on a larger scale.

Enhancement of adsorption of contaminants on titania

As mentioned earlier, the adsorption capabilities of titania are ineffective; hence, improving the adsorption of contaminants on the titania surface can significantly

enhance photocatalytic activity. Another approach to improving the photodegradation of pollutants is to combine titania with an adsorbent with a high surface area, particularly activated carbon [95]. This can be expressed as the diffusion of pollutant species from the adsorbent to the photocatalyst surface or the disintegration of pollutants on the adsorbent by ROS generated by titania. Hence, the synergistic effect of both phases results in superior pollutant degradation properties. The optimum ratio of adsorbent/titania is crucial, as it can affect the interfacial area and ultimate performance of the material. As previously described by Foo *et al.* [42], biphasic activated carbon and titania composites facilitate the modification of the microstructure, chemical and physical properties, chemical interactions, and energy bandgap of titania, consequently improving the thermal, mechanical, and optical properties of the composite and enabling visible-light photocatalysis as well as improving the durability and strength of the material.

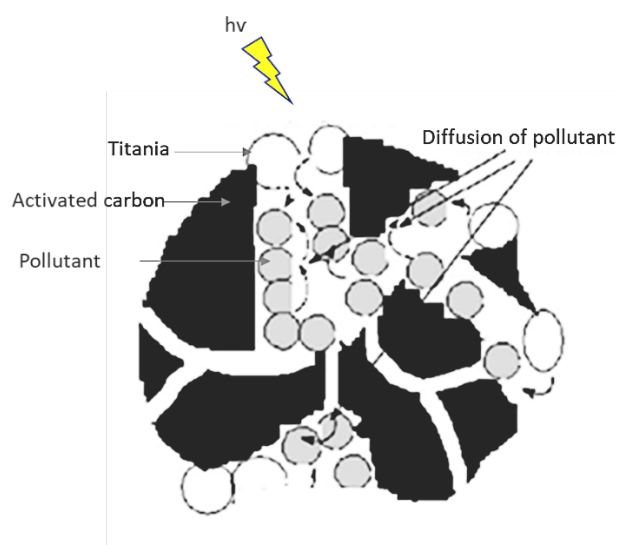


Figure 1.9 Schematic illustration of pollutant interaction with porous titania/activated carbon material [96].

Several other forms of carbon, mentioned earlier, have been created to achieve unique structures and properties. Their increased absorption capability and photocatalytic activity are due to their large surface area, good conductivity/efficient charge transfer, improved quantum efficiency, and efficient photon absorptivity under visible-light irradiation. Additionally, the properties of these carbon materials can be tuned to achieve the desired characteristics, such as a high surface area, and the desired

porosity of activated carbon can be obtained for enhanced entrapment of photogenerated e^-/h^+ as well as effective adsorption of pollutants on the surface of titania. Thus, it demonstrates a synergistic effect and exceptional photocatalytic activity under visible light superior to other forms of doped titania [97].

Stabilisation/aggregation/effective dispersion of titania nanoparticles

In some photodegradation processes, a high surface area might be a deciding factor because a significant number of adsorbed pollutants enhance the reaction kinetics [98]; however, titania nanoparticles tend to aggregate which may reduce the photocatalytic activity because of increased recombination rate. The stabilisation of titania nanoparticles on support matrices may be an effective approach to resolve this problem. Previous research has shown the immobilisation of titania onto materials such as glass, fabric, fibres, stainless steel, activated carbon, alumina, and zeolites, as demonstrated in a review paper by Shan *et al.* [99]. However, a shortcoming of this approach is that not all suspended titania nanoparticles are exposed to irradiated light which consequently reduces efficiency. To circumvent this, the final material can be obtained as thin coating or titania nanoparticles can be immobilised in a highly porous three-dimensional network. In addition to preventing aggregation, the immobilisation strategy can improve the dispersion of nanoparticles as well as surface chemistry for enhanced adsorption. Surface properties determine the charge transfer of photogenerated charge carriers, redox reactions, and photodegradation of pollutants. Recent interest has drawn attention to photocatalysts that offer morphology with a greater proportion of highly responsive facets [100], as high-energy facets promote the adsorption of pollutants on the surface of the photocatalyst, leading to efficient photocatalytic processes. These modifications can be accomplished by prudent selection of an appropriate synthesis scheme. Additionally, immobilising strategy can also prevent nanoparticle leaching and ease the post-treatment removal method [101].

Separation of titania post treatment

Although the reactive surface area of finely dispersed titania nanoparticles is considerable, it is challenging to separate and recover them from the liquid phase. The regeneration and reuse of titania particles are essential for determining their future applications in terms of cost-effectiveness. In photocatalytic systems, it is difficult to

efficiently immobilise or separate the TiO₂ particles. Two potential solutions have been investigated to address this separation issue: immobilised titania onto a support and the design of a magnetic photocatalyst for separation by an external magnetic field. He *et al.* [102] reported recoverable magnetic core shell titania nanoparticles, and the regeneration of the photocatalyst was attributed to the magnetic properties of the material, including supermagnetism, magnetic irreversibility, and saturation. A few examples of magnetic core materials include iron (III) oxide, nickel ferrite, cobalt ferrite and cobalt tetraoxide. Recently, research has focused on developing multicomponent photocatalysts with increased visible-light photoactivity and recyclability. Tang *et al.* [103] designed a multicomponent system, graphene doped magnetic titania, which exhibited excellent photocatalytic properties, easy photocatalyst recovery, and efficient reusability (only 3% loss after eight successive cycles). Excellent performance was attributed to titania photocatalysis, high adsorption of pollutant and enhanced charge transfer properties provided by graphene and effortless separation by applying external magnetic field.

Despite its widespread application and development over the last few years, titania-based photocatalysis continues to face technical challenges, and the approach is impeded by many major technical challenges, including inefficient use of visible light, limited adsorption capacity for hydrophobic pollutants, homogeneous dispersion in aqueous suspensions, and post-treatment recovery of titania nanoparticles after water treatment, thus restricting its commercialisation. Therefore, additional research and development in this field are required to alleviate these limitations and expand the use of titania-based materials for photodegradation.

Chapter 2: Literature Informed Development of New Composite Materials

In recent decades, there has been a paradigm shift from the bulk to nanomaterials, which has resulted in significant advances in nanotechnology for the development of nanomaterials. This has provided new opportunities for their use in environmental applications, including water remediation. The physiochemical properties of materials at the nanoscale have drawn researchers' attention to the development of nanomaterials to eliminate a wide selection of organic and inorganic pollutants, including emerging pollutants, from surface waters. Many studies have mentioned the harmful impact of these nanomaterials; nevertheless, the control of these nanomaterials and their impact on human health, plants, and aquatic ecosystems remains a challenge. Therefore, the development of materials using a green approach is necessary for water remediation without potential toxicity for safe applications [104].

In the light of understanding developed through literature, adsorption, among several water treatment techniques, is an efficacious approach and economically viable new materials are being explored to enhance the adsorption capacity and target a wide array of pollutants to remediate water pollution. A well-designed adsorbent with large surface area and adsorption capacity can effectively be employed for pollutant removal. However, a drawback of this technique is incomplete elimination or disintegration of pollutants. Photodegradation, as previously explained, has potential to break down contaminants without producing toxic disinfection by-products. In this context, titania is already recognised photocatalyst due to its high photocatalytic efficiency, high stability, and affordability. Nevertheless, since titania only activates upon UV irradiation, its electronic configuration must be tuned for visible light activated photodegradation to occur. To solve this, carbon has been proven to be an excellent dopant to reduce bandgap of titania and expand the adsorption edge of titania to the visible region of the electromagnetic spectrum. Numerous carbon-based materials are reported to have increased the adsorption capacity of pollutants, shifted the absorption edge, and exhibited efficient pollutant degradation performance under visible light irradiation. Hence combining adsorption and photodegradation techniques is a rational approach by exploiting the synergistic effect of titania and carbon materials.

Although various studies have combined titania and carbon materials for water remediation, physiochemically stable and sustainable materials with all the essential characteristics required for exceptional pollutant removal are still lacking. Therefore, it is essential to design a stable multifunctional material that incorporates the attributes of visible-light photocatalysis and has a high adsorption capacity for combined adsorption-photodegradation. To accomplish this, the selection of basic materials and synthesis techniques must be carefully designed. Generally, the integrated material should have a high surface area and porosity for greater adsorption of pollutants, the photocatalyst must be homogeneously dispersed, and there should be effective charge separation of photogenerated charge carriers and rapid charge transfer to the surface for redox reactions. In addition, the material should be economical, stable, nontoxic, can completely degrade a wide range of pollutants, do not produce harmful by-products, and be easily separable and recyclable.

2.1 Porous Carbon Gels

Three-dimensional porous carbon materials with large surface areas and tuneable porosities are ideal host materials. In this regard, carbon gels, a form of porous organic polymers, have been employed in various fields such as electrode materials [105, 106], hydrogen storage [107], and support for heterogeneous catalysts [108, 109].

Carbon gels were first discovered as aerogels by Kistler in 1931 [110]. The gels were successfully created by the sol-gel method and utilising the supercritical liquid evaporation method, which ensured that the internal structure did not alter or shrink, which was a breakthrough in colloid chemistry. However, it has taken more than half a century to synthesise and manufacture carbon gels for rediscovery and exploration. Resorcinol is a phenolic trifunctional compound to which formalin can be added at the 2, 4 and/or 6- positions in the aromatic ring. The polycondensation reaction occurred under alkaline conditions (produced by the catalyst) and formed a mixture of addition and condensation compounds. Pekala *et al.* [111] developed a procedure to synthesise resorcinol–formaldehyde (RF) gels with two main reactions: the addition reaction to form hydroxymethyl derivatives of resorcinol, as shown in Figure 2.1, and the condensation of these derivatives to form methylene and methylene ether-bridged compounds followed by disproportionation of the methylene ether bridges. The

reaction mixtures were then dried at 85°C for several days, after which solvent exchange procedures were essential before the critical drying process, inert gas was flowed to replace the solvent, and organic aerogels were obtained.

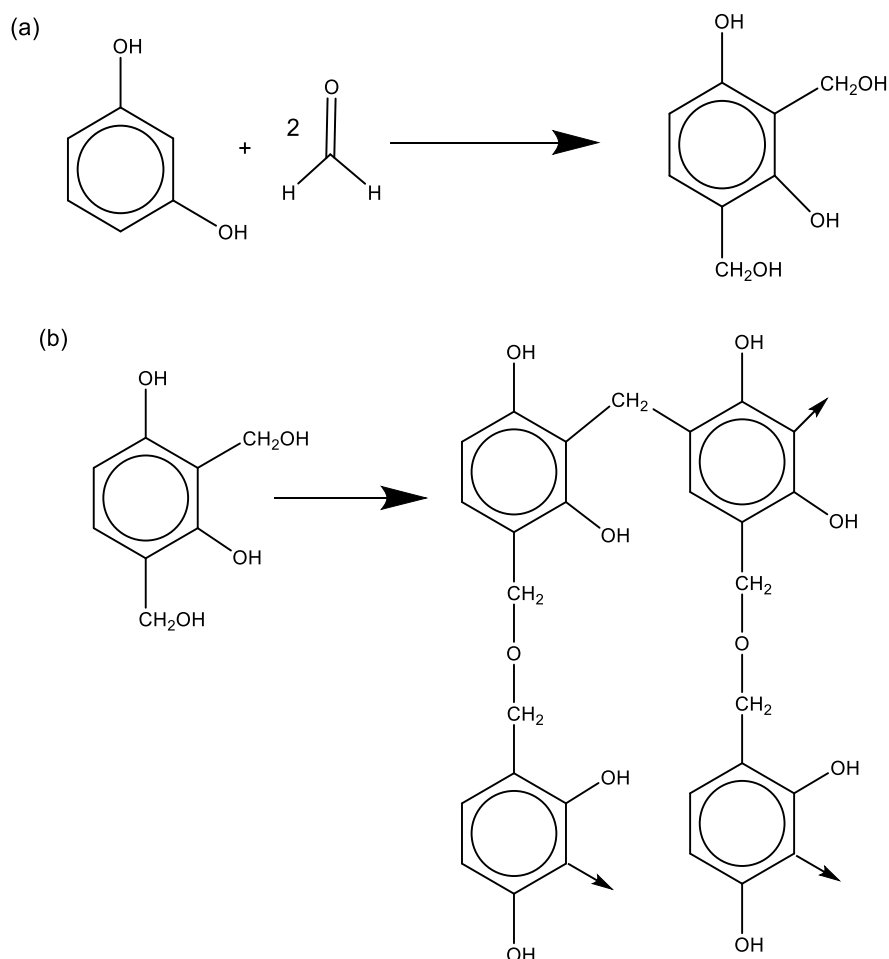


Figure 2.1 Reaction scheme of resorcinol-formaldehyde gels (a) addition and (b) polycondensation reaction.

The sol-gel polymerisation of resorcinol-formaldehyde produces materials with a large surface area (in the range 200-1000 m²g⁻¹, depending on the synthesis methodology) and uniform mesoporosity [112]. The textural properties depend on the drying procedure of the gels. To be classified as aerogels, wet RF gels must undergo supercritical drying following gelation, which involves heating the system over the critical temperature and pressure of the pore fluid to achieve its supercritical state, which is often performed using CO₂, and the water within the gels must be replaced with an organic solvent before drying, ensuring the miscibility of liquid CO₂ [113]. Supercritical drying has some drawbacks: it is an expensive process that requires

specialised equipment, making it less appropriate for industrial use. Alternative drying techniques produce xerogels and cryogels that are dried using a subcritical drying approach and freeze drying, respectively. Although the subcritical drying approach is cost-effective compared to other drying methods, significant shrinkage of the porous structure may occur. To obtain cryogels, the liquid trapped within the gel pores is frozen and removed via sublimation [114].

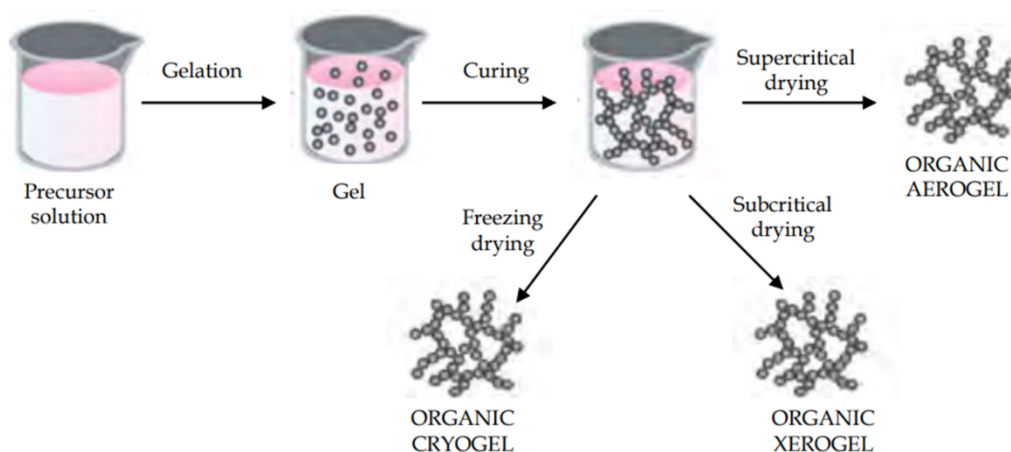


Figure 2.2 Schematic representation of the steps and drying methods to obtain organic gel [114].

The renaissance of carbon gels is beneficial for extensive applications and is still widely explored in various sectors attributed to their tunability, large surface area, porosity, and high electrical conductivity. Until recently, substantial research has been reported on RF-based carbon gels for energy storage applications owing to their properties such as high surface area, which provides efficient adsorption of ions, resulting in enhanced energy storage [115]. Additionally, the interconnected porous network can provide a continuous, unhindered transportation pathway for ions, thereby improving the efficiency of these gels for electrochemical use. In contrast to other carbon structures such as carbon nanotubes, carbon nanorods or fibres, and graphene, the 3D structure of RF gels can be considered useful for accomplishing a high mass loading of active materials such as transition metals. In addition, these gels can be considered as robust supports for incorporating active materials owing to their high mechanical strength.

Based on these characteristics, RF gels can potentially be used for water remediation applications based predominantly on the removal of pollutants through adsorption. The features of these RF gels, such as well-developed porous networks with large surface areas and porosities [113], resemble activated carbon which is currently the most extensively utilised adsorbent and is commonly used to remove complex dyes, metals, and microbes from contaminated water owing to its large surface area and pore volume which intuitively promotes the adsorption capacity and enhances the diffusion of pollutants into the internal pores of the adsorbent [116]. Nevertheless, owing to high processing costs, the persistent application of activated carbon for water treatment is often limited. Another drawback of conventional activated carbon is that pollutants are only separated from contaminated water and are not destroyed [117]. Nonetheless, these porous carbon materials can potentially be tailored to target the required pollutants because the adsorbent-based technique is a sustainable choice for water remediation [116]. To improve the adsorption capacity and engineer a suitable adsorbent for adsorbing targeted pollutants, the adsorption mechanism was elucidated.

2.1.1 Previously Developed Porous Carbon Modified Titania

Referring to the characteristics of porous carbon materials reviewed in the previous section, the tunability of RF gels enables their use in various fields. The flexibility of carbon gel synthesis allows tailoring the properties of materials and can act as potential hosts to achieve synergistic properties.

Yin *et al.* [118] successfully integrated titania into carbon gels to improve photocatalytic water splitting. Their work showed that an appropriate carbon aerogel content can improve the structure and electrochemical performance of the electrode. Zhao *et al.* [119] employed carbon gels to modify titania to increase its adsorption capacity and conductivity performance of a photoelectrode material made of titania/carbon aerogels, where the carbon aerogel was synthesised by the catalysed polycondensation of resorcinol-formaldehyde. The carbon gel was submerged in a titania sol, and the mixture was sintered to obtain a photoelectrode material. To probe the textural properties, several characterisation techniques, such as scanning electron microscopy (SEM), X-ray diffraction (XRD), Raman spectroscopy, and N₂ isothermal

adsorption and desorption studies, were conducted. Their study concluded that the excellent photocatalytic properties were attributed to anatase-phase titania and enhanced electrochemical properties owing to the carbon aerogel. Hence, a higher photodensity and electrosorption process resulted in the successful degradation of methylene blue dye. Likewise, successful degradation of methyl orange was reported by a synthesised titania/carbon aerogel composite, obtained by combining titanium isopropoxide and carbon aerogel in alcohol media. The study established that a highly mesoporous structure exhibited maximum degradation of dye when compared with macroporous titania/carbon aerogels. The micropores could not contain large sized dye molecules whereas macropores were too large to accommodate dye molecules inside the porous network of gels, hence mesoporous composites were claimed to be effective towards adsorption and photocatalytic reaction [120].

Jin *et al.* [121] reported the combined electrosorption, adsorption, and photocatalytic performance of carbon/titania composites. These composites were prepared by dispersing the prepared carbon aerogel into a titania precursor solution and subjecting it to subcritical drying. The final composite material was probed using scanning electron microscopy (SEM), EDS (energy dispersive spectroscopy (EDS), TG/DTA (Thermogravimetric Analysis/Differential Thermal Analysis (TG/DTA), nitrogen sorption (analysed using Brunauer-Emmett-Teller theory), Electrochemical Impedance Spectroscopy (EIS), and Raman spectrometry. The application tests performed against dye reduction showed ~97% dye reduction in 240 min (initial dye concentration of 400 mg L⁻¹). Their work also validated the good stability of the composites, where the efficiency was reduced by only 5% after five repeated cycles. The possible synergistic effects of electrosorption and photocatalysis are shown in Figure 2.3. This indicates that pollutant molecules adsorb on the surface of the electrode by electrosorption, while titania photogenerated electron/hole pairs and redox reactions occur as a typical photocatalytic mechanism of titania, as explained in Section 1.1. However, in this case, the photogenerated charge carriers are separated by applying a voltage across the titania to avoid the recombination of charge carriers. Overall, the synergy between titania and carbon aerogels improved the dye degradation performance.

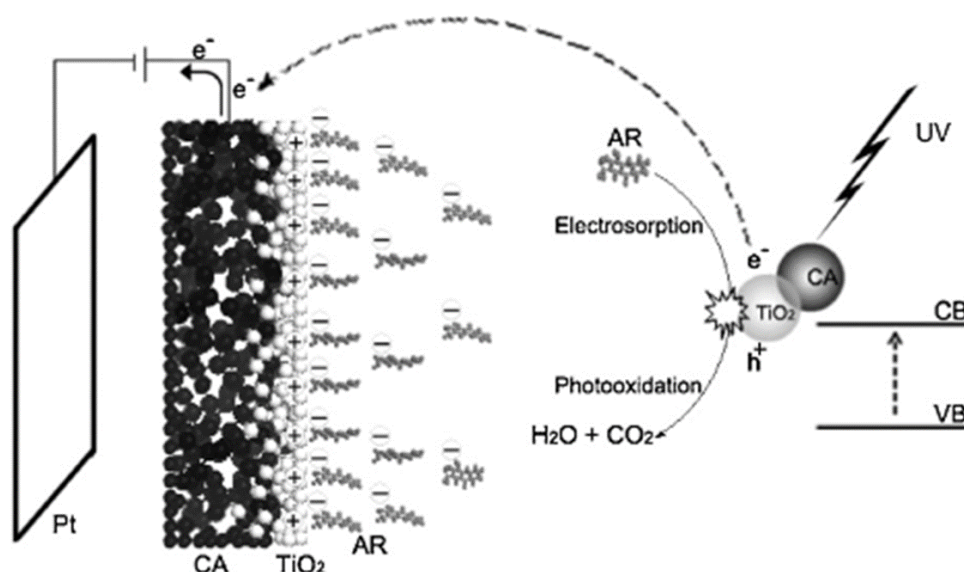


Figure 2.3 Schematic of synergistic electrosorption and photocatalysis by titania/carbon aerogels for dye degradation (CA carbon aerogel, CB conduction band, VB valence band AR Alizarin red dye) [122]

Furthermore, improvements have been made to increase the light absorption capacity of titania. The titania/carbon aerogel composite acted as a photoelectrode and mineralised 90% of the dye upon visible light irradiation, which was attributed to the transfer of charge carriers through surface complexes [121]. The visible light response of such systems has improved and is red-shifted from 380 to 532 nm [123]. Shi *et al.* [124] discovered that the photocatalytic activity of titania can be improved by forming composites with carbon aerogels and creating secondary pores to enhance wettability. Their study revealed that mesoporous materials with a diameter of ~ 9 nm demonstrated the highest photocatalytic activity against the degradation of dimethyl phthalate (DMP), while those with pore diameters of ~ 4 nm exhibited inferior results. The designed composite showed a synergistic effect whereby the photogenerated charge carriers were captured by the carbon phase, improving the charge separation and inhibiting electron/hole recombination. The mechanism of DMP degradation by titania/carbon aerogels is shown in Figure 2.4. According to the scheme, (I) hydroxyl radicals form on the titania surface upon contact with water, (II) photogenerated charge carriers migrate to the internal carbon surface, (III) photogenerated charge carriers are trapped by carbon, (IV) further reactive species are produced, and (V)

DMP is oxidised by the reactive oxide species on the inner and outer surfaces of the composite material.

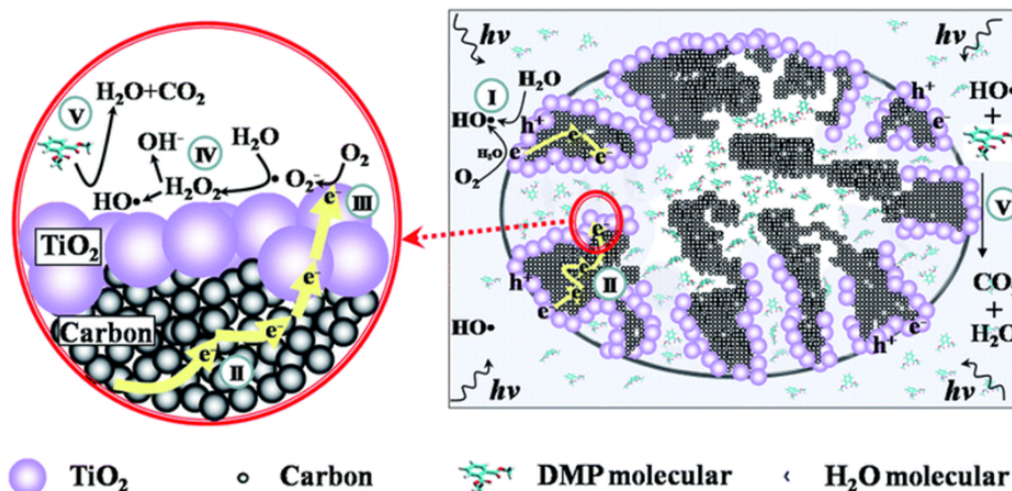


Figure 2.4 Schematic representation of degradation of pollutant DMP by titania/carbon aerogel composite [124].

The synergistic adsorption-photodegradation performance of integrated titania and carbon gels has been tested successfully against the removal of several dyes, and further modifications may potentially expand the technique for a wide range of pollutants. However, the processing of carbon aerogels require] an intensive energy input process, along with a significant amount of precursors. Furthermore, the photocatalytic process usually requires an additional energy source for the photoactivation of titania. In addition, studies on these composite materials lack an understanding of adsorbate-adsorbent interaction mechanisms.

2.2 Development of New Carbon-Titania Xerogels

According to the literature, carbon derived from RF gels is an efficient porous material with enhanced adsorption capacities and is an ideal host for nanomaterials such as titania. Inspired by the notion, the conventional synthesis method to obtain RF gels is modified in this work and a new approach is developed to combine carbon/titania materials.

Previous research has shown that three-dimensional mesoporous structural design of carbon xerogels with high surface may be produced under certain parameters, implying that the material is suitable to attain high adsorption capacity of pollutants. In

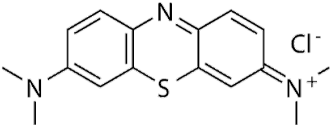
this work, the modification in synthesis method of carbon xerogels is modified to incorporate titania nanoparticles by adding titania precursor during the polymerisation of carbon xerogels. The sol-gel route employed would allow chemical crosslinking between the carbon and titania phases hence controlled morphology and a stable structure obtained would overcome the previously mentioned limitations such as leaching and aggregation of nanoparticles. Additionally, typically obtained gels by sol-gel route under given conditions are in the form of monoliths, allowing facile separation post-treatment.

The integration of carbon/titania results in bandgap reduction and may increase the absorption edge to the visible region thereby less energy is required for photogeneration of charge carriers which undergo redox reaction to produce ROS responsible for pollutant degradation. Now this charge transfer depends on effective charge separation of photogenerated charge carriers which is determined by the design of the material particularly implying an optimal amount of integrated carbon and titania. The notion is as explained earlier- an optimum amount of dopant is required in carbon/titania composites for enhanced visible light photocatalysis. Effective charge separation occurs below an optimum amount while recombination of photogenerated charge carriers occurs beyond the optimum amount, therefore, poor charge transfer may hinder the redox reactions and ultimate generation of ROS. In order to determine an optimal concentration, an extensive study is required by synthesising a suite of samples with different amounts of integrated carbon xerogels and titania, followed by pollutant degradation tests. This way the synergistic adsorption-photodegradation efficacy of material depending on different amounts of both phases can be determined and an optimal amount which shows maximum pollutant degradation may be beneficial for future works.

Owing its high adsorption and photodegradation capabilities, new integrated carbon xerogel and titania materials are anticipated to target a wide range of contaminants such as heavy metals, dyes, and microbes. In this work, the pollutants adsorption and degradation performance are examined against reduction of indicator dyes and microbes. As regards dyes, methylene blue (MB) dye as a model pollutant was selected in this work. MB is a cationic dye composed of a polyaromatic structure (specification shown in Table 2.1), commonly used as a model dye to study the

adsorption properties of carbon-based materials due to its stability and therefore is extremely difficult to breakdown into small inorganic compounds using conventional techniques. MB is commonly used in textile industries and its effluents are found in natural water sources that can be hazardous to human health. MB is toxic and non-biodegradable, and it can endanger human health and have a detrimental environmental effect. Human health risks from MB include nausea, diarrhoea, vomiting, dizziness, heartache, fever, anaemia, irritation of mouth, throat and stomach, irritation of skin with redness and itching discolouration of urine and bladder irritation.

Table 2.1 Specifications of Methylene blue.

IUPAC	[7-(dimethylamino) phenothiazin-3-ylidene]-dimethylazanium chloride
Molecular Weight	319.85 g mol ⁻¹
Molecular diameter	0.80nm
Chemical Formula	C ₁₆ H ₁₈ N ₈ SCl
Absorption Wavelength	663 nm
Class	Cationic thiazine dye
Structure	

Parameters affecting MB adsorption

Generally, the adsorption process is influenced by parameters such as the surface area of the adsorbent, functionality of the adsorbate, initial concentration of the adsorbate, solution pH, temperature, amount of adsorbate, and contact time.

- (i) **Adsorbent surface area:** Adsorption being a surface phenomenon is proportional to the surface area of the adsorbent. Thus, the adsorbent material should be highly porous for higher adsorption per unit mass of the adsorbent, implying that the higher the surface area, the higher would be the degree of adsorption.

-
- (ii) Adsorbent surface functionality: Adsorbate solubility is particularly important in determining the adsorption capacity and the adsorption rate. If the adsorbate is entirely soluble in the solvent, the affinity of the solute for the solvent is high [123]. Consequently, the extent and rate of adsorption of the adsorbate are reduced; hence, suggesting an inverse relationship between the adsorption degree and solute solubility.
- (iii) Initial concentration: The concentration gradient or the driving force for mass transfer is established by the initial concentration of the adsorbate in the solution. At lower concentrations, the ratio of solute to adsorbate surface was low, which became independent of the initial concentration of the solute after some time. However, at high concentrations, the solute-to-adsorbate surface ratio increases, suggesting that the number of unoccupied adsorption sites decreases, and the adsorption capacity depends on the initial concentration. Hence, with an increase in the initial concentration, the adsorption uptake capacity reduces; however, the variations are minimal [125].
- (iv) Solution pH: The surface charges influence the adsorption uptake. Dissociation of functional groups occur at the adsorbate due to the presence of H^+ and OH^- , resulting in changes in adsorption kinetics. It is generally known that with an increase in pH, the amount of negatively charged sites increase while amount of positively charged sites reduces. It is often reported that adsorption of anions is favoured at low pH attributed to the presence of H^+ ions, where it is responsible for adsorbing cations at higher pH due to OH^- ions. Since the surface of adsorbent is positively charged at low pH, an attractive electrostatic force between positively charged adsorbate molecules and anionic molecule would result in maximum adsorption process. The surface charge can be determined by studying the point of zero charge i.e., when surface charge on the adsorbent is zero [126].
- (v) Temperature: The influence of temperature depends on the nature of the adsorption. In the case of physisorption, the adsorption capacity decreases with temperature and is an exothermic process. In the case of chemisorption, the adsorption capacity increases initially with increase in temperature and then starts to decrease [44].

- (vi) Adsorbent dosage: The impact of adsorbent dose is another important aspect to consider, as it specifies the adsorption uptake and calculates the cost of the adsorbent required per unit of solution. Generally, with an increase in adsorbent dose, there is initially an increase in the adsorption efficiency which starts to decrease after reaching a plateau [127].
- (vii) Contact time: The adsorption efficiency increased with increasing contact time. The amount of adsorbate adsorbed onto the adsorbent surface increases rapidly, then slows down, and remains constant [42].

Based on abovementioned parameters, the degradation capabilities of synthesised carbon xerogel/titania against reduction of MB dye were studied and the adsorbent-adsorbate interactions were studied adsorption equilibrium data using adsorption isotherm and kinetics, explained in Chapter 7. Additionally, the photodegradation performance of synthesised samples was tested for its antimicrobial activity post adsorption phase. Here, TiO_2 is mainly responsible for the degradation of microbial contamination, due to its ability to generate ROS, which attack the cell wall of microbes and disintegrate the cell structure, causing leakage of cell matter as well as disrupting its growth. Figure 2.5 shows possible antimicrobial effects of photocatalyst TiO_2 .

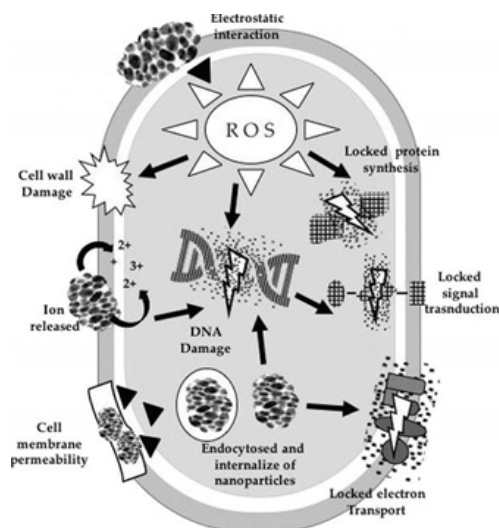


Figure 2.5 Mechanism of antimicrobial effect from a photocatalyst [128].

Most recently Ghumro *et al.* [129] reported visible light activated carbon doped TiO_2 for the reduction of *E. coli*, under visible light, possible due to a tuned band gap (2.62

eV). Their results showed ~86% reduction in bacterial survivability, which was attributed to the incorporated carbon content facilitating entrapment of charge carriers for enhanced charge separation, and resulting in increased bacterial inactivation under sunlight. No activity was reported under dark conditions, which confirmed that cell lysis was photoinduced instead of via chemical breakdown of the cell. For visualisation, an SEM image of the morphology of *E. coli*, reported earlier, is shown in Figure 2.6. It is obvious that, in the absence of visible light, the TiO₂ doped material did not show any activity and the structure of *E. coli* remained intact. Upon visible light irradiation, the rod like continuous *E. coli* membrane deformed, due to cell rupture [18] as indicated by the arrows in the image, showing a cracked cell surface in Figure 2.6 d, confirming photoinduced destruction of *E. coli*.

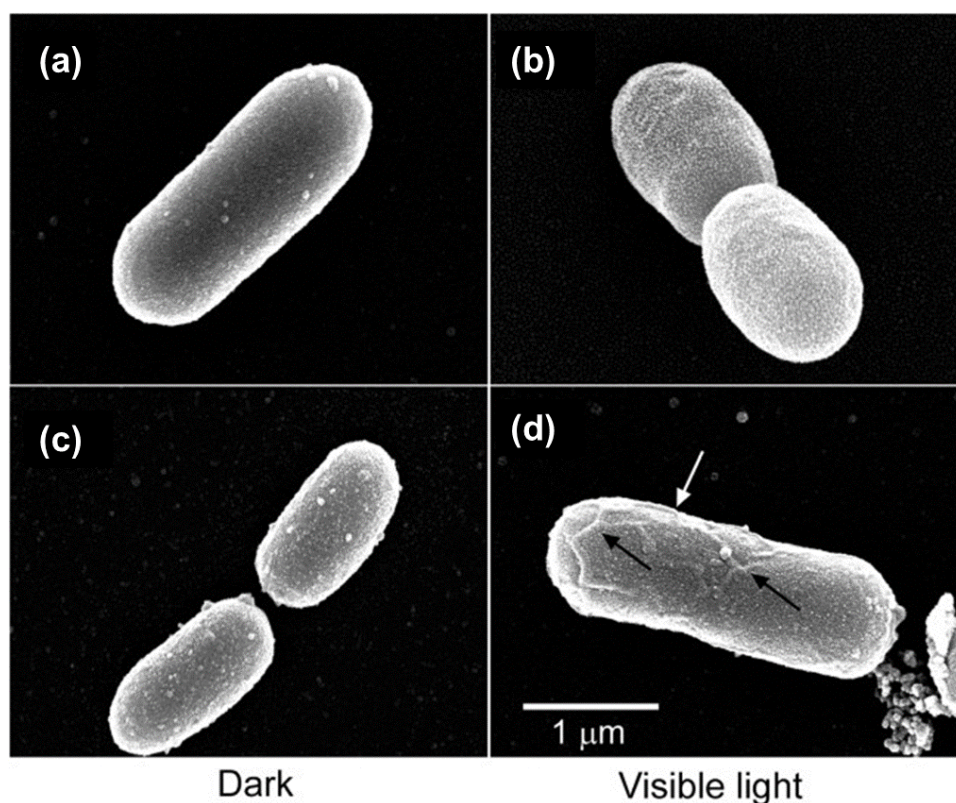


Figure 2.6 SEM image of *E. coli* in dark (a, c) and when subjected to visible light (b, d), arrow in d indicates change in morphology of *E. coli* which ultimately leads to cell destruction upon attack of reactive oxide species [18].

The antimicrobial performance can be tested against a biological indicator, coliform bacteria (generally referred to as faecal coliform, bacterial grouping shown in Figure 2.7), which is commonly employed as an indicator of faecal contamination because

they behave similarly to most pathogenic bacteria in the environment and are abundant and simple to detect during treatment. Faecal coliforms are microscopic bacteria which typically live in the faeces of warm-blooded animals and are expelled by their digestive system. When faecal coliform bacteria are abundant in a water sample, it indicates that the water has acquired faecal matter from some sources. Consumption of water contaminated with faecal matter is a health risk as it causes typhoid, viral infections, and hepatitis A. Untreated faecal matter is a risk to aquatic life since its presence depletes the oxygen levels.

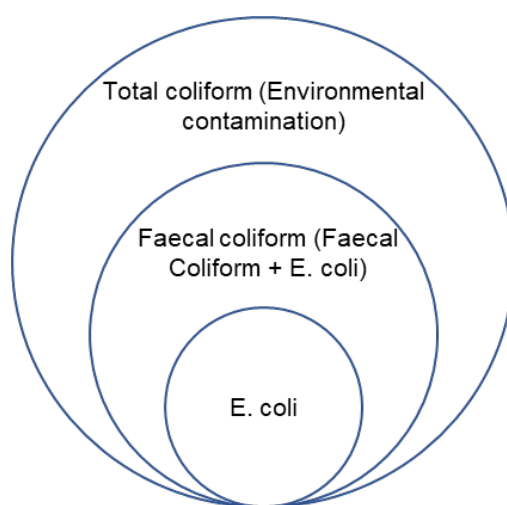


Figure 2.7 Bacterial grouping: faecal coliforms are a subset of total coliform bacteria; *Escherichia coli* (*E. coli*) is a subset of faecal coliform bacteria.

Although faecal coliform bacteria are not always disease causing agents, their presence may signal the existence of disease-causing organisms that reside in the same environment as faecal coliform bacteria. The presence of faecal coliform bacteria in freshwater environments suggests that the water has been polluted by pathogens and viruses. Generally, the preferred method for faecal coliform detection is membrane filtration. Hence, in this work, membrane filtration method is used to detect the presence of total coliform faecal coliforms and *Escherichia coli*.

2.3 Aims and Objectives

As discussed in the previous chapter, the properties of titania can be modified to accomplish visible light activated photocatalysis through combination with other materials, such as nano carbon. Exploiting the synergy between carbon and titania

can be an efficient approach for water remediation applications; however, the choice of materials for optimised adsorption and processing is critical. Therefore, this study aims to develop an efficient material that exhibits combined adsorption and photocatalysis, achieved via the following objectives:

1. Development of a synthesis scheme to integrate resorcinol-formaldehyde (RF) and titania (TiO_2) composite gels by developing a strategy based on an established formation mechanism for resorcinol-formaldehyde gels.
2. Synthesis of a suite of materials using a range of RF and TiO_2 ratios in RFTi gels to gain insight into the influence of changing this ratio on the structure-property relationship, and its subsequent effect on adsorption and photodegradation applications.
3. Probe the effect of varying ratios in RFTi gels by analysing:
 - Textural properties to determine the morphology, surface charge properties, surface area and pore size distribution
 - The chemical linkages between RF and TiO_2 , providing corroboration of hypotheses
 - The electronic structure of TiO_2 , through redshift to the visible light absorption edge, and consequent reduction of the band gap
 - The thermal degradation of RFTi gels
4. Experimentally determine the efficacy of RFTi gels in the mineralisation of pollutants, using methylene blue as a model pollutant, and evaluating:
 - Adsorption performance with respect to the ratios used to synthesise RFTi gels
 - Adsorption kinetics for methylene blue removal, in relation to the dependence on RF: TiO_2 ratio, and interpretation using kinetic models and mass transfer kinetic models
 - Adsorption isotherms for methylene blue removal, and dependence on RF: TiO_2 ratio, through fitting of the equilibrium adsorption data to isotherm models, in order to gain an understanding of the adsorbate-adsorbent interactions.
 - The effect of temperature, through thermodynamic analysis of RFTi gel performance

5. Assess the visible light activation performance of RFTi gels, with respect to changes in the optical properties of RFTi gels.
6. Determine the antimicrobial performance of RFTi gels, under visible light irradiation, against indicator microorganisms, using a membrane filtration method.

2.4 Summary

Exploiting the exceptional adsorption properties of porous organic carbon gels and photocatalytic properties of titania nanoparticles, the development of an integrated material has the potential to be employed for water remediation. The complete eradication of a wide range of pollutants can be achieved by optimising the synergy between the carbon and titania phases, as explained in the preceding discussions. Synthesis of a suite of materials with different amounts of carbon and titania and study on combined adsorption-photodegradation based on their structure property relationship could substantially increase their applicability beyond water remediation.

Chapter 3: Synthesis and Characterisation of RFTi Composites

This chapter describes the experimental procedure used to synthesise the integrated carbon xerogels. A suite of composite gels was synthesised by incorporating TiO_2 in carbon xerogels at 10% sequentially increasing steps, yielding a total of nine composite gels in addition to pure RF and TiO_2 for comparison, allowing the investigation of the influence of material properties on their use in targeted applications.

3.1 Methodology

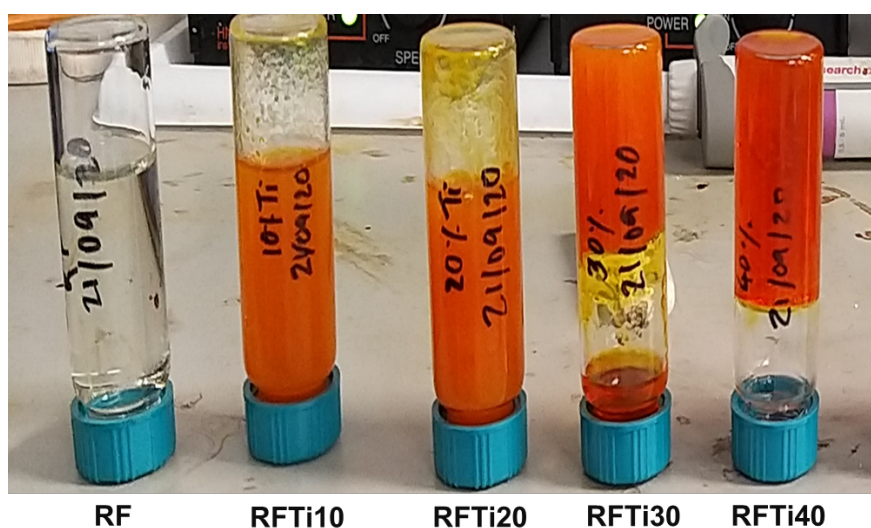
An established sol-gel method to synthesise RF gels was adapted to develop RFTi gels [111]. RF and titanium (IV) isopropoxide were used as carbon and titania precursor, respectively. The main reagents required were resorcinol (R), formalin (F), sodium carbonate, Na_2CO_3 (C), which acts as a catalyst, titanium (IV) isopropoxide (TTIP), HCl, ethanol (EtOH), and deionised water. Within the RFTi gels synthesised here, the compatibility of the inorganic-organic phase was improved by integrating TiO_2 sol during the polymerisation of the RF gel. Hence, RF and TiO_2 sols were prepared separately, prior to integration in accordance with a specified ratio of RFTi incorporated into the gels.

The amount of precursors and reagents were varied according to the gels being prepared. For TiO_2 , a constant ratio was maintained as per 1 TTIP:10 EtOH:0.3 HCl:0.1 H_2O . The solvent chosen to prepare TiO_2 sols was ethanol (EtOH), to ensure homogenisation, due to its low viscosity; while RF sols was prepared in water, maintaining a constant ratio of R:F 0.5 and R:C 300 (the relationship and optimisation of the R:F and R:C ratios are detailed elsewhere [113]), according to the reaction stoichiometry. To synthesise the pure gels, for comparison, these ratios were maintained, and the RF and TiO_2 sols were processed according to the steps described below. The initial compositions of all reagents are recorded in Appendix A, Table A1.

3.1.1 Sol-Gel Procedure

TiO₂ sol: The required volume of TiO₂ sol was first prepared in a 50 mL sealable glass bottle by dissolving TTIP (98+%, Acros Organics™) in EtOH under magnetic stirring, at room temperature. To this TiO₂ solution, a mixture of HCl (37%, Sigma Aldrich) and deionised water was added dropwise. A clear homogenous solution was obtained, and left to stir at room temperature for 2 h, after which time the pH was recorded using a Hanna Instrument benchtop pH meter.

RF sol: In order to prepare the RF sol, 50 mL of deionised water (Millipore Elix 5 with Progard 2) was added to a sealable jar, and the required amount of resorcinol (Sigma Aldrich, Reagent Plus, 99%), weighed out, with an accuracy of 10⁻⁵ g, and added to the jar. After the flakes of resorcinol were completely dissolved, under constant stirring, the corresponding amount of C (Na₂CO₃ Sigma Aldrich, anhydrous, ≥99.5%) was weighed and added to the system. The required amount of formalin (Sigma Aldrich, 37 wt% formaldehyde, with 15 wt% methanol and 53 wt% water) was added to the mixture. During the polymerisation reaction of the RF sol, the initially prepared TiO₂ sol was gradually incorporated and the RFTi sol was agitated for 30 min. After the stirring period, the magnetic stirrer bar was removed from the mixture solution and the pH was recorded using a Hanna Instrument pH meter. Photographs of integrated sols are shown Figure 3.1 (transferred from jars to vials). The jar lids were then tightened and placed in an oven (Memmert UFE400), preheated to 85°C, for 72 h.



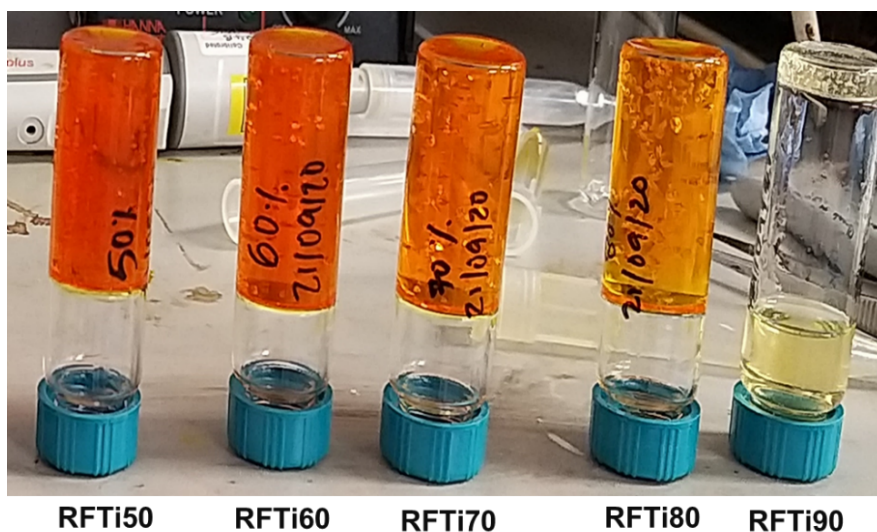


Figure 3.1 Photographs of integrated RFTi sols.

3.1.2 Solvent Exchange

Solvent exchange is part of drying process, performed to remove solvent (water in this case) from the pores of the gel by exchanging it with acetone to assist the drying process. After 72 h, the jars were taken out from the oven and allowed to cool to room temperature. The wet gel samples were then cut into small pieces of approximately equal size, in order to maximise the surface area and, hence, improve solvent exchange. Following a standard solvent exchange procedure: 100 mL of acetone (Sigma Aldrich, $\geq 99.5\%$) was added to the jar, and the jar gently shaken for a few seconds to wash off water from the gel surface and walls of the jar. Then, the acetone was drained, and 150 mL of acetone was added to the jar. The jar was then resealed with paraffin film to reduce solvent evaporation and placed on a shaker unit (VWR 3500 Analog Orbital Shaker) at a shaking speed of 4 (~ 400 rpm). The acetone was emptied and refilled with 100 mL of acetone after approximately 24 to 72 h. If the gel structure seemed too weak (for example, the samples with very high content of titania), the solvent exchange was carried out as mentioned and the jars were kept on the lab bench instead of placing them on the orbital shaker, in order to prevent any damage to the gel structure. Acetone was drained from the jars after 72 h, after which the samples were dried.

3.1.3 Vacuum Drying

Aluminium foil was used to cover solvent-exchanged RFTi gel samples, and the foil was perforated to avoid cross-contamination of other samples in the oven, in the case of rapid acetone evaporation. The covered jars were then placed in a vacuum oven (Towson and Mercer 1425 Digital vacuum oven). The rubber gasket seal was ensured to be intact before closing the vacuum oven door. The temperature was set at 110 °C, corresponding to 85±5 °C inside the oven (monitored using a thermometer placed inside the oven). A vacuum pump, with two solvent traps attached to the oven, was switched on. Solvent traps were encased with ice packs to condense acetone evaporated from the samples and the traps were monitored to ensure drying of the gel sample. To ensure safety, the oven and vacuum pump were operated during laboratory working hours (approximately 8 h) for two consecutive days. After 48 h, when no more acetone condensed in the solvent traps, the gel samples were collected and transferred to labelled sample vials, indicating the amount of titania present in the sample, along with the synthesis date. The sample codes are indicated as RFTi X%, where 'X' indicates the percentage of titania present in the sample. Figure 3.2 shows the dried RFTi30 gel pieces as a reference. The chemical scheme for this synthesis is illustrated in Chapter 4, Figure 4.23.



Figure 3.2 Photograph of vacuum dried RFTi gel (approximate scale bar shown).

3.2 Materials Characterisation Techniques, Application and Theory

The experimental techniques employed to study the properties of the RFTi gels synthesised in this study are discussed. The instrumentation, and theory behind these techniques, are explained to gain an insight into the material properties probed using these methods. At the end of the discussion for each technique, the specific experimental procedures used to obtain data within this work are outlined. This Chapter discusses a range of methods used to probe the overall characteristics of the materials. As regards surface analysis, the changes in morphology of the samples, with varying ratios of RF and TiO_2 in the samples were studied through micrographs obtained from field emission scanning electron microscopy. In addition, the point of zero charge at the sample surface was experimentally evaluated by the drift method. The textural characteristics of RFTi gels were examined through adsorption analysis, providing information on surface area and pore size measurements. Regarding the chemical properties of the gels, Fourier transform infrared (FTIR) spectroscopy was used to study the chemical linkages present within the material. FTIR was also employed as an assistive technique to corroborate the changes in material properties post-adsorption. Furthermore, the theoretically calculated composition of RF and TiO_2 , experimentally deposited during synthesis, was validated by thermal gravimetric analysis, while different thermal methods were employed to analyse the thermal

stability of the material. UV-Vis Spectroscopy was used to measure light absorption by RFTi gels, with the data collected used to evaluate the change in band gap values of these materials. The performance of RFTi gels against the removal of dyes were studied by solution analysis, using UV-Vis spectroscopy to determine the solution concentration. Lastly, microbiological examination of water was conducted using membrane filtration methods.

3.3 Field Emission Scanning Electron Microscopy

Scanning electron microscopy (SEM) can provide topographical information of a sample, which includes the surface features of an object, its appearance, texture, allowing the determination of direct relations between these features and material properties. Secondly, the morphology of a sample, including the shape and size of the particles that make up an object, can be determined, which can provide a direct relation between the structure and material properties. Furthermore, SEM can provide a relationship between composition and material properties through compositional information, while crystallographic information can be obtained to gain an understanding of the arrangement of atoms in the material. Compared to SEM, field emission scanning electron microscopy (FESEM) produces clear, less electrostatically distorted images with better spatial resolution.

To study the morphology of a material and gain an insight of its characteristics at the microscale, micrographs are usually obtained using FESEM. The simplest way to understand the working principle of this technique is through the schematic diagram shown in Figure 3.3 b. There is a source of electrons, which is called the electron gun, from which fast-moving electrons accelerate down the central axis of the SEM column, which is similar to the optic axis in an optical microscope, where a central beam of light passing through lenses constitutes the optical axis. The electromagnetic lenses focus the beam of electrons, which are accelerated through a potential field. The electrons, being negatively charged, will move towards the anode and the large potential difference, resulting in increased kinetic energy as the velocity of the electrons increases, which will cause them to flow through the anode to the optical axis; this is then controlled by the magnetic lenses to ensure alignment in a central path directed to the top of specimen [130].

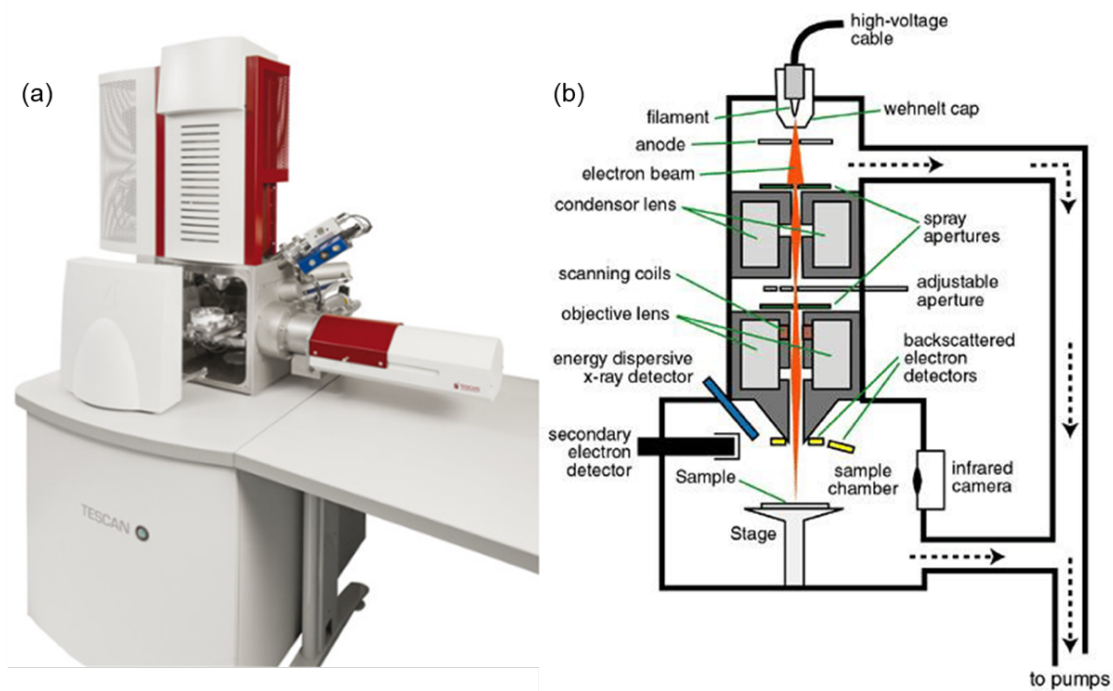


Figure 3.3 (a) TESCAN MIRA3 field emission scanning electron microscope (b) Schematic cross-sectional diagram of a scanning electron microscope [130] .

To avoid the electron beam straying, it is necessary to maintain the SEM column under a very high vacuum. The column of an SEM assembly is composed of an electron gun, with a gun alignment control to ensure that the electrons are directed downwards. The airlock valve beneath the electron gun safeguards a system of evacuation when the electron beam enters this part of the objective lens. The objective lens comprises condenser lenses, which ensure that the magnetic field is adjusted in a way to keep electrons travelling down the optical axis, where after there is an objective aperture, which controls the size of the electron beam. This is followed by a scanning coil system, which ensures scanning of the electron beam on the surface of the aperture. Fundamental principles suggest that a small aperture will improve the resolution of the image, or, in other words, smaller width of the electron beam produces well-defined details; hence, resolution can be improved by reducing the aperture. However, this reduces the intensity of the electron beam, therefore, careful selection of appropriate settings is crucial. The control of the lens power, or lens focus, is undertaken by adjusting the magnetic field generated by these magnetic lenses. Beyond the scanning coils is the objective lens system, which is, again, an electromagnetic lens adjusted to

ensure the convergence of the electron beam on the specimen. Finally, there is a sample stage.

The interactions generated between the electrons bombarding the specimen and the sample, leads to generation of back scattered electrons, secondary electrons, and X-rays (Figure 3.4), which are sensed using suitable detectors placed at critical locations in close proximity to the specimen, thereby capturing all of the electrons being emitted. The electrons escaping from the surface are detected by a secondary electron detector situated at a low angle because these are low-energy electrons and do not require a very high energy to capture the electrons by the detector. The secondary electron mode can provide a high depth of field, where a contrast image is produced depending on the secondary electron generated at different areas of the specimen. Since the specimen has a rough surface, the difference in height will produce more secondary electrons due to edge effects, and brighter spots will appear on the micrographic image while some secondary electrons produced in a trough of the specimen are difficult to deflect and, therefore, will be detected as a dark area on the image. The backscatter detector is located right around the optical axis to ensure that electrons undergoing elastic rebound with the specimen are captured, since these are high energy electrons. In summary, the secondary detector captures the secondary electrons to provide morphological information, while the backscatter detector captures backscattered electrons to provide compositional contrast, and the energy dispersive spectroscopy detector (EDS), for X-rays, provides information about phases.

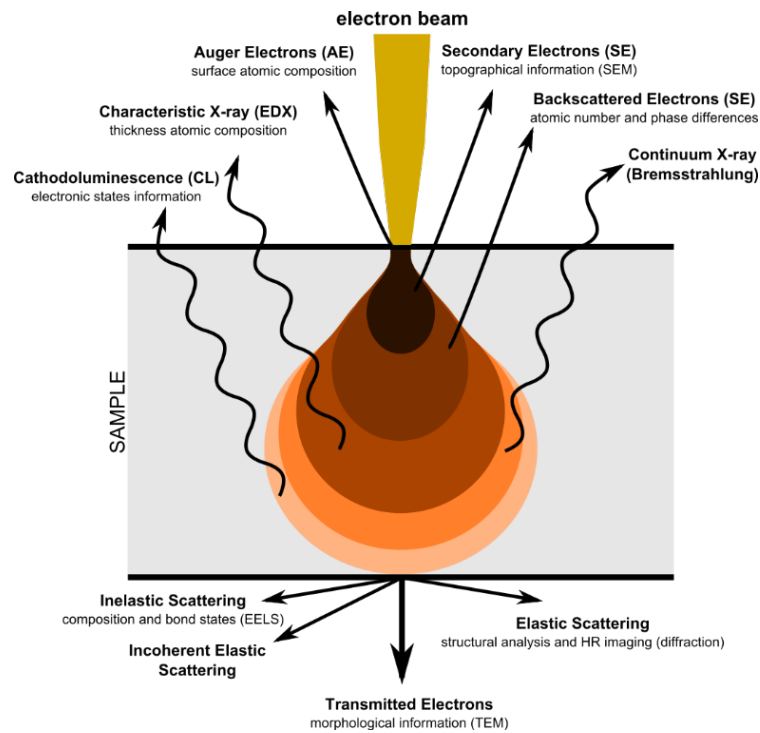


Figure 3.4 Electron–matter interaction volume and types of signals generated [130].

3.3.1 Imaging of Non-Conductive Samples

It is important to note that when imaging of electrically insulating materials, the surface of the specimen may be electrically isolated when bombarded with electrons, which leads to charge build-up on the specimen, making imaging or other analysis difficult. Consequently, electrically non-conducting samples can absorb electrons and negative surface charge can be accumulated which may repel the incident electron beam, thereby destroying the image. To counteract this, the sample is coated with a thin conductive film. A schematic representation of a sputter coating mechanism is shown in Figure 3.5 b and c. The basic layout of a sputter coater consists of an evacuated bell jar with a cathode comprised of the target material (coating material), an anode, and the sample stage. The chamber is filled with inert gas, which is energised by the formation of a glow discharge. The procedure includes intense particles eroding atoms from a suitable target and then deposition of these atoms on the sample at a low vacuum. This causes target atoms to be deflected in all directions, by collisions with gas atoms, and finally deposit on the cold surface of the sample. Although the overall drift is toward the anode, the random motion of individual metal atoms causes the

deposition to be multidirectional on the surface scale, allowing even rugged surfaces to be evenly covered [131].

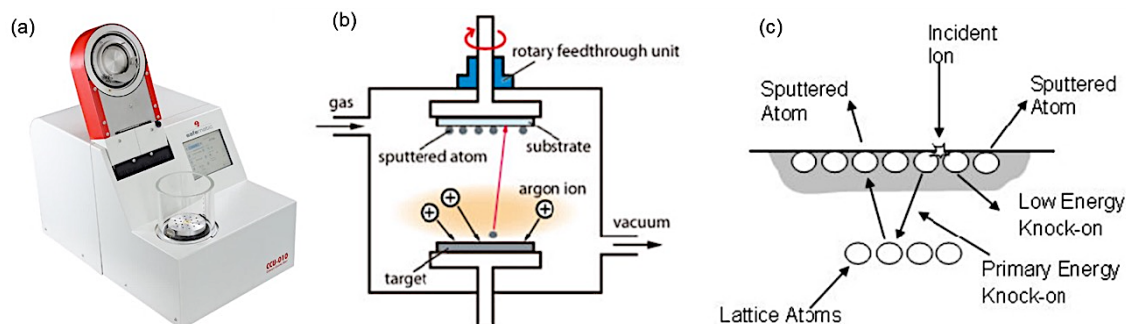


Figure 3.5 (a) Laboratory sputter coater CCU-010 HV, (b) and (c) schematic diagrams of sputtering process [132].

3.3.2 Sample Preparation and Analysis

In this work, prior to collecting micrographs, clean sample stubs were taken, and a small amount of fractured sample was mounted on the stub using conductive double-sided carbon tape. Excess sample was removed by gently tapping the sample stub on the table, which was then placed in the sputter coater to deposit a thin layer of gold. In this work, a sputter coater, CCU-010 HV (Figure 3.5 a), was used to coat the RFTi gel samples with ~ 5 nm thickness of gold coating under a process pressure 5×10^{-3} mbar and a process current 30 mA. For morphological analyses, a TESCAN MIRA3 High-resolution analytical FESEM (Figure 3.3 a) was used and images were collected at a range of magnifications. In this work, the imaging was done at 10 kV to obtain an appropriate beam penetration, considering the density of RFTi materials. The images at different magnifications were acquired mainly in secondary electron mode, and back scattered mode was used to differentiate between phases. The surface related information and features of RFTi samples, such as RF spheres and their size were determined through images obtained via a secondary detector. In order to investigate the porous structure of RFTi gel samples, images were collected in backscattering mode. Theoretically, as the backscattered intensity is a function of atomic weight, the phases that appear bright have a higher atomic density in contrast to the phases that appear dark, hence, in the case of voids or pores there is zero reflectivity, and the surface will look black. The X-ray images provided insight regarding phases,

particularly the dispersion and agglomeration of TiO₂ nanoparticles in the RFTi samples.

3.4 Adsorption analysis

Adsorption analysis is generally employed to assess the textural characteristics of porous materials. This is conducted by using inert gas, for example, nitrogen, since it has a smaller diameter to penetrate the narrow pores and channels, which can adsorb and desorb without affecting the sample material. In the following sections, the adsorption process, theories underpinning the applied adsorption analysis and the associated models, including Brunauer-Emmet-Teller [133] and Barrett-Joyner-Halenda [134], used to interpret the sorption data, will be discussed in detail. Additionally, the shapes of the isotherms were correlated with the adsorption mechanism and the pore network. The analysis is helpful in determining the textural properties of the synthesised materials and how the pore network changes with the addition of nano-additives.

3.4.1 Adsorption Process

Generally, adsorption processes can take place via physisorption (by physical means) or chemisorption (by chemical means). In a gas-solid system, physisorption is a general phenomenon that occurs when an adsorptive (absorbable gas) encounters the surface of the adsorbent (material which adsorbs). In physisorption phenomena, the adsorptive adheres to the adsorbent through van der Waals forces of attraction, which are weak and thus it is a reversible process. Conversely, chemisorption occurs when bonds form between the adsorptive and the adsorbate, mainly through electron pairing; since bond formation is involved, high energies are required to break these bonds, therefore, this phenomenon is irreversible. An illustration of both the processes is shown in Figure 3.6.

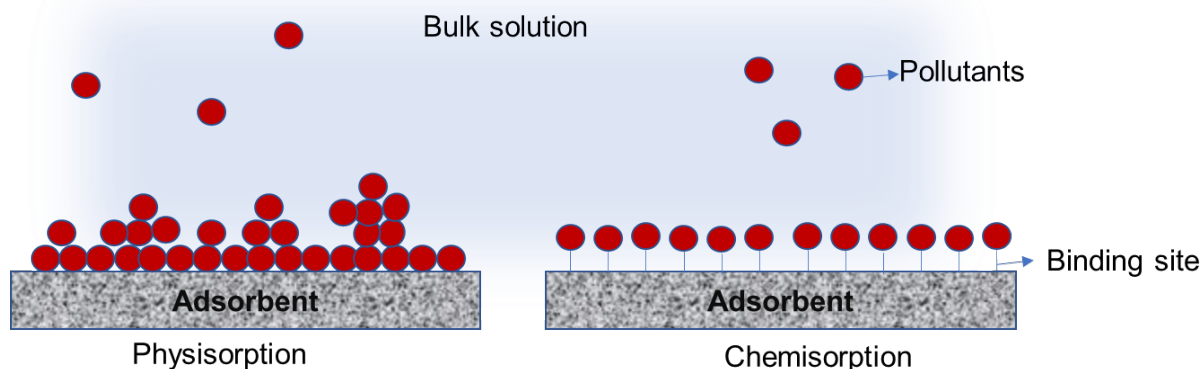


Figure 3.6 Mechanism of adsorption process for the removal of pollutants.

3.4.2 Adsorption Isotherm Features

The data obtained from adsorption study is represented in the form of an isotherm, a graphical representation, showing the relationship between adsorption volume and relative pressure of the adsorbate. Relative pressures, p/p_0 (p is the equilibrium pressure and p_0 is the saturation pressure), range from 0 to close to 1, which represents saturation of the adsorbate. Proceeding from vacuum to higher relative pressures, adsorption occurs, and the isotherm is obtained; reducing the pressure, allows the desorption isotherm to be collected. Adsorption is viewed as the interaction with the adsorbate atoms or molecules (the adsorptive becomes the adsorbate once in contact with the surface) and the surface of the sample, and this is influenced by its porous structure, also called the textural properties. When present in the sample, different characteristics of porosity result in particular isotherm shapes with different features. These profiles indicate pore type, size, shape, and geometry, as shown in Figure 3.7. Regarding pore sizes, the established definition, by the International Union of Pure and Applied Chemistry (IUPAC), is micropores have diameters < 2 nm, mesopores have widths between 2-50 nm and macropores are those larger than 50 nm. These dimensions refer to either diameter of a cylindrical pore or the width of a slit shaped pore, typically of a carbon material [7].

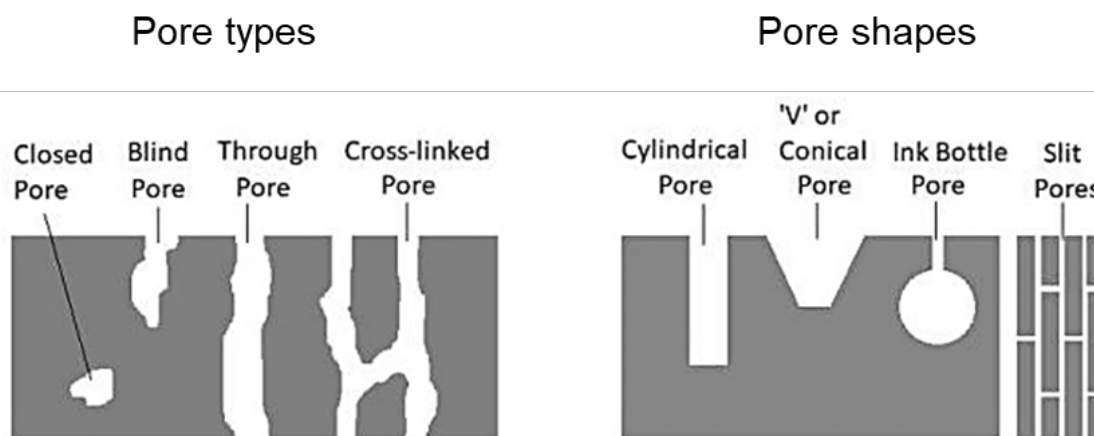


Figure 3.7 Different pore types and shapes within a porous structure [135].

Different isotherm profiles form as the adsorption proceeds, depending on the porous features of the material, which gives a good picture of the range and complexity of possible isotherm profiles. The adsorption process, with increasing pressure, is depicted in Figure 3.8. At first, micropore filling occurs at low pressure if the adsorbent is composed of a microporous network since their size being less than 2 nm in diameter, these dimensions range less than that of the size of an adsorbate atom or molecule to just a few times consequently, micropores will be filled with adsorbate very quickly and this is generally complete at very low relative pressures due to high energy interactions. Around the same pressure range, the isotherm starts curving towards a plateau, which shows that no further adsorption occurs, since the micropores are completely filled with adsorbate. This curvature is usually complete around $0.005 p/p_0$ and it is worth noting that micropore isotherms usually start at very low p/p_0 , typically in the order of 10^{-6} mmHg. Once the micropores are filled, further increases in p/p_0 result in the adsorbate gradually covering the external surface of the sample and forming a layer coating the internal walls of larger mesopores and macropores. This region is used to determine the specific surface area of the sample, most commonly used in the Brunauer-Emmet-Teller (discussed later). Essentially this portion of the isotherm comes in the approximate range p/p_0 0.05 to 0.35 (this range is mentioned here as it represents a classical BET range of p/p_0 in which monolayer adsorption occurs, critical to the calculation of BET surface area, however, of course, the entire range is not necessarily used and each isotherm must be inspected and the appropriate range fitted for each sample individually). As relative pressure is increased

beyond this range, large pores begin to fill the larger pores present within the sample and the p/p_0 at which this occurs depends on the pore sizes present within the sample. In the case of a mesoporous sample, the adsorbate will start filling mesopores at a sufficiently high p/p_0 , the larger the pores the higher the p/p_0 required to fill them. The isotherm then starts to curve at higher p/p_0 as pores start to fill with the adsorbate until saturation is approached, at p/p_0 closer to 1.

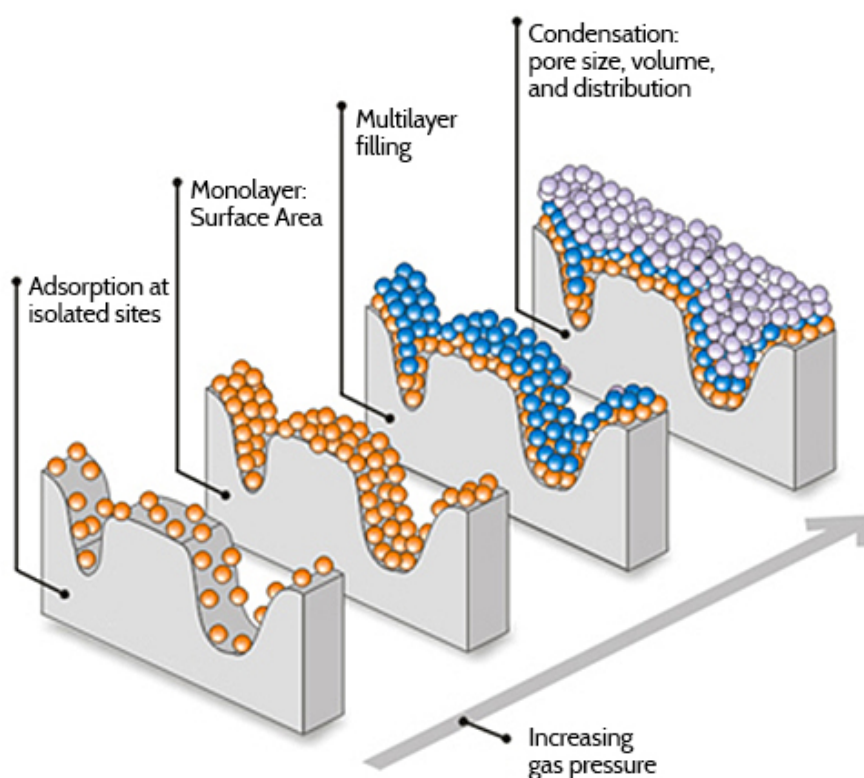


Figure 3.8 Illustration of different states of an adsorption process with increasing pressure.

Adsorption isotherms can be conveniently described by the Brunauer-Deming-Deming-Teller classification [35], as shown in Figure 3.9, which was adopted by IUPAC in the 1980s. The isotherms are classified according to their shape or profile. A Type I adsorption isotherm shows rapid adsorption at very low p/p_0 , followed by a sharp turn of the isotherm, called the isotherm knee, after which the isotherm is horizontal to the pressure range for the remainder of the pressure range, due to there being no further adsorption as p/p_0 increases. This isotherm is found with microporous materials. The plateau of the isotherm shows that there is no further porosity in the mesopore or small macropore range. With improvements in analytical capabilities, the

quality and definition of recorded adsorption isotherms has increased, and this has been coupled with more classes of microporous materials being developed. This led to the realisation that porosity may be confined to the micropore region as in the case of this isotherm or it can be extended into the mesopore region therefore it can be subdivided into two sub types, Type Ia and Type Ib. Type 1b has a broader isotherm knee due to the presence of larger micropores and the extension of these into the distribution of mesopores.

The Type II isotherm has positive curvature at low p/p_0 , due to adsorption on energetically favourable sites, before being located on the less energetically favourable sites, where Point B indicates the stage at which monolayer forms on the surface, after which the adsorption uptake tends to plateau. Consequently, we can calculate the monolayer adsorption volume and from this we can calculate specific surface area. The second region of adsorption occurs at higher p/p_0 , and the feature of Type II isotherms is that this continues to increase as saturation is approached. Essentially this increase in adsorption volume is asymptotic to the volume axis due to multilayer adsorption of adsorbate on adsorbate on the surface of a non-porous material or due to incomplete pore filling. Type IV isotherms result from adsorption on mesoporous materials. At low p/p_0 , Type IV follows the same profile as a Type II isotherm, again due to monolayer and subsequent multilayer adsorption on the outer surface and pore walls. As p/p_0 is increased, an increase in adsorption volume due to pores being filled by adsorbates is observed, involving a process of liquefaction, or capillary condensation, whereby gaseous adsorbate condenses into its liquid state. A unique feature of Type IV isotherms is the plateau at high relative pressures, which occurs as saturation is approached. The presence of a plateau indicates that the pores are small enough to ensure complete filling with adsorbate, unlike the Type II isotherm.

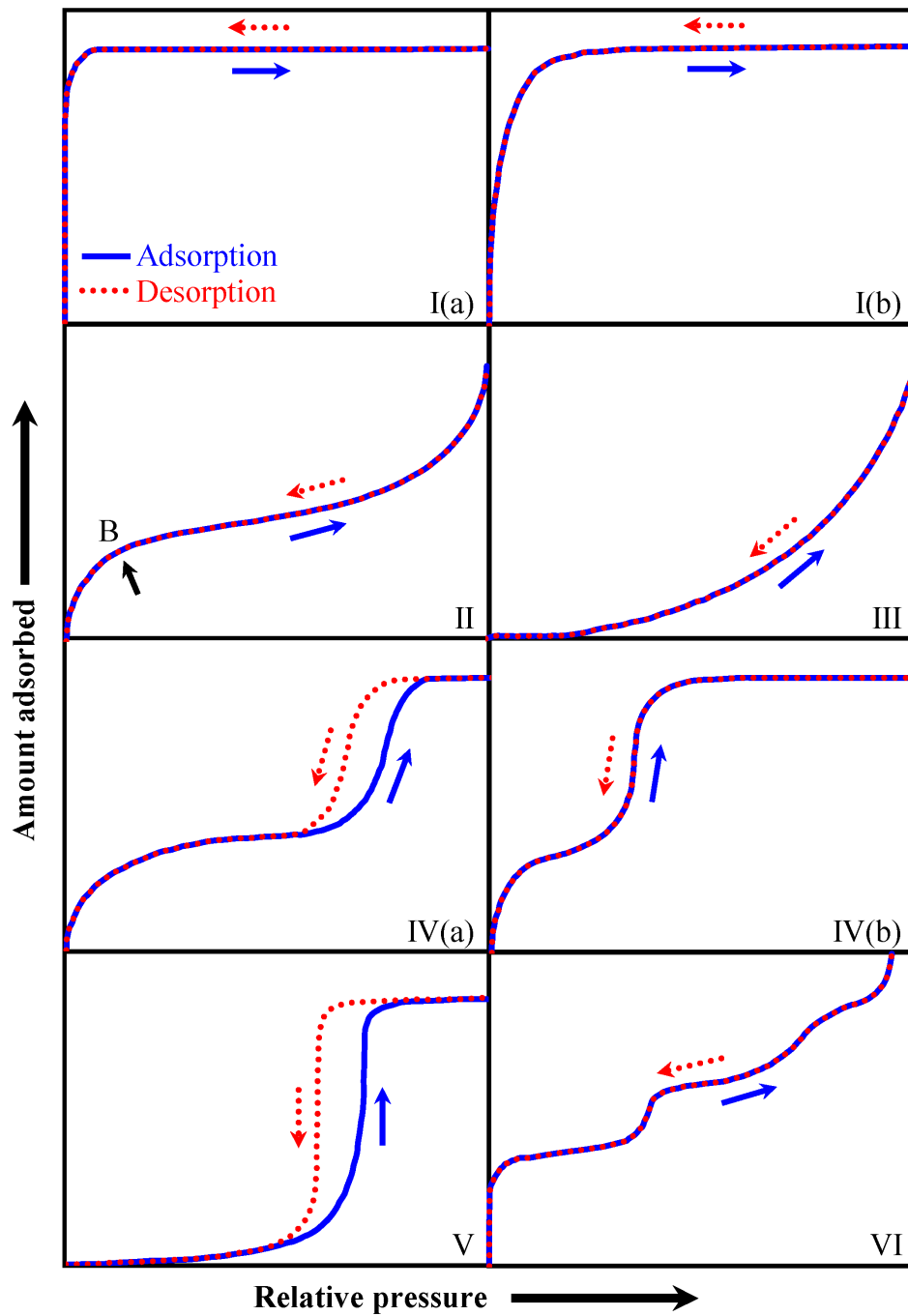


Figure 3.9 IUPAC classification of isotherms [35].

Type III and V follow the same profile at low p/p_0 and do not have positive curvature at low p/p_0 , due to weak adsorbate-adsorbent interactions. Adsorption is likely to be located around the most favourable surface sites or is due to the self-associating adsorbate-adsorbent interactions, rather than interaction with the surface consequently, it is not possible to determine an adsorption monolayer volume and

therefore is not possible to calculate the specific surface area of/from the isotherms. At higher p/p_0 , both isotherms show an increase in adsorption volume. With Type III isotherms, this could be due to multilayer adsorbate on adsorbate adsorption, which may apply to non-porous samples, or it could be due to incomplete pore filling of a macropore sample. With Type V isotherms, the adsorption volume, which commences at lower p/p_0 to the Type III isotherm, is typically associated with the filling of mesopores or small macropores present within the sample, so it is genuine porosity rather than multilayer adsorption. Type VI isotherm consists of a number of steps increases with increase in p/p_0 and are usually due to successive adsorption layers on the surface of a sample; these are incredibly rare to observe.

Desorption is the reverse process to adsorption, in practical terms once the highest adsorption pressure has been attained and the adsorption volume has been determined, the pressure is gradually reduced, and adsorption volume is measured as adsorbate is removed from the sample. In the case of a theoretical isotherm on a non-porous sample, the desorption branch of the isotherm would be expected to follow the adsorption, meaning that the process of adsorption is completely reversible. By contrast, the isotherm of a porous material, for example, nitrogen adsorption on a mesoporous sample (Figure 3.9, Type IV isotherm), and considering the simplest pore geometry with open-ended pores of cylindrical geometry, may produce a desorption branch that does not follow the adsorption branch. In this case a hysteresis is observed between the two isotherm branches, which is due to differences in the physical processes of adsorption-desorption. The mechanism of pore filling during adsorption is by process of condensation, whereas pore emptying during desorption is by process of evaporation. The process of condensation occurs from the pore walls inwards to the centre of the pore, here a process of successive multilayer adsorption of adsorbate on adsorbate occurs until all pores are completely filled, as illustrated in Figure 3.10.

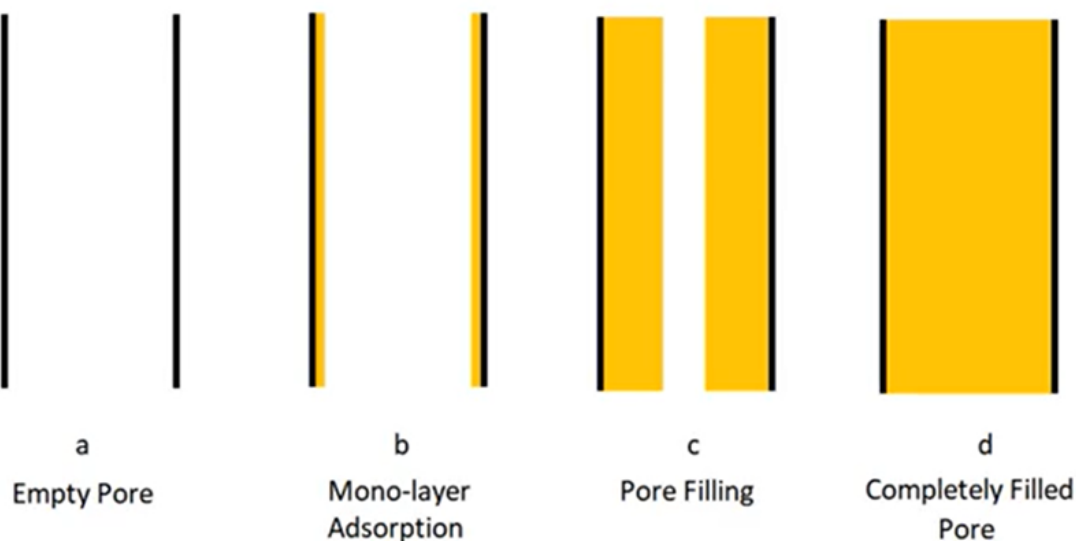


Figure 3.10 Representation of a progressing adsorption process.

In contrast to the condensation observed during adsorption, pore emptying during desorption processes (Figure 3.11) occurs by evaporation from the surface of the adsorbate and that is from the top of the pore downwards, of course this is very much oversimplified, but it does give a good illustration of the two processes. If the pores were open-ended cylinders and uniform, as in the example discussed here, both the adsorption the desorption isotherms would present as very steep profiles due to the narrow range of pore diameters or widths.

There are six general classifications of hysteresis, as illustrated in Figure 3.12. These profiles vary according to the shape of the adsorption and desorption isotherms and the approach to describing this is similar to the adsorption isotherms and their relationship with the pore sizes, discussed previously. Both adsorption and desorption isotherms provide useful information; adsorption isotherms describe the size of pore cavities or pore bodies, and the desorption isotherm describes the dimensions of pore entrances or the restrictions within the porous network. Type H1 hysteresis with a Type IV adsorption isotherm indicates that the sample is mesoporous. The steep volume changes in both adsorption and desorption isotherms in the respective regions of pore filling and pore emptying are generally associated with mesopores of uniform, open geometry in a narrow range of pore sizes, and reasonably free of restrictions. A clear hysteresis between adsorption and desorption is caused by delayed adsorption into

the open pore structure and a thermodynamic equilibrium between the condensed liquid phase in the pores, and vapour phase external to the pores, is established upon desorption. This isotherm type can also be observed for systems containing ink-bottle pores, having a pore neck and cavity with similar dimensions.

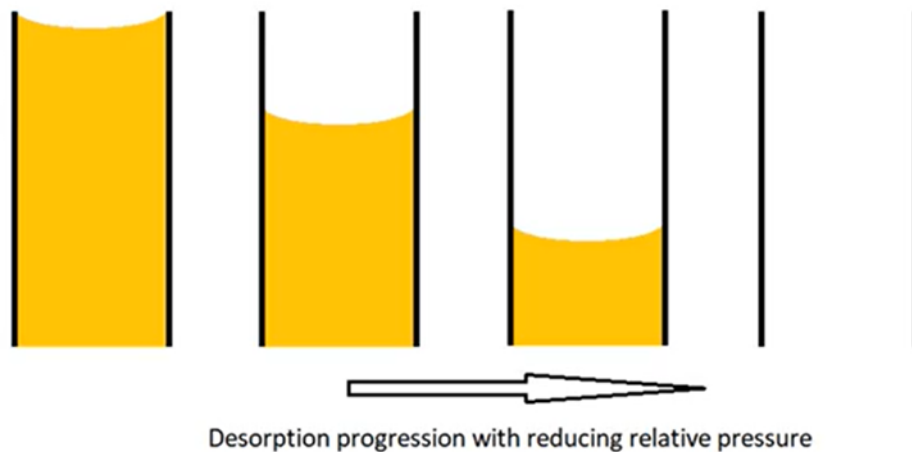


Figure 3.11 Representation of a progressing desorption process.

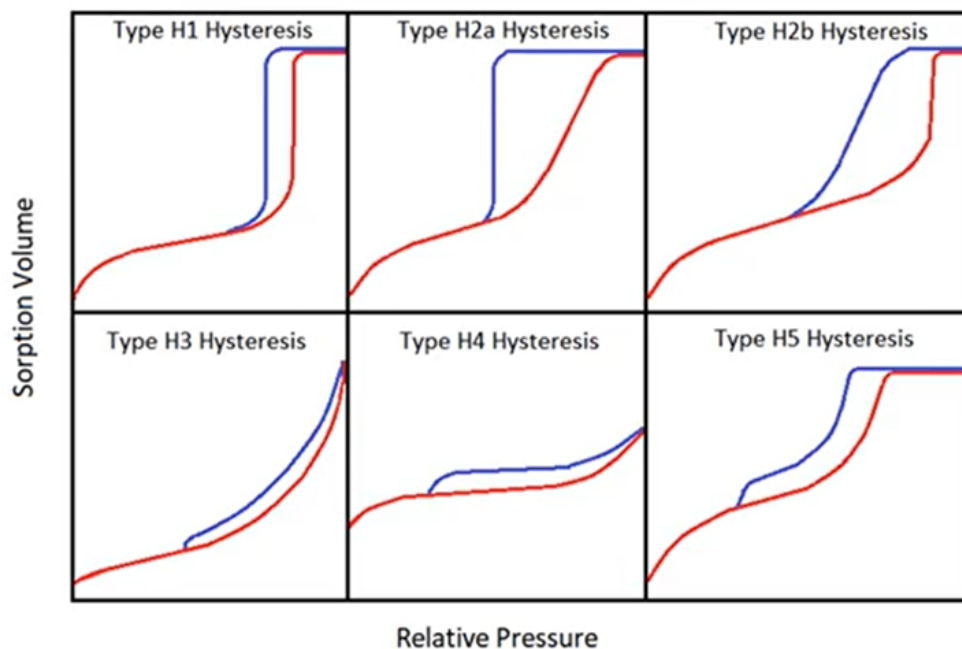


Figure 3.12 Types of hysteresis [35] .

As with Type I hysteresis, Type II hysteresis can also occur with Type IV adsorption isotherms. Both Type H2a and Type H2b are associated with more complex pore

structures than Type H1, such as structures having internal restrictions or pore blocking. In Type H2a the desorption isotherm is steep with respect to the volume change, and this is due to the size of the pore entrances or the size of the restrictions being quite uniform. The gradual slope of the isotherm is suggestive of larger pore cavities lying beneath, or beyond, the pore neck with greater variability in size. The converse is true for Type H2b hysteresis, where the more gradual slope is indicative of the size restrictions of pore entrances covering a greater range, thus being less uniform.

In the case of Type II isotherms, the presence of hysteresis strongly suggests the presence of porosity, with pores exhibiting plate-like or layered structures. A key feature of H3 hysteresis is sharp and abrupt closure of the desorption branch to the adsorption branch, occurring as a result of cavitation phenomena and, hence, the desorption isotherm becomes less useful for describing porous characteristics. Type H4 hysteresis is comparable to Type H3 hysteresis; however, the adsorption profiles of Type H4 are hybrid, showing high adsorption volume at low p/p_0 , typical of Type I isotherms, followed by Type II character at high p/p_0 , therefore, the sample material possesses porosity within the microporous, mesoporous, and small macroporous ranges.

3.4.3 Surface Area Measurement

As mentioned earlier, the occurrence of multilayer adsorption isotherms is recognised and accounted for in the Brunauer-Emmet-Teller (BET) theory [133], which was proposed in 1938, and is a modified form of the Langmuir adsorption isotherm. These modified assumptions are:

1. Physical adsorption results in the formation of multilayers
2. Solid surface possesses uniform localised sites.
3. There are no interactions between adjacent adsorbed molecules.
4. There is a dynamic equilibrium between successive adsorbed layers.
5. The initial layer adsorbed onto the material's surface displays a heat of adsorption, whereas successive layers has a heat of condensation.

The BET equation, developed on the basis of these assumptions, is presented in Equation 3.1, where p is the pressure at equilibrium, p_0 is the saturation vapour pressure and C is a dimensionless constant related to the adsorption energy.

$$\frac{p}{V(p_0 - p)} = \frac{1}{V_m C} + \frac{(C - 1)p}{V_m C p_0} \quad \text{Equation 3.1}$$

A graph of $\frac{p}{V(p_0 - p)}$ against $\frac{p}{p_0}$ can be plotted to calculate the values of V_m and C from the gradient and intercept and these values can be used to calculate the accessible surface area.

3.4.4 Pore Size Distribution

The pore size distribution of the nitrogen adsorption method is calculated using the Barrett-Joyner-Halenda (BJH) method [130], based on the Kelvin equation. This approach is a combination of Wheeler theory and physical adsorption and capillary condensation, for direct calculation of the pore size distribution from sorption data. Nevertheless, the following postulations should be satisfied: (i) pores are cylindrical and the pore passage is rigid, (b) micropores are absent, (iii) all the pores are completely filled at the highest $\frac{p}{p_0}$. On the basis of Kelvin equation (Equation 3.2), the capillary radius (r_c) is calculated upon condensation. The relationship curve of the liquid molar volume and r_c can then be described, which is also the cumulative pore volume distribution curve.

$$\ln \frac{p}{p_0} = \frac{2\gamma V_m}{r_c RT} \quad \text{Equation 3.2}$$

Where $\frac{p}{p_0}$ is the relative pressure, V_m is the liquid molar volume, R is the universal gas constant and T is absolute temperature. It is noteworthy that there are limitations of the BJH method and errors in the pore size distribution are large, due to the presence of micropores and complex pore structures, such as non-cylindrical pores.

3.4.5 Nitrogen Adsorption Analysis of Synthesised Samples

Adsorption analyses of synthesised RFTi gels were performed using a Micromeritics ASAP 2420 Surface Area and Porosity Analyser (Figure 3.13).

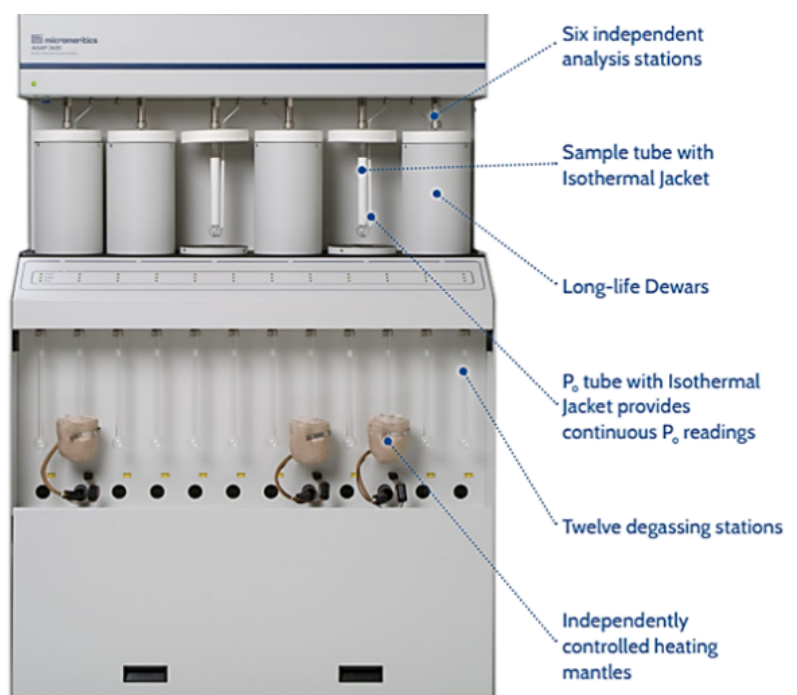


Figure 3.13 Micromeritics ASAP 2420 Surface Area and Porosity Analyser.

The subsequent isotherms obtained were analysed to provide details of sample properties, such as surface area and pore size. Before the sorption measurements were taken, the RFTi gel samples were degassed following procedures discussed below.

Degas procedure

In order to obtain accurate values of textural properties from gas sorption measurements, the sample surface has to be cleaned of any impurities adsorbed onto it, which would mask some of the surface characteristics present and affect the obtained sorption isotherm. Removal of these impurities, before measurement, is usually achieved by exposing the sample to elevated temperatures and reduced pressure. For complete removal of adsorbed molecules on the sample surface, it is important to use an appropriate combination of degas temperature, pressure, and time. Firstly, ~0.3 g of the RFTi gel sample was weighed to an accuracy of 10^{-4} g and

the precise mass was recorded. A degas port was connected to the sample tube carrying the sample, and the tube bulb (where the sample resides) was covered with an independently controlled heating mantle. For accurate measurements it was ensured that the heating mantle was placed correctly, and the thermocouple was in full contact with the glass, since overheating may disrupt the degas process. The degassing procedure involved elevating temperature gradually, to 110 °C at a rate of 5 °C min⁻¹, with continued unrestricted evacuation for 120 min. Afterwards the sample tube was cooled at room temperature and nitrogen gas was automatically filled back to a pressure of 760 mmHg. After degas, the sample mass was recorded, and the masses in the system were adjusted for sorption measurements. The difference in masses here relates to substances desorbed during the degas process.

Sorption Measurements

Following the degassing procedure, a volume displacement insert was added to reduce the free volume in the sample tube, which increases the accuracy of the measurements. Low temperature nitrogen sorption measurements were performed at atmospheric pressure at -196 °C (nitrogen boiling point). Prior to analysis, the liquid nitrogen bath was filled using a Dewar depth gauge to help maintain the temperature throughout sorption analysis. However, the evaporation of liquid nitrogen may occur from the Dewar, as the analysis progresses, which would decrease the area of contact between the sample tube and the liquid nitrogen, therefore, an isothermal jacket was slid over the neck of the tube to keep a constant area between the sample tube and isothermal jacket. For samples running for an extended period, the liquid nitrogen liquid was carefully refilled, during the equilibration period, to the appropriate level. The sample tube was screwed to the analysis port and the saturation pressure tube was set right next to the sample tube.

The isothermal jacket and saturation pressure tube were aligned to have the same temperature profile throughout the analysis. A Dewar cover was placed on the top end of the isothermal jacket and, finally, a splash guard was placed to cover the respective port unit. The mass in the software system was updated with the degassed mass. All samples were analysed using 40 data points for adsorption and 30 points for the desorption cycle with the equilibration time set to 5 s. The isotherm data obtained was

analysed using the Micromeritics ASAP 2420 equipment software using the BET and BJH methods, discussed in sections 3.4.3 and 3.4.4, respectively. This allowed for the identification of useful characteristics such as the distribution of pore sizes, total pore volume, accessible surface area, and average pore width.

3.5 Point of Zero Charge

The surface charge characteristics of RFTi gels synthesised in this work were determined through point of zero charge (pzc) analysis, commonly defined as the pH at which the net charge of the total adsorbent surface equals zero, at a given ambient temperature, applied pressure, and aqueous solution composition. As regards adsorption, the reason for the increased interest in pH is due to the adsorption of some chemicals being highly dependent on pH [126]. The surface charge is created due to the protonation or deprotonation of the surface functional groups, which may be due to adsorption or binding of ions, replacement of ions or unsatisfied bonds at the variable charge surface by means of ionisation.

3.5.1 Experimental Procedure to Measure Point of Zero Charge

In this work, point of zero charge (pzc) of RFTi gels was determined by the drift method [136]. The experimental analysis involved addition of 50 mL of 0.01 M NaCl into a series of Erlenmeyer flasks. The pH was adjusted from 2 to 12 using 0.01 M HCl and 0.01 M NaOH. The initial pH was recorded after addition of a weighed amount of RFTi, and the flasks were placed on a shaker (150 rpm, 23°C for 24 h). After attainment of equilibrium, the solutions were filtered, and the final pH of the subsequent filtrates were recorded using a Hanna Instruments benchtop pH meter (Leighton Buzzard, Bedfordshire, UK). Finally, the differences between initial and final pH were plotted against initial pH and the line of intersection at the initial pH axis was determined as the pzc value.

3.6 Thermal Analysis

A thermal gravimetric analysis technique is used to quantify the weight changes of a sample at a specific time and temperature. A thermogravimetric analyser (TGA) provides quantitative and qualitative information about physical changes in a sample in response to the temperature, heating rate and the atmosphere. Besides data on

material properties, such as decomposition and thermal stability, TGA can quantify major constituents of a material or content of fillers and is employed as secondary means of material identification.

A basic TGA subjects a relatively small sample of material to a temperature in an inert atmosphere, usually nitrogen, or oxygen, under dynamic temperature ramp in a furnace, and measures weight changes of the sample. The most common TGA experiment involves heating the sample to a high temperature so that the organic matter of the sample decomposes. The sample is loaded into a sample pan, which is balanced, and then placed in a sealed furnace with a thermocouple that detects temperature (labelled diagram in Figure 3.14b). The equipment measures weight and temperature multiple times per second, allowing changes in both the weight of sample and the rate of corresponding weight changes to be recorded as a function of time or temperature. The TGA results highly depend on the heating rate, the atmosphere in the furnace, and the maximum temperature achieved during testing. Heating programs can be selected based on the material properties to be identified. For instance, decomposition kinetics and lifetime prediction measurements are performed under isothermal conditions, where the sample is maintained at a constant temperature for a period, during which the changing weight is recorded. As another example, compositional analysis is carried out with stepwise isothermal heating, where the sample is heated to a constant weight at each of a series of increasing temperatures and, therefore, provides better resolution for compositional analysis. Likewise, to determine filler content, many TGA programs involve switching from an inert atmosphere such as nitrogen gas to an oxygen-rich atmosphere at a given temperature.

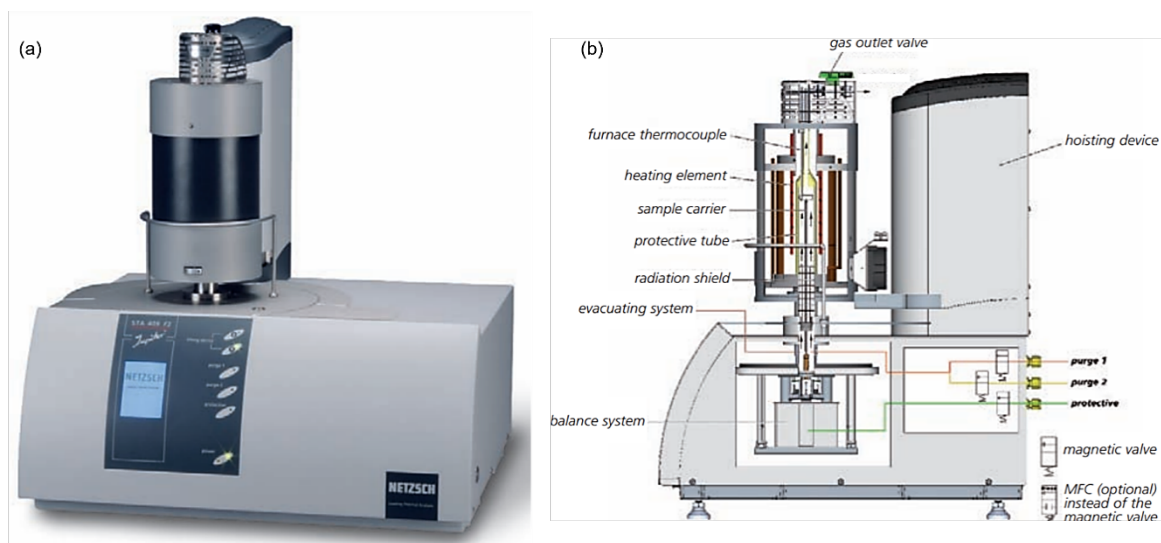


Figure 3.14 (a) Laboratory thermal gravimetric analyser- NETZSCH STA 449 F3 Jupiter and (b) labelled diagram of the instrument.

A typical thermograph is plotted against temperature on the horizontal axis and percentage of the original weight remaining of the sample, called weight percent curve, on the vertical axis. There is usually a right vertical axis on the plot showing a derivative curve of the weight percent with respect to temperature. This allows clear visualisation of the decomposition steps, to accurately assess the exact temperature at which maximum decomposition has occurred and evaluation of the maximum changing rate of decomposition.

Most TGA curves display weight loss, typically due to physical and chemical processes. Physical transitions occur due to loss of vaporisation, desorption, or drying processes, whereas chemical reactions include decomposition, loss of volatiles, and combustion. When performing calculations with TGA data, researchers start with interpretation of the derivative curve, which clearly shows the decomposition steps. Information that can be gathered from the derivative curve are the start and end of each decomposition step, as well as the temperature at which the maximum decomposition rate has occurred. For example, in the case of polymer within a plastic material, the temperature at the peak is generally referred to as the decomposition temperature for that polymer. After defining each decomposition step in the derivative curve, the amount of weight loss can be assessed for each decomposition step on the weight percent curve by selecting one point prior to the weight loss and another selected after the weight loss. The difference in weight percent between the starting

and ending points is the weight change at that particular decomposition step. Furthermore, the percentage of material that is left on the pan after completion of the experiment is referred to as the residue for that sample, which is calculated by selecting a single point after all decomposition steps are complete. The residue can include any trace inorganic elements in the sample material. Finally, the weight of other volatiles can be calculated by selecting the range of temperatures prior to any decomposition in the sample.

3.6.1 Thermal Analysis Procedure

A thermal gravimetric analyser-NETZSCH STA 449 F3 Jupiter (Figure 3.14 a) was used to analyse the thermal decomposition and compositional analysis of the samples synthesised in this work. Briefly, Al_2O_3 crucibles were employed for analysis, ~20 mg of respective samples was heated to 800°C at 5°C min^{-1} in N_2/O_2 atmosphere. The mass flow controller (MFC) was set to purge gas 1 $\text{MFC-50 mL min}^{-1}$, purge gas 2 $\text{MFC-50 mL min}^{-1}$, and protective MFC flow was set to 110% of combined purge gas 1 and 2. The thermographs were obtained using the attached software for further evaluation and compositional analysis was carried out according to the ASTM E1131-03 procedure [137].

3.7 Spectroscopic Analysis

Spectroscopy relates to the study of interactions between electromagnetic radiation (EMR) and matter. When EMR is incident on matter, it interacts with the molecule, which absorbs some portion of this radiation. The main properties of radiated energies are important to the study the spectroscopy, including distinctive wavelength (λ), frequency (ν) in and wavenumber ($\bar{\nu}$), which is the reciprocal of λ . According to Planck's quantum theory, the energy of radiation (E) is directly proportional to the frequency (ν) as given in Equation 3.3:

$$E = h\nu \quad \text{Equation 3.3}$$

where h is Planck's constant. Since $\nu = \frac{c}{\lambda}$,

$$E = \frac{hc}{\lambda} \quad \text{Equation 3.4}$$

$$E = hc\bar{\nu} \quad \text{Equation 3.5}$$

Where c is the speed of light. Equation 3.4 shows that the energy of the radiation is inversely proportional to the wavelength of light while, according to Equation 3.5, the energy of radiation is directly proportional to the wavenumber.

3.7.1 Fourier Transform Infrared Spectroscopy

The interactions between radiation and matter allow interpretation of the nature of a compound. The principle behind this is, when a covalent bond has a certain dipole moment, the bond vibrates with a particular frequency, which upon exposure to infrared radiation (IR), will absorb a particular energy equal to the vibrational frequency of the bonds. A spectrum obtained through Fourier transform infrared (FTIR) spectroscopy can allow elucidation of the nature of the bonds, as it is characteristic to the bond frequency.

The IR spectrum shows the IR transmitted through the sample, with the vertical axis showing percentage transmission, indicating absorbance bands shown by downward peaks at a particular frequency or wavenumber ($\bar{\nu}$, cm^{-1}), as represented on a horizontal axis. The transmitted radiation (T), that is the ratio of intensity ($\frac{I_0}{I}$), can be expressed in the form of absorbance (A), as in Equation 3.6: 100% transmission means no absorption occurred at that frequency, while height, width and position of peaks provide valuable information that can be interpreted to identify a molecule.

$$A = \log\left(\frac{I_0}{I}\right) = -\log(T) \quad \text{Equation 3.6}$$

A conventional IR spectrum is complex with multiple peaks in the low energy range. This is due to the different molecular vibration modes, mainly branched into stretching and bending vibrations, due to changes related to bond length and bond angles, respectively. The spectrum can be studied by dividing it into a functional group region, ranging from $5000\text{-}1300\text{ cm}^{-1}$ and fingerprint region in the range $1300\text{-}667\text{ cm}^{-1}$, as

shown by the divided IR spectrum in Figure 3.15, where the position of characteristic bands of certain groups have been labelled. The fingerprint region mainly provides information on the identity of a compound, and by comparing with a target compound the exact identity of the compound can be determined.

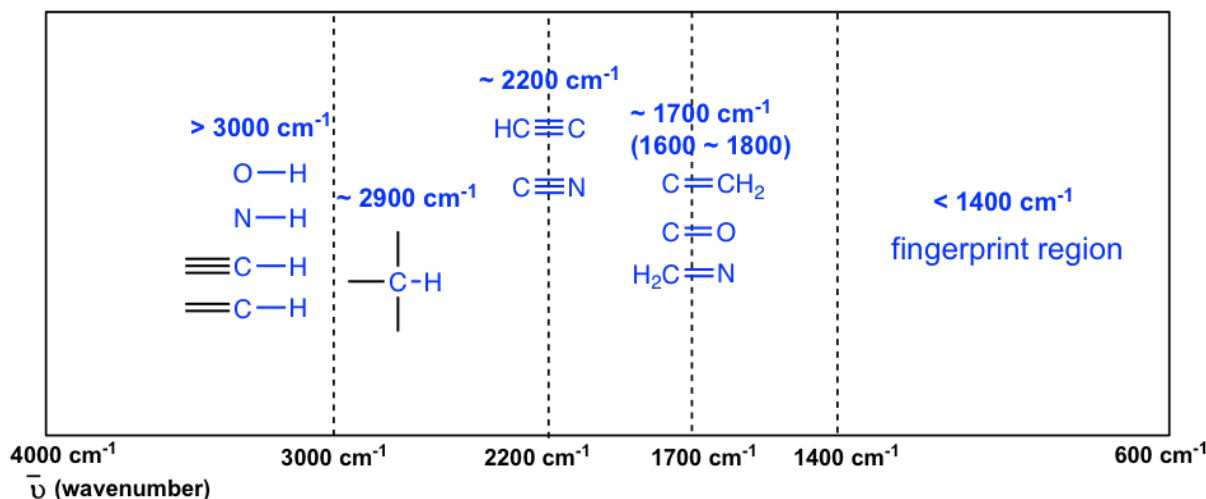


Figure 3.15 Labeled functional groups as reference for identification of certain groups in an FTIR spectrum.

FTIR Analysis Procedure

The equipment used for FTIR analysis within this work was an ABB MB3000 FTIR Spectrometer (Figure 3.16). The acquisition mode was transmittance, and other acquisition parameters were resolution 16, scans 16, measurements 3, wavenumber range 400-4000 cm^{-1} , and the detector gain settings were adjusted to achieve a signal of around 80% for maximum accuracy, before associated absorbance values recorded. Prior to initiating FTIR spectroscopy of a sample, the program requires an air FTIR measurement, which is used as a reference for subsequent experiments.



Figure 3.16 Laboratory FTIR Spectrometer ABB MB3000.

3.7.2 UV-Vis Spectroscopy

UV-Vis spectroscopy is an analytical technique that measures the amount of UV or visible light absorbed by different molecules at different wavelengths, corresponding to electronic transitions in different bonding environments. These transitions are specific to a material hence can be used to analyse material properties. A representation of electronic excitations upon UV-Vis radiation is shown in Figure 3.17.

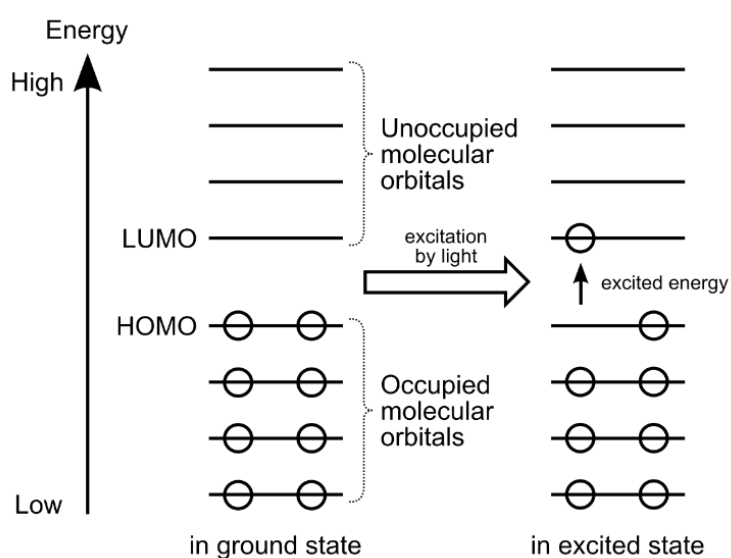


Figure 3.17 Energy band and electron hopping.

Figure 3.18 shows the different types of transitions. Bonding molecular orbitals are those which have energy less than the average energy of the overlapping molecular

orbitals, whereas antibonding are those which have energy greater than the average energy of the overlapping molecular orbitals, and non-bonding molecular orbitals have equal to the average energy of the overlapping molecular orbitals - they have no influence in the formation of bonds. The types of transitions with respect to energy, are in the order of $\sigma\text{-}\sigma^* > \pi\text{-}\pi^* > n\text{-}\sigma^* > n\text{-}\pi^*$.

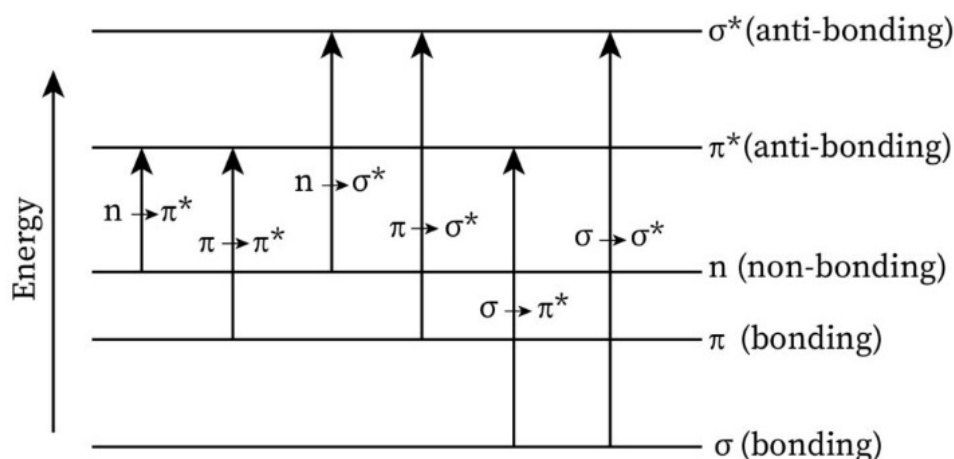


Figure 3.18 Electronic transitions upon UV-Vis radiation.

The working and construction of a double beam spectrophotometer are illustrated in Figure 3.19 and Figure 3.20 b. Essentially, EMR is collected by collimating convex lenses, which directs the light to the monochromator, and a particular wavelength exits the monochromator. The light beam is then split into two beams with the help of mirrors, reaching reference and sample cuvettes, before finally being incident on the detector, where a photomultiplier tube emits electrons to generate an absorbance signal against wavelength. The value of wavelength where the absorbance is maximum is called lambda max (λ_{\max}), which can be used for the qualitative analysis of a sample. In this work, the data for absorbance vs wavelength was used for further analysis, including evaluation of the band gap and concentration measurements from absorbance data.

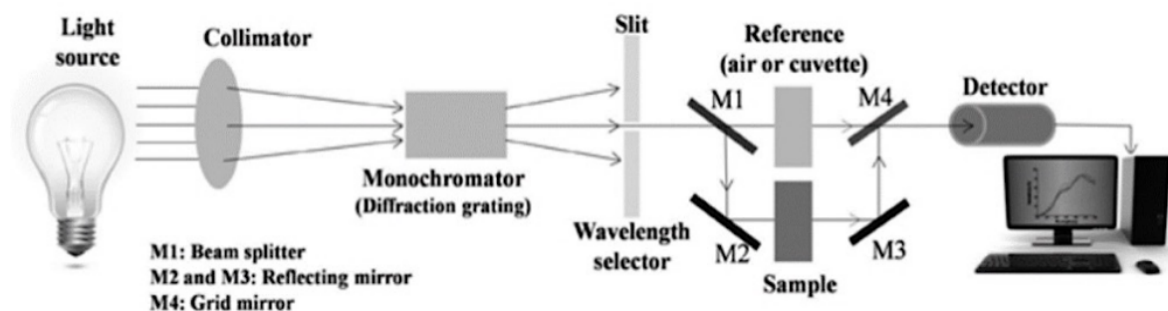


Figure 3.19 Schematic of a double beam spectrophotometer.

UV-Vis absorption spectra

To evaluate the behaviour of synthesised RFTi gels, absorbance vs wavelength spectra were recorded using a Cary 5000 UV-Vis Spectrophotometer (Figure 3.20 a). To set up, the wavelength range was selected from 200-400 nm and a baseline was collected, before taking the measurements, to obtain accurate results. Since baseline corrections were used, a blank was prepared using pure solvent, allowing the software subtract it from the actual spectrum. To obtain precise results, quartz cuvettes were used in this work, with the translucent sides of the cuvette arranged front to back. The transmission obtained from the blank sample was then set to 100% and measurements were continued for the test solutions.

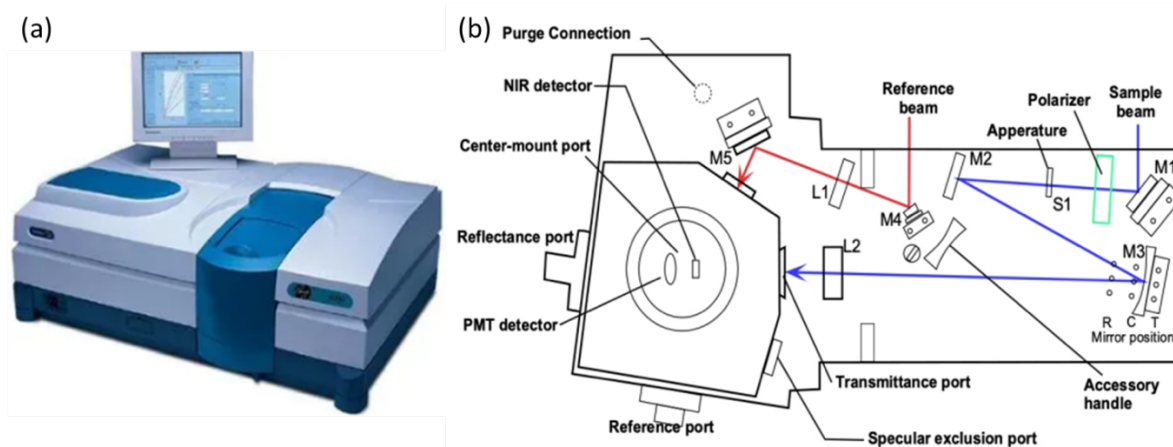


Figure 3.20 (a) Cary 5000 UV-Vis Spectrophotometer and (b) its construction.

Evaluation of Band gap

In 1968, Tauc used Equation 3.7 to calculate the band gaps of amorphous semiconductor materials using their absorption data [138].

$$(\alpha h\nu)^\gamma = A(h\nu - E_g) \quad \text{Equation 3.7}$$

Where α is the absorption coefficient, h is Planck's constant, ν is the photon frequency, A is the proportionality constant, determined by the index of refraction and is generally taken as 1 for amorphous materials, E_g is the energy band gap and γ denotes the nature of the electronic transitions, i.e. when $\gamma = 2$, it is a directly allowed transition and when $\gamma = 1/2$ it is an indirectly allowed transition. The basic approach for Tauc analysis is to collect optical absorbance data for a sample with energies ranging from below the band gap transition to above it.

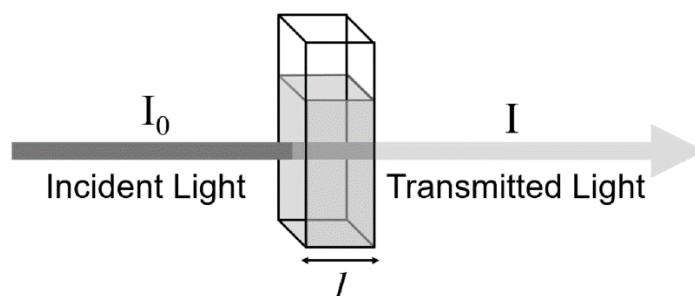


Figure 3.21 Illustration of Beer-Lambert's law; incident and transmitted light through a cuvette in UV-Vis spectroscopy [139].

A Tauc plot allows the energy to be evaluated by the extrapolation of the intersecting linear regions onto the x-axis, giving the band gap or absorption edge energy. In order to understand the absorption coefficient, α , it is essential to consider the Beer-Lambert law, which explains that the transmitted intensity is equal to the exponentially decaying incident intensity, as expressed in Equation 3.8:

$$I = I_0 e^{-\alpha x} \quad \text{Equation 3.8}$$

Where x is the thickness of solution through which the incident light passes, as illustrated in Figure 3.21. Rearranging Equation 3.8, and setting $x = l$, that is the standard length of a cuvette or the thickness of a solution through which light is passing, Equation 3.8 can thus be expressed as Equation 3.9:

$$\frac{I}{I_0} = e^{-\alpha x} = e^{-\alpha l} \quad \text{Equation 3.9}$$

Utilising the logarithmic relation, the above equation can be written as:

$$\log\left(\frac{I}{I_0}\right) = \log(e^{-\alpha l}) = -\alpha l \log(e) \quad \text{Equation 3.10}$$

The value of $\log(e) = 0.434$, hence, the expression can be defined as:

$$A = \alpha l(0.434) \quad \text{Equation 3.11}$$

Rearranging to express in terms of absorption coefficient, α , and putting $l=1$ cm as the internal dimension of a standard cuvette, the expression becomes:

$$\alpha = 2.302 \frac{A}{l} = 0.2302 A \text{cm}^{-1} \quad \text{Equation 3.12}$$

Thus, from the UV-Vis absorption data, it is possible to directly use the value of absorbance to obtain α in the units of cm^{-1} .

Converting the values of incident energy into acceptable units, recalling Equation 3.4, and substituting in values of h and c , gives:

$$E = hv = \frac{hc}{\lambda} = \frac{6.625 \times 10^{-34} (\text{Js}) \times 2.998 \times 10^8 \left(\frac{\text{m}}{\text{s}}\right)}{\lambda (\text{m})} \quad \text{Equation 3.13}$$

The band gap energy is determined in eV ($1 \text{ eV} = 1.602 \times 10^{-19} \text{ J}$), so the above equation can be rewritten as Equation 3.14:

$$E = \frac{1.986 \times 10^{-25} (\text{eVm})}{\lambda (\text{m}) \times 1.602 \times 10^{-19}} \quad \text{Equation 3.14}$$

Which evaluates to:

$$E = \frac{1.240 \times 10^{-6}(\text{eVm})}{\lambda (\text{m})} \quad \text{Equation 3.15}$$

Since the experimental data obtained using the UV-Vis spectrophotometer is in $\lambda(\text{nm})$, Equation 3.15 can be rewritten as;

$$E = \frac{1240 \times 10^{-9}(\text{eVm})}{\lambda (\text{nm})} \quad \text{Equation 3.16}$$

$$E = \frac{1240 \times (\text{eV nm})}{\lambda (\text{nm})} = \frac{1240}{\lambda} \text{eV} \quad \text{Equation 3.17}$$

In order to proceed with band gap calculation, absorbance vs wavelength is plotted. Here, the absorption coefficient, α , can be determined using Equation 3.12 and energy (E) is determined using Equation 3.17. Then, $(\alpha h\nu)^Y$ is plotted against $h\nu$, and the linear region of this plot is extrapolated to the x-axis. The value of the x-intercept finally gives the band gap value.

3.8 Application Tests

3.8.1 Evaluation of Concentration an Adsorption Measurement

The remaining concentration of solution post adsorption or photocatalytic treatment can be determined from UV-Vis measurements. Based on Beer-Lambert law, the absorption is directly proportional to the concentration of a solution, expressed as Equation 3.18:

$$A = c\epsilon l \quad \text{Equation 3.18}$$

Where, A is absorbance, c is molar concentration, ϵ is the molar absorptivity coefficient, and l is the path length that light travels in the solution (note that a standard cuvette is 1 cm in width).

The concentration of a solution can be analysed using a calibration curve, which is principally based on Beer-Lambert's law. In order to find the concentration of an unknown, absorption is determined for a suite of solutions of standard solutions of

known concentrations. Absorption of all concentrations were measured at this same fixed wavelength, that is 663 nm, at which maximum absorption of methylene blue (MB) dye occurs. The absorbance of the standard solutions was plotted against the concentration of known solutions and fitted with straight line curves using the Cary 5000 UV-Vis spectrophotometre software. A dye solution of unknown concentration was then run on a spectrophotometre to measure the absorbance. This value of absorbance was then entered in the software to obtain the concentration of unknown MB dye solution, based on the acquired parameters of slope and intercept according to straight line equation (See Equation 3.18, where y is A , slope is $c\epsilon$).

The equilibrium adsorption capacity, q_e (mg g^{-1}), was calculated using:

$$q_e = \frac{(C_o - C_e) \cdot V(l)}{W} \quad \text{Equation 3.19}$$

While the respective percentage removal of MB was calculated by:

$$\text{Removal \%} = \frac{C_o - C_e}{C_o} \times 100\% \quad \text{Equation 3.20}$$

where C_o and C_e are the initial MB concentration and MB concentration at equilibrium, respectively. W is the weight (g) of the adsorbent and V is the volume (L) of MB solution. The photodegradation experiments were conducted post adsorption analysis, by exposing the system to visible light, with irradiance 111 Wm^{-2} , and concentration was recorded using UV-Vis spectrophotometer.

3.8.2 Antimicrobial Analysis

The coliform group, especially *Escherichia coli* (*E. coli*), are used as indicators of faecal pollution in water, to assess the effectiveness of water treatment and disinfection, and for monitoring water quality. Antimicrobial analysis was conducted using a membrane filtration (MF) technique, which is reproducible, can be used to test relatively large sample volumes, and usually yields numerical values more rapidly than other antimicrobial procedures [140]. In this work, total coliforms, coliform and *E. coli* were used as indicator organisms. Details of the procedure employed, based on standard membrane filtration technique 9222, are described in the following sections.

Cultivation of Micro-organisms

Bacteria were grown using a nutrient broth (500 g CM0001 pH 7.4 ± 0.2 at 25 °C), which is a general-purpose fluid medium for the cultivation of micro-organisms. Since these media include all of the components that most bacteria require for development and are non-selective, they are employed for general cultivation and maintenance of bacteria in laboratory-culture collections. Firstly, 200 mL of deionised water was measured, using a graduated cylinder, and 175 mL was added to a 250 mL flask. Then, 2.6 g of nutrient broth was weighed, added to the flask, and left to stir at room temperature for 2 min. The residual 25 mL of water was then added from the graduated cylinder, and solution was stirred until all visible clumps were broke down. The flask was covered with aluminium foil and labelled as nutrient broth, with the date and time, using an autoclave tape. Next the autoclave (lab tech LAC-5100SD) was used to sterilise the media. The heat from the autoclave also helps the agar to properly dissolve in the water. The autoclave was powered on and the drain valve was closed. Deionised water was added to the level of indicator line. The flask of culture media was placed into the autoclave and the temperature was set to 121 °C (held for 15 min at this temperature) using the control panel, and a complete cycle was run for 90 min. Once the cycle was complete, and the pressure gauge read 0 psi, the sterilised flask was removed, and the media was stirred gently using a stirrer plate and allowed to cool to ~45 °C.

The broth was transferred into a tube and bacteria was then added, using an *E. coli* inoculation loop ATCC® 25922, for the growth of bacteria. After incubation, for ~24 h at 35 °C, this tube (labelled as source) was transferred to a bottle containing tap water [141]. The bottle was agitated and left at room temperature for 48 h. Later, the water appeared turbid due to rapid bacterial growth. The volume ratio of source to tap water was 1:100.

Preparation of agars

The agar plates were prepared using m-Endo and m-FC agar solutions (extracted from prepared stock agar solutions) for the detection of *E. coli* and faecal coliform. The mEndo medium contains lactose which changes colour upon fermentation and production of acid. m-Endo agar was prepared according to Standard Method 18th

9222 A, B and Federal Register V 68; 2 139 (7/21/2003) [142] water for coliforms, by a two-step membrane filtration procedure. 51 g of the medium was suspended in 1 L of purified water containing 20 mL of non-denatured ethanol. The solution was agitated and boiled to completely dissolve the medium. The m-FC agar was prepared according to Standard Method 9222 D and Federal Register V 68; 2 139 (7/21/2003) [138]. 52 g of the medium was suspended in 1 L of purified water containing 10 mL of 1% rosolic acid in 0.2 N NaOH. If necessary, the pH was adjusted to 7.4 with 1N HCl. The solution was agitated and boiled to fully dissolve the medium and then cooled to 45-50 °C to be poured into plates.

Coliforms generally create a golden metallic sheen during incubation due to the substantial generation of aldehydes and acid from lactose fermentation. Colonies of atypical total coliforms are dark red, mucoid, or have a dark centre but lack a metallic sheen, while *E. coli* colonies will have a metallic sheen. M-FC medium, on the other hand, includes bile salts, which inhibit all bacteria except enteric. Aniline blue is a pH indicator that becomes blue when the pH is acidic. In this medium, faecal coliform develop blue colonies and *E. coli* colonies will appear flat and dark blue.

Subsequently, the prepared media were poured into petri dishes. The volume did not have to be exact, but it was ensured that the bottom surface of the plates was fully covered, which requires 20 mL for standard size petri dishes. After cooling, the medium solidified, and the plates were turned over to inhibit moisture from collecting on the agar surface.

Water sample preparation

The prepared, contaminated lab water sample was used as a reference sample for quantitative measurements. 250 mL of sealed sterile water bottles were taken and filled with 200 mL of contaminated water. According to standard microbiological examination (9000), the suggested sample volume to be filtered by membrane filtration, for coliform or *E. coli* testing in drinking water, is 100 mL. Therefore, 100 mL of each treated sample was run twice, once for detection of *E. coli* and the remaining 100 mL for detection of faecal coliform. The bottles were labelled with appropriate sample codes and the corresponding amount of RFTi gel samples were weighed and added to the bottle. After preparation, sample bottles were placed on an orbital shaker

(VRN 360 Gemmy, Taiwan) at 200 rpm for 60 min. Next, the sample bottles were exposed to sunlight for 90 min.

3.8.3 Membrane Filtration Procedure

First, all petri dishes were labelled, and the filtration apparatus was assembled with a portable funnel base (labelled 1, vacuum support) attached to the filtering head, as shown in Figure 3.22. The base was connected to a hand pump for convenient filtration. To begin with, a Bunsen burner was turned on to sterilise the forceps in order to aseptically transfer the membrane filter. The membrane filter (labelled 2 on Figure 3.22, MF-millipore, pore size of $0.45\ \mu\text{m}$) was used with a rated pore diameter to provide complete retention of coliform bacteria. Presterilized membrane filters were transferred to the porous holder with a pair of forceps by dipping in ethanol, excess ethanol was tapped off before passing it once through the flame and letting it cool for ~ 5 s. The filter, with grid side facing upwards, was placed on the base of the filter and the funnel was replaced. 100 mL of water sample was gradually passed through the filter and the biological contaminants entrapped onto the membrane filter. Next, the funnel was lifted, and the membrane filter was carefully removed and transferred to the respective agar plates, as shown in Figure 3.22 c. After repeating the same procedure for all treated water samples, the plates were placed upside down in the incubator (Thermo Scientific Heratherm IMC18 Incubator) for 24 h as the colonies of *E. coli* and faecal coliform appear within 18 to 24 h. The incubation temperature for m-Endo agar plates was $35\ ^\circ\text{C}$ and m-FC agar plates were incubated at $44\ ^\circ\text{C}$.

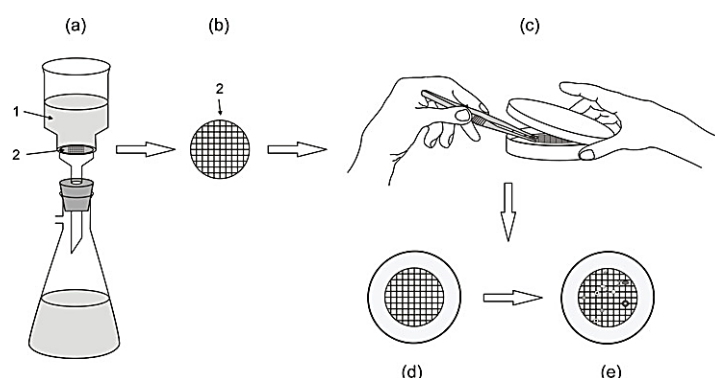


Figure 3.22 Membrane filtration procedure [143] .

For the detection of *E. coli*, mEndo agar plates were removed after ~ 24 h from the incubator and the dark red colonies with metallic sheen counted were counted. For the

detection of faecal coliform, m-FC agar plates were removed after ~24 h from the incubator and blue colonies were counted, which indicate faecal coliform colonies.

The calculation for *E. coli* and faecal coliform was carried out after counting the number of colonies, colony forming units (CFU per 100 mL), developed post incubation colonies grown on the grid after 24 h. The density was estimated from the volume of the sample filter and the number of colonies counted on the membrane. As counts are reported per 100 mL of sample, the per mL values must be multiplied by a factor of 100 as shown in Equation 3.19.

$$\text{no. CFU per 100 mL} = \frac{\text{coliform colonies counted}}{\text{mL sample filtered}} \times 100 \quad \text{Equation 3.19}$$

As large volumes of the sample can be filtered, the membrane filtration technique can detect the presence of a very low number of bacteria. For drinking water samples, if no total coliform colonies are observed then total coliform colonies were counted/reported as < 1 CFU per 100 mL.

3.9 Summary

In conclusion, this chapter discusses the theories that explain the experimental approaches employed in this study, laying the groundwork for subsequent methodologies utilised for material characterization and application testing. This includes probing, chemical, compositional, electronic, surface, and textural properties of the synthesised RFTi gels (Chapter 4), as well as techniques used for application tests for pollutant degradation, such as concentration determination of indicator dyes and bacterial viability (results are discussed in Chapter 5, 6 and 7).

Chapter 4: Characterisation and Analysis of Materials

Analyses of material characteristics are critical for evaluating the application potential of any material; hence, understanding material properties is essential for its optimisation. This chapter focuses on probing the material properties and investigating the impact of varying concentrations of RF and TiO₂ in integrated RFTi gels, synthesised as explained in Chapter 3. The experimental techniques and procedures discussed were employed to determine the structure and property relationship of each RFTi gel, and the results were analysed and discussed considering theory and previously reported literature. A few results presented in this chapter have been published in 'Gels' [144] and 'Molecules' [145], a complete manuscript can be found in Appendix H.

4.1 Morphological Analysis

Field-emission scanning electron microscopy. Pure RF samples showed a typical three-dimensional structure of carbon xerogels, as demonstrated by Czakkel *et al.* [146]. The micrographs show RF polymers having an interconnected compact structure and uniform microspheres with smooth surfaces bonded together, as shown in Figure 4.1 **Error! Reference source not found.**

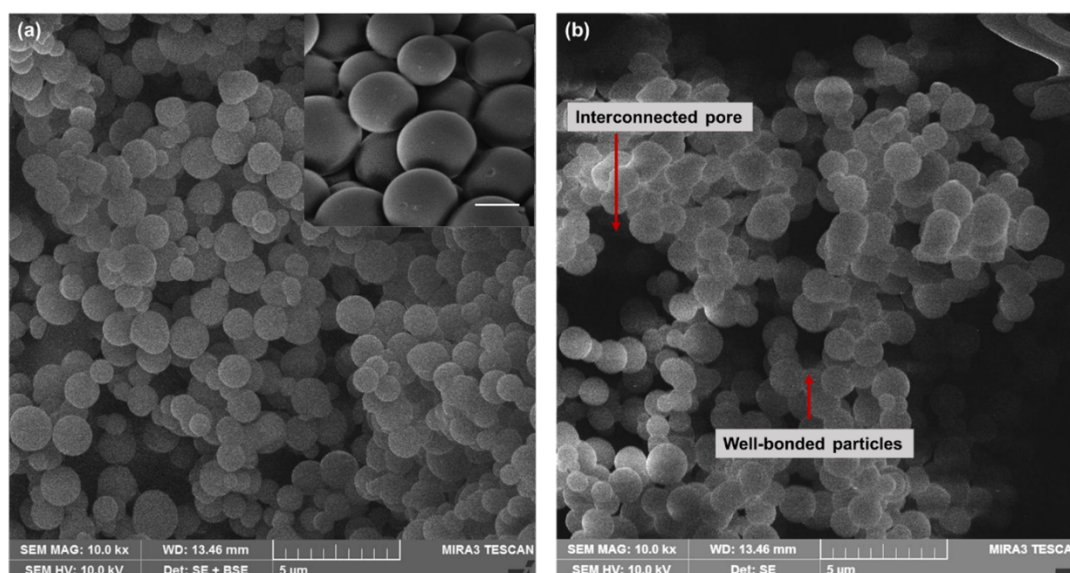


Figure 4.1 Micrographs of RF gels.

After the addition of 10% TiO_2 , the obtained RFTi samples maintained a regular spherical shape with an overall homogeneous smooth surface without differentiation between the organic and inorganic phases (Figure 4.2 a, b).

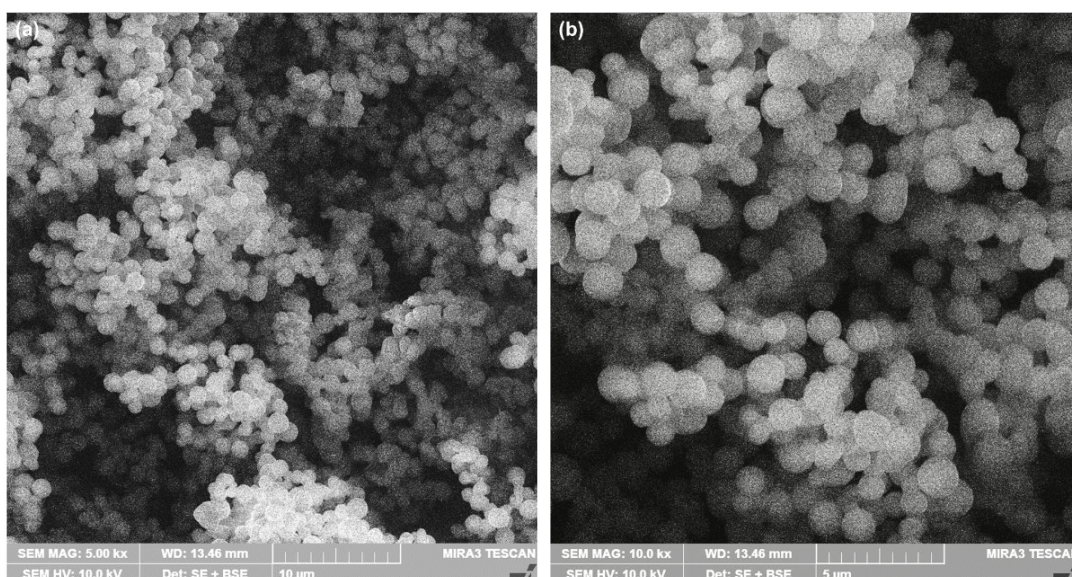


Figure 4.2 Micrographs of RFTi10.

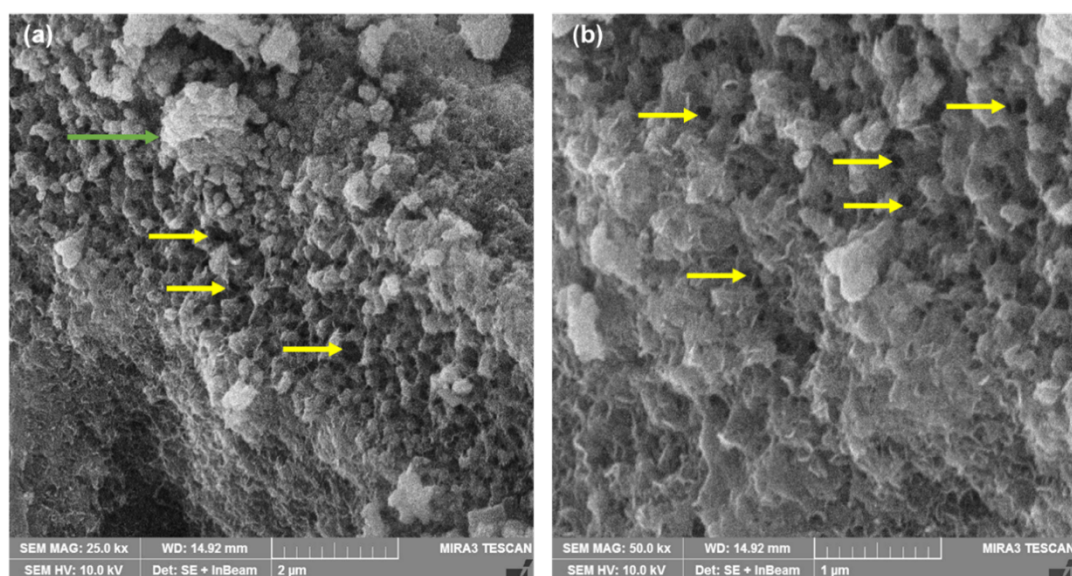


Figure 4.3 Micrographs of RFTi30 (green arrow-surface heterogeneity due to TiO_2 aggregation, yellow arrows-retained porosity).

With the further addition of TiO_2 , heterogeneity and surface roughness began to appear, as marked by the green arrow in Figure 4.3 a, and the porosity of the RFTi

gels was retained, as indicated by the yellow arrows in Figure 4.3 b, for RFTi30. The homogenous distribution of TiO_2 along all the samples was dependent on TiO_2 loading in each RFTi gel. Low amount of TiO_2 (10-30%) was homogeneously distributed in the carbon matrix (corroborated by distribution of TiO_2 nanoparticles shown in the Appendix B).

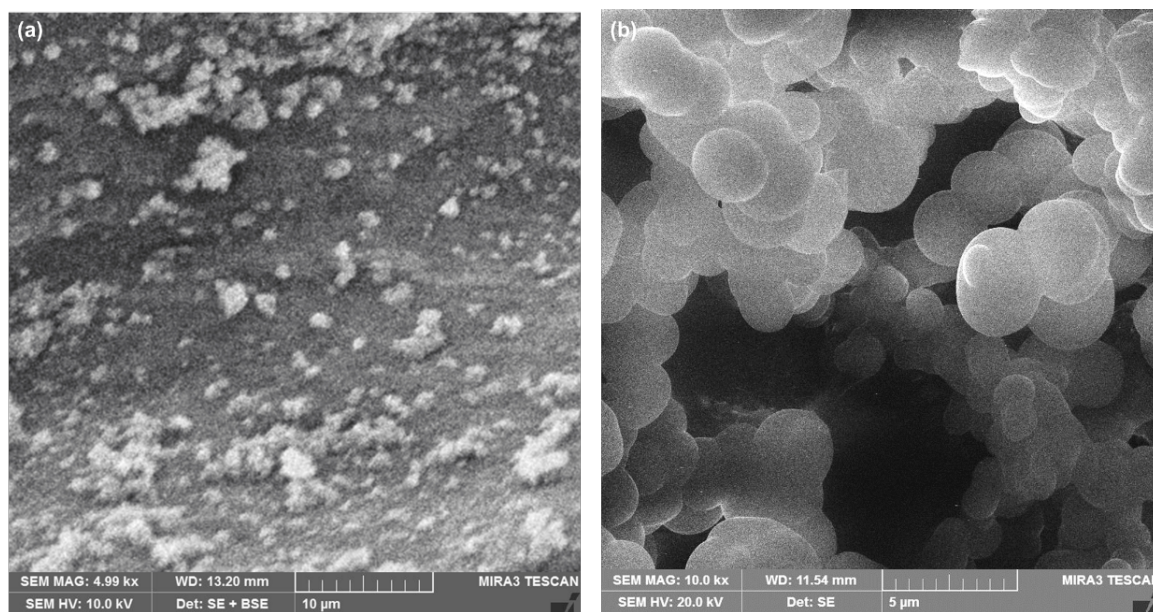


Figure 4.4 Micrographs of RFTi40.

Figure 4.4 a shows micrograph of RFTi40, in which spherical form of carbon spheres persist, implying well-distributed TiO_2 nanoparticles, with retained porosity and interconnected carbon spheres (Figure 4.4 b). Garcia *et al.* [95] reported that the homogenous distribution of TiO_2 was independent of the TiO_2 loading in the organic phase, which in this case was true for samples with TiO_2 in the range 10-50%; however, their study was limited to 40% TiO_2 incorporated in the carbon phase. In this study, the distribution was dependent on TiO_2 loading beyond 50% owing to the reduction in the organic phase as well as the tendency of TiO_2 to aggregate, resulting in a heterogeneous distribution of TiO_2 clusters. It has been previously reported that an increase in the nanoparticle content in the porous carbon structure results in a substantial decrease in the pore structure parameters, resulting in a decrease in the mesopore volume, indicating partial or complete pore blocking with nanoparticles. According to Ju *et al.* [147], the number of pores decreases with increasing titania nanoparticles in porous carbon because titania nanoparticles fill and block some

pores. Similarly, in this study, the heterogeneity and surface roughness increased, while the porosity tended to decrease with further addition of TiO_2 .

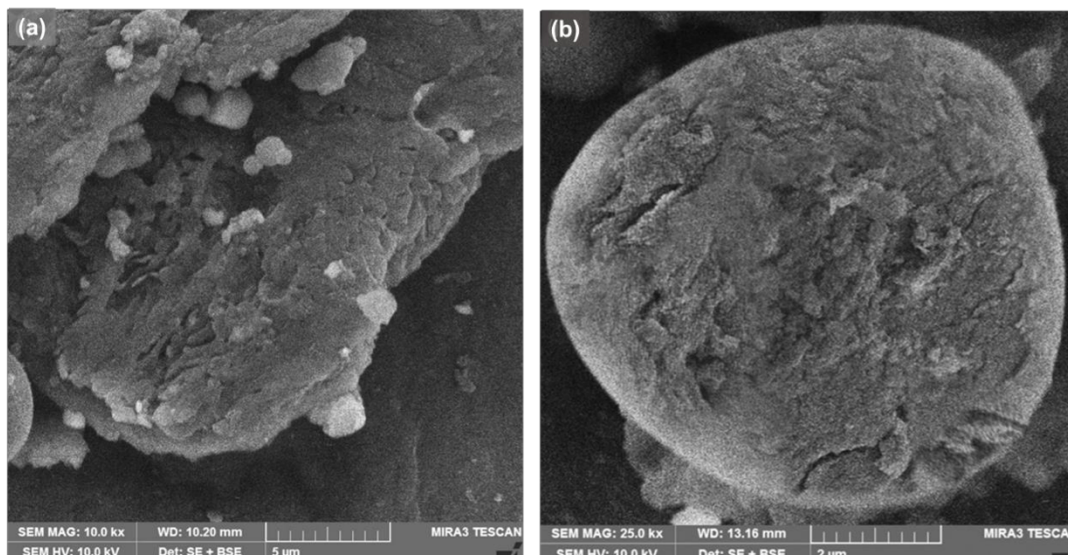


Figure 4.5 Micrographs of RFTi60.

With further TiO_2 loading, the micrographs show the evolved crystalline structure of TiO_2 , as shown in Figure 4.5 a for RFTi60, and a heterogeneous surface manifested with a different surface roughness on a spherical form of carbon. In this case, the carbon phase was engulfed by TiO_2 nanoparticles, as evidenced by the surface detail, demonstrated in Figure 4.5 b. This observation is similar to that reported by Simonetti *et al.* [148] who demonstrated the presence of TiO_2 crystallites, marked with red arrows on Figure 4.6, enveloping carbon spheres with the presence of pores indicated by yellow arrows.

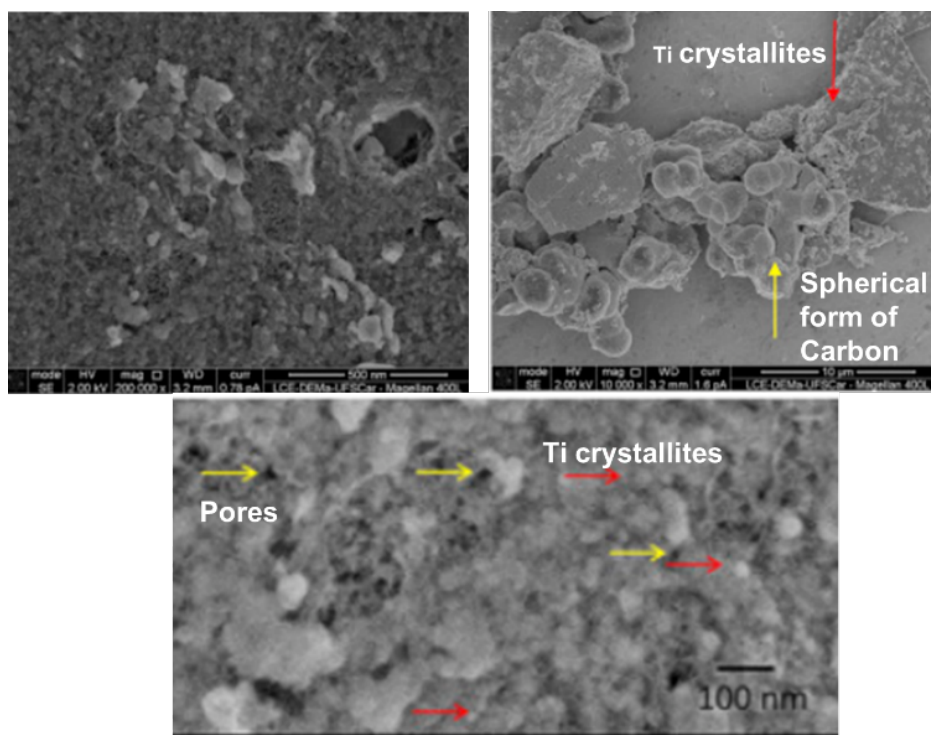


Figure 4.6 Micrographs of Titania/carbon composites prepared by Simonetti *et al.* [148].

The TiO_2 crystallites continued to grow, as shown in the micrographs for RFTi70 (Figure 4.7 a, b) and RFTi80 (Figure 4.8 a, b) demonstrating an increase in TiO_2 aggregates with greater surface roughness (green arrows) and reduced porosity (yellow arrows) in comparison with the highly porous smooth carbon surface of pure RF gels and RFTi gels with low amounts of TiO_2 (10-30%). Finally, the discreteness of the carbon spheres became less evident owing to further very high TiO_2 phase and the pores could not be identified, as seen in Figure 4.9 for RFTi90.

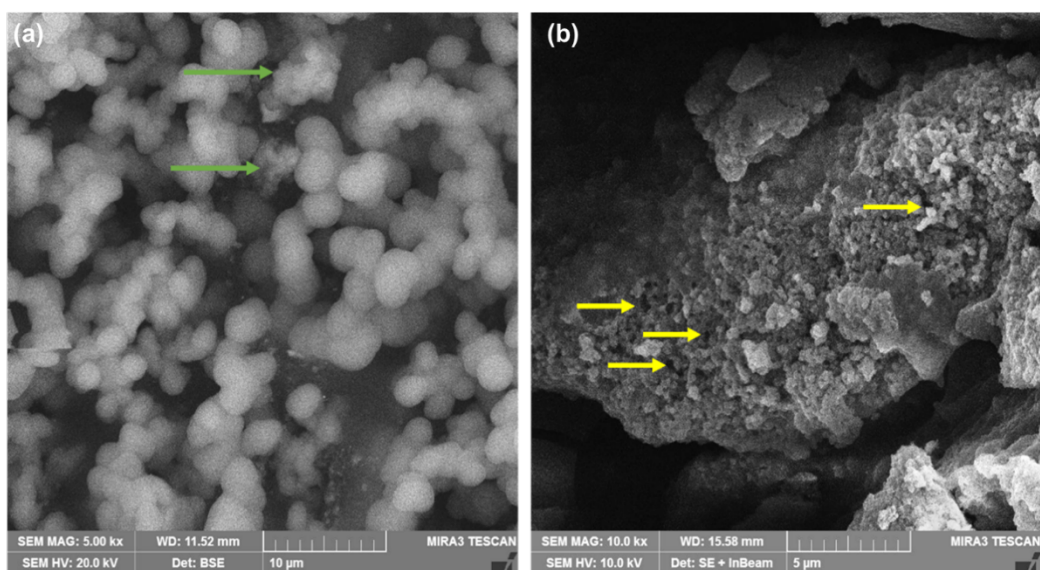


Figure 4.7 Micrographs of RFTi70.

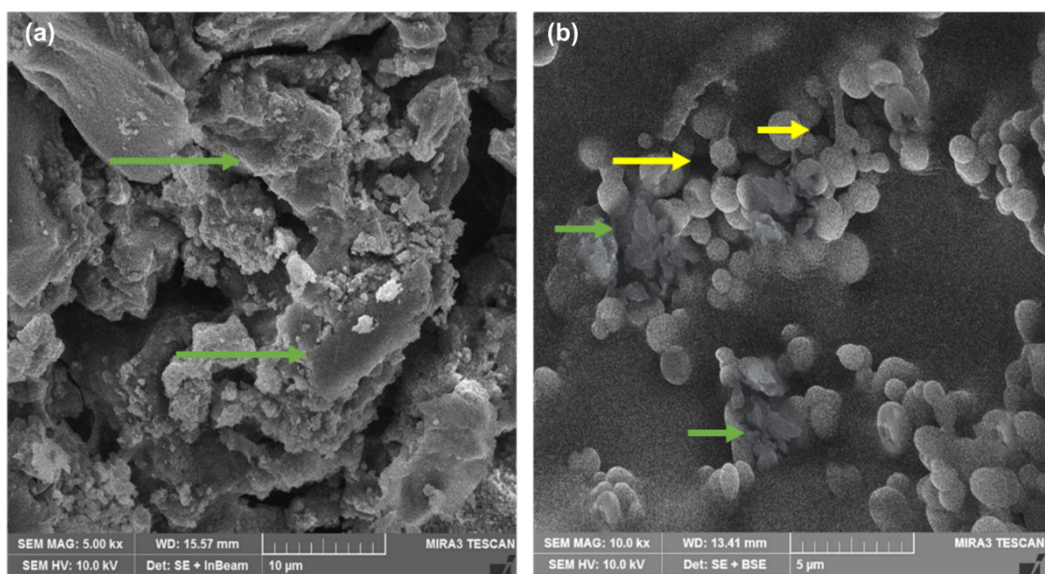


Figure 4.8 Micrographs of RFTi80.

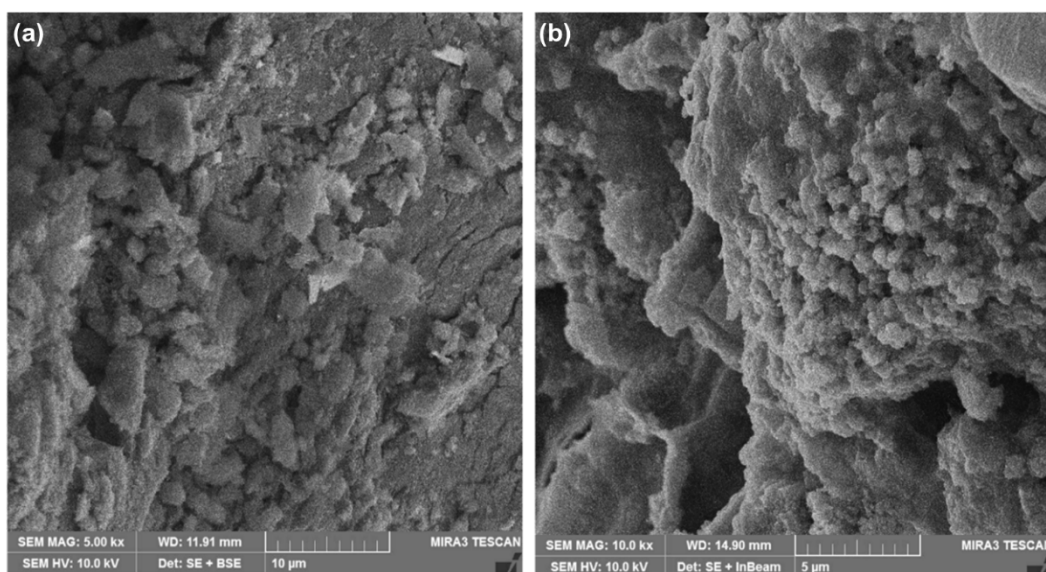


Figure 4.9 Micrographs of RFTi90.

4.2 Surface Area and Pore size Analysis

Adsorbents and photocatalysts with large surface areas and high porosities are desirable for the enhanced adsorption and degradation of contaminants, as demonstrated in detail in Chapter 1. The large surface areas facilitate higher adsorption owing to the presence of abundant active sites, so the contaminants can be adsorbed in large quantities onto the surface of an adsorbent-photocatalyst. Any available porosity can accelerate contaminant access, adsorption, and photodegradation, providing dimensions suitable for the target species to enter and migrate along the surface of the pores.

In this work, the role of carbon is to provide a high surface area and mesoporous framework, as well as immobilise and disperse titania nanoparticles for enhanced application performance. Carbon derived from RF gels generally possesses high surface areas and porous structures that can be modified as desired when synthesised via the sol-gel route (demonstrated in Chapter 3), enabling physical and chemical interactions in the sol, ultimately resulting in the formation of porous gels with high surface area and pore volumes [113]. The N_2 adsorption isotherm obtained for the RF gel synthesised in this study is shown in Figure 4.10 and the corresponding pore size distribution is displayed in the inset. The shape of the isotherm is typical for RF gels or mesoporous carbon [37], which, according to IUPAC classification, fits Type IV and

hysteresis loop type H1, with well-distinguished regions. A sharp knee at p/p_0 0.05 corresponds to complete monolayer layer coverage, and the following curvature shows the overlap of monolayer formation and the onset of multilayer adsorption. A linear relationship for the adsorption isotherm can be observed in the range of $0.1 < p/p_0 < 0.5$. At slightly higher relative pressures, the multilayers gradually built up and underwent pore condensation, via a hysteresis loop, validating the presence of a mesoporous structure in the RF gel. The loop observed is typical of capillary condensation, which is delayed because of the existence of metastable adsorption fluid in the adsorption branch, while evaporation occurs via equilibrium from an open pore. Furthermore, the shape of the hysteresis loop revealed the presence of ordered mesopores with a uniform cylindrical open-ended three-dimensional pore network [149]. It was observed that pore condensation was accompanied by hysteresis, implying that the pores were wider than 4 nm. The calculated surface area of RF gels was $538 \text{ m}^2\text{g}^{-1}$ with corresponding pore size and pore volume of $\sim 8 \text{ nm}$ and $0.9 \text{ cm}^3\text{g}^{-1}$, respectively. These results were comparable to the BET surface area of the base-catalysed carbon xerogels obtained via a similar route employed in this work, which was $446 \text{ m}^2\text{g}^{-1}$ with an average pore width of 11 nm , as reported by Martin *et al.* [150].

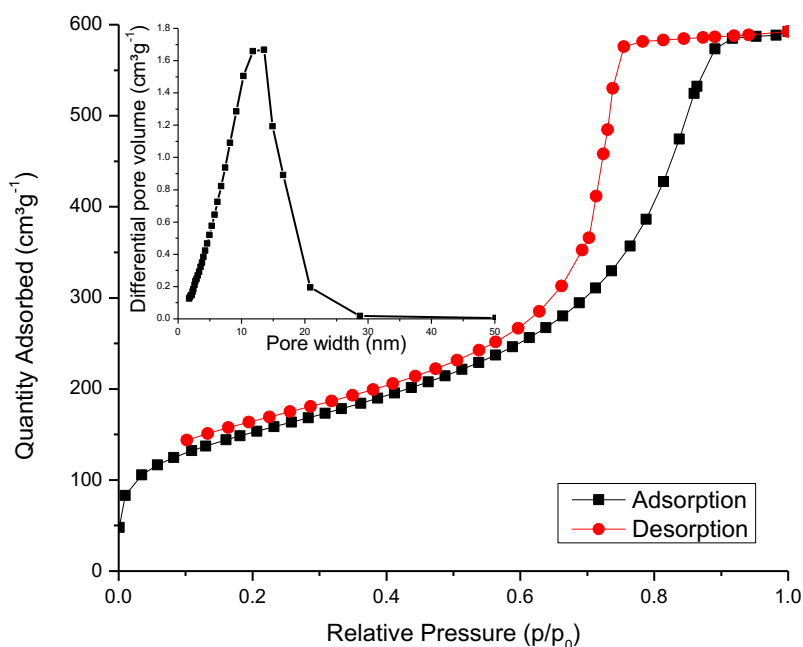


Figure 4.10 N₂ isotherm and BJH pore size distribution (inset) of pure RF gel.

When TiO_2 was added to the RF gel, the surface area of the sample decreased depending on the TiO_2 content, implying that some pores in the RF gel network were blocked by titania nanoparticles. It is important to note that these pores or voids are necessary to host other materials; however, excess nanoparticles and consequent blockage may reduce the surface area and application potential of composite materials. In the case of RFTi10 (Figure 4.11), the gel characteristics were similar to those of pure RF gels demonstrated in this work, signifying the presence of ordered open-ended mesoporous. The BET surface area and pore volume were calculated to be $439 \text{ m}^2\text{g}^{-1}$ and $0.855 \text{ cm}^3\text{g}^{-1}$ with a narrow pore size distribution observed and the average pore width was calculated to be 9.4 nm. It was observed, through the shape of the hysteresis loops, that ordered mesoporosity was sustained until 30% of TiO_2 added in the RF gel network (Figure 4.12). The shape of the pores was classified according to IUPAC classification defining hysteresis loop shapes and their correlation to network and adsorption mechanism [35].

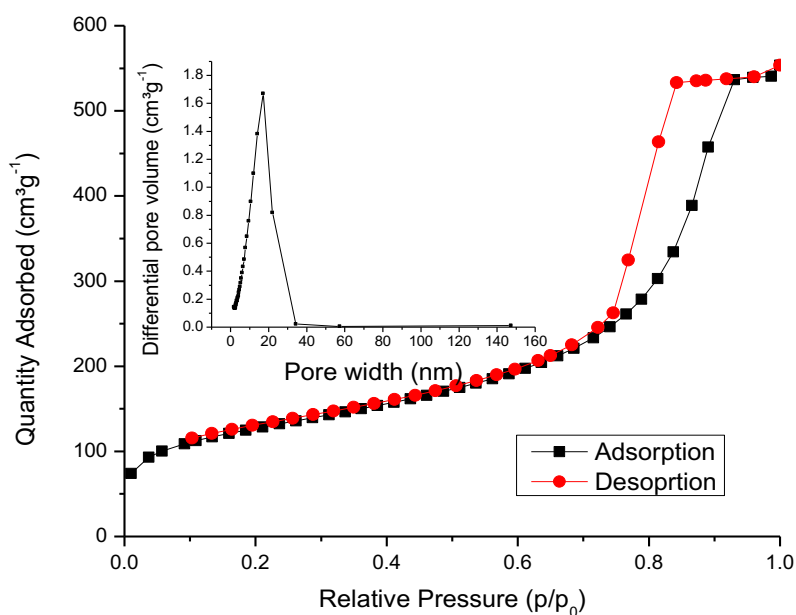


Figure 4.11 N_2 isotherm and BJH pore size distribution (inset) of RFTi10 gel.

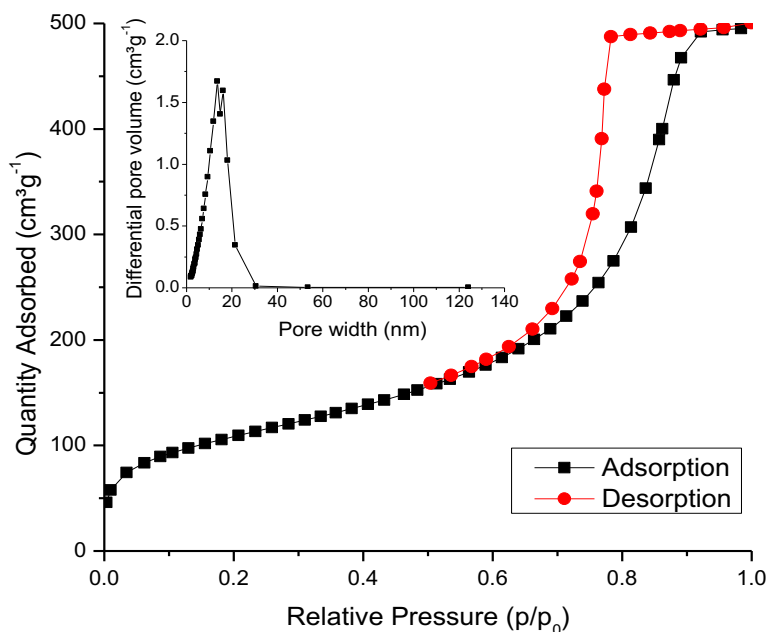


Figure 4.12 N_2 isotherm and BJH pore size distribution (inset) of RFTi30 gel.

With a further increase in the TiO_2 concentration, the change in the hysteresis loop suggests disordered porosity in the RFTi structure, which is consistent with the morphological analysis of RFTi samples with higher amount of TiO_2 , illustrating blockage of the RF pore network. As shown in Figure 4.13, for RFTi50, H2 type hysteresis observed implies disordered pores, suggesting that samples with larger amounts of TiO_2 nanoparticles resulted in increasingly complex pore systems due to TiO_2 aggregates occupying the pore sites, consequently leading to a significant reduction in the surface area. Therefore, the calculated BET surface area is relatively low at $290 \text{ m}^2\text{g}^{-1}$, pore size and pore volume calculated was 4 nm and $0.2 \text{ cm}^3\text{g}^{-1}$, respectively. The shape of the isotherm suggested that the porous network was comprised of wide neck-like or ink bottle-shaped pores in which the pore evaporation was delayed, and desorption at equilibrium did not occur through open pores, while the wide pores remained filled until low p/p_0 was reached, evaporation occurred from the neck section, leading to H2 type hysteresis.

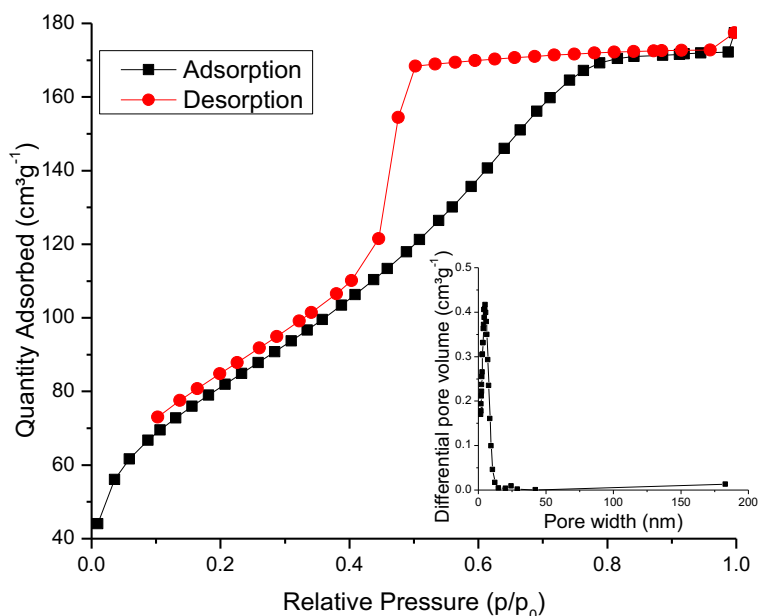


Figure 4.13 N_2 isotherm and BJH pore size distribution (inset) of RFTi50 gel.

The nature of the pores in RFTi50 can further be classified as H2(a) [151], which means that the neck portion is much narrower than the wider pore cavities, thus generating a sharp desorption isotherm exhibiting pore-blocking effects. Analysis of the shape of the isotherms revealed consistent findings for the samples RFTi60 (calculated measurements shown in Table 4.1) and RFTi70 (Figure 4.14).

Furthermore, with an increase in TiO_2 , changes in pore size and pore volume in RFTi gels were observed owing to the loss of oxygen functional group side chains, this may prevent the formation of methylene ether bridges because TiO_2 nanoparticles debilitates polymer chain formation and would either form Ti-O-C bonds with the RF gel, or excess TiO_2 nanoparticles may diffuse into the RF network, leading to smaller reduced porosity and small pore sizes. A similar phenomenon was reported in a previous study on TiO_2 polymer nanocomposites [152] which indicated that the incorporation of nanofillers heterogeneously distributed within a polymer host may constrain the main polymer chains. The strong interactions between the polymers and nanofillers may reduce the movement of the polymer chains, and thus, the loading capabilities of the fillers decrease. Likewise, in this case, a large amount of TiO_2 reduced the size of the cavities and voids in the RF gel network, leading to a progressive reduction in surface area and change in the conformation of the RFTi gels, as evidenced by the appearance of bimodal pore-size distribution for RFTi80 (Figure

4.15 inset), indicating primary intra-aggregates and secondary inter-aggregates centred at 13 and 37 nm, respectively. A similar observation was reported by Yu *et al.* [153] for Titania/C60 composites, indicating that pore size distribution results from two types of aggregates where mesopores are usually related to primary intra-agglomeration and larger pores are associated with secondary inter-aggregation.

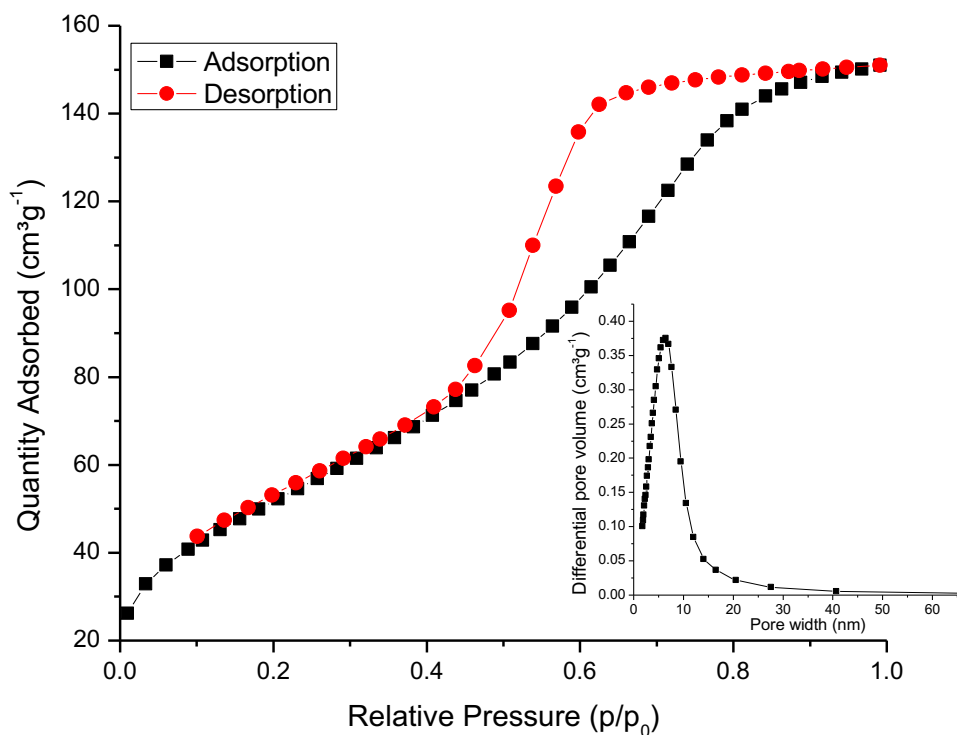


Figure 4.14 N₂ isotherm and BJH pore size distribution (inset) of RFTi70 gel.

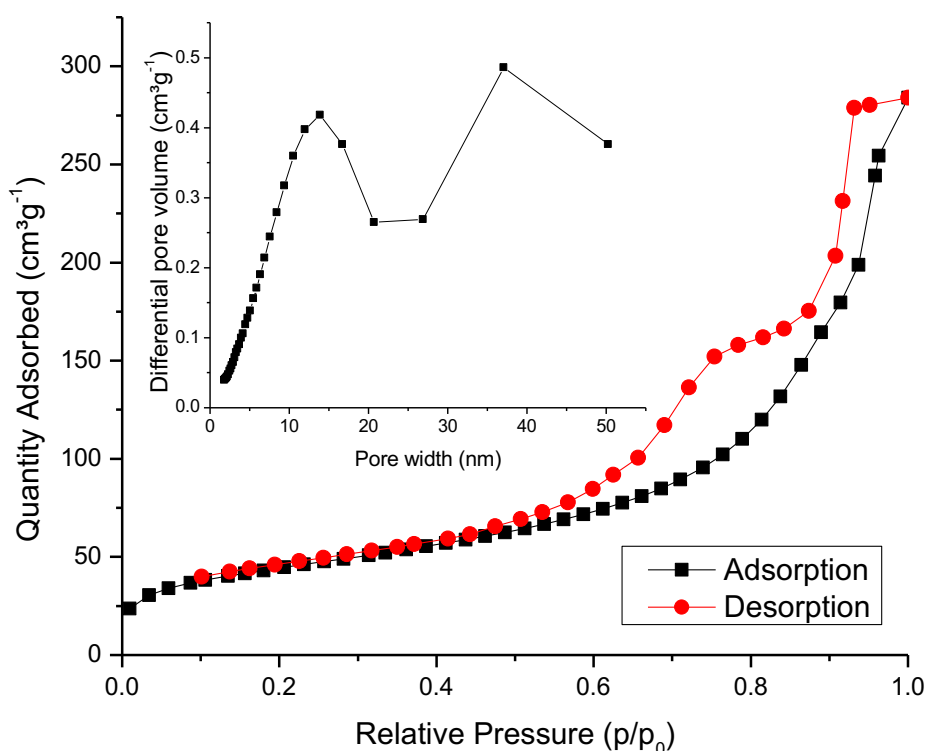


Figure 4.15 N_2 isotherm and BJH pore size distribution (inset) of RFTi80 gel.

Figure 4.16 shows the N_2 isotherm obtained for the sample RFTi90, which appears similar to that of pure TiO_2 synthesised in this work shown in Figure 4.17. The calculated parameters are shown in Table 4.1. Both the isotherms are Type H3 with the hysteresis loop confined in the range $0.7 < p/p_0 < 1.0$ demonstrating a wide pore size distribution in the range of 2-100 nm, as also previously reported for low carbon/ TiO_2 composites [148] or pure TiO_2 nanoparticles [153]. This classification of hysteresis implies the existence of aggregates (loose accumulations) of plate-like particles forming slit-like pores [154]. Such characteristics have been reported for mesoporous TiO_2 nanoparticles synthesised through sol-gel route for photocatalytic applications [155]. However, the textural properties obtained for TiO_2 nanoparticles in this study are superior to commercial Degussa P25 (titania photocatalyst used for its photocatalytic activity) having a specific surface area of $\sim 57 \text{ m}^2\text{g}^{-1}$ [156].

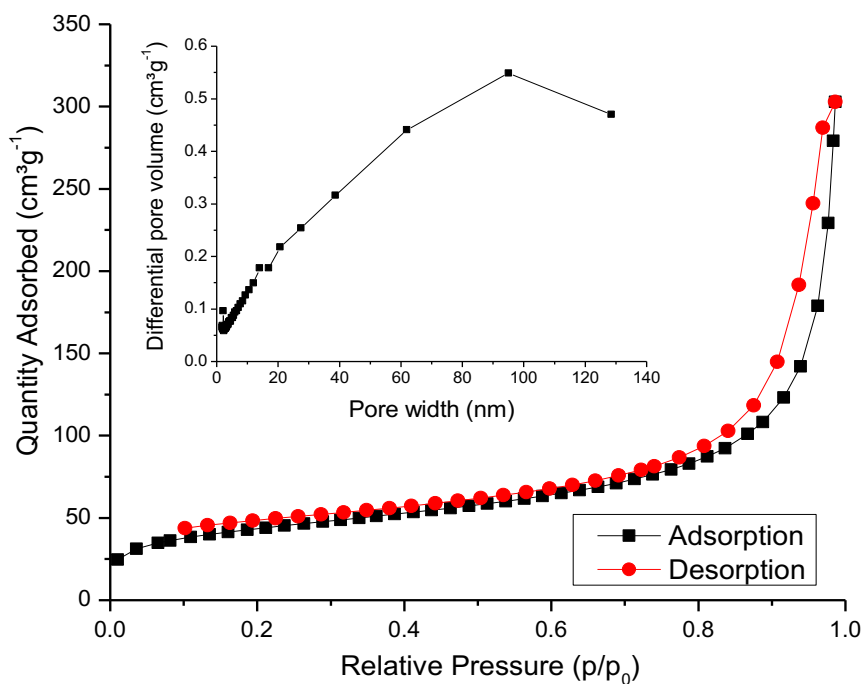


Figure 4.16 N_2 isotherm and BJH pore size distribution (inset) of RFTi90 gel.

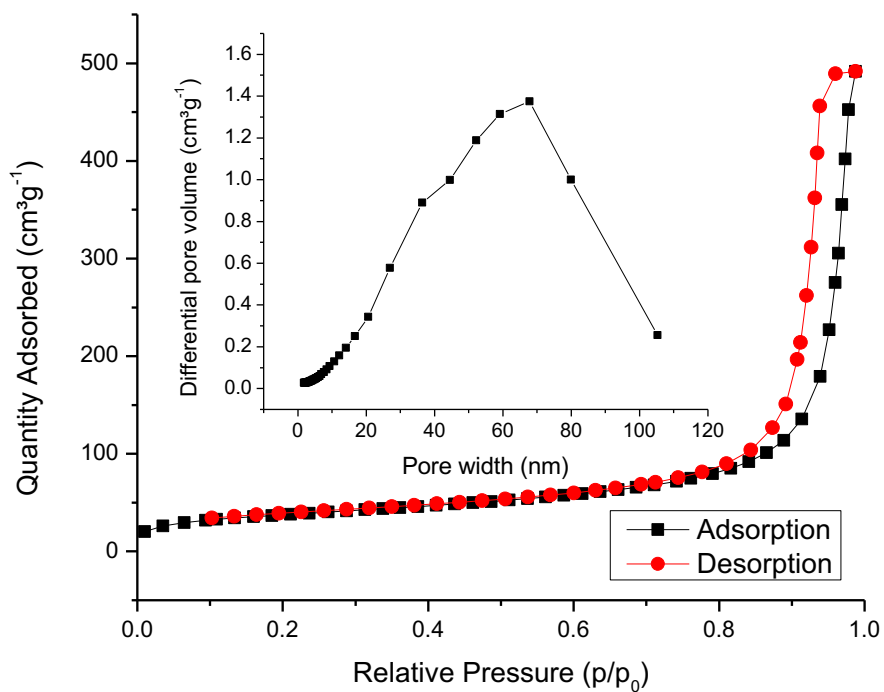


Figure 4.17 N_2 isotherm and BJH pore size distribution (inset) of pure TiO_2 .

Table 4.1 Surface area and pore size measurements of synthesised samples.

Sample	Surface area (m ² g ⁻¹)	Pore size (nm)	Pore volume (cm ³ g ⁻¹)
Pure RF	538	8	0.9
RFTi 10	439	9	0.7
RFTi 20	409	5	0.4
RFTi 30	384	8	0.8
RFTi 40	349	6	0.4
RFTi 50	290	4	0.2
RFTi 60	257	5	0.2
RFTi 70	193	5	0.2
RFTi 80	133	11	0.4
RFTi 90	150	16	0.4
Pure TiO ₂	131	28	0.5

A well-developed mesoporous structure and large surface area are projected to enhance adsorption and photocatalytic activity. The textural characteristics of the synthesised RFTi gels discussed in the previous section elucidated the structure and property relationship of these materials for their optimisation, which is required for enhanced application performance.

4.3 Fourier Transform Infrared Spectroscopy

The FTIR spectra of the synthesised samples were collected according to the methodology described in Section 3.7.1, and peaks were assigned using the characteristic functional groups listed in the handbook on Infrared and Raman

Characteristic Group Frequencies [157]. Figure 4.18 shows the FTIR spectra of pure RF, pure TiO_2 and RFTi30.

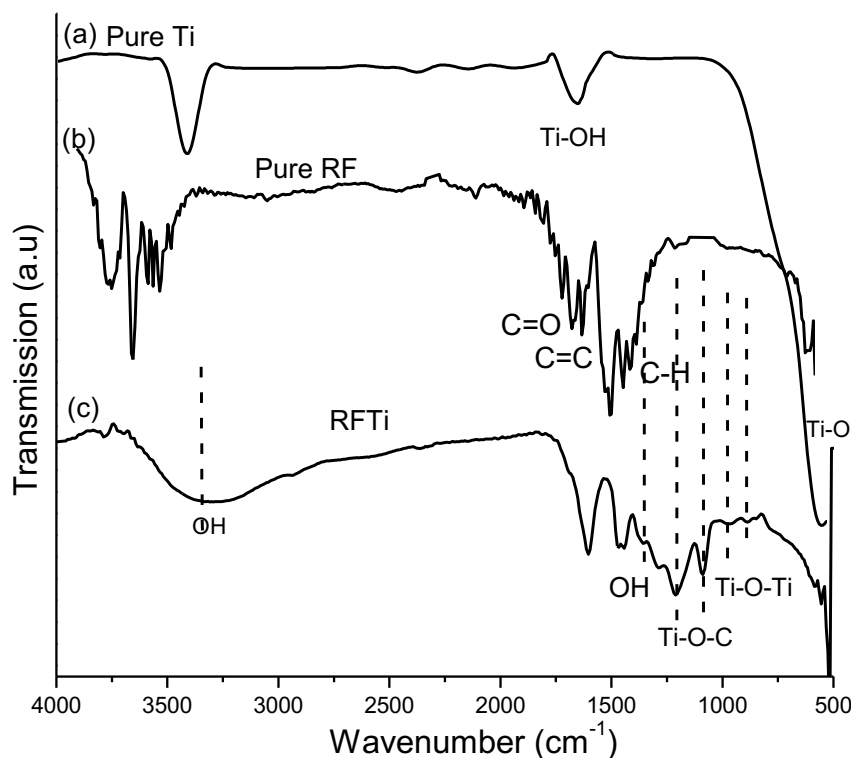


Figure 4.18 FTIR spectra of synthesised (a) RF, (b) TiO_2 and (c) RFTi30 samples.

The FTIR spectrum of TiO_2 (Figure 4.18 a) obtained in this work was analogous to that previously reported in the literature, demonstrating the main peaks of Ti-O and Ti-OH at 480 and 1620 cm^{-1} , respectively [158]. The main features of the RF gels (Figure 4.18 b) were observed with clear peaks for C=C stretching, CH_2 , and C-O-C of aromatic rings, methylene bridges, and methylene ether bridges. A small peak with moderate intensity appeared at 2932 cm^{-1} due to the stretching of CH bonds of the aromatic ring, while weak vibrations in the range of 2000-1700 cm^{-1} were attributed to CH bending of aromatic compounds. A complete sol-gel polymerisation reaction of resorcinol-formaldehyde was validated by the absence of peaks expected in the range 1740-1720 cm^{-1} , associated with the C=O stretching of aldehyde, which is consistent with previous studies. Additionally, the bands at 1605, 1467, and 1440 cm^{-1} , corresponding to aromatic ether bridges, were attributed to the polycondensation of resorcinol to form the RF gel network. The signals for C-O-C at 1206 and 1084 cm^{-1}

were associated with the C–O–C stretching vibrations of methylene ether bridges between the resorcinol molecules [159].

Compared to the pure constituents, the RFTi spectrum (Figure 4.18 c) shows additional transitions, which are marked in the fingerprint region. For carbon/TiO₂ composites, it is generally known that the oxygenated surface moieties of carbon support the attachment of Titania [160]. In this work, the OH peak of RF around 1400 cm⁻¹ appeared weak in the RFTi spectrum, signifying the crosslinking of RF and TiO₂ via hydroxyl groups. New peaks at 1200 and 1084 cm⁻¹ suggested the formation of Ti–O–C chemical bonds between both phases. Similar crosslinking has been reported for several other carbon/TiO₂ composites [160-162], and with regard to photocatalytic applications, it has been validated that the formation of this heterojunction is mainly responsible for tuning the electronic configuration of TiO₂ for visible-light response [163].

4.4 UV-Vis Spectroscopy

The integration of RF with TiO₂ was hypothesised to modify the electronic structure of the composite material for absorption and photodegradation under visible light irradiation, as discussed in Chapter 1; therefore, the UV-Vis spectra of the synthesised materials were collected according to the methodology explained in Section 3.7.2. Investigation of the extension of the absorption edge and modification of the electronic configuration of the synthesised material will elucidate its capability to activate and degrade pollutants under visible light.

According to a few studies [164-166], RF has a unique structure, comprising aromatic rings and OH groups, that can serve as a semiconductor, and thus, be used for energy conversion. Section 4.4.1 briefly explains the structure of the RF before proceeding to the results and analysis of the integrated RFTi, discussed in Section 4.4.2

4.4.1 UV-Vis Analysis of RF Gels

The UV-vis absorbance spectrum of the synthesised RF sample is shown in Figure 4.19 a, and the energy bandgap, estimated by the Tauc method (according to section 3.7.2), is shown in Figure 4.19 b. In contrast to other carbonaceous materials, which typically exhibit absorbance in the range 180-260 nm [167], the maximum absorbance

range of synthesised RF gel was observed in the range 220-500 nm, i.e., in the UV-Vis region of the electromagnetic spectrum and the calculated bandgap (4.48 eV) resembled that of an activated carbon [168]. The absorption shift to extended wavelengths is associated with the change in density of the electronic states of the aromatic rings upon polymerisation of resorcinol and formaldehyde, which shifted $\pi - \pi^*$ transitions toward the visible region [169].

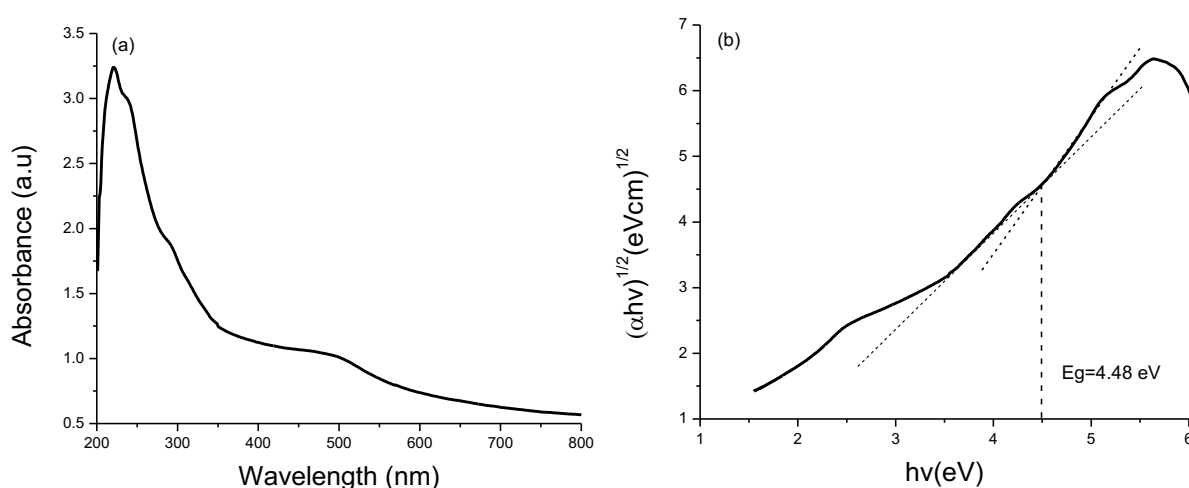


Figure 4.19 (a) UV-Vis absorption spectrum of pure RF gels synthesised in this work and (b) corresponding Tauc plot.

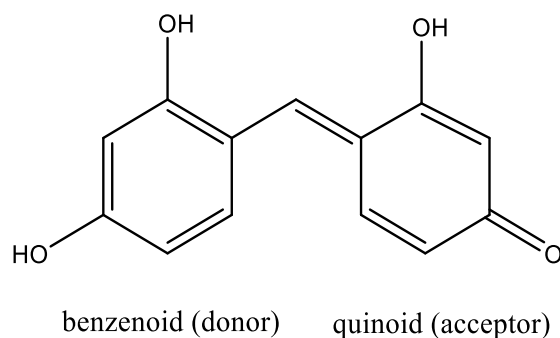


Figure 4.20 π -conjugated donor (D)-acceptor (A) couple.

It is known that the energy states in carbon depend on sp^2/sp^3 ordering, as well as disordering of π states [170]. In the case of RF, the crosslinking that occurs during polymerisation increases the content/size of sp^2 groups, and π states are significantly increased. This is because during polymerisation, several resorcinol is created as quinoid, which are π conjugated with a benzenoid form, and act as a donor-acceptor couple (Figure 4.20) that is capable of separating the charge upon photoexcitation.

Owing to this property, Shiraishi *et al.* [164] employed RF resins as metal free semiconductor photocatalyst for energy conversion. The donor and acceptor couples with highest occupied molecular orbital (HOMO) and lowest unoccupied molecular orbital (LUMO) gaps are crosslinked with methylene linkers (Figure 4.21). The π stacked interaction of donor-acceptor units cause hybridisation of HOMO and LUMO levels between the chains and π conjugation along the polymer chain (Figure 4.22). The donor-acceptor couples, hybridised by their π stacking, result in low band gap of the RF resins, where the valence band consists of a benzenoid unit, and the conduction band is a quinonoid unit. The benzenoid unit acts as a light harvesting group, which determines the photoexcitation of charges. The low bandgap obtained in their study was due to the RF resins synthesised at a high hydrothermal temperature (250°C), consequently forming a larger number of quinoid units.

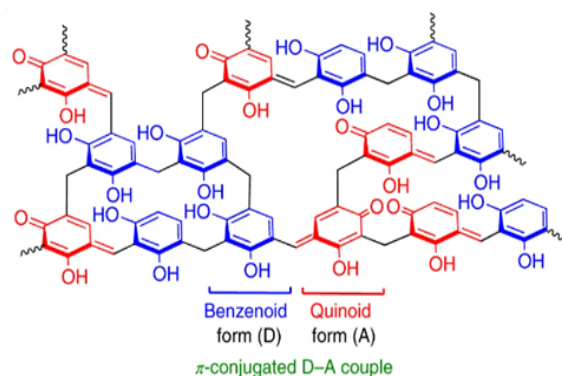


Figure 4.21 Structural representation of π stacked donor (D)-acceptor (A) units [164].

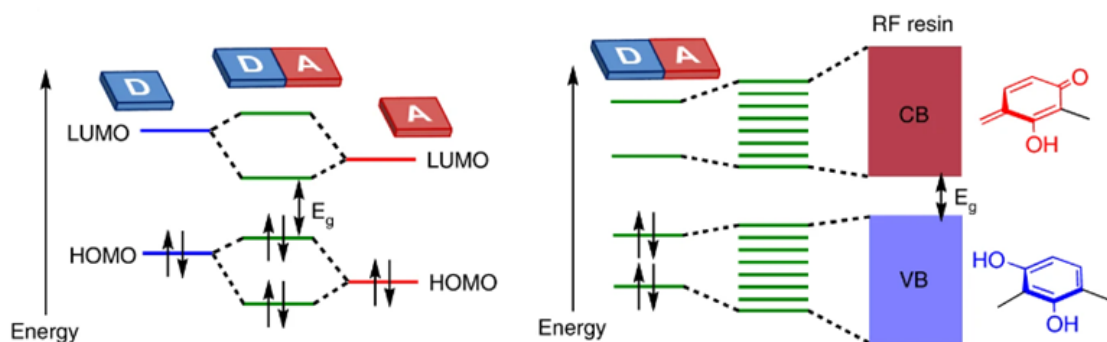


Figure 4.22 Electronic structure representation of π stacked donor (D)-acceptor (A) units [164].

Other studies by Yuan *et al.* [169] and Higashimoto *et al.* [171, 172] have also reported an experimental demonstration of the enhanced formation of donor-acceptor units with

an increase in preparation temperature. Nevertheless, these studies are primarily focused on improving the photocatalytic properties of RF materials while the reported materials have poor textural properties (with a surface area of $\sim 15 \text{ m}^2\text{g}^{-2}$ and pore volume of $\sim 0.04 \text{ cm}^3\text{g}^{-1}$) which are unsuitable for adsorption application. In contrast, the synthesis approach employed in this study is similar to that used by Zhang *et al.* [166], who also demonstrated that gelation and curing of RF carried out at relatively low temperature showed a red shift. However, a few reports mention that donor-acceptor couplings in structures such as RF are known to show quenched excited states in protic media; hence, the charge transfer efficiency is low [164, 173]. Additionally, because of the amorphous nature of the RF structure the charge transfer efficiency is low hence, RF alone is not recommended as a photocatalyst. To increase the efficiency a precise molecular structure is preferred to promote charge transfer efficacy. Therefore, attempts have been made to enhance the properties of RF by adding nitrogen, which further lowers the band gap to 1.8 eV owing to enhanced $\pi - \pi^*$ transitions and formation of new energy levels within the band gap [166].

4.4.2 UV-Vis Analysis of RFTi Gels

The chemical linkages formed between RF and TiO_2 , demonstrated via FTIR analysis (Section 3.7.1), determines the visible light absorption capabilities of the synthesised material for photodegradation under visible light irradiation. Proposed charge transfer complex is demonstrated in Figure 4.23. The Ti-O-C bond formation introduces a new absorption band in the visible region whereby the modified electronic structure will require less energy for photoactivation [163]. Previous studies have described these chemical linkages as charge transfer complexes which can be grafted onto a semiconductor surface through functional moieties [174]. For example, researchers have employed novolac type phenolic resin to enhance the complexation with TiO_2 via multiple hydroxyl functional groups of a polymeric resin; where TiO_2 strongly binds through condensation, and charge transfer occurs from the highest occupied molecular orbital (HOMO) of the resin to the conduction band of TiO_2 [165]. Similarly, in this study, structure of RF is electron rich composed of a large number of methylol and phenolic OH which can react with surface functional groups of TiO_2 , creating new electronic interactions between RF and TiO_2 . Additionally, RF possesses excellent

thermal and chemical properties, due to its stable structure hence, when both RF and TiO_2 are combined, a visible light responsive dyadic structure is attained, which makes RFTi a potential candidate for visible light photocatalysis for water remediation.

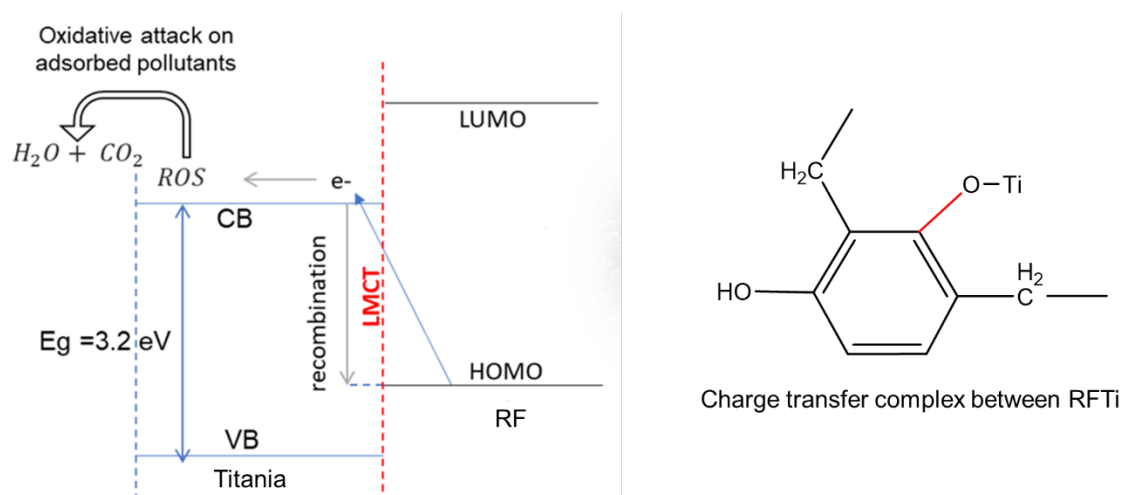


Figure 4.23 Suggested photocatalytic mechanism of RFTi under visible light irradiation and charge transfer complexation between both the phases.

The chemical bonding between RF and TiO_2 was anticipated to strengthen the electronic coupling and promote charge transfer efficiency, thereby improving the optical properties of the material [175]. The predicted mechanism involved photoexcitation of an electron from the ground state of the mesoporous RF matrix (without involving the excited state of the RF) to the TiO_2 conduction band, as represented in the schematic shown in Figure 4.23. The bonding through the hydroxyl group would enable strong coupling due to ligand-to-metal charge transfer (LMCT) surface complexation where a phenolic ligand is separated from TiO_2 by a single oxygen atom. The formation of LMCT complexes results in modification of the overall electronic structure and induces visible light absorption [162, 174]. The process occurs when a photoexcited charge carrier transfers from HOMO of the adsorbent (RF) to the conduction band of TiO_2 , bypassing the LUMO state of the adsorbent, resulting in creation of a new absorption band in the visible region. Thus, it is possible to extend the absorption edge in the visible region by transfer complexation between RF and TiO_2 . Regarding the photodegradation mechanism of pollutants, when light will fall on the surface of RFTi, photogenerated charge carriers (electron and hole pairs) will transfer from the highest occupied molecular orbital (HOMO) of the RF to the conduction band of TiO_2 , similar to other chemically combined carbon/ TiO_2 systems

[165]. Charge carriers successfully transferred to the surface of the photocatalyst participate in redox reactions and produce reactive oxide species (ROS), including hydroxyl radicals ($\cdot\text{OH}$) and superoxide radicals ($\text{O}_2^{\cdot-}$) which can efficiently decompose adsorbed pollutants [172, 176-178]. Here, the role of RF is to enhance the adsorption capability and avoid the recombination of photoexcited charge carriers by capturing and transferring them to the surface. Several experimental demonstrations corroborate a similar phenomenon of optical absorption owing to the formation of surface complexes between TiO_2 and hydroxyl groups. For example, Fujisawa *et al.* [174] published a study in which they explained that chemical interaction between TiO_2 and phenol caused a structural change around the hydroxy group, suggesting formation of a Ti-O-C linkage. Electron coupling between the benzene ring and Titania, via oxygen bridging results in interfacial charge transfer transitions between TiO_2 and π -conjugated molecules, which enables visible light absorption. Similarly, Shi *et al.* [179] utilised the surface complexation of phenol with TiO_2 for visible light driven oxidation of amines to imines by anchoring the hydroxyl group of phenol onto TiO_2 .

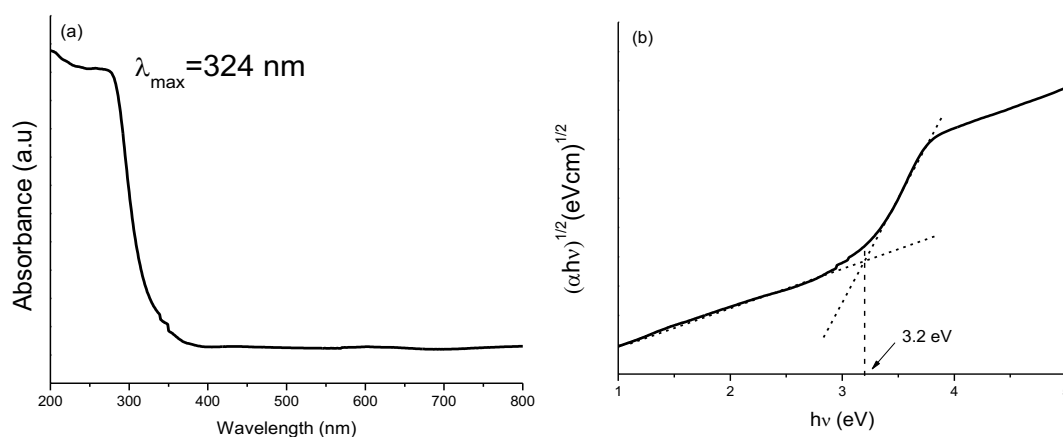


Figure 4.24 (a) UV-Vis absorption spectrum of pure TiO_2 synthesised in this work and (b) corresponding Tauc plot.

This argument regarding shift of absorption edge in this work was validated by analysing the optical responses of the synthesised RFTi samples. For comparison, the UV-Vis spectrum of pure TiO_2 synthesised in this work is shown in Figure 4.24, demonstrating maximum absorbance (λ_{max}) at 324 nm and the evaluated band gap of 3.2 eV which is in good agreement with commercial P25 or undoped TiO_2 , comprising of anatase phase TiO_2 , as reported in the literature [156, 177]. Anatase

phase of TiO₂ in this work was verified using X-ray diffraction analysis, as shown in the Appendix C. Figure 4.25 shows the UV-Vis spectrum of RFTi10, indicating λ_{max} at 410 nm with calculated bandgap value of 2.97 eV, thereby synergy of RF and TiO₂ and modification of electronic structure was corroborated by observed red shift of the absorption edge to the visible region.

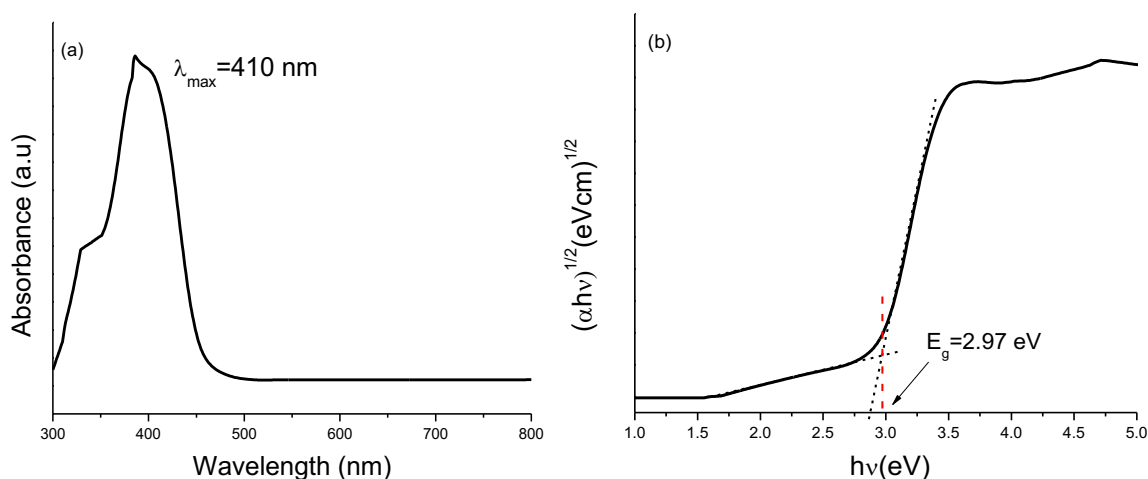


Figure 4.25 (a) UV-Vis absorption spectrum of RFTi10 synthesised in this work and (b) corresponding Tauc plot.

The formation of a charge transfer complex, modification of the electronic structure, charge transfer efficacy, and the consequent optical response are related to the composition of the constituents of the material; hence, the shift of the absorption edge and the lowering of the bandgap were dependent on the amount of RF and TiO₂ in each sample. It was observed that increasing the amount of TiO₂ to 40% improved the absorption intensity, whereby resultant red shift of the absorption for these samples covered the wavelength spectrum up to 650 nm. As shown in Figure 4.26 for RFTi30 and RFTi40, the arrow on the UV-Vis spectra indicated red shift, possibly owing to more absorption complex formation between RF and TiO₂, resulting in broadened spectra along with hyperchromic and bathochromic shifts.

No further red shift was observed with increasing TiO₂ concentration in RF; instead, a slight blue shift was observed. As seen the Figure 4.27 for RFTi50, the spectrum blue shifted by 43 nm relative to the maximum absorption recorded for RFTi40, along with an increase in the band gap of 0.38 eV. Visible light absorption was observed until

RFTi60, and beyond that, the spectra continued to shift toward regions of lower wavelengths.

A continual blue shift is evident with an increase in TiO_2 , as shown in Figure 4.27, indicating that surface complexation decreases owing to the reduced carbon content in the RFTi samples; hence, the deficiency of optimal surface complexes between RF and TiO_2 results in a poor optical response of RFTi samples with very high amounts of TiO_2 . A consistent correlation between carbonaceous and TiO_2 content and its effect on optical response has been previously reported, where the authors asserted that absorption was reduced with low carbonaceous content in the photocatalyst [94, 178]. These studies rationalised the correlation between the mesoporous carbon content and the change in the UV-Vis spectrum. The observed blue shift is attributed to a decrease in the surface electric charge of the oxides in the photocatalyst due to higher amounts of TiO_2 , which deteriorated the modifications of the fundamental process of electron and hole pair formation when exposed to visible light and increased the recombination rate of photogenerated electron/hole pairs. Additionally, as observed in the FESEM analysis (Section 3.3), abundant TiO_2 in these samples did not disperse well and, therefore, caused the aggregation of TiO_2 nanoparticles, which supports the observation of poor optical response.

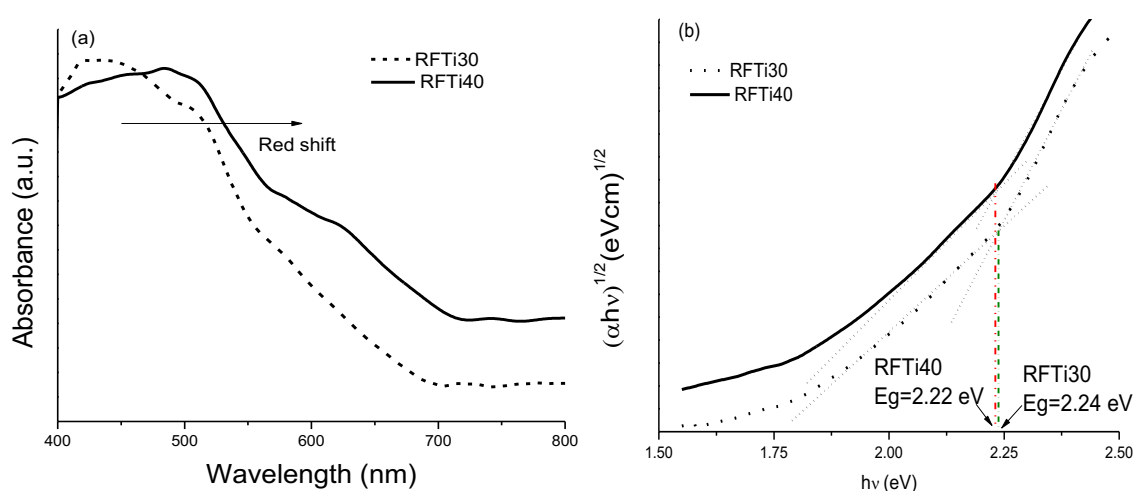


Figure 4.26 (a) UV-Vis absorption spectra of RFTi30 and RFTi40 synthesised in this work and (b) their corresponding Tauc plot.

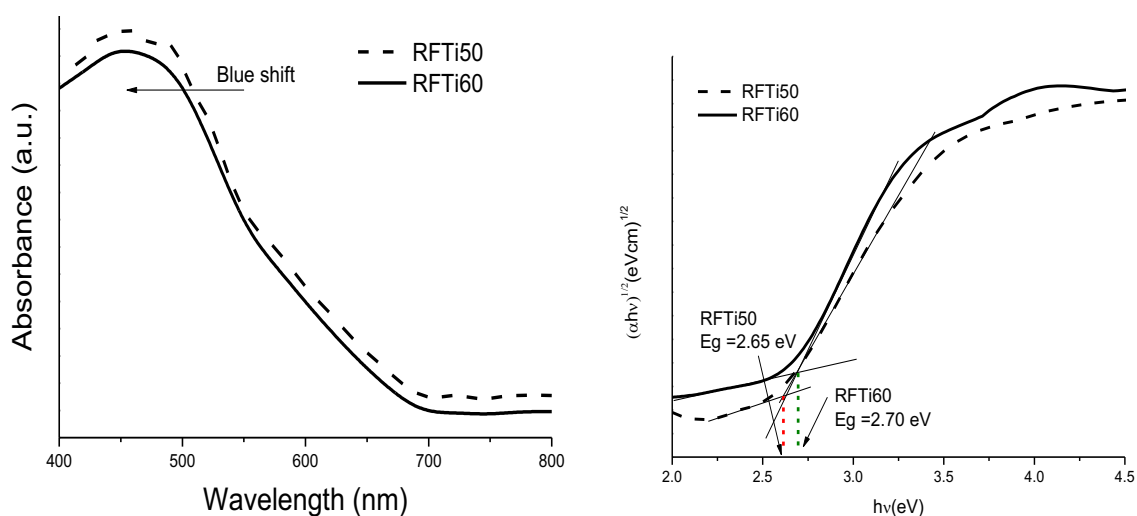


Figure 4.27 (a) UV-Vis absorption spectra of RFTi40 and RFTi50 synthesised in this work and (b) their corresponding Tauc plot.

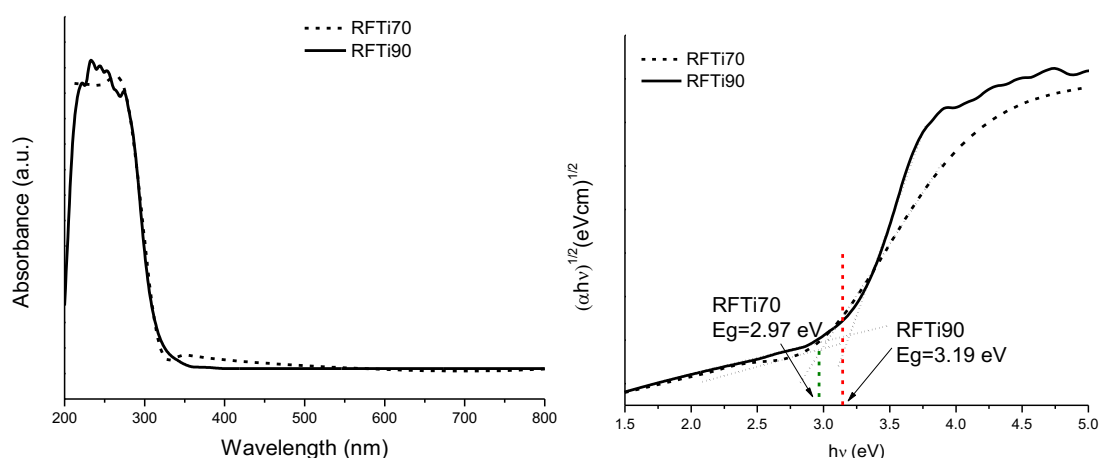


Figure 4.28 (a) UV-Vis absorption spectra of RFTi70 and RFTi90 synthesised in this work and (b) their corresponding Tauc plot.

4.5 Compositional and Thermal Analysis

TGA analysis of synthesised RFTi samples was performed according to methodology described in Chapter 3. After combustion of all organic phase (RF), the residual amount at 800°C was recorded to estimate the weight percent TiO₂ present in the synthesised RFTi samples, shown in Table 4.2. Additionally, thermal degradation of crosslinked RFTi was analysed.

Table 4.2 Overview of TGA parameters.

Sample	Onset degradation Temperature °C	Max degradation Temperature °C	Residue (%) at 300 °C	Residue (%) 650 °C	Residue (%) 800 °C
RF	153	408	97.0	4.75	0
RFTi10	117	446	97.2	12.5	11.1
RFTi50	154	313	96.7	68.8	52
RFTi70	85	300	85.3	72.6	72.5
RFTi90	104	250	92.4	89	89
TiO₂	140	-	98	97.6	97.5

The recorded residual masses of the samples were slightly higher than the theoretical TiO₂ contents which can be ascribed to the segments of the RF phase trapped in the TiO₂ phase. In contrast, the residual amounts of TiO₂ in samples with very high amount of TiO₂, for example RFTi90, the residual inorganic phase is slightly lower than the theoretical amounts, which may have resulted from insufficient hydrolysis and condensation of the TiO₂ precursor during materials synthesis. These arguments are in agreement with previous work for composite systems with Ti/carbon and Ti/epoxy resins [95, 180, 181].

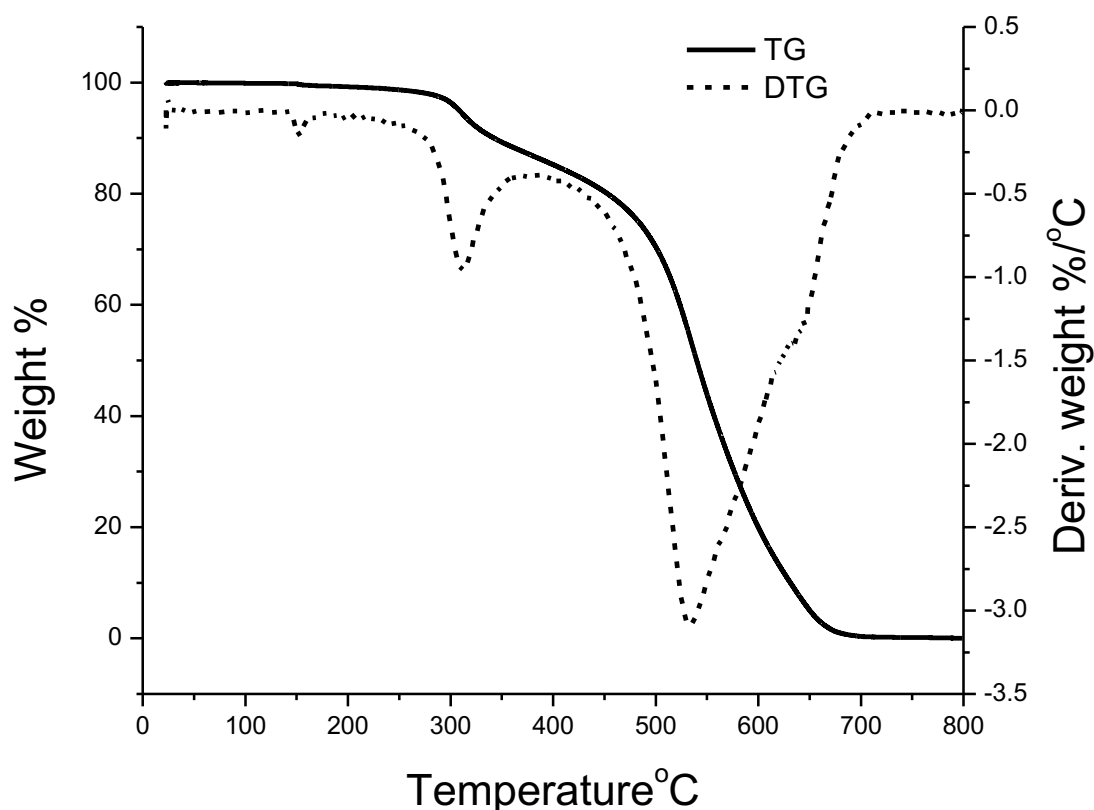


Figure 4.29 TGA/DTA profile of pure RF.

To study the effect of concentration of inorganic phase on thermal degradation behaviour of the synthesised RFTi samples, the TGA data recorded were analysed, including thermal profiles for pure RF and TiO_2 as reference. The rate of weight loss was expressed by the derivate of TGA (DTG), the peak of the DTG curve representing the main thermal events; the thermal stability was compared using main decomposition temperatures. Figure 4.29 shows the thermal profile of pure RF. It was observed that RF structure remained intact until 300°C and decomposed rapidly via oxidation pathways in the air atmosphere leading to complete decomposition of the resorcinol and aromatic network of the RF gel. Initially, 25% weight loss occurred in the temperature range $25\text{-}250^\circ\text{C}$. According to several reports [159, 182], this step involves oxidation of the methylene ether bridges into methylene bridges, which was validated by detection of carbonyl groups on the FTIR spectrum of a residual sample, collected at 300°C (Figure 4.31). Additionally, weight loss at this stage may be due to

the loss of monomers, solvent evaporation, and release of some volatile compounds, with reference to Figure 4.29. In the second stage, at temperatures above 300°C, immediate decomposition of the sample was observed, resulting in ~78% weight loss. The DTG curve shows maximum degradation at a temperature of 531°C, which signifies the collapse of the RF gel network. Awadallah *et al.* [159] mentioned analogous findings, demonstrating main decomposition temperatures of 72, 100 and 583°C, attributed to release of volatile compounds, moisture loss and decomposition of functional groups or bridging functional moieties, respectively.

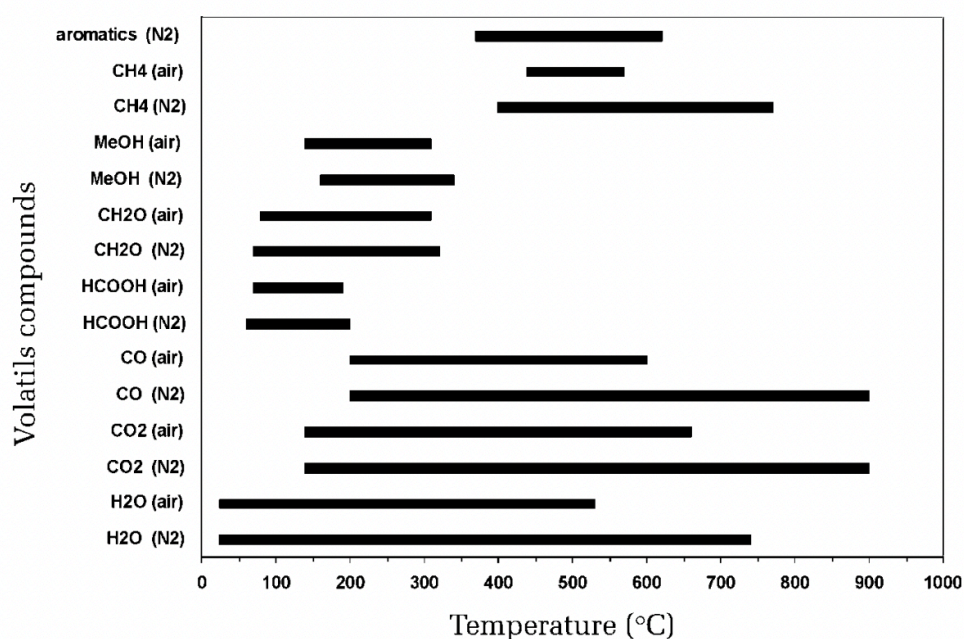


Figure 4.30 Temperature ranges of release of volatile compounds under inert and oxidising atmosphere from crosslinked samples [182] .

Table 4.3 Summary of main decomposition reactions.

Temperature range °C	Main decomposition reactions	
	RF	RFTi
25-200	loss of moisture, polycondensation, dehydration between small chains	loss of moisture of Ti-OH, polycondensation, dehydration between small chains and curing
200-600	Oxidation	Formation of Ti
600-800	Pyrolysis	Phase transformation of Ti

In the third stage, with a further increase in temperature, the released volatiles create pathways in the porous channels of the RF gel matrix, allowing air to penetrate the core of the sample and the crosslinked polymer begins to disintegrate, resulting in the breakdown of functional moieties and, aromatic compounds [183]. The FTIR spectrum recorded for a residual sample obtained at 500°C confirms this statement; the RF gel presumably degrades according to a mechanism defined elsewhere [182, 184]. Typical peaks for C=C stretching, CH₂, and C-O-C of aromatic rings, methylene bridges, and methylene ether bridges were not observed at high temperatures (Figure 4.31 spectrum labelled 500°C). Eventually, the greatest weight loss due to oxidation led to complete decomposition of the RF network in the third step. The intensity of the OH band at approximately 3300 cm⁻¹ disappeared at 500°C. These findings are comparable to those of previous studies using TGA analysis in combination with IR, which reported that the phenolic network degrades at higher temperatures with an ultimate release of CH₄, CO, CO₂, and H₂O [182, 183]. No further weight loss was observed at T > 700°C, indicating complete degradation of the synthesised RF gel network. Table 4.3 summarises main thermal decomposition reactions in different temperature ranges and Table 4.4 shows corresponding changes in chemical linkages from FTIR spectra collected at 300 and 500°C.

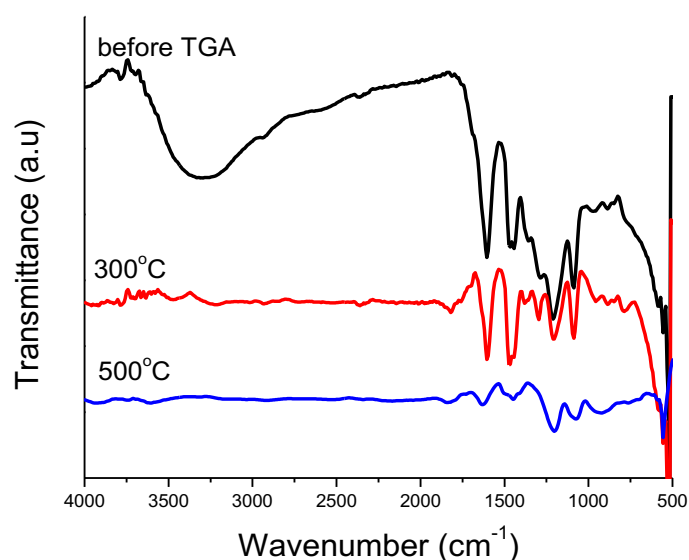


Figure 4.31 FTIR spectra of RF sample recorded after thermal decomposition at 300 and 500°C.

Table 4.4 FTIR analysis of RFTi spectra corresponding to Figure 4.31.

Wavenumber cm ⁻¹	Peak assigned to	300°C	500°C
3318	OH phenolic ring	Diminished	Disappeared
1611, 1509, 1594, 1487	C=C phenolic ring	Weak	Disappeared
1455, 1361	CH ₂	Weak	Transformation of polymer network
1237	C-O	Present	C-O of primary alcohols and C-O-C of ethers disappeared
1150, 1160	CH ₂ -O-CH ₂	Present	Weak
1038	C-O hydroxymethyl	Present	C-O of primary alcohols and C-O-C of ethers disappeared
887, 827, 757	CH phenol meta, ortho, para positions	Diminished	Diminished
645	Vibrating Ti-O	Present	Present

For the RFTi sample, it was assumed that upon completion of the thermal analysis, all organic phase was removed in the form of CO₂ and CO, and the residue was the concentration of TiO₂ present in each sample. Figure 4.32 shows the TGA and DTG data of RFTi10. The residue determined at 800 °C was 11%, which was close to the (expected) theoretical amount of TiO₂ deposited. Regarding the thermal degradation process, thermal stability improved relative to pure RF gel because TiO₂ has a tendency to form Ti-O bonds with a bond energy of 662 kJ mol⁻¹, which is much higher than the bond energy of C-C (340 kJ mol⁻¹) [185]. Therefore, a slower degradation rate (exhibited by a widened DTG peak) was observed, as compared with pure RF. The onset temperature increased by 37°C, indicating an increase in the thermal stability. This confirmed that the introduction of TiO₂ into RF can reduce the mobility of RF polymer chains owing to crosslinking between the functional groups of RF and TiO₂ (verified Ti-O, Ti-C, and Ti-O-C bonds via FTIR). These newly formed chemical bonds are stronger and would obstruct the mobility of RF chains, and the consequent breakdown process requires higher energy. Firstly, the peak labelled at 117 °C

suggests the release of moisture, including the elimination of water from hydrous TiO_2 . In the second step, the main decomposition temperature also increased by 41°C , which confirmed the crosslinking of RF and TiO_2 . The peak designating the maximum degradation at 446°C is attributed to the breakdown of the RF polymeric network, as well as Ti-O-C bonds (bonds between RF and Ti). Only one major degradation step was observed, which could be attributed to fragmentation and decomposition of the RF gel network. At this stage, the weight loss is approximately the same as that for pure RF, whereas the weight loss is lower than that of pure RF in the third region. These findings are similar to those of a study conducted by the Liu group on zirconium-modified phenolic resins. The sample synthesised by the group that contained 10% zirconium showed an analogous thermal degradation pathway, ascribed to the crosslinking between zirconium and phenolic OH groups, enhancing the thermal stability via the formation of new chemical bonds (Zr-OC), which have energies much greater than C-C bonds, and because of the formation of these chemical linkages, thermal degradation occurs at higher temperatures [186].

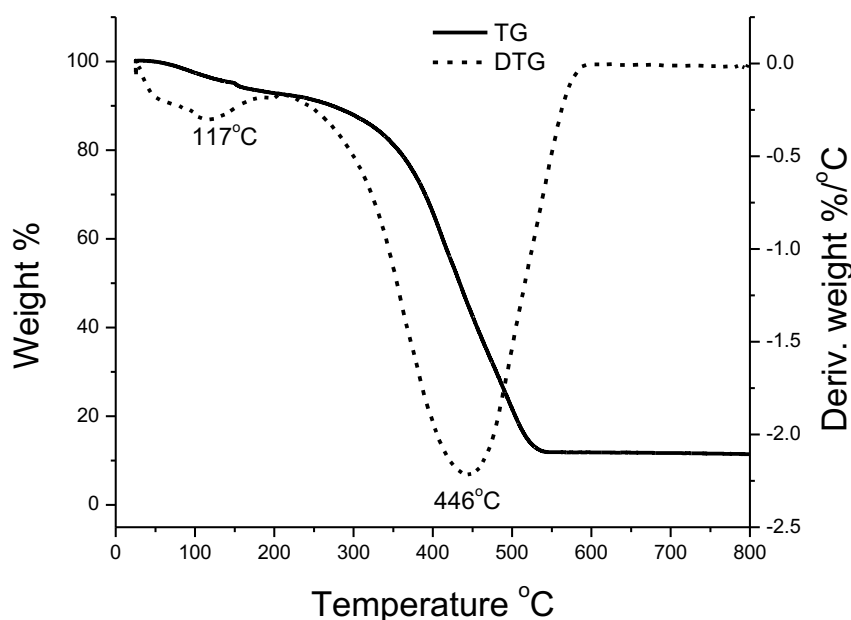


Figure 4.32 TGA/DTA profile of RFTi10.

The phenomenon of increasing the thermal stability with increasing TiO_2 concentration [187] was further documented. As shown in Table 4.2, a further increase in the

concentration of TiO_2 improved the thermal stability of the samples, as indicated by an increase in the onset temperature. This is explicable by the notion that the interaction between RF and TiO_2 increases with an increase in the amount of Ti; hence, decomposition requires higher temperatures to disintegrate the RF-bonded TiO_2 structure. The thermal profile of RFTi50 is shown in Figure 4.33. The onset temperature recorded was higher than that of the previous samples, occurring at 152°C , indicating improved thermal stability owing to the addition of TiO_2 . In the first region ($T < 250^\circ\text{C}$), the main reactions were due to the loss of moisture and RF oligomers. Remarkably, a delay in combustion was identified in the TG profile and the main decomposition steps were recorded by multiple peaks, as represented in the DTG curve. The reason for multiple degradation steps may be attributed to the strength of the bonding between TiO_2 and the RF matrix because of the considerable amount of TiO_2 incorporated within the sample. The first inflection point at 311°C was associated with the unbonded or partially bonded RF phase. A gradual decomposition is evident at 512 and 634°C , which may be induced by the strongly bonded RF and TiO_2 (mainly Ti-O 662 kJ mol^{-1} and Ti-C 435 kJ mol^{-1}), which causes steric hindrance of the RF chain and, therefore, requires higher combustion temperatures. Once again, the weight loss is lower than that of RFTi10 because a greater amount of TiO_2 hinders the RF polymer chains.

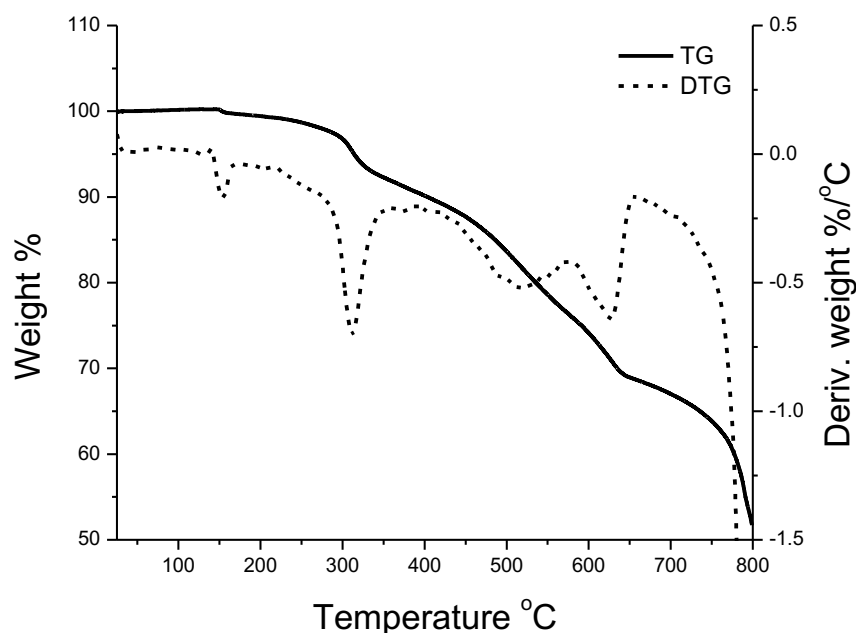


Figure 4.33 TGA/DTA profile of RFTi50.

For RFTi with a very high amount of TiO_2 , the main degradation peaks were observed in the range 200-300 °C. A shift of inflection points to a lower temperature range was observed, attributed to the weak overall RFTi structure due to the reduced inorganic phase; hence, rapid degradation at relatively low temperatures may be attributed to insufficient crosslinks between RF and TiO_2 . Additionally, upon thermal excitation, TiO_2 forms free oxygen or oxygen vacancies in the lattice. The oxygen vacancies can entrap electrons to form active catalytic sites in the structure, and free oxygen promotes the formation of radicals which promote the dissociation of the RF polymer chains, while the presence of unbonded TiO_2 also acts as a thermal barrier against the dissociation of the composite structure [188]. The thermal profile of RFTi90 (Figure 4.34) validates the arguments made, demonstrating that the main degradation peak appeared at 250 °C, and this onset temperature may be attributed to the dominance of Ti-O and negligible Ti-C bonding owing to the low RF. Notably, this decomposition temperature was slightly lower than that of the pure RF gel owing to the reduced carbon phase. Most likely, the overall structure became stable because of the directly formed TiO_2 nanoparticles [189]. In addition, the polymerisation of the RF chains may have been interrupted by a large amount of TiO_2 aggregated within the sample during

synthesis. Hence, RF monomers or oligomers are presumed to degrade rapidly, which can be predicted by the wide distinct main exothermic peak [105]. Furthermore, it can be concluded that the deposited TiO_2 was highly pure because no other degradation steps were observed.

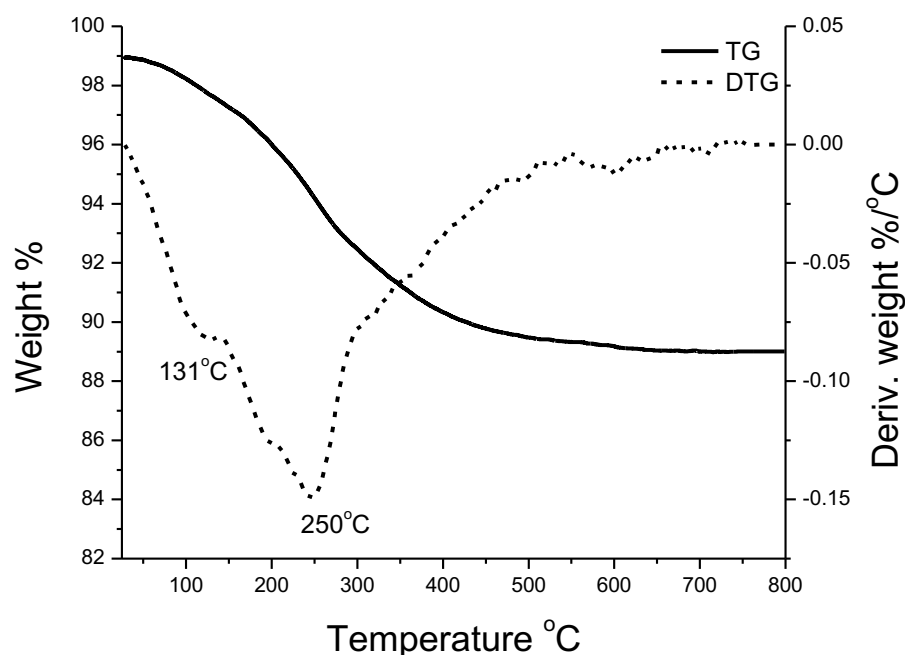


Figure 4.34 TGA/DTA profile of RFTi90.

The thermal profile obtained for pure TiO_2 (Figure 4.35) shows a typical thermal degradation sequence [16]. In the first stage, from to 100-300 °C, there was a weight loss of 2%, which may be due to the removal of solvent residue and moisture from TiO_2 . There is a further (1%) weight loss until 350°C because of the removal of the OH groups attached to the surface of TiO_2 . From 350-800 °C, 0.5% weight loss was observed, and overall, 3% of organic matter was decomposed. The TiO_2 phase was thermally stable until 650°C, when it may have begun to convert to the rutile phase [189], as can be determined from the DSC graph (Figure 4.35). 97.5% of the residual material was recorded at 800°C.

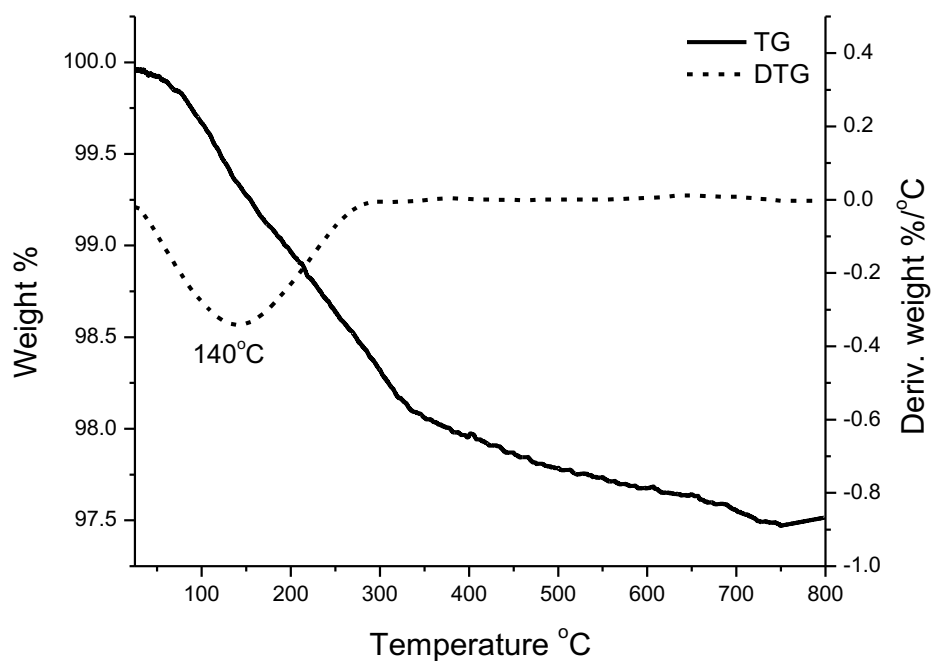


Figure 4.35 TGA/DTA profile of pure TiO_2

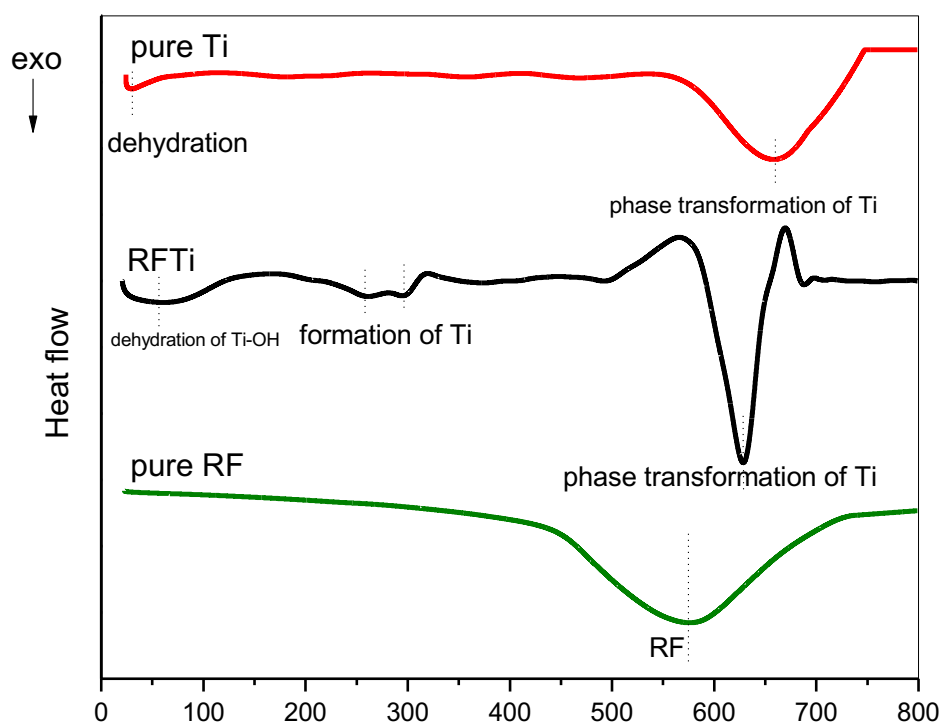


Figure 4.36 DSC curves for pure RF, RFTi50 and TiO_2 .

Figure 4.36 shows the DSC recorded for the synthesised samples. Compared with RF, an additional exothermic peak is observed in the DSC curve of RFTi at

temperatures below 100°C, which is related to the dehydration of Ti-OH and may be explained by the mass loss in the first region. The second step mainly corresponds to thermal decomposition and carbonisation. No other peak in this region corresponded to the remaining carbon, further confirming the formation of carbon only from the thermal analysis of the RFTi gel samples. Overall, the RFTi gel structures showed good thermal stability in DSC analysis, suggesting that strong chemical bonds were formed between RF and TiO₂. The peak in the third region corresponds to the phase transformation of TiO₂ from anatase to rutile, according to the phase diagram of the Ti-O system [190].

4.6 Summary

Analysis of the results obtained from the characterisation techniques revealed that the synthesised RFTi samples possessed excellent textural properties with high surface area and porosity, corroborated by surface area analysis and micrographs obtained from FESEM, making them suitable adsorbents for water remediation applications. Successful synergy between RF and TiO₂ was observed via chemical linkages validated by FTIR analysis. The Ti-O-C bond formation between both phases resulted in the modification of the electronic structure of RFTi, which was proven by the extended absorption edge to the visible region of the electromagnetic spectrum, as recorded in the UV-Vis spectra. The corresponding decrease in bandgap was calculated to be smaller than that of commercial TiO₂ used for photocatalysis; hence, RFTi can activate under visible-light irradiation to generate ROS for the photodegradation of pollutants. Nevertheless, it is important to note that the synergy between RF and TiO₂ to yield optimal performance depends on the amount of each constituent, as very low or very high amounts of TiO₂ would deteriorate the overall synergistic effect. Therefore, the properties of the entire suite of synthesised materials were discussed to gain insight into the structure and property relationship, which may be helpful for numerous applications, including water remediation.

Chapter 5: Adsorption Performance

The properties of a suite of RFTi samples with different ratios of constituents were investigated in Chapter 4, providing insight into their impact on the synergistic effect and final material properties. The experimental analysis of these materials against the reduction of pollutants, would be advantageous for their direct application in environmental remediation. Therefore, this chapter discusses the efficacy of the RFTi samples synthesised in this work, using methylene blue as a model pollutant to evaluate the adsorption performance with respect to time, initial concentration, and temperature. The equilibrium measurements were acquired according to the methodology described in Section 3.8.1, and the data were fitted to the adsorption isotherm and kinetic models to interpret the adsorption behaviour. Research articles presenting findings using the same methodology for two RFTi samples from the synthesised range has been published in the journal 'Gels' [144] and 'Molecules' [145]; a complete manuscript can be found in the Appendix H.

The standard for the classification of porous materials as efficient adsorbents depends on the surface area and porosity [7]. Other factors, such as surface chemistry or surface functionality, also influence the interactions between the target species [191]. Porous adsorbents with high surface areas facilitate higher adsorption or contaminant access owing to the presence of abundant active sites, and adsorption using porous materials has demonstrated to be an effective route for contaminant removal.

The design of an adsorbent material is crucial for determining the adsorption capacity of contaminants. In the present study, composite materials were synthesised to enhance the efficiency of the adsorbent material. However, as discussed in Chapter 4, the concentration of each constituent significantly influences the material properties. Hence, it is important to study the effects of these properties on final material applications. The following sections discuss the experimentally determined adsorption capacity of the synthesised RFTi samples and the adsorption performance based on their structure-property relationships. The adsorption uptake varies depending on the textural and functional properties of the sample, which fundamentally determine the adsorption affinity toward MB, possibly owing to enhanced pore filling, increased electrostatic and π - π interactions, n - π electron donor-acceptor interactions, ionic and

cationic exchange, as well as hydrogen bonding between MB and the gel surface [192, 193]. As demonstrated in Section 3.5, the determination of the point of zero charge is crucial to determine the adsorption behaviour; therefore, a preliminary analysis of pHpzc was conducted and is discussed in Appendix D.

5.1 Experimental Analysis of Adsorption Capacity

Data for the experimentally determined adsorption capacities of the synthesised samples as a function of the initial MB concentration (50-200 mg L⁻¹) and contact time (0-240 min), were recorded. Overall, it was studied that for all samples, the adsorption capacity increased with increasing initial concentration over time. The reason is ascribed to the immediate occupancy of available active sites due to the increase in driving force provided by the higher MB concentration, which overcomes the resistance to mass transfer between the adsorbate and the adsorbent [194]. Hence, a higher concentration gradient results in an increased frequency of collisions between the MB molecules and sample surface [195]. From the data obtained, it was observed that the trend of adsorption uptake by all synthesised samples was similar; that is, the adsorption capacity increased initially, and the process then gradually slowed down because the mass transfer rate slowed down owing to the saturation of active sites, which made it difficult for MB molecules to further adsorb on the sample surface; hence, the system attains equilibrium. The adsorption capacity at equilibrium for each sample depended on the concentration of MB and the adsorption affinity of individual adsorbent. A common behaviour of adsorption processes for all types of synthesised adsorbents demonstrates faster attainment of equilibrium at low initial concentrations than at higher concentrations, attributed to rapid diffusion of the adsorptive into the pores as well as abundant active sites available for adsorbent-adsorbent interaction [196]. At higher initial adsorptive concentrations, the aggregation of MB or charge repulsion of MB dye species may decelerate the adsorption process, and it takes longer for the adsorptive to diffuse deeper into the pores of the adsorbent [176]. Although the adsorption trend is same for all the samples, with increase in contact time and concentration, the extent of adsorption affinity depends on the nature of the adsorbent, as adsorbent surface chemistry also plays a vital role in adsorption uptake.

To better understand the synergy of RF and TiO₂ on adsorption capacity, the calculated data of pure materials is shown in Figure 5.1 and Figure 5.2 for TiO₂ and RF, respectively and the corresponding data at equilibrium is recorded in Table 5.1 (experimental conditions: pH ~7, T=23°C, adsorbent dose 0.01 g). The adsorption capacity of RF at equilibrium was significantly higher than that of TiO₂. This is attributed to the uniform three-dimensional mesoporous structure of RF, which provides a high surface area and porosity with abundant active sites for MB uptake (as demonstrated in Sections 4.1 and 4.2). It was noted that, at low concentration, there is a significant uptake of MB, and the adsorption capacity attains equilibrium. In the case of adsorption uptake at higher concentrations, a gradual increase in uptake was observed owing to MB diffusion into the fine pores of the highly mesoporous structure.

Table 5.1 Experimentally determined adsorption capacities of synthesised samples at different initial concentrations at equilibrium.

	50 mg L⁻¹ (mg g⁻¹)	100 mg L⁻¹ (mg g⁻¹)	150 mg L⁻¹ (mg g⁻¹)	200 mg L⁻¹ (mg g⁻¹)
RF	96	174	192	198
RFTi10	109	176	201	212
RFTi20	106	180	206	213
RFTi30	113	217	220	221
RFTi50	100	161	203	211
RFTi70	95	140	171	191
RFTi90	69	95	100	104
TiO₂	38	87	99	101

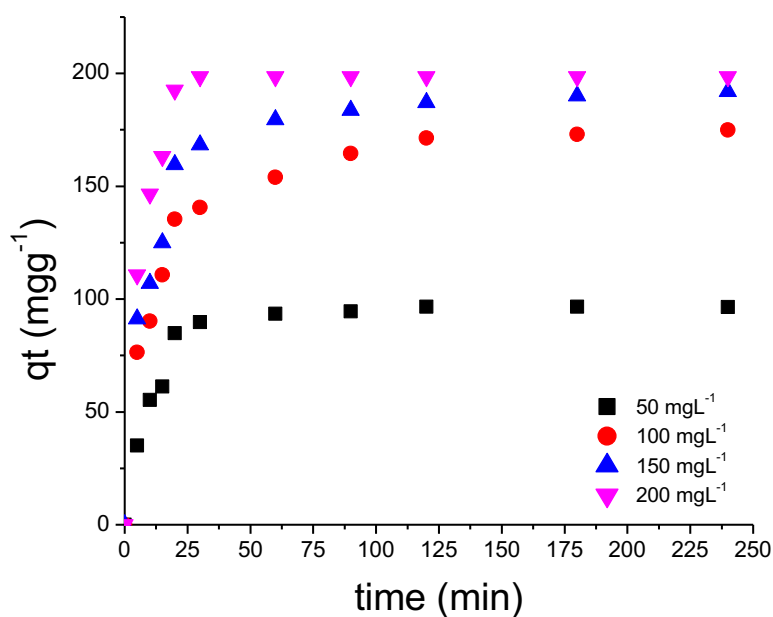


Figure 5.1 Effect of contact time and initial concentration on experimentally determined adsorption capacity of MB for pure RF.

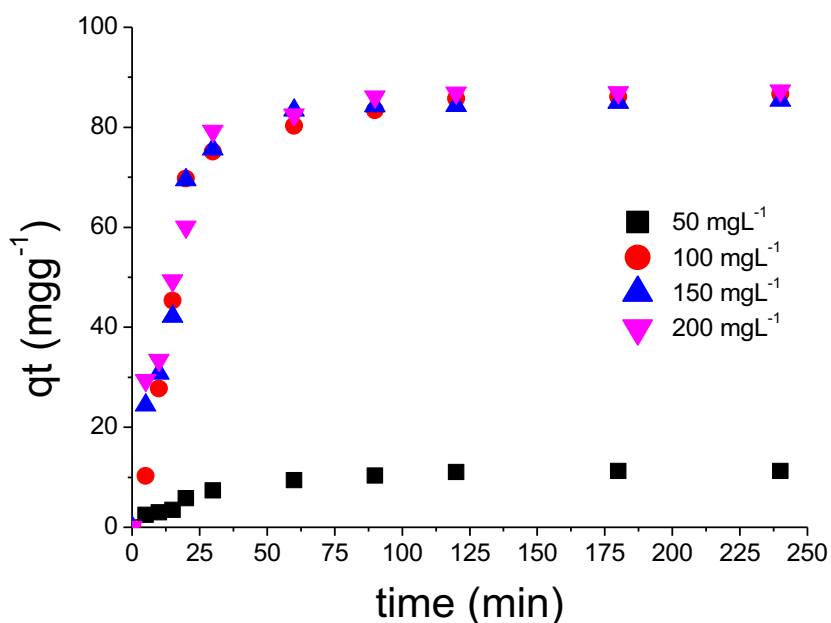


Figure 5.2 Effect of contact time and initial concentration on experimentally determined adsorption capacity of MB for pure TiO₂.

The analysis of adsorption capacity on RFTi samples is explained by classifying the samples into three different groups: low loading of TiO₂ represents samples with 10-30% TiO₂, mid-range includes samples with 40-60% TiO₂, and high loading of TiO₂

consists of sample with 70-90% TiO₂. RFTi synergy improved the adsorption capacity for RFTi with TiO₂ 10-30%, as seen in Table 5.1 (Figure 5.3– data for RFTi20). A steep initial increase in MB uptake with a pronounced slope was observed for these samples, showing the highest MB uptake at equilibrium due to favourable surface chemistry and sufficient porosity, leading to strong π - π interactions between aromatic groups of sample and MB molecules. This enhancement is attributed to the change in surface functionality owing to the formation of new surface-active sites when RF and TiO₂ interact to form a complex (Ti-O-C or Ti-C). A related study by Gracia *et al.* [197] also showed that the equilibrium adsorption capacity of TiO₂-carbon composites improved from 9.28 to 11.4 mg g⁻¹ with the addition of 30% TiO₂ in carbon, owing to improved textural properties, resulting in an enhanced number of active sites, thereby improving the adsorbent-adsorbate contact. The mid-range samples (Figure 5.4 – data for RFTi50), showed that a contact time of 150 min was sufficient to attain adsorption equilibrium due to a change in surface chemistry and the porosity of the adsorbent gel, indicating weaker π - π interactions due to reducing carbon phase. The adsorption uptake by samples with a high loading of TiO₂ showed a slow rate and poor adsorption uptake (Figure 5.5 and Figure 5.6- data for RFTi70 and RFTi90, respectively). The results obtained are consistent with the surface area and textural analysis, indicating blockage of pores which result in slower mass diffusion and a reduced number of active sites cause weaker MB interaction, predominantly by hydrogen bonding, hence signifying the importance of optimising the concentration of TiO₂ in the RF matrix to yield the maximum adsorption capacity.

In terms of porosity, there may be restrictions on diffusion into the narrow pores of the adsorbent, ultimately affecting the adsorption capacity. Thus, it is crucial to consider an optimal amount of TiO₂ deposited in the RF matrix for the pores to be accessible, so that both physisorption and chemisorption can improve the removal process. The obtained experimental data validated this hypothesis. One of the detrimental factors for adsorption on RFTi is the size of TiO₂ nanoparticles or the size of aggregates due to overcrowded TiO₂ nanoparticles, which may lead to pore blocking, as also observed in other studies [198]. Another factor is the change in the surface chemistry of the adsorbent, which affects the surface acidity and functionality and essentially determines the interaction between MB and RFTi. Therefore, the results corroborate

that changing the composition of the adsorbent gel changes the nature of the surface (surface area/pore structure and surface chemistry), ultimately affecting the uptake of MB. Similar studies have been reported for MB adsorption on activated carbon and other carbon based adsorbents [191, 199]. In addition, regarding the influence of pore size, it has previously been reported that a pore size of up to 6 nm is sufficient for MB uptake, whereas other researchers suggest that a pore size of 3.3 nm exhibited the highest adsorption capacity (the dimension of MB in water is $0.400 \times 0.793 \times 1.63$ nm) [191]. In this work, the pore size of samples with low amounts of TiO_2 was > 5.5 nm and high amounts narrowed the pore size to just 4 nm, implying that diffusion restrictions may be another reason for the low adsorption uptake in these samples. It is noteworthy that the adsorption capacity is not related to the micropore volume, but rather to the mesopore volume, implying several diffusion restrictions of MB onto the narrow pores. Overall, a linear relationship between the adsorption capacity and mesoporosity of the adsorbent gels was observed, suggesting the preferential adsorption of MB on the mesoporosity.

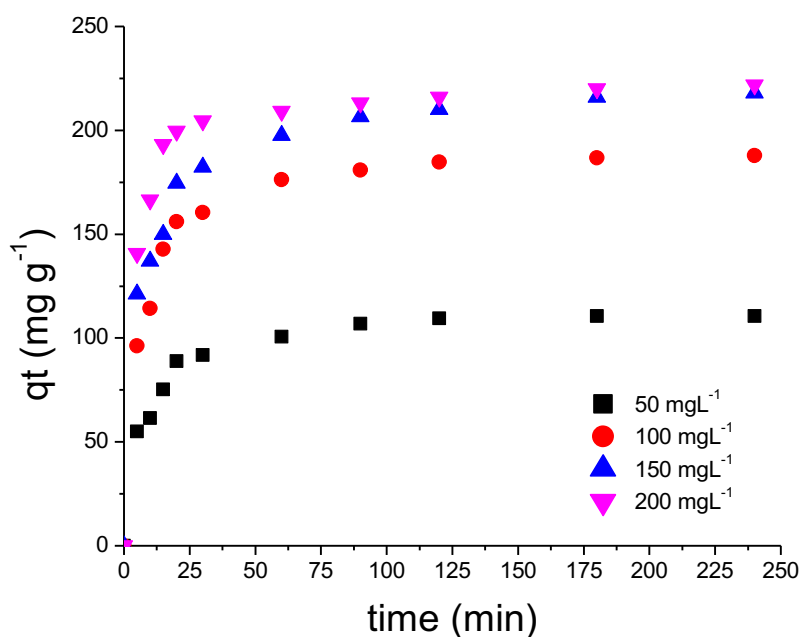


Figure 5.3 Effect of contact time and initial concentration on experimentally determined adsorption capacity of MB for RFTi20.

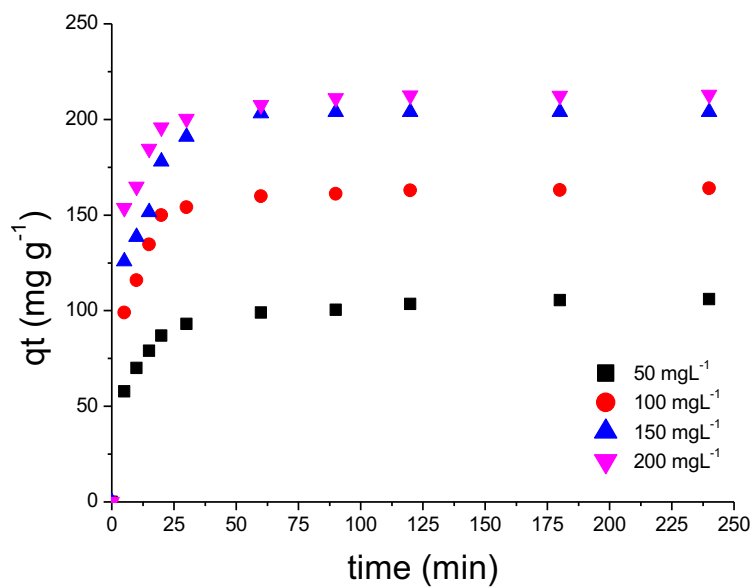


Figure 5.4 Effect of contact time and initial concentration on experimentally determined adsorption capacity of MB for RFTi50.

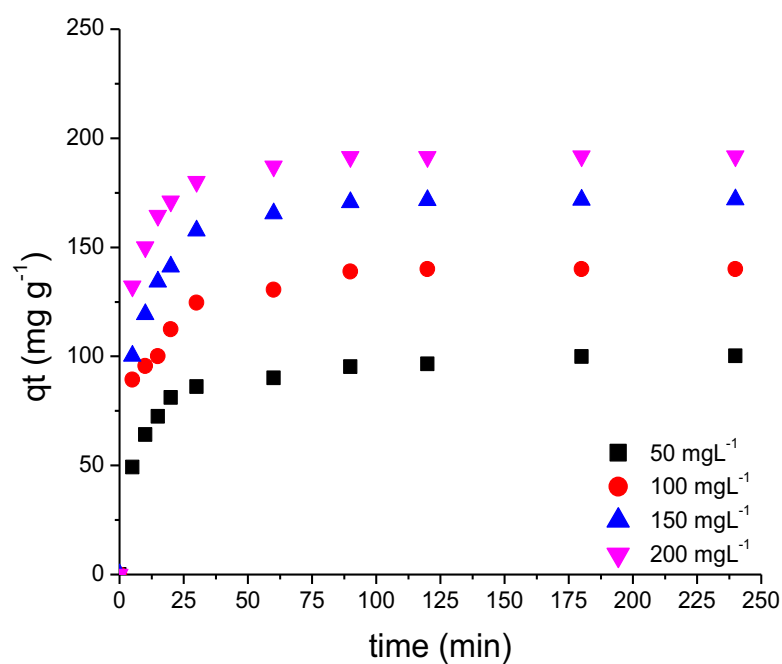


Figure 5.5 Effect of contact time and initial concentration on experimentally determined adsorption capacity of MB for RFTi70.

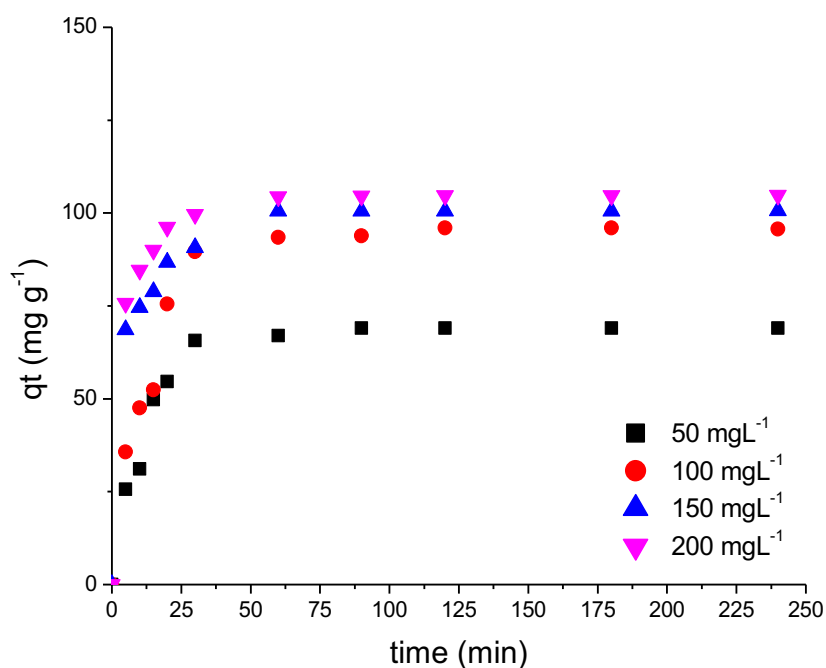


Figure 5.6 Effect of contact time and initial concentration on experimentally determined adsorption capacity of MB for RFTi90.

An analogous analysis of the interactions between MB and such adsorbent surfaces was performed by Dalto *et al.* [200]. Activated carbon combined with TiO₂ in different proportions was tested for MB reduction. The removal percentage increased by 23%

with the addition of TiO₂. A large amount of activated carbon (91% carbon, 8.5% Ti) showed the highest adsorption capacity, leading to significant MB uptake. The adsorption capacity was reduced, but MB uptake was rapid when tested with samples containing a relatively low carbon content (56% carbon, 43% Ti). Studies on other carbon/TiO₂ systems, such as graphene and TiO₂ composites, have concluded that oxygenated basic surface groups enhance physicochemical properties through dominant hydrogen bonding between the adsorbent surface and MB [201].

5.2 Modelling of Experimental Adsorption Processes

For the overall enhancement of adsorption mechanism pathways and efficient design of an adsorption system, interpretation of adsorption equilibrium data is imperative. Thus, to predict the mechanics of different adsorption systems, modelling experimental data from adsorption processes is important. Kinetic and isotherm modelling of adsorption equilibrium data is discussed in sections 5.2.1 and 5.2.2.

Linear regression analysis has recently become one of the most popular methods for determining the best fitting adsorption models due to its ability to quantify the distribution of adsorbates, analyse the adsorption system, and confirm the consistency of the theoretical assumptions of the adsorption isotherm model [202]. Several statistical parameters including coefficient of determination (R^2), adjusted R^2 ($\text{adj}R^2$), nonlinear chi-square test (X^2), sum squares error (SSE), mean square error (MSE) and hybrid fraction error function (HYBRID) applied to evaluate the performance of the adsorption isotherm, kinetic and diffusion models are reported in literature. In this work, R^2 , which represents the variance about the mean; is used to analyse the fitting degrees of isotherms and kinetic models with experimental data [203]. Wang *et al.* [40] have highlighted that R^2 is the most calculated statistical parameter as more than 60% literature reports have compared R^2 values to determine the best fit to adsorption isotherm, kinetic and diffusion models, whereas frequency of application of other parameters is 11%, 11% and 10% for X^2 , SSE, and HYBRID equations, respectively. Error analysis of adsorption kinetics and isotherms are reported in detailed by Ayawei *et al.* [203] and a summary of error functions are listed in Appendix G.

5.2.1 Adsorption Kinetics

The experimental kinetic data collected were analysed by models including Pseudo-first Order (PFO), Pseudo-second Order (PSO), Elovich and Intra-Particle Diffusion model (IPD), equations. Several studies on such porous systems have reported kinetic analysis based on these four models to provide a better understanding of adsorption process. For example, kinetic and equilibrium adsorption studies using mesoporous carbons, as adsorbents for removal of industrial waste, was recently reported by Ahmad *et al.* [204]. Likewise, the kinetics for removal of dyes (such as congo red, methylene blue, methyl orange) by adsorption mechanisms has been broadly studied using these models. Kinetic models used in this work are demonstrated as follows:

The PFO model [43] has been frequently used to describe kinetic processes under non-equilibrium conditions. PFO is based on the assumption that the rate of adsorption at given time (q_t) is proportional to the driving force, i.e., the difference between equilibrium concentration and solid phase concentration. The integrated form of the PFO model is given in Equation 5.1:

$$q_t = q_e(1 - e^{-k_1 t}) \quad \text{Equation 5.1}$$

By contrast, the PSO equation assumes that the overall adsorption rate is proportional to the square of the driving force. The integrated form of PSO model is given in Equation 5.2:

$$q_t = \frac{k_2 t q_e^2}{1 + k_2 t q_e} \quad \text{Equation 5.2}$$

In both equations shown above, q_t (mg g^{-1}) and q_e (mg g^{-1}) are the concentrations of MB dye molecules at time t and at equilibrium, respectively. K_1 ($\text{g mg}^{-1} \text{min}^{-1}$) and k_2 ($\text{g mg}^{-1} \text{min}^{-1}$) are the PFO and PSO rate constants, respectively.

The Elovich equation is useful in describing chemisorption processes, which involve valence forces through sharing or exchange between the adsorbate and the adsorbent. The removal efficiency decreases with time because of the coverage of active sites [43, 205]. The Elovich model is generally expressed as Equation 5.3:

$$q_t = \frac{1}{B} \ln(AB) + \frac{1}{B} \ln(t) \quad \text{Equation 5.3}$$

where A ($\text{mg g}^{-1} \text{min}^{-1}$) and B (g mg^{-1}) are the initial rate of adsorption and desorption constant, respectively.

Data in Figure 5.7-5.12 show the experimentally determined adsorption capacity fitted to PFO, PSO and Elovich models. The corresponding calculated parameters are recorded in Table 5.2 and 5.3. The correlation coefficient, R^2 , was calculated to predict the best fit ($R^2 > 0.90$) [40]. It was observed that the adsorption data for RF and RFTi fitted well to the PSO kinetic model, where values of calculated adsorption at given time are closer to q_{exp} (experimentally determined adsorption values). Thus, interpretation of the interaction between the surface of the adsorbent and adsorptive can be chemically ascribed, which is in agreement with FTIR analysis, obtained after the adsorption of MB [145]. The change in spectra is evident with extended peaks associated with functional groups of RFTi, including C-H, C-O-C and C=C. A review published by Wang *et al.* [40] reported numerous modified adsorbents owing to their abundant active sites, which chemically interact with the adsorbate and exhibit fits to the PSO model. Similar observations have also been made for other carbon/ TiO_2 systems including Ti/CNTs [206, 207], Ti/graphene [208, 209] and Ti/activated carbon [210].

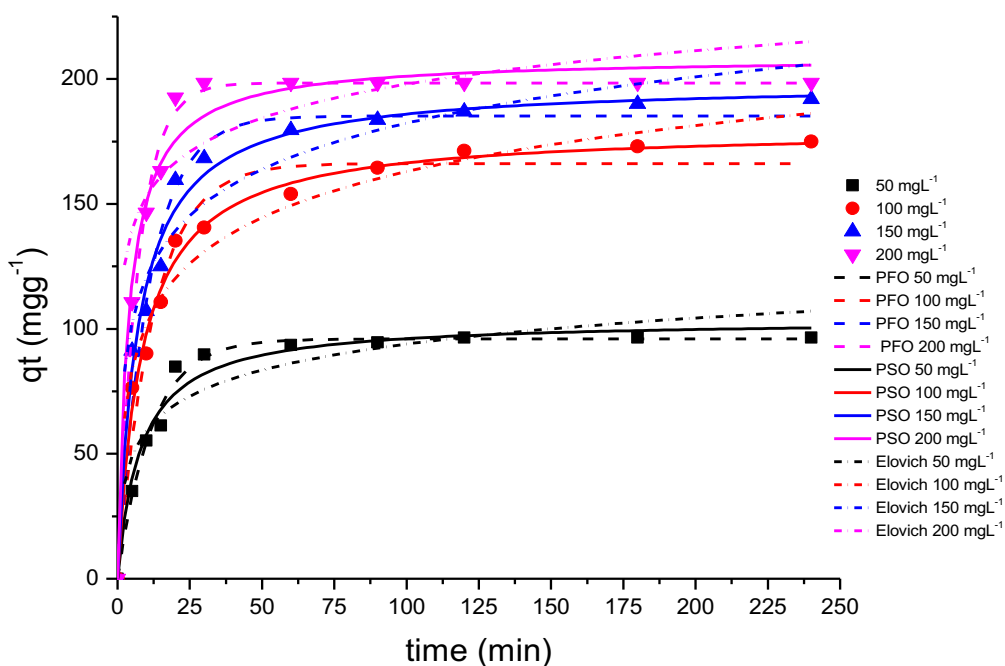


Figure 5.7 Adsorption kinetic models applied to adsorption of MB on pure RF solid line pseudo-first order, dashed line pseudo-second order and short dashed line is Elovich model.

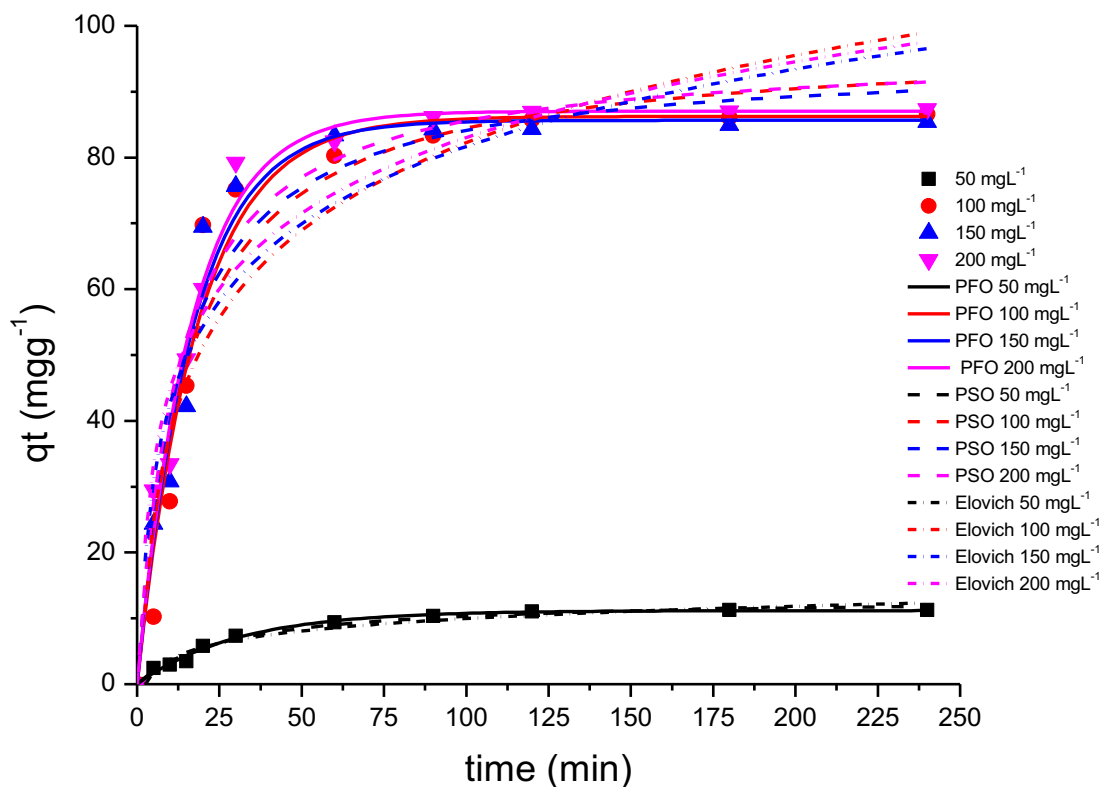


Figure 5.8 Adsorption kinetic models applied to adsorption of MB on pure Ti; solid line pseudo-first order, dashed line pseudo-second order and short dashed line is Elovich model.

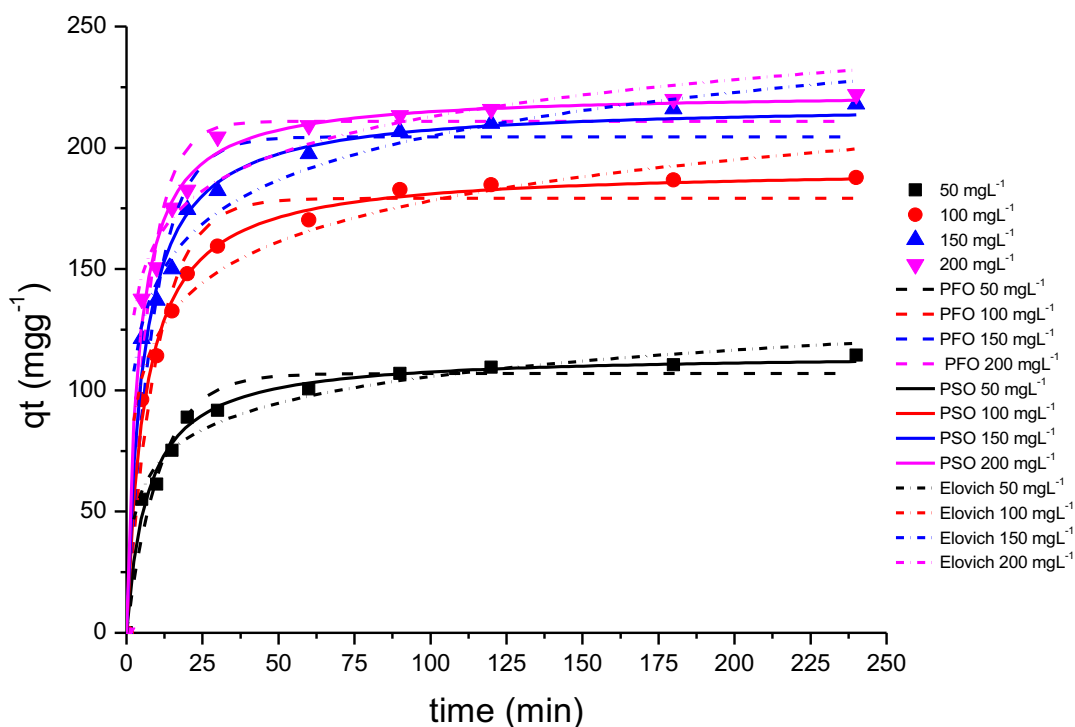


Figure 5.9 Adsorption kinetic models applied to adsorption of MB on RFTi20 dashed line pseudo-first order, solid line pseudo-second order and short dashed line is Elovich model.

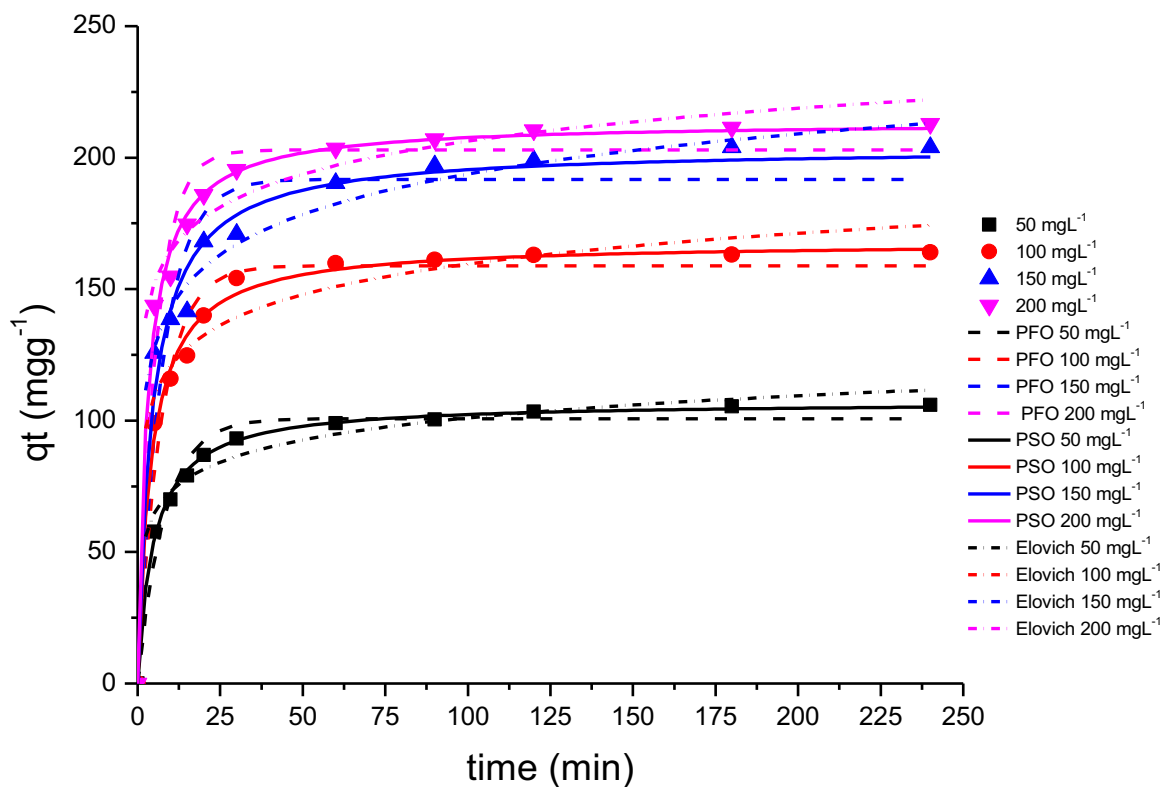


Figure 5.10 Adsorption kinetic models applied to adsorption of MB on RFTi50 dashed line pseudo-first order, solid line pseudo-second order and short dashed line is Elovich model.

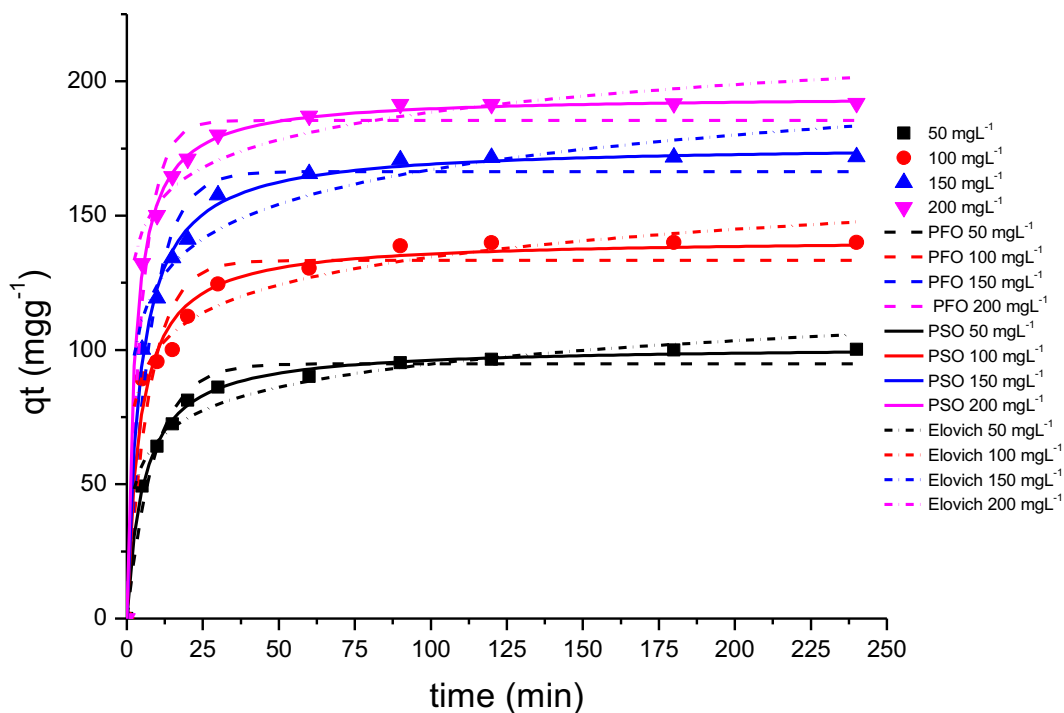


Figure 5.11 Adsorption kinetic models applied to adsorption of MB on RFTi70 dashed line pseudo-first order, solid line pseudo-second order and short dashed line is Elovich model.

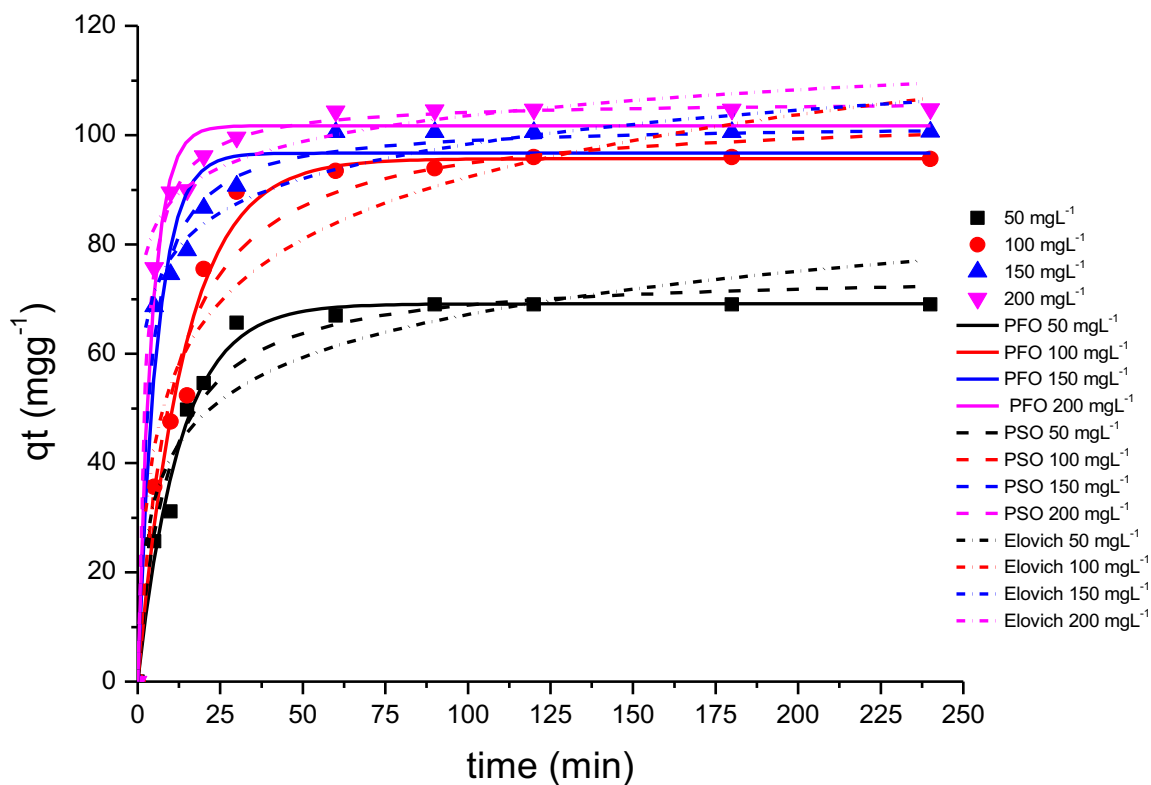


Figure 5.12 Adsorption kinetic models applied to adsorption of MB on RFTi90 solid line pseudo-first order, dashed line pseudo-second order and short dashed line is Elovich model.

Table 5.2 Parameters of pseudo-first order and pseudo-second order kinetic models for MB adsorption on synthesised adsorbent gels.

	PFO				PSO		
	q_{exp} mg g ⁻¹	q_t mg g ⁻¹	K_1 (min ⁻¹)	R^2	q_t mg g ⁻¹	$k_2 \times 10^{-4}$ g ⁻¹ mg min ⁻¹	R^2
RF							
50 mg L ⁻¹	96.0	95.9	0.085	0.987	103	12.2	0.968
100 mg L ⁻¹	174	166	0.082	0.966	180	6.67	0.989
150 mg L ⁻¹	192	185	0.092	0.973	198	7.30	0.984
200 mg L ⁻¹	198	198	0.143	0.991	208	12.6	0.980
RFTi20							
50 mg L ⁻¹	110	106	0.091	0.956	115	12.3	0.988
100 mg L ⁻¹	187	179	0.103	0.961	191	8.70	0.994
150 mg L ⁻¹	218	204	0.115	0.943	218	8.73	0.990
200 mg L ⁻¹	221	210	0.147	0.957	223	11.8	0.991
RFTi50							
50 mg L ⁻¹	105	100	0.012	0.968	107	19.4	0.997
100 mg L ⁻¹	163	158	0.139	0.965	167	14.9	0.993
150 mg L ⁻¹	203	191	0.134	0.924	204	11.4	0.979
200 mg L ⁻¹	212	202	0.181	0.959	213	15.8	0.994
RFTi70							
50 mg L ⁻¹	100	95.3	0.111	0.973	101	17.7	0.998
100 mg L ⁻¹	140	133	0.136	0.923	141	16.9	0.980
150 mg L ⁻¹	171	166	0.133	0.966	176	13.1	0.996
200 mg L ⁻¹	191	185	0.200	0.973	195	19.8	0.999
RFTi90							
50 mg L ⁻¹	49.6	69.1	0.078	0.990	74.9	15.1	0.965
100 mg L ⁻¹	97.9	95.7	0.071	0.980	104	9.67	0.964
150 mg L ⁻¹	100	96.7	0.174	0.940	102	31.1	0.987
200 mg L ⁻¹	104	101	0.239	0.980	106	45.5	0.987

TiO₂							
50 mg L⁻¹	38.0	11.1	0.032	0.988	13.2	27.4	0.981
100 mg L⁻¹	86.8	86.2	0.055	0.959	97.4	6.71	0.928
150 mg L⁻¹	99.0	85.6	0.059	0.969	95.1	8.05	0.942
200 mg L⁻¹	101	87.0	0.060	0.983	96.2	8.34	0.967

For some adsorption systems, the Elovich model provided a reasonable fit to the data (Table 5.3), indicating that there may be a chemical component for the interaction of MB with the RFTi adsorbents. Overall, all these data suggest that MB adsorption is better represented by the PSO kinetic model with regards to higher correlation coefficients, as compared to PFO and Elovich models, suggestive of MB adsorption on RFTi gels via chemisorption mechanism [211]. Also, the calculated adsorption capacity from PSO model fitting was closer to the experimentally determined values. This observation is valid for all RFTi samples except RFTi90, which showed an inclination toward the PFO model fitting. The analyses of such systems are often described by PFO kinetic model [212-215]. Hence, corroborating the arguments, outlined earlier, regarding low adsorption affinity and physisorption predicted for this sample.

Table 5.3 Parameters of Elovich equation for MB adsorption on synthesised adsorbent gels

Sample	A (mg gmin ⁻¹)	B (g mg ⁻¹)	R ²
RFTi20			
50 mg L ⁻¹	46.5	0.063	0.977
100 mg L ⁻¹	134	0.041	0.979
150 mg L ⁻¹	247	0.038	0.986
200 mg L ⁻¹	1291	0.045	0.978
RFTi50			
50 mg L ⁻¹	183	0.082	0.978
100 mg L ⁻¹	814	0.059	0.969
150 mg L ⁻¹	522	0.045	0.990
200 mg L ⁻¹	5938	0.055	0.984
RFTi70			
50 mg L ⁻¹	90.1	0.079	0.975
100 mg L ⁻¹	445	0.067	0.984
150 mg L ⁻¹	544	0.053	0.974
200 mg L ⁻¹	17955	0.067	0.983
RFTi90			
50 mg L ⁻¹	15.4	0.088	0.901
100 mg L ⁻¹	16.5	0.061	0.912
150 mg L ⁻¹	1784	0.111	0.983
200 mg L ⁻¹	94618	0.146	0.984

Analysis using PFO, PSO and Elovich models do not provide an insight into any internal diffusion mechanisms, hence, an IPD model (Equation 5.4) was applied to the experimental data to understand such diffusion behaviour.

$$q_t = k_{ip}t^{0.5} + C \quad \text{Equation 5.4}$$

The mechanism of adsorption generally involves three steps of which any step or combination of steps can be a rate-limiting step (i) external diffusion of dye molecules across the boundary of the adsorbent; (ii) intra-particle diffusion and mass transfer

from the adsorptive to the external surface of the adsorbent, depending upon the nature of the adsorption process; (iii) diffusion of adsorbate molecules to the pores and attachment of the adsorptive to the internal surface of the adsorbent [202]. If the rate limiting step is the intra-particle diffusion, then the amount of adsorption at any time should be directly proportional to the square root of contact time [43]. Figure 5.13 shows a linearised plot of the intra-particle diffusion model for RFTi20, RFTi50, RFTi70 and RFTi90 (Note: the data here is presented for q_t at C_0 100 mg L⁻¹, since all systems at different initial concentration showed similar behaviour whereby the adsorption capacity was not diffusion dependent, and several other factors contributed to the rate determining step).

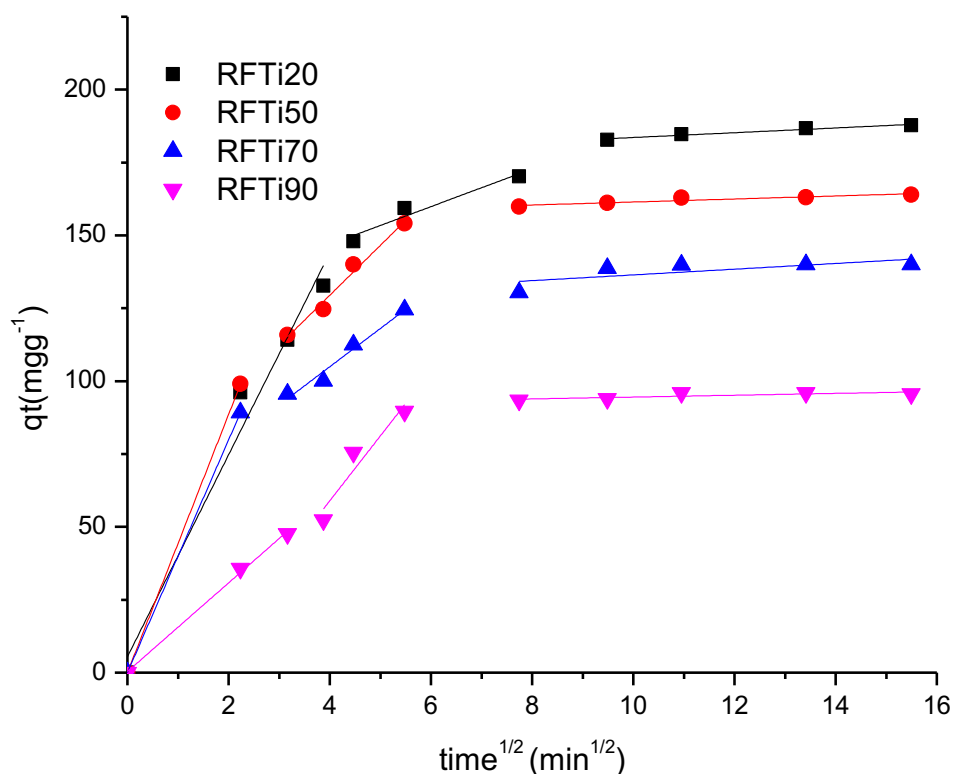


Figure 5.13 Linearised plot of intra-particle diffusion model fitted for experimental data at equilibrium for RFTi20, RFTi50, RFTi70 and RFTi90.

The multi-linearity of the plot indicates a multi-step adsorption process. Each plot can be divided into three stages for RFTi samples, and none passes through the origin indicating that IPD was not rate limiting [42]. Piece-wise fitting parameters are listed in Table 5.4. The adsorption process seemed to follow the adsorption principle, beginning with diffusion of MB from the bulk phase to the external surface of the

adsorbent. The chemical potential of the RFTi samples-MB interactions controls mass transfer, where diffusion depends on change in concentration of dye with time. For all the samples, the initial steep step of external diffusion was more rapid than the rest of the steps, as denoted by the calculated rate (k_{ip}) values. This may be explained by the fact that, at the beginning of reaction, the thickness of the outer surface of the adsorbent is comparable to external diffusion within the mesopores, MB dye molecules are confined to be in close proximity to the surface. In addition, faster adsorption rates are expected, due to immediate availability of a large proportion of adsorption sites.

Table 5.4 Parameters of intra-particle diffusion model for MB adsorption on synthesised adsorbent gels.

Sample		Stage 1	Stage 2	Stage 3
RFT20	intercept	5.43	121	175
	k_{ip}	34.6	6.47	0.819
	R^2	0.963	0.893	0.942
RFTi50	intercept	-	61.0	156
	k_{ip}	44.3	17.1	0.517
	R^2	0.979	0.835	0.957
RFTi70	intercept	-	52.4	126
	k_{ip}	39.2	13.1	0.98
	R^2	0.996	0.844	0.504
RFTi90	intercept	0.37	-	91.4
	k_{ip}	15.2	22.5	0.316
	R^2	0.960	0.985	0.984

The rate of the second step, that is, diffusion of the adsorptive into the porous structure of the adsorbent was slower due to higher resistance, provided by the boundary layer effect of the adsorbent material, indicated by the intercept C values. The third stage suggests an equilibrium stage, where intra-particle diffusion starts to slow down, due to low adsorptive concentration or saturation of active sites for surface reactions to continue [202, 216]. Again, this is evident from the decreasing trend of diffusion rate constant for the third stage, thereby indicating the diminishing role of intra-particle

diffusion. This implies that other mechanisms are involved in the adsorption process. It was noted that RFTi50 and RFTi70 and RFTi90 show negative intercept values, which is explained by the combined effects of diffusion across the boundary layer and surface reaction control, which may have delayed IPD diffusion [43, 194]. Similar phenomena have been explained for porous TiO₂ and other carbon/TiO₂ porous composite materials, where it may have taken longer for the adsorptive to diffuse deeper into the fine pores of the adsorbent [144, 217, 218]. The analysis drawn from IPD suggests that both surface adsorption and IPD contributed to the rate determining step during the adsorption of MB by RFTi adsorbent gels.

Table 5.2 shows the experimentally determined values of adsorption capacity (q_{exp}). It was observed that equilibrium adsorption capacity improves from 58 to 71% with addition of 20% TiO₂ in RF gel. This trend was attributed to the formation of new surface-active sites. Additionally, as seen in Chapter 4, the surface area and porosity decreased with incorporation of TiO₂ in the RF matrix, due to pore blocking. So, the effect of surface area and porosity on adsorption capacity is another important factor to consider. The low adsorption capacity of MB, observed for samples with high TiO₂ loading, was due to clustering/agglomeration of TiO₂ (in agreement with morphological analysis), blocking the pores of the RF gel matrix, hence, providing fewer active sites for MB to adsorb on the sample surface, and diffuse into the porous structure of the adsorbent, or undergo mass transfer processes. Thus, again, the notion of optimal RF and TiO₂ concentration is important to consider for maximum efficiency. Also, there may be restrictions for diffusion into narrow pores of an adsorbent, ultimately affecting the adsorption capacity. Thus, it is crucial to consider an optimal amount of TiO₂ deposited in the RF matrix for the pores to still be accessible, so both physisorption and/or chemisorption can improve the removal process. The experimental data shown in Table 5.1 validates this notion. With further increase in TiO₂, a slight decrease in the adsorption uptake for RFTi50 (adsorption uptake 68%) was recorded, with further reduction to 40% for RFTi90. Hence, one of the detrimental factors here for adsorption on RFTi can be the size of TiO₂ nanoparticles, or the size of aggregates due to overcrowded TiO₂ nanoparticles, which may lead to pore blocking, as also observed in other studies [198]. Another factor is the change in surface chemistry of the adsorbent affecting the surface acidity and functionality, which essentially determines

the interaction the MB and RFTi. The results, therefore, corroborate that changing the composition of the adsorbent gel changes the nature of the surface (surface area/pore structure and surface chemistry), ultimately impacting the adsorption uptake of MB. Similar studies have been reported for MB adsorption on activated carbon and other carbon based sorbents [191, 200].

5.2.2 Adsorption Isotherms

Adsorption isotherms are an important method to explain the interaction between the adsorbent and adsorbate at equilibrium and are essential in gaining insight of the system for their application in water remediation. Adsorption isotherms obtained in this study were analysed according to the nonlinear form of Langmuir, Freundlich, and Sips, and values of associated parameters were calculated using Origin software. These models are widely applied for adsorption on carbon-based adsorbents [219]. The model showing the best fit to the experimental data was selected, based on determination of the correlation coefficient (R^2). The adsorption isotherm models employed in this work were as follows:

The Langmuir isotherm model is a simple theoretical model, which describes monolayer adsorption on a homogeneous surface [203]. The model considers the following assumptions (i) there are a well-defined and fixed number of active sites; (ii) adsorption forms a monolayer; (iii) the active sites are identical and cannot host multiple molecules; (iv) the adsorption sites possess the same energy, thus, are energetically equivalent, and therefore the adsorbent surface is homogenous; (v) the adsorbed molecules do not interact with neighbouring active sites; and (vi) the system is in equilibrium [42, 203]. Equation 5.5 describes the nonlinear Langmuir model:

$$q_e = \frac{q_L K_L C_e}{1 + C_e K_L} \quad \text{Equation 5.5}$$

Where q_e (mg g^{-1}) is the MB uptake at equilibrium, C_e (mg L^{-1}) is the equilibrium concentration, q_L (mg g^{-1}) is the amount of adsorbate at complete monolayer coverage, and K_L is the Langmuir constant related to the energy of adsorption, which can be used to determine the extent of adsorbate-adsorbent interaction.

Furthermore, adsorption favourability can be determined by a dimensionless constant called the separation factor, R_L , expressed by:

$$R_L = \frac{1}{(1 + K_L C_0)} \quad \text{Equation 5.6}$$

Where, C_0 refers to the initial concentration of the adsorbate in (mg L^{-1}) and K_L is Langmuir constant related to the adsorption capacity. If the value of $R_L > 1$, the adsorption is unfavourable, and favourable when $0 < R_L < 1$.

The Freundlich isotherm model can be applied to adsorption processes that occur on highly heterogenous surfaces. This model assumes that adsorption at multiple sites may occur with formation of multilayers of different adsorption energies. This leads to an exponential decrease in energy, as coverage of the surface progresses. The strength of the bonds is not homogeneous, due to the physicochemical characteristics of the adsorption sites, or the number of molecules already adsorbed. In particular, as more molecules adsorb onto a site, it is less likely that another molecule will join the same site because it requires higher energies. The Freundlich equation can be expressed as:

$$q_e = K_F C_e^{1/n_F} \quad \text{Equation 5.7}$$

Where q_e (mg g^{-1}) and C_e (mg L^{-1}) are as defined in the Langmuir equation, adsorption affinity is related to the adsorption constant K_F , and n_F indicates the magnitude of the adsorption driving force and is used to evaluate the adsorption favourability. When $1/n_F$ is greater than 0 ($0 < 1/n_F < 1$), adsorption is favourable, when $1/n_F$ is greater than 1, the adsorption process is unfavorable, and it is irreversible when $1/n_F = 1$. Also, the adsorption intensity or surface heterogeneity, and the energy distribution, as well as the adsorbate site heterogeneity is indicated by $1/n_F$. A value of n_F between 2 and 10 represents good adsorption indicating a high adsorption capacity, while values between 1 and 2 indicate moderate adsorption capacity, and values less than 1 indicate a small adsorption capacity.

To further understand the adsorption process of MB in the mesopores of RFTi gels, the adsorption data obtained at equilibrium were fitted to an adsorption model based

on three parameters. The Sips isotherm model is a combination model of the most widely applied Langmuir and Freundlich isotherms and is represented as:

$$q_e = \frac{q_s K_s C_e^{n_s}}{1 + K_s C_e^{n_s}} \quad \text{Equation 5.8}$$

Where q_e (mg g^{-1}) and C_e (mg L^{-1}) are as defined in the Langmuir and Freundlich equations, K_s is the Sips isotherm model constant (L g^{-1}), and n_s is the Sips isotherm exponent, which is related to the heterogeneity factor that represents the deviation of the linearity of adsorption. A value of n_s close to or equal to 1 is given in adsorbents with homogeneous active sites, while a value of n_s close to 0 defines a surface with heterogeneously distributed active sites. It is considered an appropriate isotherm model, since it avoids the restriction of increasing concentration, in contrast to the Freundlich isotherm model (which assumes infinite number of active sites). The Sips isotherm reduces to the Freundlich isotherm model at low concentration, while it reduces to the Langmuir isotherm model at higher concentrations, thereby, appropriately predicting monolayer adsorption [203, 220]. The heterogeneity of adsorbents in the equation is illustrated by $1/n_s$, if $1/n_s < 1$, the adsorbent surface is heterogenous and if $1/n_s \sim 1$, the surface is homogenous [8].

Figure 5.14-5.18 show the fits of the Langmuir, Freundlich, and Sips adsorption isotherm models to the experimental data for adsorption of MB on synthesised samples. All isotherms are L shaped curves, a commonly observed adsorption isotherm shape for adsorption from aqueous solutions the solid-liquid interfaces [221]. These isotherms are described by an increased adsorption uptake at low concentrations, which forms a plateau and adsorption uptake starts to decrease tending to attain equilibrium at higher concentrations. All models showed acceptable fits to the experimental data, with correlation factors of R^2 greater than 0.90. Therefore, the reported parameters are reliable, and the applied models present a good prediction of the experimental results.

The results obtained by applying the two-parameter Langmuir and Freundlich isotherm models are presented in Table 5.5. From this data, the correlation coefficients for

Langmuir isotherm are seen to be higher than those for the Freundlich isotherm model, for all adsorbents. A good fit to the Langmuir equation indicates extended monolayer adsorption with addition of TiO₂ content, correlated with the textural characteristics of the gel adsorbents. The adsorption capacity, K_L , showed that the extent of interaction between adsorbent and adsorbate was improved for RFTi20 as compared to RF. Garcia *et al.* [197] also associated K_L with the adsorption binding energy, which here may imply an increase in active sites and adsorption affinity with addition of TiO₂ to RF. According to the values of R_L obtained from application of the Langmuir model, all the systems show favorable adsorption capacity, i.e. $0 < R_L < 1$. High and favourable adsorption capacities are indicated by low values of R_L , as shown in Table 5.5. Additionally, K_L changes in the same manner, with a rapid increase in the case of RFTi20, suggestive of improved mesoporous structure.

Considering q_m and K_F , which measure adsorption capacity, are consistent with the experimental results. The values of $1/n_F$ in Table 5.5 are less than unity, implying that the dye is favourably adsorbed by RFTi. The Freundlich exponent (n_F) increases with addition of TiO₂ in RF, suggesting increasing homogeneity of the TiO₂ nanoparticles.

The results obtained using the three parameter Sips equation are presented in Table 5.5. It can be observed that the Sips model appropriately predicts the experimentally determined values of adsorption capacity better than both two-parameter models, except for RFTi90, which is found to be comparable to the results determine from the Langmuir model. This may be due to the ability of the Sips isotherm model to predict adsorption over wide adsorbate concentration ranges. The values of the heterogeneity factor, n_s , are greater than 1, therefore, the adsorption surface is predicted to be heterogenous, with the exception of data obtained for RFTi90. n_s , determined for RFTi90, is less than unity and is characteristic of a homogeneous surface. The Sips model reduces to a Langmuir form when $n_s = 1$, hence monolayer adsorption for this system can be predicted [40]. With very high amount of TiO₂ in the samples, for example RFTi90, the values of $1/n_s$ tend to move closer to 1, indicating surface homogeneity and surface-active sites are dominated by homogeneously distributed functional moieties of TiO₂.

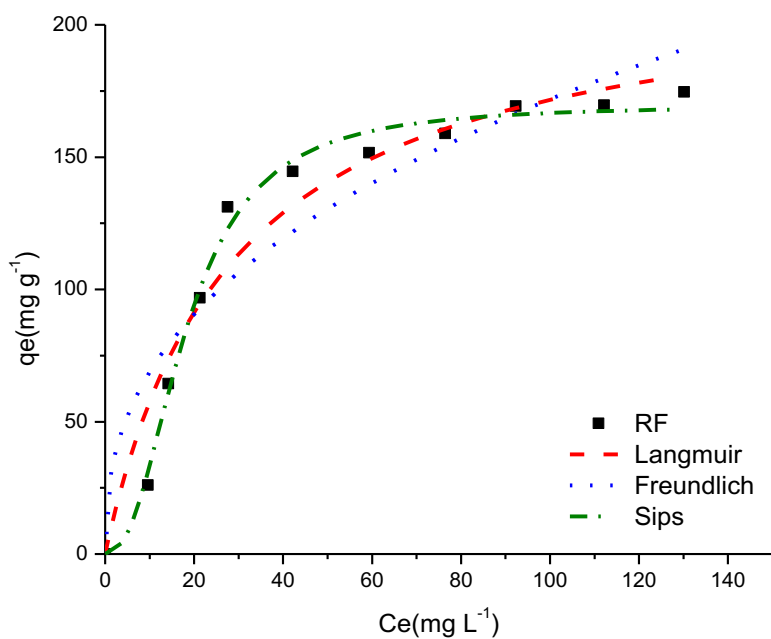


Figure 5.14 Non-linear fitting of Langmuir, Freundlich and Sips isotherm models to isotherms of MB on RF.

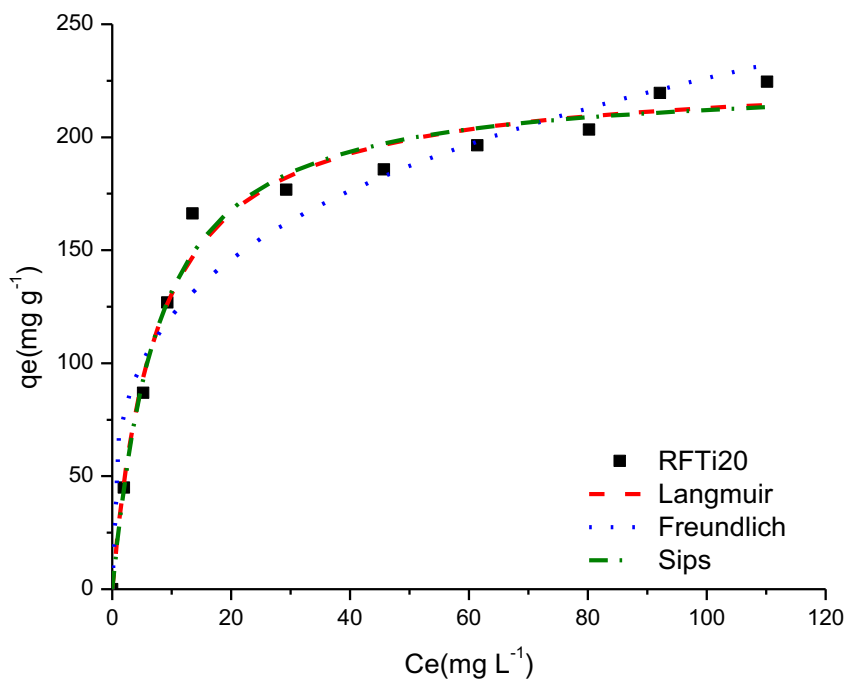


Figure 5.15 Nonlinear fitting of Langmuir, Freundlich and Sips adsorption isotherm models for MB on RFTi20.

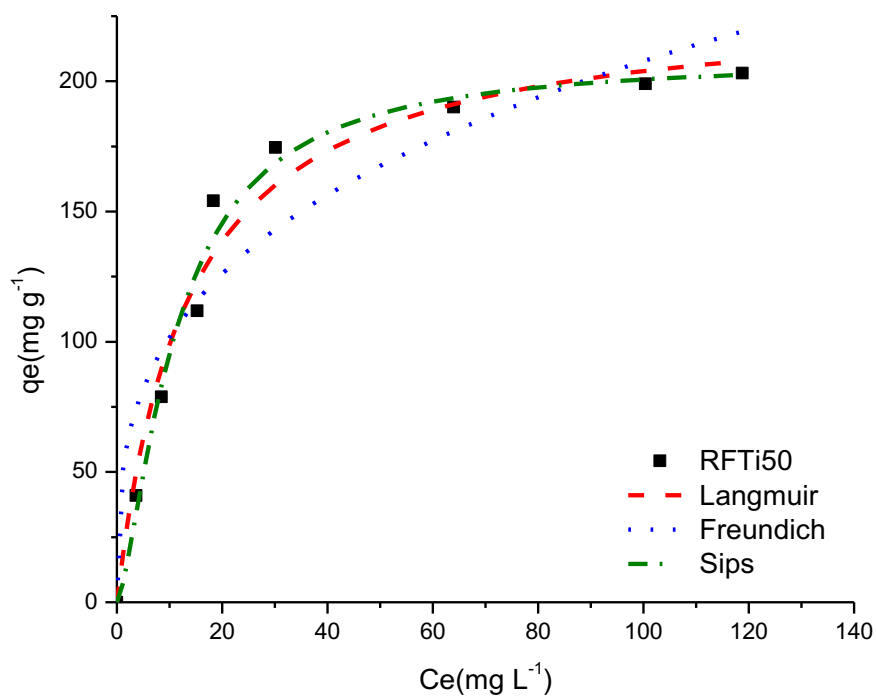


Figure 5.16 Nonlinear fitting of Langmuir, Freundlich and Sips adsorption isotherm models for MB on RFTi50.

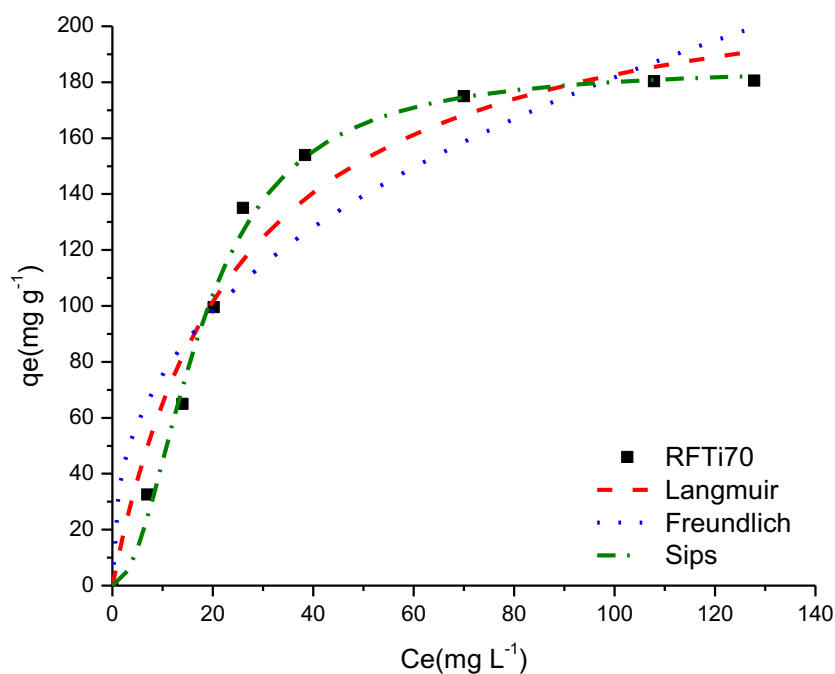


Figure 5.17 Nonlinear fitting of Langmuir, Freundlich and Sips adsorption isotherm models for MB on RFTi70.

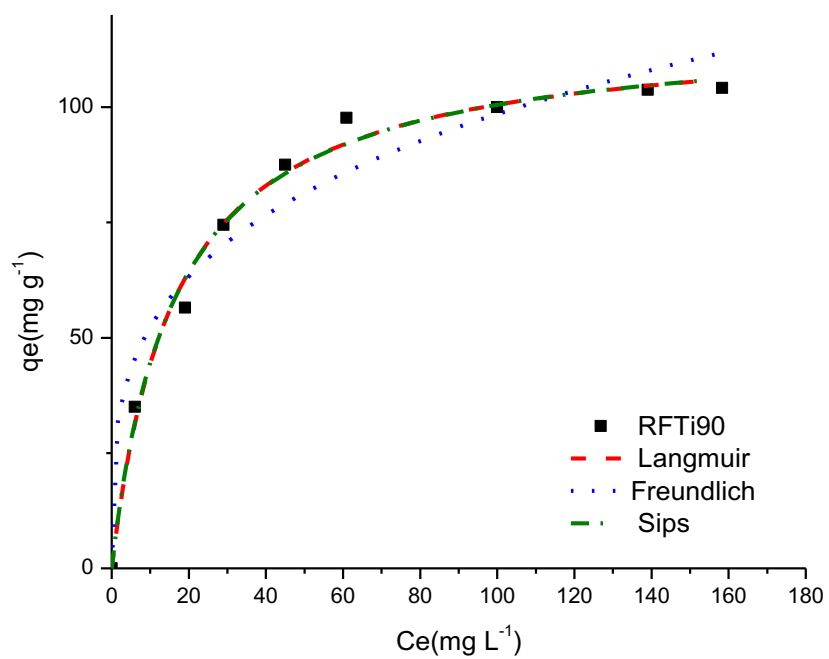


Figure 5.18 Nonlinear fitting of Langmuir, Freundlich and Sips adsorption isotherm models for MB on RFTi90.

Table 5.5 Results of application of the Langmuir, Freundlich and Sips isotherm models to the adsorption isotherms for MB on RFTi adsorbent gels at 296 K.

Parameters	Sample				
	RF	RFTi20	RFTi50	RFTi70	RFTi90
q_{exp}	174	224	215	195	104
Langmuir					
q_L (mg g ⁻¹)	220	228	231	222	116
K_L (Lmg ⁻¹)	0.0354	0.133	0.108	0.036	0.061
R_L	0.220	0.0847	0.118	0.200	0.141
R^2	0.949	0.983	0.974	0.958	0.990
Freundlich					
K_F	27.5	64.3	47.7	28.1	27.7
n_F	2.51	3.68	3.22	2.39	3.60
$1/n_F$	0.398	0.272	0.311	0.420	0.278
R^2	0.888	0.941	0.900	0.927	0.951
Sips					
q_s (mg g ⁻¹)	169	225	209	185	117
K_s (Lmg ⁻¹)	0.001	0.122	0.029	0.003	0.0636
n_s	2.34	1.06	1.45	2.01	0.983
$1/n_s$	0.427	0.943	0.689	0.497	1.017
R^2	0.991	0.982	0.983	0.993	0.998

Based on analyses conducted within this study, the isotherms for MB adsorption on synthesised adsorbent gels were most appropriately fitted in the following order:

- RF Langmuir > Sips > Freundlich
- RFTi20 Sips > Langmuir > Freundlich
- RFTi50 Sips > Langmuir > Freundlich
- RFTi70 Sips > Langmuir > Freundlich
- RFTi90 Langmuir > Sips > Freundlich

The adsorption data was also manipulated to obtain Scatchard plots. These plots supported the interpretations discussed above, regarding the nature of the adsorption sites. The Scatchard equation is represented by Equation 5.9:

$$\frac{q_e}{C_e} = Qb - q_e b \quad \text{Equation 5.9}$$

The Scatchard adsorption constants are defined by Q (mg g^{-1}) and b (L mg^{-1}). A plot of q_e/C_e vs q_e is obtained, where, if a plot shows linearity, a homogenous surface is expected with only one type of binding site. By contrast, if the plot deviates from a straight line, more than one type of binding site is implied [222].

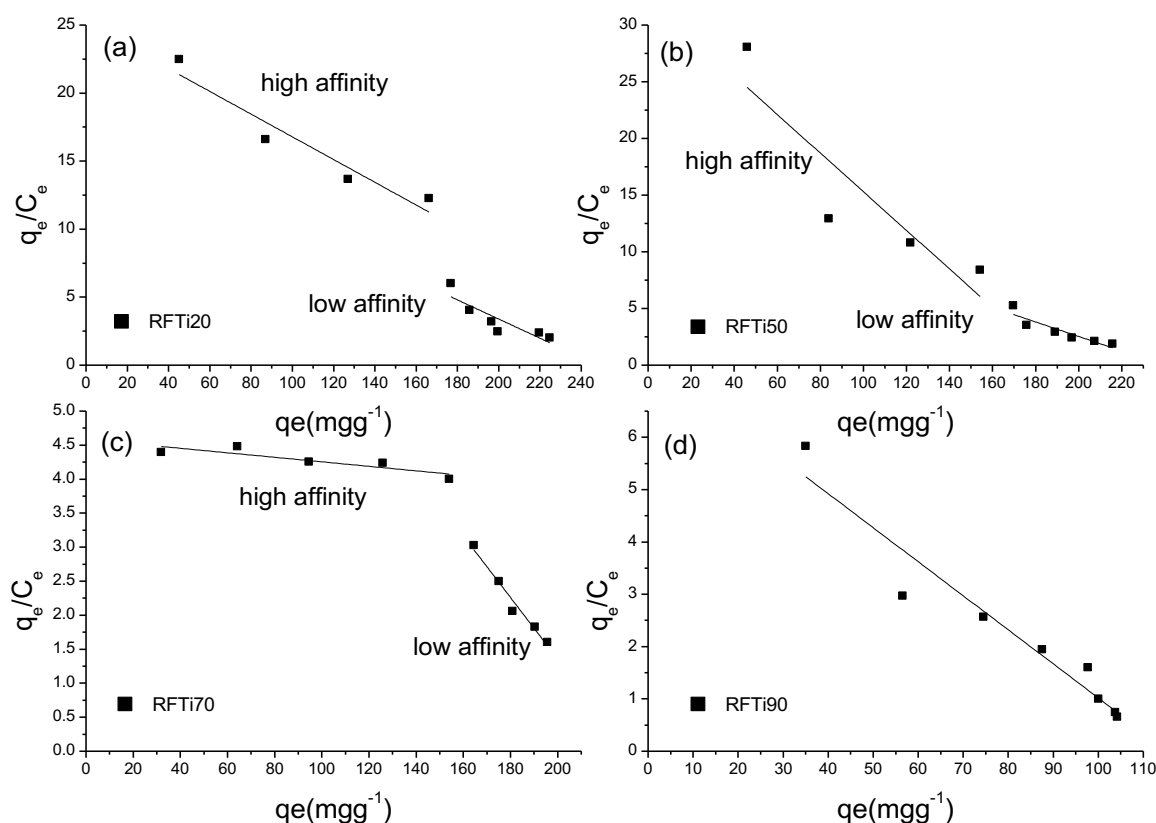


Figure 5.19 Scatchard plots for adsorption of MB on (a) RFTi20, (b) RFTi50, (c) RFTi70 and (d) RFTi90 samples.

MB can bind to RFTi gel adsorbents through various mechanisms, such as electrostatic interactions, π - π interactions, electron donor-acceptor relationships, and hydrogen bonding. It was found that samples with a large proportion of the carbon

phase exhibited plots deviating from linearity, as shown in Figure 5.19 a-d; thus, indicating multiple types of binding affinities, that is, high affinity and low affinity binding sites, attributed to the strong interaction (high affinity) of the carbon phase with MB via electrostatic and π - π interactions. Samples with large amounts of $\text{TiO}_2 > 70\%$ tended to exhibit linear Scatchard plots, as shown in Figure 5.19 d for RFTi90, thereby suggesting weaker interactions. This analysis correlates with the adsorption behaviour and interpretation derived from adsorption isotherm model fittings.

5.3 Effect of Temperature on Adsorption and Thermodynamics

Adsorption reactions are typically exothermic, while some are endothermic. This indicates that, when the temperature increases, the adsorption capacity of the adsorbent may increase or decrease. The adsorption capacity increases with temperature, indicating an endothermic process, whereas a decrease in the adsorption capacity with increasing temperature implies an exothermic process. Temperature has a significant impact on the interactions between adsorbent and adsorbate molecules [8]. The influence of temperature on removal of MB using synthesised RFTi samples was studied under 281, 296, 305 and 313 K.

Figure 5.20 show the performance of selected synthesised samples for MB dye adsorption. The analysis of the data revealed that, for samples with low amounts of TiO_2 , the uptake was observed in three stages at low temperatures and two stages above 296 K. At low temperatures, adsorption tended to reach equilibrium at higher concentrations. At high temperatures, the data show a rapid increase in adsorption capacity for low MB concentrations, whereas the adsorption uptake decreases with slow, continuous increase in MB uptake. The adsorption behaviour was comparable to that of the pure RF gel, except that the adsorption uptake was slow, which may be due to the formation of new active sites upon complexation of RF and TiO_2 , enhancing the adsorption uptake owing to the immediate availability of surface-active sites. Likewise, the adsorption capacity increases at high temperatures due to a gain in kinetic energy by adsorptive molecules resulting in increased diffusivity across the boundary layer of the porous structure. A continued gradual increase is therefore observed at higher temperatures due to high porosity and abundant availability of surface-active sites. Similar to the nature of highly porous sorbents, the increased

adsorption capacity at high temperatures is attributed to higher diffusion of MB dye and increased rate of mass transfer from the bulk to the active sites of the RFTi gel adsorbent, leading to enhanced interaction between the functional groups of MB and adsorbent surface. Another reason for the observed behaviour may be the formation of new active sites on the adsorbent surface at elevated temperatures, as mentioned in a previous work [223]. Another report on the uptake of MB by activated carbon suggested that an increase in temperature may increase the tendency for deaggregation; thus, the uptake of MB monomers increases [224]. It has been suggested that, when using activated carbon as adsorbents, decreasing viscosity and increasing kinetic energy at elevated temperatures has been observed. Hence, a high temperature allows the easy uptake of the adsorptive into the porous structure and enhances the adsorption capacity [125]. In the case of adsorbents with higher amounts of TiO_2 in the RFTi gel (for example data for RFTi50 and RFTi70, as shown in Figure 5.20 c, d, the uptake was observed to occur in three stages at $T < 296$ K, indicating gradual uptake of MB, whereas at higher temperatures two stages of uptake were observed. The data shows adsorption capacity for these types of systems tended to attain equilibrium due to saturation of the active sites. Additionally, the decrease in the porosity of these samples hindered the rapid diffusion of adsorptive molecules. Although increasing the temperature resulted in an improvement in the adsorption capacity, the uptake was much lower in comparison to the previously discussed RFTi samples.

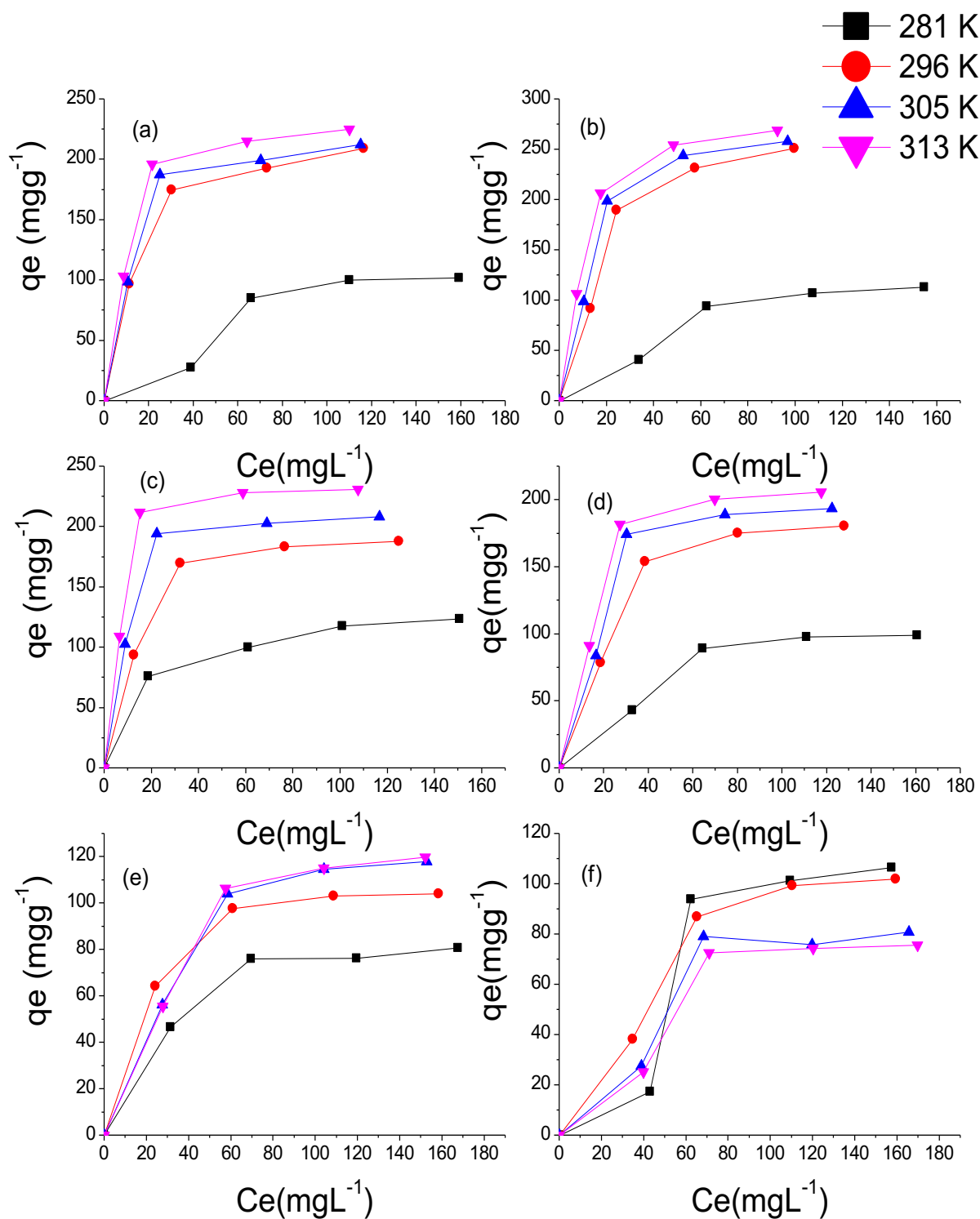


Figure 5.20 Effect of temperature on MB adsorption at 281, 296, 305 and 313 K on synthesised (a) RF, (b) RFTi20, (c) RFTi50, (d) RFTi70 and (e) RFTi90 and (f) TiO_2 samples.

In contrary to these systems, the adsorption uptake tested against RFTi90 (sample with highest amount of Ti), exhibited maximum uptake of MB at 296 K, beyond which the adsorption capacity decreased due to weakened adsorbate-adsorbent interactions. Also, low surface area and porosity is also a major reason of poor adsorption capacity. This conclusion is similar to adsorption behaviour by pure TiO₂, described here and elsewhere [225], mainly describing that adsorption is favourable at low temperatures. Unlike carbon-based sorbents, this argument is in agreement with the adsorption theory, which states that the adsorption capacity decreases with increasing temperature and previously adsorbed molecules desorb at higher temperatures [57, 226].

Studies of adsorption thermodynamics are beneficial for understanding adsorption systems therefore, the mechanism of the temperature-dependent adsorption processes was further understood by employing experimental data obtained from the adsorption procedures to evaluate the critical thermodynamic parameters. In this regard, thermodynamic properties that cannot be measured directly, such as activation energy, changes in Gibbs free energy (ΔG), enthalpy (ΔH), and entropy (ΔS), are required for the evaluation and prediction of the adsorption mechanism. Free energy refers to the maximum amount of energy available to do useful work. It is related to the ΔH , ΔS and temperature (T). These parameters are critical and one of the basic requirements for the optimisation of an adsorption process to determine the spontaneity and viability of such processes therefore, the focus of this chapter is an extensive analysis of adsorption thermodynamics, such as Gibbs free energy (ΔG), change in enthalpy (ΔH), and change in entropy (ΔS).

The thermodynamic behaviour of adsorption from aqueous solution is useful in determining the nature of adsorption (physisorption or chemisorption), as well as understanding the spontaneity of an adsorption process. Negative ΔG at a given temperature signifies spontaneity of a chemical reaction. ΔH and ΔS are considered to determine ΔG [227]. These parameters are calculated using van't Hoff analysis [12], expressed as follows:

$$\ln K = -\frac{\Delta H}{RT} + \frac{\Delta S}{R} \quad \text{Equation 5.10}$$

where $K = \frac{C_e}{C_i}$ is the adsorption equilibrium constant, ΔH and ΔS were calculated from the slope and intercept of van't Hoff plots of $\ln K$ vs $1/T$ (plots shown Appendix E). The values obtained from these plots were used to calculate the free energy change, ($\Delta G = -RT \ln K$, calculation procedure is detailed in [44]).

Table 5.6 shows the calculated thermodynamic parameters for the samples, obtained through van't Hoff plots, for RFTi20, RFTi50, RFTi70, RFTi90, RF and TiO₂ sample at 281, 296, 305 and 313 K (Appendix E). Overall, negative ΔG values were obtained, indicating that all the adsorption systems were feasible and spontaneous at all temperatures. As temperature increased, ΔG values were found to decrease consistently from for low amounts of TiO₂ in the samples. A decrease in the negative value of ΔG , with an increase in temperature, indicates that the adsorption process of MB is more favourable at higher temperatures. This is due to increased kinetic energy gained by the MB ions/molecules and the fact that the affinity of the adsorbent and adsorbate becomes higher at higher temperatures. In the case of RFTi70 and RFTi90, a slight increase in the values of ΔG was observed, indicating that the adsorption process for these systems becomes independent of temperature at $T > 296$ K. ΔG data for TiO₂ showed an increasing value with increase in temperature, indicative of an exothermic adsorption characteristic [44].

The results for ΔH are important to determine the nature of the adsorption process. Generally, an adsorption process is expected to be exothermic bearing a negative value, due to bond formation between the adsorbent and the solute, and adsorption quantity decreases with increasing temperature. This phenomenon is associated with a physisorption mechanism [219]. Contrastingly, in this case, the adsorption quantity for most of the adsorption systems exhibited an increase with increasing temperature, since positive ΔH values were obtained, implying a distinct endothermic adsorption mechanism due to RF-TiO₂ complexation. This phenomenon is associated with chemisorption. The value of ΔH , for a chemisorption process, is high (80-200 kJ mol⁻¹) due to chemical interactions between the adsorbent and adsorptive [44]. ΔH for the RF gel was +45.2 kJ mol⁻¹, and the value obtained is similar to that determined by Zhou *et al.*, where a mesoporous RF polymer was employed as an adsorbent for the removal of Cr (VI). A resulting ΔH value, of +42.5 kJ mol⁻¹, was reported, conclusive

of the adsorption process belonging to the chemisorption classification [223]. The obtained ΔH values for RFTi20, RFTi50, RFTi70 and RFTi90 show a variation (Table 5.6), which may signify the extent of interaction between the adsorptive and RFTi gels. In the case of RFTi20 (or samples containing high amount of RF), the ΔH value obtained is slightly lower than for RFTi50. This may be attributed to binding of adsorptive at high energy sites, reflecting an increase in ΔH . Here, it is predicted that the RFTi50 gel surface possesses higher energy sites than RFTi20, due to surface complexation of RF and TiO_2 . Hence, maximum enthalpic value was observed for this system, attributed to covering of strongest binding sites resulting in greatest MB interaction, which is a combination of surface complexation and chemical adsorption. For the adsorption system using RFTi70, a low ΔH indicates less favourable interactions, followed by formation of multilayers. The enthalpic value indicates a combination of both physical and chemical interactions, since ΔH is slightly less than 40 kJ mol^{-1} . The ΔH value further reduces for the adsorption system with RFTi90, and ultimately pure TiO_2 exhibited exothermic adsorption, since the bond breaking energy is less than the bond making energy, also suggestive of physisorption.

Table 5.6 Calculated thermodynamic parameters for synthesised RFTi20, RFTi50, RFTi70, RFTi90, RF and TiO₂ gel adsorbents at 291, 296, 305, 313 K.

Sample	T (K)	ΔG (kJ mol ⁻¹)	ΔH (kJ mol ⁻¹)	ΔS (J mol ⁻¹)
RFTi20	281	-0.962	47.5	174
	296	-5.07		
	305	-5.77		
	313	-6.42		
RFTi50	281	-1.10	49.3	179
	296	-4.09		
	305	-5.49		
	313	-6.86		
RFTi70	281	-0.759	36.9	134
	296	-3.41		
	305	-4.44		
	313	-4.93		
RFTi90	281	-0.212	12.4	45.2
	296	-1.16		
	305	-1.46		
	313	-1.61		
RF	281	-0.273	45.2	164
	296	-4.56		
	305	-4.84		
	313	-5.44		
TiO₂	281	-0.957	-8.73	-27.4
	296	-0.703		
	305	-0.368		
	313	-0.063		

Whether the adsorption process is an associative or dissociative mechanism can be evaluated based on ΔS . A negative value of ΔS indicates an associative mechanism,

as the system tends to become more ordered. Additionally, negative ΔS indicates no occurrence of significant changes in the internal surface of the adsorbent during the adsorption process. Whereas, a positive ΔS suggests an increase in disorder of the adsorption system involving a dissociative adsorption mechanism, suggestive of changes in internal structure of the adsorbent. In this case values of ΔS were positive, indicating affinity between RFTi and MB molecules. Increase in disorder of the system may be due to solvent molecules displaced by MB molecules, resulting in increase of translational entropy, therefore, randomness of the system prevails [44]. Additionally, positive ΔS is also indicative of increased degree of freedom of the adsorbed MB molecules. The higher ΔS value for RFTi50 clearly showed an increase in disorder at the adsorbent interface, validating the synergy between RF and TiO_2 resulting in increased energetic interactions between the adsorbent and MB molecules. The low ΔS value for RFTi90, on the other hand, indicates fewer adsorbate-adsorbent interactions, also suggestive of no significant structural changes of the adsorbent occurring during the adsorption process. Such conclusions also translate into hydrogen bonding or van der Waals forces, attributed to a dominant TiO_2 phase in the adsorbent sample. Therefore, the adsorption process using RFTi90 was endothermic and predominantly described a physisorption phenomenon. These findings are analogous to mesoporous nano- TiO_2 used for adsorption and photosorption processes, which demonstrated a spontaneous adsorption process with positive ΔS and ΔH indicating an endothermic physisorption process [228]. It is noteworthy that adsorption by all RFTi gel adsorbents was entropically driven, since $T\Delta S > \Delta H$. For the adsorption system with pure TiO_2 , the data suggested an enthalpically driven adsorption process, and decreased adsorption capacity was observed with increasing temperature. The negative magnitude of ΔS for pure TiO_2 showed that the disorder of the adsorption process decreased, suggesting decreased randomness at the adsorbate interface. The enthalpy of MB adsorption onto TiO_2 was -8.7 kJ mol^{-1} , suggesting an exothermic profile and ΔS was -27.5 J mol^{-1} , attributed to MB migrating to an ordered state on the TiO_2 adsorbent surface [229]. Negative ΔG , for this system, indicates a spontaneous adsorption process, which is unfavourable at higher temperatures. These results are consistent with previously studied TiO_2 adsorbent systems [176, 230], indicative of physical adsorption via weak electrostatic interactions

between active sites and MB ions. Likewise, a study on the thermodynamics of carbon doped TiO₂ by Simonetti *et al.* [148] concluded that the process was endothermic with increased randomness of the system and decreasing ΔG indicating spontaneity at elevated temperatures. This corroborated that overall magnitude of adsorption depended on the properties of adsorbents, further validated through the literature. Lin *et al.* reported the adsorption of ionic liquids using macroporous RF polymers; the analysis suggested that adsorption of ionic liquids onto RF polymers was attributed to physisorption. Positive enthalpy and entropy values indicated endothermic processes, and disorder at the RF/solution interface increased, since water molecules desorbed from pores to the surface of the RF when the ionic liquid was adsorbed on to RF polymer [231]. In another instance, a RF xerogel adsorbing MB exhibited a high ΔS of +172.35 J mol⁻¹, demonstrating increased randomness at the MB-RF interface during adsorption. ΔH was positive for the same process; hence a spontaneous endothermic chemisorption process was followed. Adsorption occurred via chemical interactions between the adsorbent and RF surface by either sharing or transfer of electrons [232, 233]. Similar behaviour was observed in the present study for synthesised RFTi samples < 70%; chemisorption is predominantly the adsorption process followed. A spontaneous adsorption process, decreasing with increasing temperature, signifies an endothermic process while positive entropy is indicative of an entropically driven adsorption process. The enthalpy decreases for samples with higher TiO₂ owing to weak interactions between MB and the RFTi surface, hence a combination of physical and chemical processes is predicted.

Activation energy (E_a) is an important factor for determining the temperature dependence of reaction rate of adsorption processes [44]. In terms of adsorption systems, E_a is the minimum energy required by the adsorbate to interact with the surface and functional moieties of the adsorbent. Also, the nature of adsorption can be understood by evaluating the E_a of adsorption, which can predict if the adsorption process was physical or chemical [234]. E_a is graphically determined (Figure 5.21) by manipulating the Arrhenius equation, the linear form used is shown in Equation 5.11 [44]:

$$\ln K_2 = -\frac{E_a}{RT} + \ln A \quad \text{Equation 5.11}$$

Where K_2 is the rate constant obtained from nonlinear analysis using the pseudo-second order model, E_a is the Arrhenius activation energy, A is the Arrhenius factor (collision frequency), R is the gas constant ($8.314 \text{ J mol}^{-1} \text{ K}^{-1}$) and T is the absolute temperature. Figure 5.21 shows $\ln k_2$ plotted against $1/T$, E_a was obtained from the slope (E_a/R). Additionally, the nature of adsorption is physisorption if E_a is between 1-8 kJ mol^{-1} ; if adsorption is an ion exchange mechanism, then E_a is 8-16 kJ mol^{-1} ; and for chemisorption mechanisms, E_a is $> 40 \text{ kJ mol}^{-1}$. In contrast, modified mesoporous RF in this study shows chemisorption phenomenon. E_a values obtained for the adsorption of MB onto RFTi20, RFTi40 and RFTi70 gel adsorbents were 99.5, 113, 66.3 and 50.7 kJ mol^{-1} respectively. Thus, the adsorption of MB by RFTi gel adsorbents occurred via mainly chemisorption mechanisms [45], depending on the properties of the adsorbent, which determines the adsorption affinity and is consistent with the discussed thermodynamic parameters. The calculated values of E_a were less than 120 kJ mol^{-1} , indicating faster rate of adsorption for all samples [203]. A positive value of E_a suggests that the adsorption process was favoured at high temperature, since high temperature overcomes the energy barrier in the adsorption process, hence the adsorption processes for all samples are considered as endothermic [44, 203]. Similar observations have been reported by Fan *et al.*, who employed activated carbon for the adsorption of MB [235].

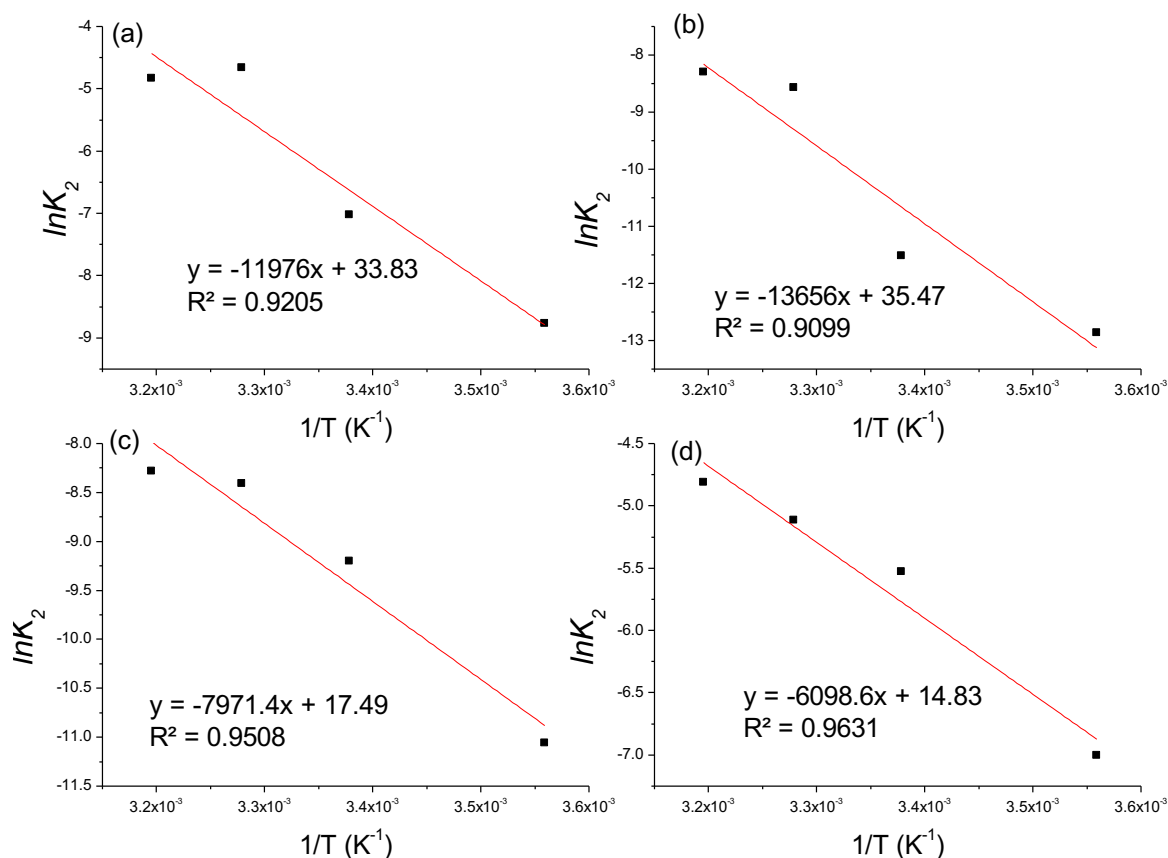


Figure 5.21 Arrhenius plots for calculation of activation energy for synthesised (a) RFTi20, (b) RFTi50, (c) RFTi70 and (d) RFTi90 gel adsorbents at 281, 296, 305 and 313 K.

5.4 Adsorption Potential

Adsorption potential (ϵ) is defined as the chemical potential during an adsorption process that occurs when adsorbate transfers from solution to the adsorbent surface, in other words, the work required to move a molecule from its location to the adsorption space [45]. Calculation of ϵ is important since liquid phase adsorption is complicated due to an adsorption competition between the adsorbate and solvent on the adsorbent surface. This value can help describe the interaction between various components and situation of chemisorption in solution and adsorption layer. The adsorption potential at solid-liquid interfaces can be expressed by Polanyi equation [236].

$$\epsilon = -RT \ln \left(\frac{C_e}{C_0} \right) \quad \text{Equation 5.12}$$

Where ε (KJmol^{-1}) is the adsorption potential an C_0 (mgL^{-1}) and C_e (mgL^{-1}) are the initial and equilibrium concentrations, respectively, $T(\text{K})$ is the adsorption temperature and R is the gas constant 8.314 Jmol^{-1} . Table 5.7 shows figures of calculated adsorption potential. For adsorption system with RFTi adsorbent gels, a trend of decreasing potential barrier was observed with increasing temperature, this implies that the dispersion forces increase the interactions in the adsorption system. Overall, values of high potential barrier were consistent with low adsorption capacity.

Table 5.7 Calculated adsorption potential data for RF, RFTi20, RFTi50, RFTi70 and RFTi90 at different initial concentrations 50, 100, 150 and 200 mgL^{-1} at 281, 296, 305 and 313 K.

	RF (KJmol^{-1})	RFTi20 (KJmol^{-1})	RFTi50 (KJmol^{-1})	RFTi70 (KJmol^{-1})	RFTi90 (KJmol^{-1})	TiO ₂ (KJmol^{-1})
50 mgL^{-1}						
281	0.93	0.93	2.31	0.99	1.09	0.35
296	3.27	3.27	3.41	2.45	1.78	0.90
305	3.99	3.99	4.39	2.81	1.52	0.63
313	4.98	4.98	5.35	3.41	1.53	0.59
100 mgL^{-1}						
281	0.87	1.10	1.16	1.03	0.85	1.10
296	3.13	3.50	2.79	2.35	1.22	1.05
305	3.32	4.03	3.81	3.03	1.36	0.96
313	3.76	4.54	4.91	3.38	1.45	0.89
150 mgL^{-1}						
281	0.73	0.78	0.93	1.98	0.53	0.74
296	1.78	2.36	1.66	3.18	0.75	0.72
305	1.92	2.66	1.97	3.74	0.85	0.53
313	2.22	2.95	2.44	3.98	0.86	0.52
200 mgL^{-1}						
281	0.53	1.14	0.66	0.51	0.41	0.56
296	1.33	7.73	1.16	1.10	0.57	0.56
305	1.40	8.47	1.37	1.24	0.68	0.48
313	1.56	9.98	1.61	1.38	0.71	0.43

5.5 Summary

The effects of parameters, such as time, concentration, and temperature, on the adsorption capacity were investigated. The experimentally determined adsorption capacity as a function of time and concentration was modelled using adsorption kinetic and isotherm models to gain insight into the adsorbent-adsorbate interactions. Analysis of the results revealed that the interactions depended on the physicochemical properties of the synthesised samples. RFTi samples are generally composed of multiple binding bonds exhibiting a combination of physisorption and chemisorption, which was evaluated by best fitting of data to pseudo-second-order kinetic and Sips isotherm models. Hence, the predicted adsorption behaviour was interpreted as a two-step process: (i) monolayer adsorption with chemisorption characteristics, where adsorbate binding occurs predominantly via electrostatic interactions and hydrogen bonding; and (ii) multilayer adsorption, which is favoured at high concentrations and temperatures, predominantly via physical interactions or weak forces of attraction, such as van der Waals forces. In addition, the adsorption process, demonstrated by all samples, was thermodynamically feasible.

Chapter 6: Photodegradation Studies

This chapter discusses the integrated adsorption-photodegradation performance of synthesised samples, according to methodology described in Section 3.8.1. To evaluate the contribution of visible light, photodegradation studies were performed after adsorption equilibrium had established in dark and no further removal of MB was recorded. This chapter discusses the photodegradation performance and corresponding kinetic analysis. Research articles presenting findings using the same methodology for two RFTi samples from the synthesised range has been published in the journal 'Gels' [144] and 'Molecules' [145]; a complete manuscript can be found in the Appendix H.

6.1 Photodegradation Performance

The maximum absorbance vs. wavelength spectra via UV-Vis spectroscopy (in the range 550–700 nm) were collected to determine photocatalytic activity through reduction in concentration of methylene blue (MB) dye, at 30 min intervals.

MB dye degradation involves opening of the aromatic rings and disintegration of the molecule to single ring structure when photogenerated reactive oxide species (ROS) attack the functional groups. Firstly, $(C-S^+=C)$ is converted to a sulfoxide $(C-S(=O)-C)$, and the central aromatic ring opens. The transition from $(C-S^+=C)$ to $(C-S(=O)-C)$ requires conversion of double bond conjugation, which causes opening of the central aromatic ring including heteroatoms, S and N. The H atoms necessary for C–H and N–H bond formation may originate from proton reduction caused by photogenerated electrons [176]. The possible degradation pathway of MB dye degradation is represented in Figure 6.1.

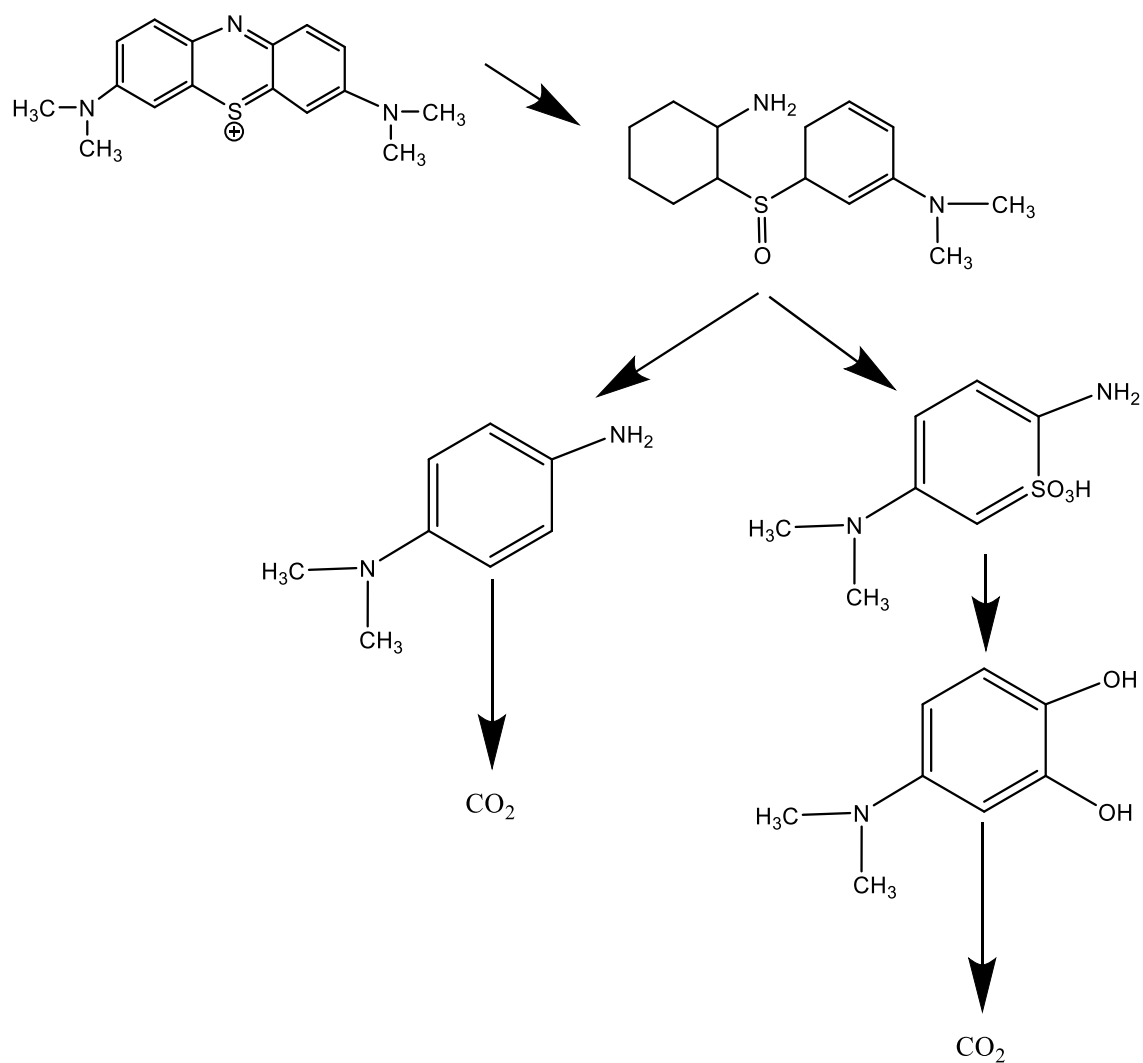


Figure 6.1 Degradation mechanism of MB dye molecule.

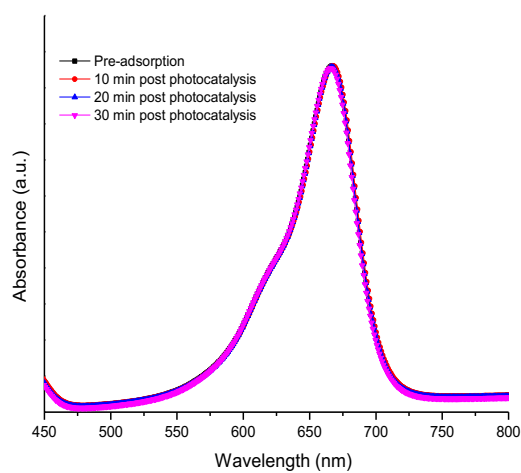


Figure 6.2 UV-Vis absorption spectrum for degradation of dye in the absence of sample.

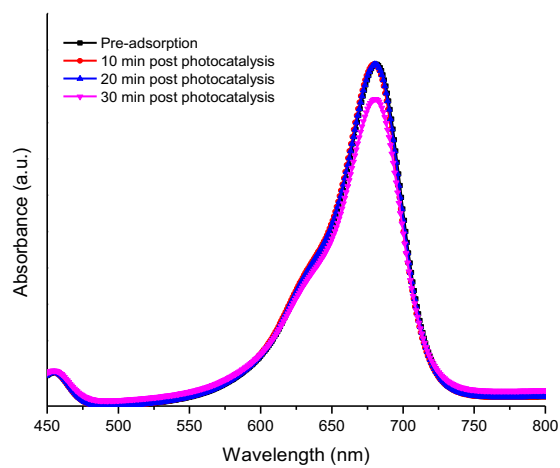


Figure 6.3 UV-Vis absorption spectrum for degradation of dye by TiO₂.

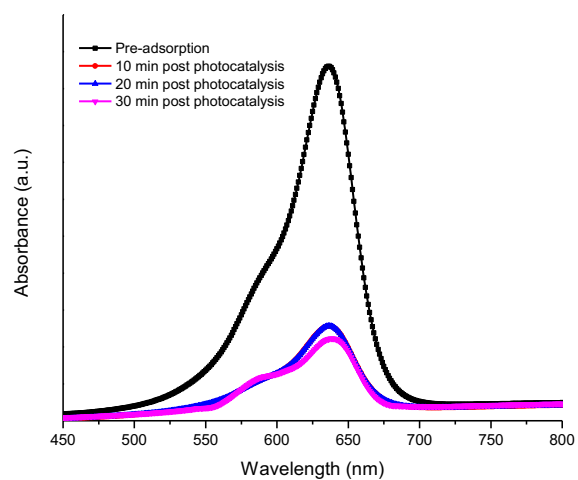


Figure 6.4 UV-Vis absorption spectrum for degradation of dye by RF.

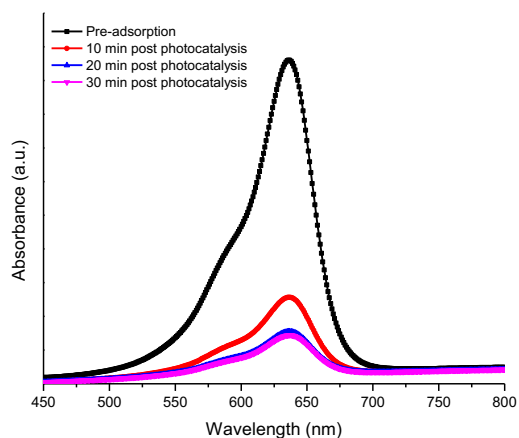


Figure 6.5 UV-Vis absorption spectrum for degradation of dye by RFTi10.

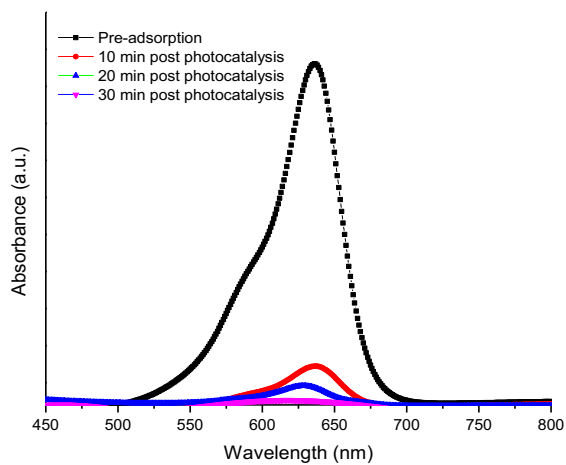


Figure 6.6 UV-Vis absorption spectrum for degradation of dye by RFTi30.

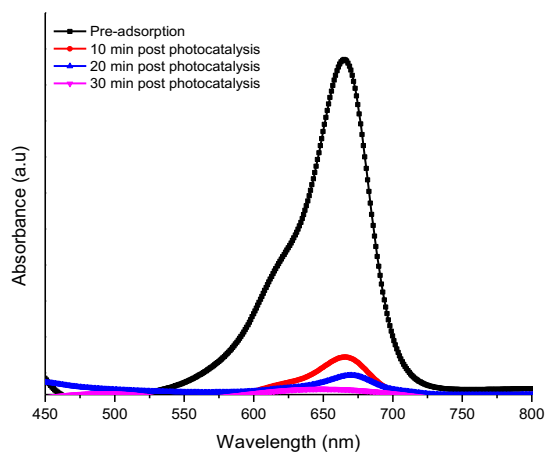


Figure 6.7 UV-Vis absorption spectrum for degradation of dye by RFTi40.

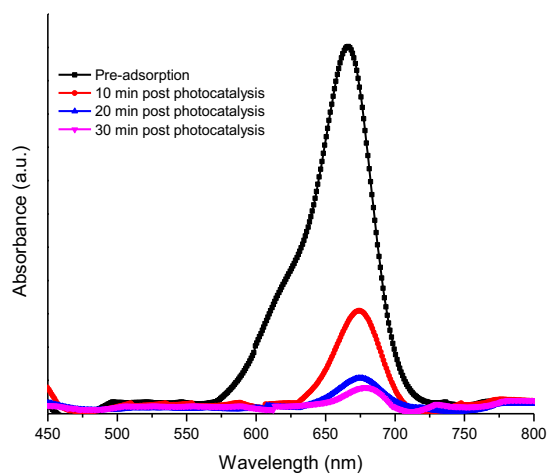


Figure 6.8 UV-Vis absorption spectrum for degradation of dye by RFTi50.

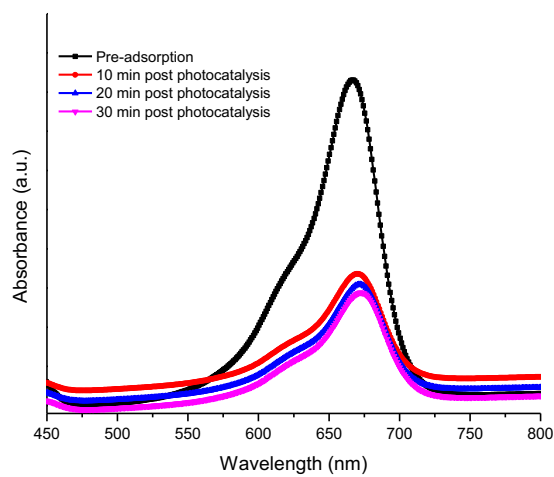


Figure 6.9 UV-Vis absorption spectrum for degradation of dye by RFTi60.

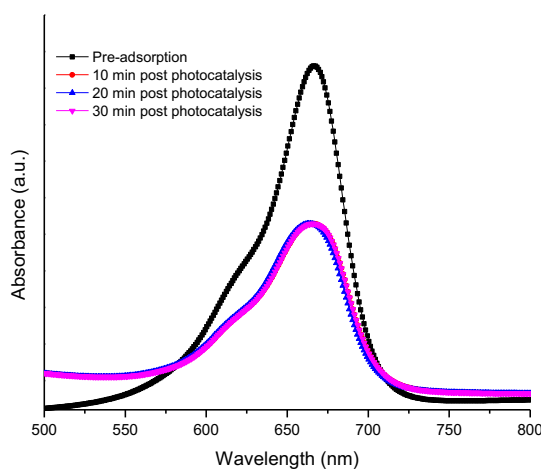


Figure 6.10 UV-Vis absorption spectrum for degradation of dye by RFTi90.

Figure 6.2-6.10 represent the MB removal efficiency by synthesised samples, determined by reduction in intensity of the main peak at 663 nm, which is attributed to the benzene ring and aromatic groups [176]. Upon visible light irradiation, the absorbance peaks of MB dye remained almost unchanged, throughout exposure, in the absence of catalyst, confirming that MB was stable under visible light. The tests conducted using pure RF and TiO₂ samples show insignificant dye degradation. The peaks reduced sharply in the presence of RFTi10, indicating that RFTi sample exhibited visible light photocatalysis. The peaks progressively reduced with increasing concentration of TiO₂, owing to greater production of photogenerated ROS, that degraded adsorbed dye molecules. As observed for RFTi40, Figure 6.7, the peak at 663 nm appeared diminished after 10 min and plateaued at 30 min of PCA. For RFTi50, Figure 6.8, the peak found at 10 min was relatively higher than for the samples already discussed, signifying poor adsorption properties exhibited by this sample. However, upon visible light irradiation, the peak intensities at 30 min appeared to be nearly similar to those of the samples with TiO₂ < 40%. This observation may be attributed to the simultaneous adsorption and photodegradation of the MB dye upon visible light exposure. As described in previous chapters, the adsorption capacity decreases with increasing TiO₂ beyond the optimal amount, while the aggregation of TiO₂ at higher concentrations reduces PCA due to the greater band gap of these samples, as well as slower electron transfer and higher charge recombination rates; therefore, there is no significant change in peak intensities for samples with TiO₂ > 70%. Additionally, PCA for RFTi90 (Figure 6.10) exhibited no PCA, and the low intensity observed implied the adsorption performance of the sample.

6.2 Kinetics of Photocatalytic Activity

The kinetics of photodegradation for RFTi samples with different concentrations validated the variation in peak intensities observed in Section 6.1.

The corresponding absorbance data recorded at given time intervals were fitted to the following first order kinetic equation:

$$\ln \frac{C_o}{C_e} = kt \quad \text{Equation 6.1}$$

where C_o is the initial MB concentration at $t = 0$, and C_e is final MB concentration at a given time. The value of the rate constant, k , was evaluated from the slope of a plot of $\ln (C_o/C_e)$ vs. time (t) in min. This value provides a measure of photocatalytic performance, as it defines the reduction in concentration of dye, which is correlated to the reacting substances, that is, the photogenerated reactive oxide species, therefore, a higher value of k signifies higher photocatalytic efficiency.

Figure 6.11 shows the data for reduction in concentration of MB after treatment with all the synthesised samples. The recorded data was modelled using pseudo-first order kinetics, shown in Figure 6.12. As observed, no dye degradation activity was observed in the absence of catalyst. Therefore, it can be concluded that the MB dye was stable and did not self-degrade. The PCA results were consistent with the optical responses (including absorption wavelength and band gap analysis) and adsorption properties of the synthesised photocatalysts. For pure RF gel, the plateau in the photodegradation section signified that no PCA occurred. During the pre-photodegradation process, the porous nature of RF gel exhibited excellent adsorption properties but when exposed to visible light, no PCA was observed. This was due to slow charge transfer properties of the RF gel structure under light irradiation. For similar reasons, Zhang *et al.* [166] concluded that RF solely may not be recommended for photocatalysis. The kinetic studies revealed a poor rate constant ($k = 3.29 \times 10^{-4} \text{ min}^{-1}$) relative to the rest of the samples and showed no dye reduction in due course. A study conducted into the preliminary evaluation of RF carbon gels for water pollutant removal established that, although RF has a strong adsorption capacity, its slow adsorption rate makes it unsuitable for continuous adsorption processes [169]. On the contrary, it was reported that copolymerisation of RF via donor-acceptor interactions can create a low band gap through π conjugation and π stacking along and between the polymer chains [164]. In the case of pure TiO_2 , a slight reduction in dye concentration at 120 min was recorded with $k = 4.21 \times 10^{-4} \text{ min}^{-1}$, which may be due to potential absorbance of UV light from the surroundings and assisted pretreatment (adsorption). Analogous to commercial TiO_2 photocatalysts, weak PCA of synthesised TiO_2 was attributed mainly to a large band gap and rapid recombination rates of the photogenerated charge carriers [237].

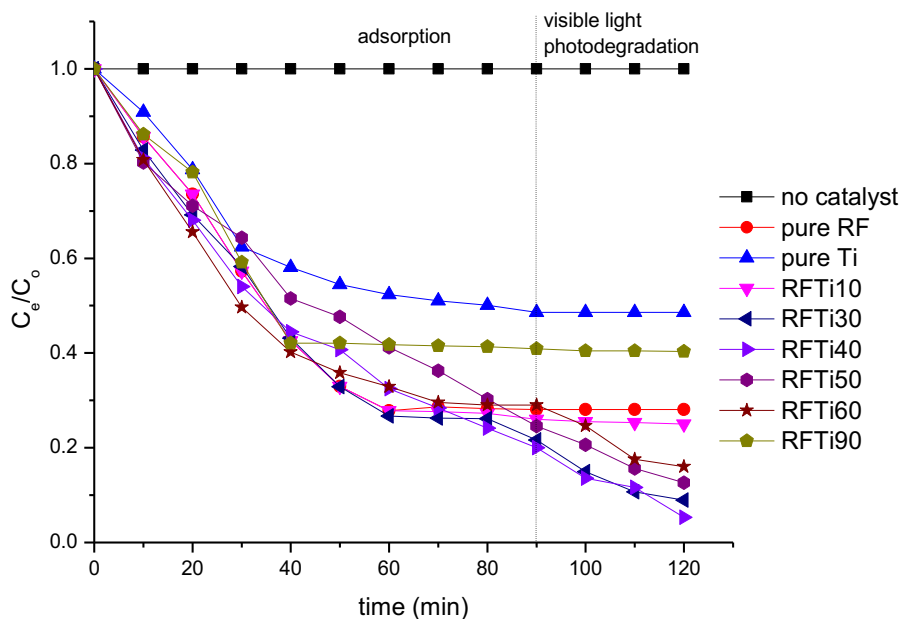


Figure 6.11 Integrated adsorption-photodegradation performance regarding MB dye degradation tested against synthesised samples (experimental conditions: pH~7, temperature 23°C, exposure to visible light after 90 min).

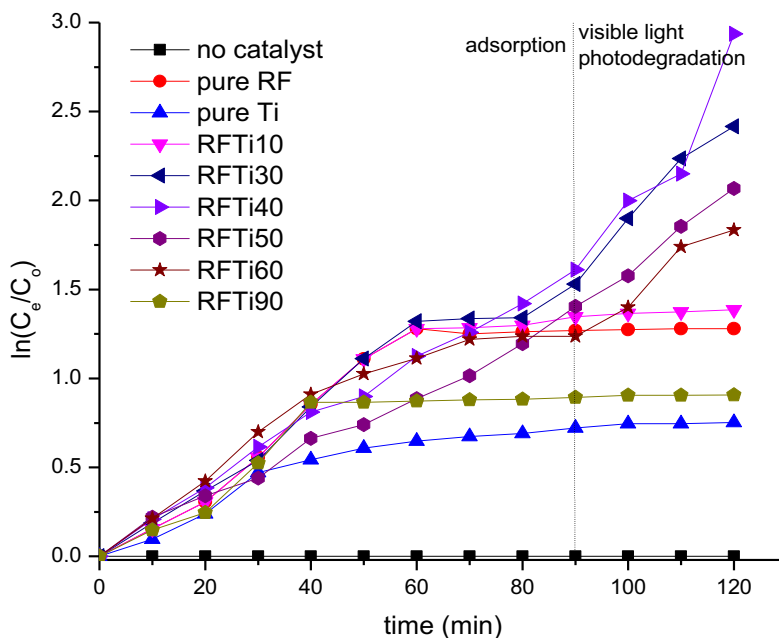
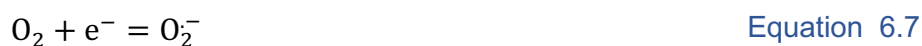
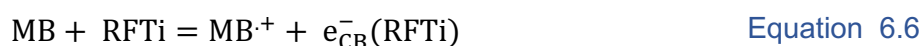


Figure 6.12 First-order kinetic data of Integrated adsorption-photodegradation performance regarding MB dye degradation tested against synthesised samples.

The data obtained after treatment with RFTi10 showed significant PCA, also evident visually through the faintness of the remaining MB dye. The photodegradation

mechanism of synthesised RFTi photocatalysts, under visible light irradiation, can be explained by the mechanism of MB photodegradation represented in Equations 6.2-6.8. The system activates when RFTi absorbs light with photon energy ($h\nu$) and generates conduction band (CB) electron (e^-) and valence band (VB) hole (h^+) pairs upon visible light irradiation. The holes interact with moisture on the surface of the adsorbent gel yielding hydroxy free radicals or reactive oxide species (H^+ or OH^\bullet), which are oxidation agents that can mineralise a wide range of organic pollutants, ultimately producing CO_2 and H_2O as end products. The reaction sequence below represents the photodegradation of MB, showing a simplified mechanism of photoactivation by a photocatalyst (Equations 6.2–6.9) [160]. For the mechanism of photoinactivation of MB in the presence of RF/TiO₂, hydroxy free radicals or reactive oxide species (H^+ or OH^\bullet) attack the aromatic ring of the MB structure, degrading it into a single ring structure product, which then finally degrades to CO_2 and H_2O (Equations 6.6–6.8) [16, 238].



The kinetic data obtained for the RFTi10 showed improved rate constants for photodegradation relative to pure RF and pure TiO₂ with k value $1.25 \times 10^{-3} \text{ min}^{-1}$. The adsorption amount was ~72% at 10 min, and remained approximately constant until

20 min. After which the removal efficiency increased to approximately 75%, demonstrating removal of MB dye was by means of visible light in the latter 30 min. The results were attributed to synergy between RF and TiO₂ whereby low bandgap enabled absorption in the visible region. The high surface area and mesoporous nature of RF network enabled the entrapment of photogenerated charge carriers produced by TiO₂, therefore, rapid generation of ROS was possible for an efficient degradation of the MB dye. However, this sample did not show an optimal efficiency, perhaps due to low TiO₂ concentration, which may not have photogenerated enough ROS. Additionally, the light absorption by TiO₂ may have been restricted by RF phase, since dispersed TiO₂ nanoparticles may have been confined by the wall of mesoporous carbon (as observed in FESEM, Section 4.1, where TiO₂ nanoparticles were indistinguishable in the micrograph obtained for RFTi10). These findings were comparable with other carbon/TiO₂ systems where synergistic effects have substantially been affected by the concentration of carbon or TiO₂ phases. For example, one study showed that an increase in concentration of mesostructured carbon, up to 40%, enhanced the photocatalytic performance of TiO₂ due to a change in the intrinsic nature of TiO₂ [178].

The present study showed an improvement in photodegradation performance for samples containing TiO₂ up to 40%. It was noted that these samples exhibited superior adsorption in the dark, leading to enhanced photodegradation upon visible light irradiation. The removal of MB increased from 85% to 99% and 75% to 96% for RF/TiO₂ 30% and RFTi 40%, respectively. This improvement is attributed to optimal adsorption and optical properties. In addition, improved k and continuous removal of MB for these samples confirmed that the amount of TiO₂ was sufficient to generate charge carriers, which were effectively entrapped and promoted by the RF matrix so their recombination was retarded and the PCA improved. However, further increase in TiO₂ content in RFTi samples resulted in declined PCA. As demonstrated in Figure 6.12, a slight decrease in PCA for RFTi60 was observed and the value of k was reduced to $2.13 \times 10^{-2} \text{ min}^{-1}$, which further slowed with increasing TiO₂, as observed for RFTi90. This mainly is attributed to low surface area and adsorption capacities of these samples. Furthermore, it is known that the heterogeneity and tendency of TiO₂

to agglomerate increases with concentration [239], resulting in higher recombination rates of photogenerated charge carrier

A report of a photocatalyst comprising a composite structure fabricated with 42% TiO₂ on a mesoporous phenolic resol [163] showed significant PCA against reduction of methyl orange, however, inadequate literature is found on the optimal concentrations of TiO₂ for high PCA in such carbon/TiO₂ systems. Though, studies on other TiO₂ ligand complexes, such as Bi-based oxide complexes, substantiate the decline in PCA with higher TiO₂ and report that 45% TiO₂ in the photocatalyst is optimal to yield highest PCA amongst a range of concentrations [242]. The present study reveals that RFTi30 and RFTi40 demonstrated excellent PCA.

Table 6.1 Summary of integrated adsorption-photodegradation performance demonstrated by synthesised sample

Sample	Band gap (eV)	Adsorption (%)	Photodegradation (%)	Rate constant min ⁻¹
Pure TiO ₂	3.20	48	51	4.21×10 ⁻⁴
Pure RF	4.70	70	72	3.28×10 ⁻⁴
RFTi10	2.97	72	75	1.25×10 ⁻³
RFTi30	2.24	85	99	2.98×10 ⁻²
RFTi40	2.33	75	96	3.13×10 ⁻²
RFTi50	2.60	59	87	2.27×10 ⁻²
RFTi60	2.75	67	84	2.13×10 ⁻²
RFTi70	2.93	64	75	6.95×10 ⁻³
RFTi90	3.10	58	60	3.99×10 ⁻⁴

6.3 Summary

The photocatalytic performance was investigated by determining the photodegradation of MB dye under visible light irradiation after the adsorption

treatment. The dye degradation activity improved depending on the physiochemical properties of the material; hence, the optimal properties were demonstrated by RFTi30 and RF40, also shown by photodegradation kinetics.

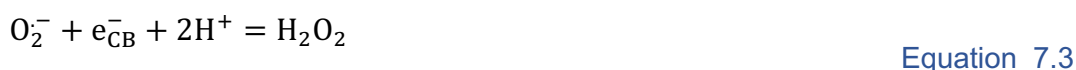
Chapter 7: Antimicrobial Analysis

This chapter describes the approach used to assess the ability of the synthesised gel samples to disinfect pathogenic bacteria. The most rudimentary test for bacterial contamination of a water source is the test for total coliform bacteria, the bacteria most prevalent in the environment, which can indicate the sanitary condition of water [240]. A subgroup of total coliform bacteria is faecal coliforms, which are present in the intestines and faeces of humans and animals. A subgroup of faecal coliforms, *Escherichia coli* (*E. coli*), indicates the presence of faecal matter in water supplies, indicating a higher risk of pathogens. Therefore, the disinfection activity undertaken in this study involved the reduction of total and faecal coliform bacteria and *E. coli* to provide a reasonable indication of the presence of pathogenic bacteria [241]. The aim of this study was to determine the practicality of using these gels as viable water disinfectants based on the required dose levels. Antimicrobial tests were conducted using a membrane filtration (MF) procedure according to the standard method (9222 membrane filter technique for members of the coliform group), as detailed in Section 4.8.2. All tests were performed thrice to provide data on the replication of the results. The numerical results obtained are displayed as bar and whisker plots, with the bars indicating average values and the whiskers showing the maximum and minimum values in each dataset. Each data point and error bar represent the mean and standard error, respectively, of independent triplicates. The antimicrobial activity was reported in terms of the remaining percentage of cultured bacteria on the petri plates (photographs of selected petri plates showing viable bacteria are shown in Appendix F). Research article presenting findings using the same methodology has been published in the journal 'Molecules' [145]; a complete manuscript can be found in the Appendix H.

7.1 Mechanism

The main mechanism of antimicrobial activity is based on the ability of TiO₂ nanoparticles to generate free radicals or reactive oxide species (ROS) upon photoexcitation of charge carriers and consequent redox reactions. These ROS have high oxidative potentials and can penetrate the microbial cell via various mechanisms leading to cell rupture, and reductions in growth and death. The process begins by

absorption of light to overcome the band gap energy of the material, thereby producing photogenerated electron (e_{CB}^-) and hole (h_{VB}^+) pairs from the conduction and valence bands, respectively (Equation 7.1). Normally, these charge carriers recombine and dissipate as heat [80], but, in this case, the entrapment of charge carriers by the RF matrix facilitates charge separation and transport of charge carriers to the surface for use in redox reactions, similar to other carbon modified TiO₂ composite materials [242, 243]. The e_{CB}^- species are available for electron transfer to reducible species adsorbed onto the RFTi surface. The conduction band reduces O₂ to O₂⁻ (Equation 7.2), which further reduces to produce H₂O₂ (Equation 7.3). OH[·] are produced by reduction of superoxide with H₂O₂ (Equation 7.4). The superoxide reacts with H₂O₂ to produce OH[·] (Equation 7.5). The valence band hole extracts electrons from absorbed oxidised species or reacts with OH⁻ or H₂O₂ to form OH radicals (Equations 7.6 and 7.7), or OH radicals recombine to produce H₂O₂ (Equation 7.8). All of the ROS produced through the photochemical reactions detailed above react with bacteria, disrupt the structure of biological cells, and lead to cell death (Equation 7.9 and Equation 7.10). It has been reported that the first usual target of ROS is the cell wall; e.g. in *E. coli* the cell wall is composed of lipopolysaccharide, peptidoglycan and phosphatidylethanolamine, which has been reported to be affected by ROS [244]. Secondly, the rupture of the cell membrane occurs, leading to leakage of cellular matter and ultimate breakdown of the cell [245]. Thirdly, the cell lysis progresses by inhibiting the respiratory chain, followed by damage of DNA [246]. Figure 7.1 shows possible antimicrobial effects of a photocatalyst.



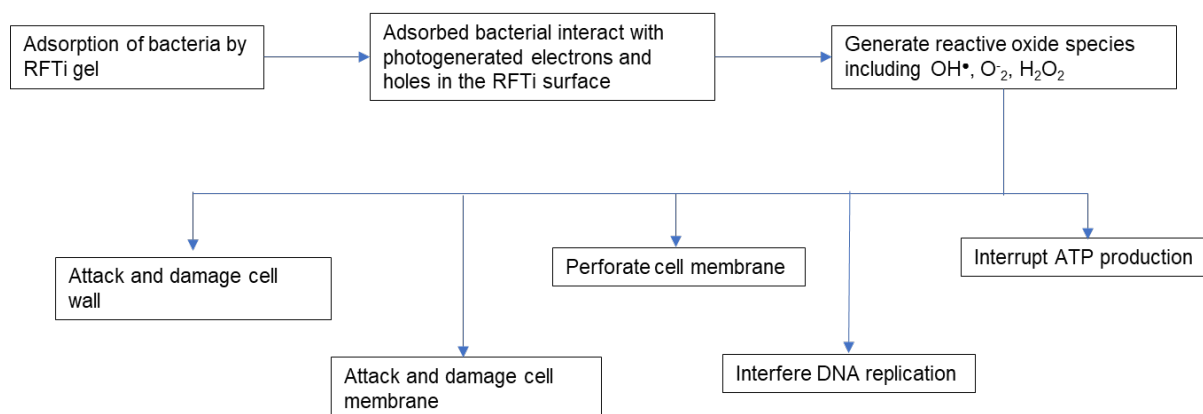


Figure 7.1 Mechanism for antimicrobial activity by synthesised gel samples.

7.2 Results and Discussion

When tested against the control culture, the antimicrobial performance of pure RF and pure TiO_2 was substantially lower than that of the results obtained for RFTi gels. Regarding the RF samples, the overall minimal antimicrobial activity observed was attributed to their poor electronic properties. As explained earlier in Section 4.4.1, the electronic structure of RF gel resembles that of a semiconductor, so the disinfection mechanism follows the photogeneration of electrons at the conduction band of RF, which reacts with O_2 to produce ROS responsible for destroying the bacteria cell membranes. Additionally, the damaged fragments of a cell may be further oxidised by holes in the valence band. However, the reason for the low productivity in this case is the rapid recombination rate of photogenerated electron and hole pairs or the shorter

lifetime of photogenerated charge carriers. This has been validated in previous studies, in which the photoluminescence spectra of RF resins showed strong photoluminescence intensity, implying recombination of photogenerated charge carriers, and the authors further reported that the photocurrent measurements of RF resins showed weak photoresponse during periodic irradiation [164, 247, 248], hence the photocatalytic activity exhibited by RF is negligible. In addition, the antimicrobial performance of TiO_2 was even lower than that of pure RF, as the experiments were carried out under visible-light irradiation, which is insufficient to overcome the energy band gap of the electronic structure of Ti; hence, it is unable to generate ROS for cell destruction. Likewise, the adsorption capabilities of pure TiO_2 are poor compared to mesoporous RF carbon gel spheres, as discussed under surface area analysis (Section 4.2).

For RFTi samples, the percentage viability of bacteria decreased compared to both pure RF and TiO_2 , as shown in Figure 7.2 and Figure 7.3, respectively. This improvement in antimicrobial performance is attributed to the synergy of RF and TiO_2 , which increases the adsorption capabilities, enhances charge separation, and modifies the electronic structure for visible-light photocatalysis. This phenomenon is similar to that previously reported for carbon/ TiO_2 composites used for bacterial reduction [129, 163, 249-251]. In all RFTi samples, the inactivation of total and faecal coliforms and *E. coli* showed dose-dependent trends, suggesting a constant increase in antimicrobial performance with increasing disinfectant dosage. This phenomenon is attributed to an increase in the number of available sites for bacterial adsorption and the production of higher amounts of ROS for cell destruction. The physicochemical properties of the RFTi samples discussed in the previous chapters are linked to their antimicrobial performance. The toxicity of the synthesised samples is mainly influenced by their structure and property relationships, which include the surface area and adsorption capability, nature of the surface and active sites, chemical composition, and electronic structure. The improvement in the antimicrobial performance trend resembles that of the dye degradation performance. The overall antimicrobial activity improved significantly for the RFTi10 gel (Figure 7.4), which was further improved by ~30% for the mid-range samples. Figure 7.5 and Figure 7.6 show RFTi30 and RFTi40, respectively.

With a further increase in TiO_2 content, the antimicrobial performance began to deteriorate; for example, the antimicrobial efficiency decreased by ~50% for RFTi70 (Figure 7.7). This is ascribed to the poor absorption of visible light, low surface area, smaller number of active sites, and ineffective separation of charge carriers due to the low carbon content. In addition, the role of enhanced dispersion of the TiO_2 photocatalyst is crucial, since a higher amount of TiO_2 tends to aggregate, reducing the charge transfer efficiency and increasing the recombination rate. The tendency of TiO_2 nanoparticles to aggregate in the RF matrix can be ascribed to the high surface energy of TiO_2 nanoparticles and their difference in chemical nature compared to the RF gel matrix.

Hence, evaluating how well the TiO_2 nanoparticles disperse and distribute in the RF gel matrix is essential, as it can influence the physicochemical properties that determine the antibacterial performance of RFTi gels. As suggested by the FESEM micrographs (Section 4.1), a low amount of TiO_2 exhibited better nanoparticle dispersion and homogenous distribution, thereby providing a large surface area for enhanced microbial interaction. Various studies have validated this notion by demonstrating that well-dispersed photocatalysts in a composite exhibit superior antimicrobial activity compared to heterogeneously distributed aggregates or agglomerates in the matrix [178, 252, 253]. Hence, samples with large amount of TiO_2 in this study exhibited inefficient antimicrobial activity under visible light irradiation.

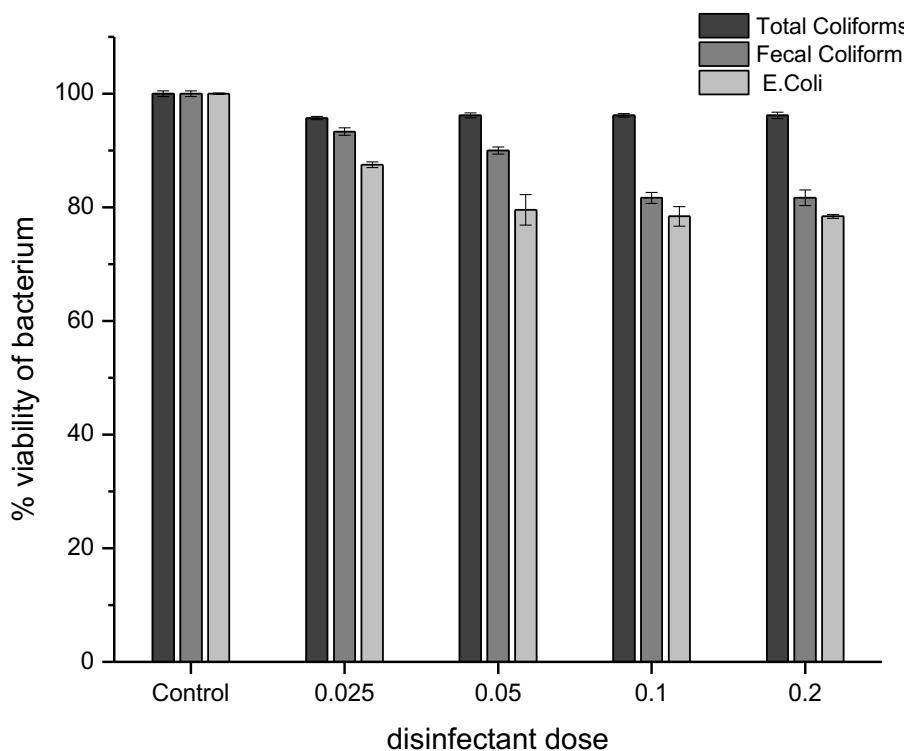


Figure 7.2 Dose-dependent percentage viability of bacteria by pure RF.

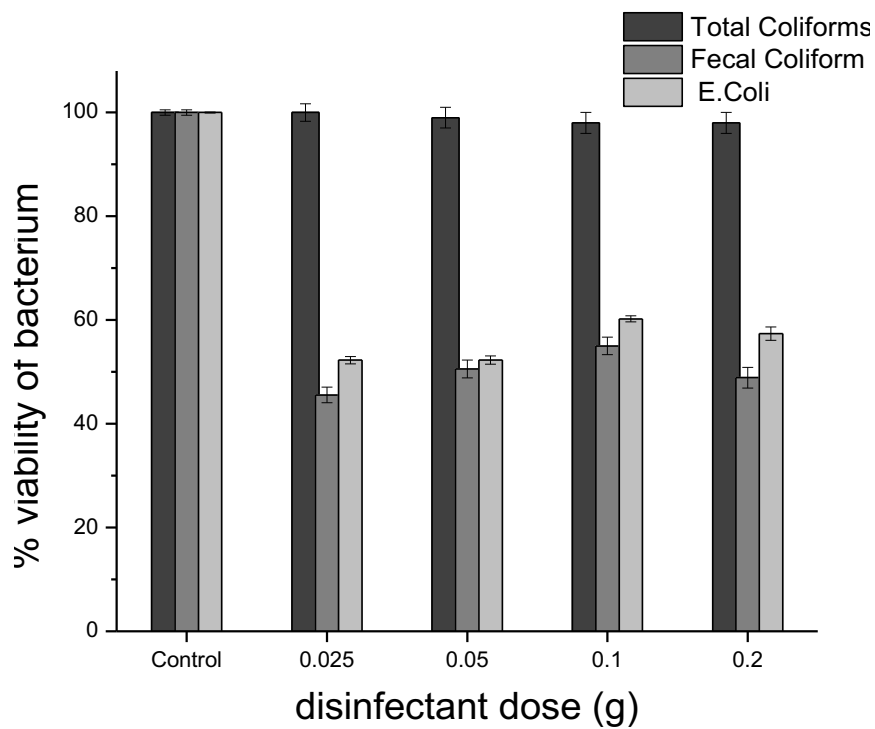


Figure 7.3 Dose-dependent percentage viability of bacteria by pure TiO₂.

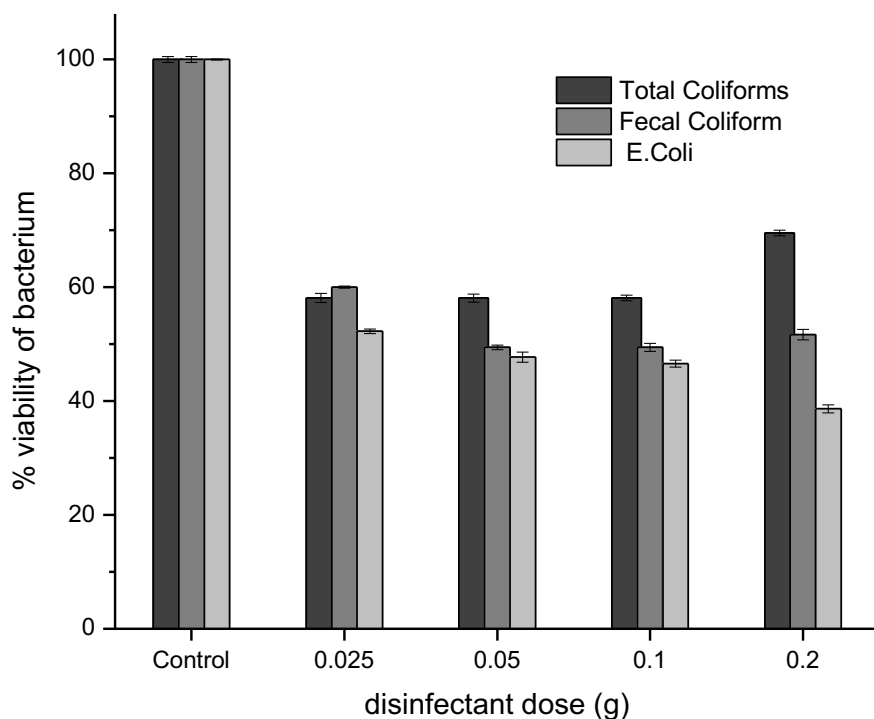


Figure 7.4 Dose-dependent percentage viability of bacteria by RFTi10.

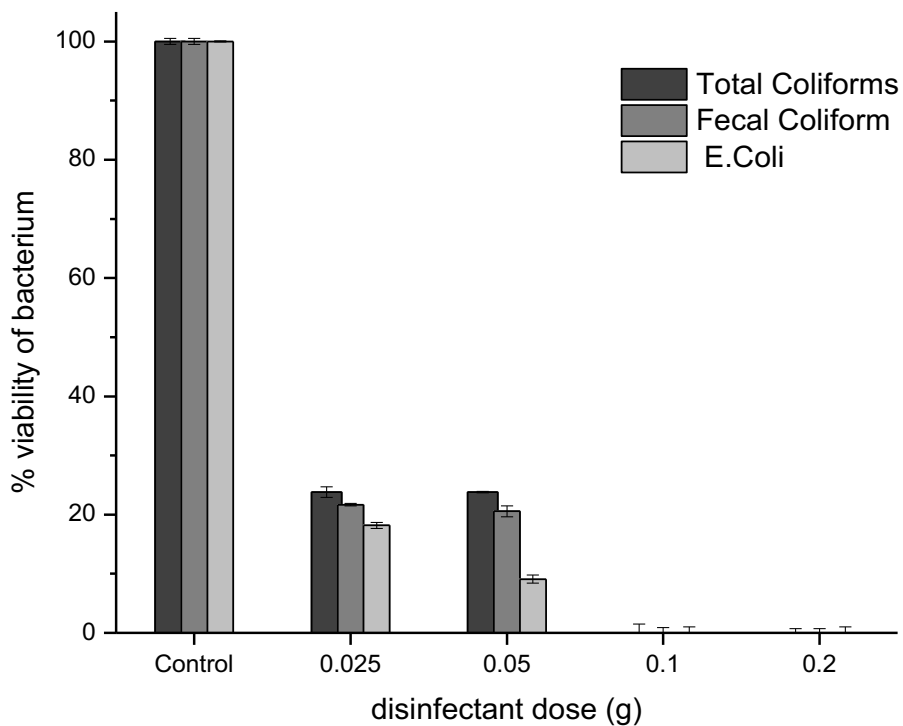


Figure 7.5 Dose-dependent percentage viability of bacteria by RFTi30.

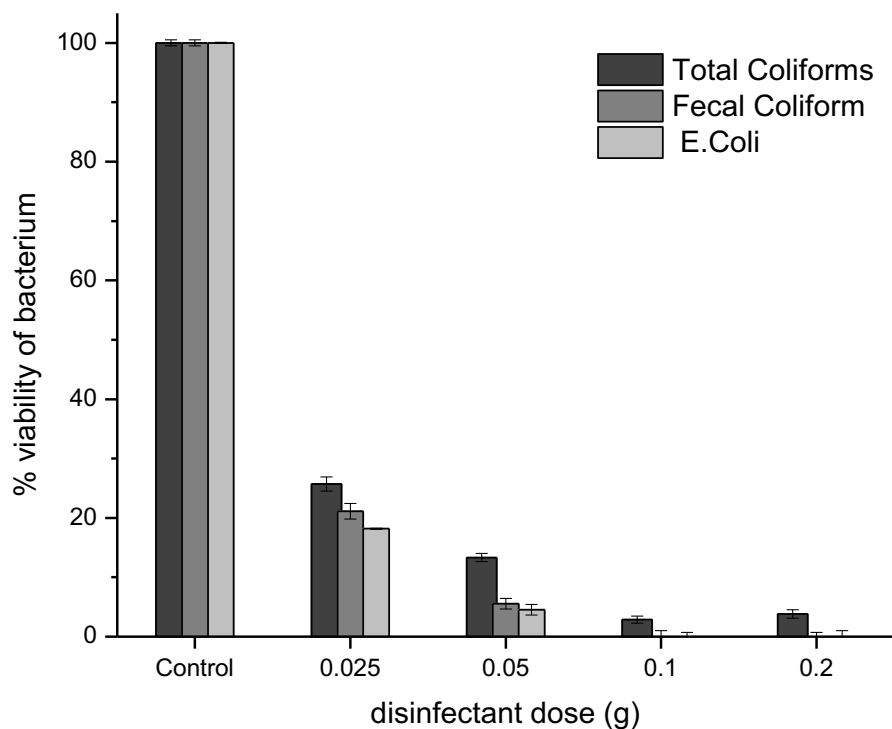


Figure 7.6 Dose-dependent percentage viability of bacteria by RFTi40.

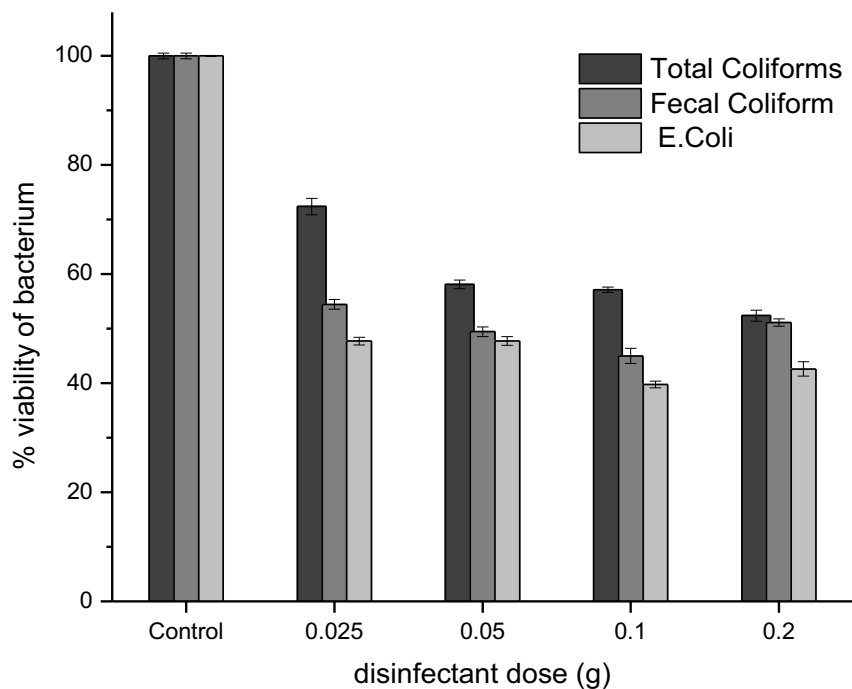


Figure 7.7 Dose-dependent percentage viability of bacteria by RFTi70.

7.3 Summary

The antimicrobial performance of RFTi was studied by conducting tests using the membrane filtration method to detect indicator microorganisms in total and faecal coliform bacteria and *E. coli* after treating contaminated water with the synthesised samples. The results were consistent with the adsorption and photodegradation performance demonstrated against the reduction of MB dye, as described in Chapters 5 and 6. In summary, excellent results were obtained for samples RFTi30 and RFTi40, owing to their optimal textural and optical properties, thereby providing a large surface for maximum adsorption and low bandgap for photoactivation of the material under visible light and generation of sufficient ROS for complete eradication of bacteria, thus providing an overall optimal synergistic adsorption-photodegradation performance. In terms of sample dose, the antimicrobial for all samples was determined at 0.1 g dosage, remaining constant with a further increase in dosage.

Chapter 8: Conclusions

The work presented in this thesis includes an experimental approach to synthesise a photoactive adsorbent, with the aim of utilising the synergistic effects of carbon and a photocatalyst to optimise the performance of these materials for use in various applications. The carbon derived from the polycondensation of resorcinol and formaldehyde (RF) gels in this study possesses high surface areas and highly porous 3D networks and has the potential to serve as hosts for metal oxides. In this work, photocatalytic titania (TiO_2) was integrated into these RF gels, providing a high surface area for adsorption and modifying the electronic structure of TiO_2 for visible-light-activated photocatalysis. Hence, these integrated materials can be used in various environmental applications, particularly for water remediation.

As adsorption-photodegradation performance is based on the relationship between structure and properties, experimental investigations were conducted to explore the effect of the ratio of carbon to TiO_2 on the synergistic effect between the two phases and their ultimate performance for the absorption-photocatalytic degradation of pollutants. The integrated gels were named RFTiX, where X represents the percentage of deposited TiO_2 . The subsequent results were discussed with respect to morphological, textural, chemical, thermal, and optical properties. Regarding adsorption applications, the performance was probed in terms of pH, gel dosage, initial pollutant concentration, contact time, and temperature, providing insight into the optimal experimental conditions for enhanced adsorption. Finally, the photodegradation performance of the RFTi gels was tested experimentally against the reduction of methylene blue dye and microorganisms by exposing the adsorbed system to visible light irradiation.

An established sol-gel method was used to obtain pure RF gels that were modified to deposit TiO_2 during the polycondensation of resorcinol and formaldehyde. The drying procedure was performed by aging the integrated mixture at 85°C , solvent exchange in acetone, and vacuum drying at 110°C to obtain the final RFTi gels. The theoretically calculated amounts of TiO_2 deposited were verified by thermogravimetric analysis, whereby combustion of the organic phase left the residual amount (at 800°C) as the TiO_2 loading, which was consistent with the theoretically calculated amounts,

confirming the estimation of wt% TiO_2 in the final RFTi gels. Enhanced photoactivity depends on a chemically bonded charge transfer complex; the sol-gel methodology employed allowed chemically linked Ti-O-C or Ti-C bonds to form via the addition of TiO_2 sol during the polymerisation of the RF gel. The chemical bonds between both phases were confirmed by the distinct peaks observed in the Fourier Transform infrared spectra. These peaks decreased with increasing amounts of TiO_2 and diminished completely for RFTi90 owing to the agglomerated excess TiO_2 . The homogenous distribution of TiO_2 plays a crucial role in the adsorption and photodegradation performance; hence, the distribution was studied using energy dispersive X-ray analysis and micrographs obtained through field emission electron scanning microscopy. The micrographs confirm the development of the carbon phase in spherical forms, which is typical for unmodified RF gels. For samples containing low amounts of TiO_2 (up to 30 wt %), the micrographs show uniform microclusters of interconnected microspheres with some surface roughness and heterogeneity. The addition of TiO_2 beyond 30 wt% resulted in a change in microstructure with indistinct spheres, as higher concentrations of TiO_2 resulted in agglomeration, masking the RF gel spheres, as also confirmed by clusters of TiO_2 observed within the micrographs. Consequently, the surface area values tended to decrease with increasing TiO_2 owing to the blockage of pores, which also resulted from agglomeration. The hysteresis loop observed in the nitrogen sorption isotherms validates the mesoporous structure of all synthesised RFTi gels, although the shape of the hysteresis loop differed; thus, the types of pores interpreted varied depending on the specific ratio used. Hysteresis within the RFTi samples synthesised with a low amount of TiO_2 (up to 30 wt%) suggests the presence of open-ended mesopores, whereas RFTi with higher amounts of TiO_2 resulted in complex disordered pore systems, the pores of which were ink-bottle-shaped.

The parameters affecting adsorption were experimentally probed to establish the optimal conditions for attaining maximum adsorption efficiency. pH_{zpc} analysis revealed zero surface charge in the range 5.5 to 6.5. A basic pH was favourable for the adsorption of cationic dyes, owing to the negatively charged surface of the adsorbent at higher pH; hence, a pH of 7.2 was maintained for all experiments to determine the adsorption capacity of methylene blue dye. An optimum adsorbent dose

(0.01 g was used against 25 mL of dye solution, i.e., 0.4 g L⁻¹), and the temperature was maintained at 23°C. A comprehensive study of the effect of initial concentration on adsorption capacity, in the range of 50-200 mg L⁻¹ and contact time of 0-240 min, showed that adsorption increased with increasing initial concentration of the solution over time. The adsorption uptake trend was consistent for all samples, exhibiting a steep initial increase in dye uptake and attainment of equilibrium due to the saturation of the active sites. The adsorption uptakes were in agreement with the structure-property relationship of the synthesised RFTi gels, demonstrating an increasing adsorption capacity until 30% TiO₂ in RF. The effective formation of charge transfer complexes between RF and TiO₂ enhanced the adsorption capacity, which was attributed to the strong electrostatic and π - π interactions between the adsorbent and dye species. These interactions weakened with increasing TiO₂ content due to a corresponding change in the physicochemical properties, where decreasing amounts of aromatic groups resulted in reduced π - π interactions between the adsorbent and adsorbate.

Kinetic models, previously applied to aqueous-phase adsorption kinetics, were used to interpret the experimental adsorption data. The fittings, assessed on the basis of the correlation factor, showed that all RFTi sorbents produced in this work followed a pseudo-second-order kinetic model, with the exception of RFTi90 and TiO₂. This indicates that chemisorption occurred during adsorption, signifying a stronger bonding between the adsorbent and adsorbate. High-quality fits to the Elovich model also suggested chemical interactions between RFTi and the dye species. In contrast, the kinetic analysis of RFTi90 and TiO₂ showed better fits to a pseudo-first-order model and poor fitting to Elovich, suggestive of a physisorption phenomenon, suggesting a low adsorption affinity, as observed by low adsorption uptakes. Furthermore, to gain insight into the internal diffusion mechanisms within these systems, the intra-particle diffusion model was applied to the experimental data, which showed multilinearity of the plot, indicating a multistep adsorption process. These interpretations implied that diffusion was not the rate-limiting step, and other mechanisms were also involved.

Adsorption isotherms are an important method for understanding the interactions occurring between the adsorbent and adsorbate, indicating equilibrium adsorption behaviour, which is essential for improving the understanding of such systems and

developing the further use of sorbents. The adsorption isotherms obtained in this work were analysed according to the nonlinear forms of the Langmuir, Freundlich, and Sips isotherm models, and interpretations were made based on the best fits according to the correlation coefficient. The experimentally determined adsorption data fit the isotherm models in the following order: Sips > Langmuir > Freundlich for all the RFTi adsorbents, indicating surface heterogeneity through the distribution of active sites. The only exception was RFTi 90, where adsorption followed the order Langmuir > Sips > Freundlich, suggesting surface homogeneity and surface-active sites dominated by homogeneously distributed moieties of TiO₂. The Scatchard plots for the data verified these interpretations by demonstrating multi-linearity, representing multiple binding sites for all RFTi samples, except for the linear plot obtained for RFTi90, corroborating a homogenous surface with only one type of binding site.

The adsorption mechanism was further probed by assessing thermodynamic characteristics, such as the adsorption potential, activation energy, Gibbs free energy, enthalpy, and entropy of the adsorption system. The negative Gibbs free energy values obtained for all RFTi samples indicate that these adsorption systems are feasible and spontaneous at all temperatures, and the adsorption uptake is endothermic; hence, the chemisorption phenomenon is entropically driven.

The antimicrobial tests showed complete degradation of bacteria upon light exposure. Complete degeneration of bacterial is attributed to sufficient adsorption of pollutants and degradation by photogenerated ROS, which attack the cell wall of bacteria and disrupt their growth hence cell lysis resulted in complete destruction of contaminants.

In conclusion, this work has focused on synthesising a range of RFTi adsorbent gels and exploring the effect of synthesis ratios on the structure-property relationship, allowing an understanding of the ratio required to achieve a wide range of desired characteristics. Progress has been made towards optimising the ratios of RF and TiO₂ for ultimate adsorption-photodegradation applications. The material characterisation techniques used in this study provided insight into the unique physicochemical properties of the designed adsorbent-photocatalyst, mainly high surface areas and mesoporosity for the effective adsorption of model pollutants, as well as a tuned electronic structure that enables visible light photoactivation for the complete degradation of model pollutants. Owing to their large surface area, mesoporosity,

chemical and thermal stability, tunable electronic properties, and antimicrobial attributes, the use of RF-TiO₂ composites may be possible over a wide range of applications, including in various environmental restoration procedures. Finally, in terms of applications of integrated RFTi samples, the optimum adsorption-photodegradation performance of RFTi was demonstrated by RFTi30 and RFTi40 for > 95% degradation of MB and complete eradication of indicator bacteria. This was attributed to the synergy of RF and TiO₂, resulting in enhanced adsorption and improved photoresponse, thereby disintegrating the structure of the model pollutants. These samples have the potential to be employed for repeated applications without significant loss in their efficiency, as demonstrated in a published article for RFTi30 [141], corroborating their application efficiency for four consecutive cycles with only 5% loss. Thus, RFTi is a promising candidate for efficient removal of a wide range of pollutants, including dyes and microbes, from industrial effluents.

Chapter 9: Future Work

The integrated RFTi gels in this work were efficient, convenient, inexpensive, and were easily retrieved post-treatment therefore, the materials' efficacy may further be tested against large volumes of contaminated water with higher concentrations. Additionally, it is believed that these materials have the potential to degrade other persistent pollutants, such as pharmaceutical wastes, hence testing its efficacy against other pollutants could be of interest.

In this work, the RFTi gels were subcritically dried, the approach is cost-effective as compared to other drying methods, such as freeze drying or supercritical drying; however, a shortcoming of subcritical drying is structural collapse during vacuum drying, and the porous structure may shrink. Alternatively, gels could be supercritically dried to preserve porosity in future syntheses. Additionally, the introduction of a morphology controlling agent, may increase mesoporosity, hence, access to the anatase facets of titania, allowing much faster charge transfer processes.

An extension to the surface characterisation of RFTi materials, through pHpzc analysis in this work, could be the study of surface hydrophilicity of synthesised gels through contact angle measurements to evaluate surface wettability. Furthermore, although the primary changes in the morphology of different RFTi gels were determined by FESEM and EDX analysis by visually studying the obtained micrographs, the surface roughness may better be understood by topographical images taken from atomic force microscopy, which may be advantageous to determine the effects of surface roughness on wettability. Materials analysis through these techniques was initially part of this work however, these could not be performed due to equipment accessibility and time constraints.

Charge separation and transfer play important roles in the photocatalytic processes. In this work, one of the synergistic advantages of combining carbon and TiO₂ was to reduce the recombination of photogenerated charge carriers and promote charge transfer, anticipated owing to the successful formation of a heterojunction between RF and TiO₂. Although its validity was proven through effective photogeneration experiments, it could be beneficial to conduct photoluminescence studies in the future to investigate charge separation and recombination, whereby recombination can be

signified by photoluminescence emission peaks and weaker peaks would indicate the presence of a heterojunction, which promotes the charge transfer efficacy.

Finally, exploring RFTi gels for electrochemical storage applications could be worthwhile. Commercial supercapacitors are made of carbon, mainly due to their cost effectiveness, good resistance to corrosion and the fact that the electrode undergoes no change during the process, thus exhibiting prolonged service lifetime; however, low surface area and porosity restrict the maximum capacitance. TiO_2 , meanwhile, provides an ideal capacitive response but exhibits low conductivity. Therefore, using integrated RF and TiO_2 could provide an optimised pore structure, while the presence of titania may promote better diffusivity. Energy storage performance depends on TiO_2 content, so the results presented here may provide some groundwork for application in this area.

References

- [1] W. H. Organization, "WHO global water, sanitation and hygiene: annual report 2019," 2020.
- [2] W. H. Organization, "Global progress report on water, sanitation and hygiene in health care facilities: Fundamentals first," UNICEF, 9240017542, 2020.
- [3] E. Emmanuel, M. G. Pierre, and Y. Perrodin, "Groundwater contamination by microbiological and chemical substances released from hospital wastewater: Health risk assessment for drinking water consumers," *Environment international*, vol. 35, no. 4, pp. 718-726, 2009.
- [4] D. Guillén *et al.*, "Prioritization of chemicals in the aquatic environment based on risk assessment: analytical, modeling and regulatory perspective," *Science of the Total Environment*, vol. 440, pp. 236-252, 2012.
- [5] O. M. Rodriguez-Narvaez, J. M. Peralta-Hernandez, A. Goonetilleke, and E. R. Bandala, "Treatment technologies for emerging contaminants in water: A review," *Chemical Engineering Journal*, vol. 323, pp. 361-380, 2017.
- [6] R. Rodil, J. B. Quintana, E. Concha-Graña, P. López-Mahía, S. Muniategui-Lorenzo, and D. Prada-Rodríguez, "Emerging pollutants in sewage, surface and drinking water in Galicia (NW Spain)," *Chemosphere*, vol. 86, no. 10, pp. 1040-1049, 2012.
- [7] G. L. Aranovich and M. D. Donohue, "Adsorption isotherms for microporous adsorbents," *Carbon*, vol. 33, no. 10, pp. 1369-1375, 1995.
- [8] M. A. Al-Ghouti and D. A. Da'ana, "Guidelines for the use and interpretation of adsorption isotherm models: A review," *Journal of hazardous materials*, vol. 393, p. 122383, 2020.
- [9] J. Wang and X. Guo, "Adsorption isotherm models: Classification, physical meaning, application and solving method," *Chemosphere*, vol. 258, p. 127279, 2020.
- [10] R. Thines, N. Mubarak, S. Nizamuddin, J. Sahu, E. Abdullah, and P. Ganesan, "Application potential of carbon nanomaterials in water and wastewater treatment: a review," *Journal of the Taiwan Institute of Chemical Engineers*, vol. 72, pp. 116-133, 2017.
- [11] S. Wadhawan, A. Jain, J. Nayyar, and S. K. Mehta, "Role of nanomaterials as adsorbents in heavy metal ion removal from waste water: A review," *Journal of Water Process Engineering*, vol. 33, p. 101038, 2020.
- [12] A. K. Prajapati and M. K. Mondal, "Comprehensive kinetic and mass transfer modeling for methylene blue dye adsorption onto CuO nanoparticles loaded on nanoporous activated carbon prepared from waste coconut shell," *Journal of Molecular Liquids*, vol. 307, p. 112949, 2020.
- [13] A. K. Prajapati and M. K. Mondal, "Hazardous As (III) removal using nanoporous activated carbon of waste garlic stem as adsorbent: Kinetic and

- mass transfer mechanisms," *Korean Journal of Chemical Engineering*, vol. 36, pp. 1900-1914, 2019.
- [14] I. Slatni *et al.*, "Mesoporous silica synthesized from natural local kaolin as an effective adsorbent for removing of Acid Red 337 and its application in the treatment of real industrial textile effluent," *Environmental Science and Pollution Research*, vol. 27, pp. 38422-38433, 2020.
- [15] T. Tatarchuk, I. Mironyuk, V. Kotsyubynsky, A. Shyichuk, M. Myslin, and V. Boychuk, "Structure, morphology and adsorption properties of titania shell immobilized onto cobalt ferrite nanoparticle core," *Journal of Molecular Liquids*, vol. 297, p. 111757, 2020.
- [16] S. Lakshmi, R. Renganathan, and S. Fujita, "Study on TiO₂-mediated photocatalytic degradation of methylene blue," *Journal of Photochemistry and Photobiology A: Chemistry*, vol. 88, no. 2-3, pp. 163-167, 1995.
- [17] M. A. Borysiewicz, "ZnO as a functional material, a review," *Crystals*, vol. 9, no. 10, p. 505, 2019.
- [18] S. Liu, B. Yu, S. Wang, Y. Shen, and H. Cong, "Preparation, surface functionalization and application of Fe₃O₄ magnetic nanoparticles," *Advances in Colloid and Interface Science*, vol. 281, p. 102165, 2020.
- [19] V. K. Gupta, I. Ali, T. A. Saleh, A. Nayak, and S. Agarwal, "Chemical treatment technologies for waste-water recycling—an overview," *Rsc Advances*, vol. 2, no. 16, pp. 6380-6388, 2012.
- [20] P. Arribas, M. Khayet, M. García-Payo, and L. Gil, "Novel and emerging membranes for water treatment by hydrostatic pressure and vapor pressure gradient membrane processes," in *Advances in Membrane Technologies for Water Treatment*: Elsevier, 2015, pp. 239-285.
- [21] R. Molinari, C. Lavorato, and P. Argurio, "Recent progress of photocatalytic membrane reactors in water treatment and in synthesis of organic compounds. A review," *Catalysis Today*, vol. 281, pp. 144-164, 2017.
- [22] L. D. Nghiem and T. Fujioka, "Removal of emerging contaminants for water reuse by membrane technology," in *Emerging membrane technology for sustainable water treatment*: Elsevier Science Oxford, 2016, pp. 217-247.
- [23] M. Baghbanzadeh, D. Rana, C. Q. Lan, and T. Matsuura, "Effects of inorganic nano-additives on properties and performance of polymeric membranes in water treatment," *Separation & Purification Reviews*, vol. 45, no. 2, pp. 141-167, 2016.
- [24] A. Sperlich, D. Warschke, C. Wegmann, M. Ernst, and M. Jekel, "Treatment of membrane concentrates: phosphate removal and reduction of scaling potential," *Water Science and Technology*, vol. 61, no. 2, pp. 301-306, 2010.
- [25] S. Rodriguez-Mozaz *et al.*, "Pharmaceuticals and pesticides in reclaimed water: efficiency assessment of a microfiltration–reverse osmosis (MF–RO) pilot plant," *Journal of hazardous materials*, vol. 282, pp. 165-173, 2015.
- [26] C. Y. Teh, P. M. Budiman, K. P. Y. Shak, and T. Y. Wu, "Recent advancement of coagulation–flocculation and its application in wastewater treatment,"

- Industrial & Engineering Chemistry Research*, vol. 55, no. 16, pp. 4363-4389, 2016.
- [27] M. Antonopoulou, E. Evgenidou, D. Lambropoulou, and I. Konstantinou, "A review on advanced oxidation processes for the removal of taste and odor compounds from aqueous media," *Water research*, vol. 53, pp. 215-234, 2014.
- [28] C. Catrinescu, D. Arsene, and C. Teodosiu, "Catalytic wet hydrogen peroxide oxidation of para-chlorophenol over Al/Fe pillared clays (AlFePILCs) prepared from different host clays," *Applied Catalysis B: Environmental*, vol. 101, no. 3-4, pp. 451-460, 2011.
- [29] M. Klavarioti, D. Mantzavinos, and D. Kassinos, "Removal of residual pharmaceuticals from aqueous systems by advanced oxidation processes," *Environment international*, vol. 35, no. 2, pp. 402-417, 2009.
- [30] A. Enesca, M. Baneto, D. Perniu, L. Isac, C. Bogatu, and A. Duta, "Solar-activated tandem thin films based on CuInS₂, TiO₂ and SnO₂ in optimized wastewater treatment processes," *Applied Catalysis B: Environmental*, vol. 186, pp. 69-76, 2016.
- [31] I. Gehrke, A. Geiser, and A. Somborn-Schulz, "Innovations in nanotechnology for water treatment," *Nanotechnology, science and applications*, pp. 1-17, 2015.
- [32] J. Völker, M. Stapf, U. Miede, and M. Wagner, "Systematic review of toxicity removal by advanced wastewater treatment technologies via ozonation and activated carbon," *Environmental Science & Technology*, vol. 53, no. 13, pp. 7215-7233, 2019.
- [33] R. Hofmann *et al.*, "Comparing methods to remove emerging contaminants and disinfection by-product precursors at pilot scale," *Journal of Water Supply: Research and Technology—AQUA*, vol. 60, no. 7, pp. 425-433, 2011.
- [34] T. A. Rebello, R. P. Roque, R. F. Gonçalves, J. L. Calmon, and L. M. Queiroz, "Life cycle assessment of urban wastewater treatment plants: a critical analysis and guideline proposal," *Water Science and Technology*, vol. 83, no. 3, pp. 501-514, 2021.
- [35] M. Thommes *et al.*, "Physisorption of gases, with special reference to the evaluation of surface area and pore size distribution (IUPAC Technical Report)," *Pure and applied chemistry*, vol. 87, no. 9-10, pp. 1051-1069, 2015.
- [36] R. C. Bansal and M. Goyal, *Activated carbon adsorption*. CRC press, 2005.
- [37] A. Dąbrowski, "Adsorption—from theory to practice," *Advances in colloid and interface science*, vol. 93, no. 1-3, pp. 135-224, 2001.
- [38] Y. Xia *et al.*, "Enhanced adsorption of Pb (II) onto modified hydrochar: Modeling and mechanism analysis," *Bioresource technology*, vol. 288, p. 121593, 2019.
- [39] G. Crini, E. Lichtfouse, L. D. Wilson, and N. Morin-Crini, "Adsorption-oriented processes using conventional and non-conventional adsorbents for wastewater treatment," in *Green adsorbents for pollutant removal*: Springer, 2018, pp. 23-71.

- [40] J. Wang and X. Guo, "Adsorption kinetic models: Physical meanings, applications, and solving methods," *Journal of Hazardous materials*, vol. 390, p. 122156, 2020.
- [41] C. S. Gulipalli, B. Prasad, and K. L. Wasewar, "Batch study, equilibrium and kinetics of adsorption of selenium using rice husk ash (RHA)," *Journal of Engineering Science and Technology*, vol. 6, no. 5, pp. 586-605, 2011.
- [42] K. Y. Foo and B. H. Hameed, "Insights into the modeling of adsorption isotherm systems," *Chemical engineering journal*, vol. 156, no. 1, pp. 2-10, 2010.
- [43] C. Aharoni and F. Tompkins, "Kinetics of adsorption and desorption and the Elovich equation," in *Advances in catalysis*, vol. 21: Elsevier, 1970, pp. 1-49.
- [44] P. Saha and S. Chowdhury, "Insight into adsorption thermodynamics," *Thermodynamics*, vol. 16, pp. 349-364, 2011.
- [45] J. Wang and S. Zhuang, "Removal of various pollutants from water and wastewater by modified chitosan adsorbents," *Critical Reviews in Environmental Science and Technology*, vol. 47, no. 23, pp. 2331-2386, 2017.
- [46] T. Kaur, A. Sraw, R. Wanchoo, and A. P. Toor, "Solar assisted degradation of carbendazim in water using clay beads immobilized with TiO₂ & Fe doped TiO₂," *Solar Energy*, vol. 162, pp. 45-56, 2018.
- [47] E. Errais, J. Duplay, and F. Darragi, "Textile dye removal by natural clay—case study of Fouchana Tunisian clay," *Environmental Technology*, vol. 31, no. 4, pp. 373-380, 2010.
- [48] S. Afroze and T. K. Sen, "A review on heavy metal ions and dye adsorption from water by agricultural solid waste adsorbents," *Water, Air, & Soil Pollution*, vol. 229, pp. 1-50, 2018.
- [49] R. Rashid, I. Shafiq, P. Akhter, M. J. Iqbal, and M. Hussain, "A state-of-the-art review on wastewater treatment techniques: the effectiveness of adsorption method," *Environmental Science and Pollution Research*, vol. 28, no. 8, pp. 9050-9066, 2021.
- [50] M. M. Alam *et al.*, "The potentiality of rice husk-derived activated carbon: From synthesis to application," *Processes*, vol. 8, no. 2, p. 203, 2020.
- [51] N. A. Khan, S. Ibrahim, and P. Subramaniam, "Elimination of heavy metals from wastewater using agricultural wastes as adsorbents," *Malaysian journal of science*, vol. 23, no. 1, pp. 43-51, 2004.
- [52] A. Bhatnagar and M. Sillanpää, "Utilization of agro-industrial and municipal waste materials as potential adsorbents for water treatment—a review," *Chemical engineering journal*, vol. 157, no. 2-3, pp. 277-296, 2010.
- [53] D. Mohan *et al.*, "Sorption of arsenic, cadmium, and lead by chars produced from fast pyrolysis of wood and bark during bio-oil production," *Journal of colloid and interface science*, vol. 310, no. 1, pp. 57-73, 2007.
- [54] V. K. Gupta, C. K. Jain, I. Ali, M. Sharma, and V. Saini, "Removal of cadmium and nickel from wastewater using bagasse fly ash—a sugar industry waste," *Water research*, vol. 37, no. 16, pp. 4038-4044, 2003.

-
- [55] Y. C. Sharma, V. Srivastava, V. Singh, S. Kaul, and C. Weng, "Nano-adsorbents for the removal of metallic pollutants from water and wastewater," *Environmental technology*, vol. 30, no. 6, pp. 583-609, 2009.
- [56] J.-L. Gong *et al.*, "Removal of cationic dyes from aqueous solution using magnetic multi-wall carbon nanotube nanocomposite as adsorbent," *Journal of hazardous materials*, vol. 164, no. 2-3, pp. 1517-1522, 2009.
- [57] Y. Yao, F. Xu, M. Chen, Z. Xu, and Z. Zhu, "Adsorption behavior of methylene blue on carbon nanotubes," *Bioresource technology*, vol. 101, no. 9, pp. 3040-3046, 2010.
- [58] S. Iijima and T. Ichihashi, "Single-shell carbon nanotubes of 1-nm diameter," *nature*, vol. 363, no. 6430, pp. 603-605, 1993.
- [59] S. S. Fiyadh *et al.*, "Review on heavy metal adsorption processes by carbon nanotubes," *Journal of Cleaner Production*, vol. 230, pp. 783-793, 2019.
- [60] L. Önnby, V. Pakade, B. Mattiasson, and H. Kirsebom, "Polymer composite adsorbents using particles of molecularly imprinted polymers or aluminium oxide nanoparticles for treatment of arsenic contaminated waters," *Water research*, vol. 46, no. 13, pp. 4111-4120, 2012.
- [61] P. Cruz, J. Santos, F. Magalhaes, and A. Mendes, "Cyclic adsorption separation processes: analysis strategy and optimization procedure," *Chemical Engineering Science*, vol. 58, no. 14, pp. 3143-3158, 2003.
- [62] J. Schneider, D. Bahnemann, J. Ye, G. L. Puma, and D. D. Dionysiou, *Photocatalysis: fundamentals and perspectives*. Royal Society of Chemistry, 2016.
- [63] K. Nakata and A. Fujishima, "TiO₂ photocatalysis: Design and applications," *Journal of photochemistry and photobiology C: Photochemistry Reviews*, vol. 13, no. 3, pp. 169-189, 2012.
- [64] G. R. Bamwenda and H. Arakawa, "The visible light induced photocatalytic activity of tungsten trioxide powders," *Applied Catalysis A: General*, vol. 210, no. 1-2, pp. 181-191, 2001.
- [65] K. M. Lee, C. W. Lai, K. S. Ngai, and J. C. Juan, "Recent developments of zinc oxide based photocatalyst in water treatment technology: a review," *Water research*, vol. 88, pp. 428-448, 2016.
- [66] S. Ristig, N. Cibura, and J. Strunk, "Manganese oxides in heterogeneous (photo) catalysis: Possibilities and challenges," *Green*, vol. 5, no. 1-6, pp. 23-41, 2015.
- [67] D. Solís-Casados, E. Viguera-Santiago, S. Hernández-López, and M. Camacho-López, "Characterization and photocatalytic performance of tin oxide," *Industrial & Engineering Chemistry Research*, vol. 48, no. 3, pp. 1249-1252, 2009.
- [68] M. Gerawork, "Photodegradation of methyl orange dye by using Zinc Oxide–Copper Oxide nanocomposite," *Optik*, vol. 216, p. 164864, 2020.

- [69] A. J. Attia, S. H. Kadhim, and F. H. Hussein, "Photocatalytic degradation of textile dyeing wastewater using titanium dioxide and zinc oxide," *E-Journal of Chemistry*, vol. 5, no. 2, pp. 219-223, 2008.
- [70] H. Li, G. Ba, Z. Liang, Q. Deng, and W. Hou, "Construction of direct all-solid-state Z-scheme pn copper indium disulfide/tungsten oxide heterojunction photocatalysts: Function of interfacial electric field," *Journal of colloid and interface science*, vol. 555, pp. 72-81, 2019.
- [71] M. Rani, U. Shanker, and J. Yadav, "Degradation of Pesticides Residue by Engineered Nanomaterials," in *Sustainable Agriculture Reviews 48: Pesticide Occurrence, Analysis and Remediation Vol. 2 Analysis*: Springer, 2020, pp. 259-310.
- [72] M. S. S. Danish *et al.*, "Photocatalytic applications of metal oxides for sustainable environmental remediation," *Metals*, vol. 11, no. 1, p. 80, 2021.
- [73] A. Fujishima and K. Honda, "Electrochemical photolysis of water at a semiconductor electrode," *nature*, vol. 238, no. 5358, pp. 37-38, 1972.
- [74] A. Kudo and Y. Miseki, "Heterogeneous photocatalyst materials for water splitting," *Chemical Society Reviews*, vol. 38, no. 1, pp. 253-278, 2009.
- [75] R. Abe, "Recent progress on photocatalytic and photoelectrochemical water splitting under visible light irradiation," *Journal of Photochemistry and Photobiology C: Photochemistry Reviews*, vol. 11, no. 4, pp. 179-209, 2010.
- [76] T. Inoue, A. Fujishima, S. Konishi, and K. Honda, "Photoelectrocatalytic reduction of carbon dioxide in aqueous suspensions of semiconductor powders," *Nature*, vol. 277, no. 5698, pp. 637-638, 1979.
- [77] L. Caballero, K. Whitehead, N. Allen, and J. Verran, "Inactivation of *Escherichia coli* on immobilized TiO₂ using fluorescent light," *Journal of Photochemistry and Photobiology A: Chemistry*, vol. 202, no. 2-3, pp. 92-98, 2009.
- [78] T. Matsunaga, R. Tomoda, T. Nakajima, and H. Wake, "Photoelectrochemical sterilization of microbial cells by semiconductor powders," *FEMS Microbiology letters*, vol. 29, no. 1-2, pp. 211-214, 1985.
- [79] K. Ikeda, H. Sakai, R. Baba, K. Hashimoto, and A. Fujishima, "Photocatalytic reactions involving radical chain reactions using microelectrodes," *The Journal of Physical Chemistry B*, vol. 101, no. 14, pp. 2617-2620, 1997.
- [80] R. Qian *et al.*, "Charge carrier trapping, recombination and transfer during TiO₂ photocatalysis: An overview," *Catalysis Today*, vol. 335, pp. 78-90, 2019.
- [81] M. N. Chong, B. Jin, C. W. Chow, and C. Saint, "Recent developments in photocatalytic water treatment technology: a review," *Water research*, vol. 44, no. 10, pp. 2997-3027, 2010.
- [82] S. N. Habisreutinger, L. Schmidt-Mende, and J. K. Stolarczyk, "Photocatalytic reduction of CO₂ on TiO₂ and other semiconductors," *Angewandte Chemie International Edition*, vol. 52, no. 29, pp. 7372-7408, 2013.

- [83] D. Hariharan *et al.*, "Green hydrothermal synthesis of gold and palladium doped titanium dioxide nanoparticles for multifunctional performance," *Journal of Materials Science: Materials in Electronics*, vol. 30, pp. 12812-12819, 2019.
- [84] V. Iliev, D. Tomova, L. Bilyarska, A. Eliyas, and L. Petrov, "Photocatalytic properties of TiO₂ modified with platinum and silver nanoparticles in the degradation of oxalic acid in aqueous solution," *Applied Catalysis B: Environmental*, vol. 63, no. 3-4, pp. 266-271, 2006.
- [85] H. Dong *et al.*, "An overview on limitations of TiO₂-based particles for photocatalytic degradation of organic pollutants and the corresponding countermeasures," *Water research*, vol. 79, pp. 128-146, 2015.
- [86] K. Imamura, T. Yoshikawa, K. Nakanishi, K. Hashimoto, and H. Kominami, "Photocatalytic reduction of benzonitrile to benzylamine in aqueous suspensions of palladium-loaded titanium (IV) oxide," *Chemical Communications*, vol. 49, no. 93, pp. 10911-10913, 2013.
- [87] S. Porcu *et al.*, "Highly efficient visible light phenyl modified carbon nitride/TiO₂ photocatalyst for environmental applications," *Applied Surface Science*, vol. 531, p. 147394, 2020.
- [88] K. Wilke and H. Breuer, "The influence of transition metal doping on the physical and photocatalytic properties of titania," *Journal of Photochemistry and Photobiology A: Chemistry*, vol. 121, no. 1, pp. 49-53, 1999.
- [89] M. Behnajady, N. Modirshahla, M. Shokri, and B. Rad, "Enhancement of photocatalytic activity of TiO₂ nanoparticles by silver doping: photodeposition versus liquid impregnation methods," *Global NEST Journal*, vol. 10, no. 1, pp. 1-7, 2008.
- [90] J. Zhang, C. Pan, P. Fang, J. Wei, and R. Xiong, "Mo⁺ C codoped TiO₂ using thermal oxidation for enhancing photocatalytic activity," *ACS applied materials & interfaces*, vol. 2, no. 4, pp. 1173-1176, 2010.
- [91] D. Chakraborty and S. S. Gupta, "Photo-catalytic decolourisation of toxic dye with N-doped Titania: A case study with Acid Blue 25," *Journal of Environmental Sciences*, vol. 25, no. 5, pp. 1034-1043, 2013.
- [92] C. Di Valentin, G. Pacchioni, and A. Selloni, "Theory of carbon doping of titanium dioxide," *Chemistry of Materials*, vol. 17, no. 26, pp. 6656-6665, 2005.
- [93] M. Janus, E. Kusiak-Nejman, and A. W. Morawski, "Determination of the photocatalytic activity of TiO₂ with high adsorption capacity," *Reaction Kinetics, Mechanisms and Catalysis*, vol. 103, no. 2, pp. 279-288, 2011.
- [94] H. Dong, C. Qu, T. Zhang, L. Zhu, and W. Ma, "Synthesis of multi-walled carbon nanotubes/TiO₂ composite and its photocatalytic activity," *Journal of nanoscience and nanotechnology*, vol. 16, no. 3, pp. 2646-2651, 2016.
- [95] A. García and J. Matos, "Photocatalytic activity of TiO₂ on activated carbon under visible light in the photodegradation of phenol," *Open Mater. Sci. J*, vol. 4, no. 2, 2010.

- [96] S. Liu, X. Chen, and X. Chen, "A TiO₂/AC composite photocatalyst with high activity and easy separation prepared by a hydrothermal method," *Journal of hazardous materials*, vol. 143, no. 1-2, pp. 257-263, 2007.
- [97] J. Matos, J. Laine, and J.-M. Herrmann, "Synergy effect in the photocatalytic degradation of phenol on a suspended mixture of titania and activated carbon," *Applied Catalysis B: Environmental*, vol. 18, no. 3-4, pp. 281-291, 1998.
- [98] O. Carp, C. L. Huisman, and A. Reller, "Photoinduced reactivity of titanium dioxide," *Progress in solid state chemistry*, vol. 32, no. 1-2, pp. 33-177, 2004.
- [99] A. Y. Shan, T. I. M. Ghazi, and S. A. Rashid, "Immobilisation of titanium dioxide onto supporting materials in heterogeneous photocatalysis: A review," *Applied Catalysis A: General*, vol. 389, no. 1-2, pp. 1-8, 2010.
- [100] R. Katal, S. Masudy-Panah, M. Tanhaei, M. H. D. A. Farahani, and H. Jiangyong, "A review on the synthesis of the various types of anatase TiO₂ facets and their applications for photocatalysis," *Chemical Engineering Journal*, vol. 384, p. 123384, 2020.
- [101] J. H. Schattka, D. G. Shchukin, J. Jia, M. Antonietti, and R. A. Caruso, "Photocatalytic activities of porous titania and titania/zirconia structures formed by using a polymer gel templating technique," *Chemistry of materials*, vol. 14, no. 12, pp. 5103-5108, 2002.
- [102] Z. He, T. Hong, J. Chen, and S. Song, "A magnetic TiO₂ photocatalyst doped with iodine for organic pollutant degradation," *Separation and purification technology*, vol. 96, pp. 50-57, 2012.
- [103] Y. Tang *et al.*, "Magnetic TiO₂-graphene composite as a high-performance and recyclable platform for efficient photocatalytic removal of herbicides from water," *Journal of Hazardous Materials*, vol. 252, pp. 115-122, 2013.
- [104] J. Singh, T. Dutta, K.-H. Kim, M. Rawat, P. Samddar, and P. Kumar, "'Green'synthesis of metals and their oxide nanoparticles: applications for environmental remediation," *Journal of nanobiotechnology*, vol. 16, no. 1, pp. 1-24, 2018.
- [105] H. Zou and Y. Lin, "Structural and surface chemical properties of sol-gel derived TiO₂-ZrO₂ oxides," *Applied Catalysis A: General*, vol. 265, no. 1, pp. 35-42, 2004.
- [106] X. Shi, Z. Zhang, K. Du, Y. Lai, J. Fang, and J. Li, "Anatase TiO₂@C composites with porous structure as an advanced anode material for Na ion batteries," *Journal of Power Sources*, vol. 330, pp. 1-6, 2016.
- [107] X. Zhang *et al.*, "Enhanced hydrogen storage properties of MgH₂ catalyzed with carbon-supported nanocrystalline TiO₂," *Journal of Power Sources*, vol. 398, pp. 183-192, 2018.
- [108] B. N. Bhadra *et al.*, "Oxidative denitrogenation with TiO₂ and porous carbon catalyst for purification of fuel: Chemical aspects," *Applied Catalysis B: Environmental*, vol. 240, pp. 215-224, 2019.

- [109] B. Bai, L. Qiu, D. Mei, Z. Jin, L. Song, and P. Du, "Firmly-supported porous fabric fiber photocatalysts: TiO₂/porous carbon fiber cloth composites and their photocatalytic activity," *Materials Research Bulletin*, vol. 148, p. 111672, 2022.
- [110] S. S. Kistler, "Coherent expanded aerogels and jellies," *Nature*, vol. 127, no. 3211, pp. 741-741, 1931.
- [111] R. Pekala, "Organic aerogels from the polycondensation of resorcinol with formaldehyde," *Journal of materials science*, vol. 24, pp. 3221-3227, 1989.
- [112] R. Pekala, "Organic aerogels from the polycondensation of resorcinol with formaldehyde," *Journal of materials science*, vol. 24, no. 9, pp. 3221-3227, 1989.
- [113] S. A. Al-Muhtaseb and J. A. Ritter, "Preparation and properties of resorcinol-formaldehyde organic and carbon gels," *Advanced materials*, vol. 15, no. 2, pp. 101-114, 2003.
- [114] E. G. Calvo, J. Á. Menéndez, and A. Arenillas, *Designing nanostructured carbon xerogels*. InTech Rijeka, Croatia, 2011.
- [115] F. Li *et al.*, "Resorcinol-formaldehyde based carbon aerogel: Preparation, structure and applications in energy storage devices," *Microporous and Mesoporous Materials*, vol. 279, pp. 293-315, 2019.
- [116] S. D. Faust and O. M. Aly, *Adsorption processes for water treatment*. Elsevier, 2013.
- [117] N. Bolong, A. Ismail, M. R. Salim, and T. Matsuura, "A review of the effects of emerging contaminants in wastewater and options for their removal," *Desalination*, vol. 239, no. 1-3, pp. 229-246, 2009.
- [118] X. Yin *et al.*, "Preparation, characterization and environmental application of the composite electrode TiO₂-NTs/SnO₂-Sb with carbon aerogels," *Journal of Chemical Technology & Biotechnology*, vol. 94, no. 10, pp. 3124-3133, 2019.
- [119] F. Zhao, Y. Shi, L. Pan, and G. Yu, "Multifunctional nanostructured conductive polymer gels: synthesis, properties, and applications," *Accounts of chemical research*, vol. 50, no. 7, pp. 1734-1743, 2017.
- [120] C. Huanan, Z. Zhenhua, S. J. L. Yeru, W. Dingcai, and L. Hong, "Influence of carbon aerogel (CA) pore structure on photodegradation of methyl orange over TiO₂/CA," *Chinese Journal of Catalysis*, vol. 32, no. 2, pp. 321-324, 2011.
- [121] Y. Jin, G. Zhao, M. Wu, Y. Lei, M. Li, and X. Jin, "In situ induced visible-light photoelectrocatalytic activity from molecular oxygen on carbon aerogel-supported TiO₂," *The Journal of Physical Chemistry C*, vol. 115, no. 20, pp. 9917-9925, 2011.
- [122] Y. Jin, M. Wu, G. Zhao, and M. Li, "Photocatalysis-enhanced electrosorption process for degradation of high-concentration dye wastewater on TiO₂/carbon aerogel," *Chemical engineering journal*, vol. 168, no. 3, pp. 1248-1255, 2011.
- [123] N. Khalid, A. Majid, M. B. Tahir, N. Niaz, and S. Khalid, "Carbonaceous-TiO₂ nanomaterials for photocatalytic degradation of pollutants: A review," *Ceramics International*, vol. 43, no. 17, pp. 14552-14571, 2017.

- [124] Z. Liang, J. Zhang, H. Liu, and J. Shi, "Enhancement of the photocatalytic activity of a TiO₂/carbon aerogel based on a hydrophilic secondary pore structure," *RSC advances*, vol. 6, no. 72, pp. 68416-68423, 2016.
- [125] Y. C. Sharma, "Optimization of parameters for adsorption of methylene blue on a low-cost activated carbon," *Journal of Chemical & Engineering Data*, vol. 55, no. 1, pp. 435-439, 2010.
- [126] G. Sposito, "On points of zero charge," *Environmental science & technology*, vol. 32, no. 19, pp. 2815-2819, 1998.
- [127] P. Yaashikaa *et al.*, "Modelling on the removal of Cr (VI) ions from aquatic system using mixed biosorbent (*Pseudomonas stutzeri* and acid treated Banyan tree bark)," *Journal of Molecular Liquids*, vol. 276, pp. 362-370, 2019.
- [128] A. L. Vega-Jiménez, A. R. Vázquez-Olmos, E. Acosta-Gío, and M. A. Álvarez-Pérez, "In vitro antimicrobial activity evaluation of metal oxide nanoparticles," *Nanoemulsions Prop. Fabr. Appl*, pp. 1-18, 2019.
- [129] S. S. Ghumro, B. Lal, and T. Pirzada, "Visible-Light-Driven Carbon-Doped TiO₂-Based Nanocatalysts for Enhanced Activity toward Microbes and Removal of Dye," *ACS omega*, vol. 7, no. 5, pp. 4333-4341, 2022.
- [130] W. Zhou, R. Apkarian, Z. L. Wang, and D. Joy, "Fundamentals of scanning electron microscopy (SEM)," *Scanning Microscopy for Nanotechnology: Techniques and Applications*, pp. 1-40, 2007.
- [131] S. L. Erlandsen, C. Frethem, and Y. Chen, "Field emission scanning electron microscopy (FESEM) entering the 21st century: nanometer resolution and molecular topography of cell structure," *Journal of Histotechnology*, vol. 23, no. 3, pp. 249-259, 2000.
- [132] S. Berg and T. Nyberg, "Fundamental understanding and modeling of reactive sputtering processes," *Thin solid films*, vol. 476, no. 2, pp. 215-230, 2005.
- [133] S. Brunauer, P. H. Emmett, and E. Teller, "Adsorption of gases in multimolecular layers," *Journal of the American chemical society*, vol. 60, no. 2, pp. 309-319, 1938.
- [134] E. P. Barrett, L. G. Joyner, and P. P. Halenda, "The determination of pore volume and area distributions in porous substances. I. Computations from nitrogen isotherms," *Journal of the American Chemical society*, vol. 73, no. 1, pp. 373-380, 1951.
- [135] K. Sing, "The use of nitrogen adsorption for the characterisation of porous materials," *Colloids and Surfaces A: Physicochemical and Engineering Aspects*, vol. 187, pp. 3-9, 2001.
- [136] P. Faria, J. Orfao, and M. Pereira, "Adsorption of anionic and cationic dyes on activated carbons with different surface chemistries," *Water research*, vol. 38, no. 8, pp. 2043-2052, 2004.
- [137] A. International, *Standard test method for compositional analysis by thermogravimetry*. ASTM international, 2003.

- [138] J. Tauc, "Optical properties and electronic structure of amorphous Ge and Si," *Materials research bulletin*, vol. 3, no. 1, pp. 37-46, 1968.
- [139] D. F. Swinehart, "The beer-lambert law," *Journal of chemical education*, vol. 39, no. 7, p. 333, 1962.
- [140] A. P. H. Association, "9222 Membrane filter technique for members of the coliform group," *Standard Methods For the Examination of Water and Wastewater*, vol. 27, 2018.
- [141] M. Daud *et al.*, "Drinking water quality status and contamination in Pakistan," *BioMed research international*, vol. 2017, 2017.
- [142] R. B. Baird, *Standard methods for the examination of water and wastewater, 23rd*. Water Environment Federation, American Public Health Association, American ..., 2017.
- [143] N. Rijal, "Bacteriological Analysis of Water," *Bacteriology*. [Online]. Available: Accessed online <https://microbeonline.com/analysis-of-water-membrane-filtration-technique/>.
- [144] A. Safri and A. J. Fletcher, "Effective carbon/TiO₂ gel for enhanced adsorption and demonstrable visible light driven photocatalytic performance," *Gels*, vol. 8, no. 4, p. 215, 2022.
- [145] A. Safri, A. J. Fletcher, R. Safri, and H. Rasheed, "Integrated Adsorption–Photodegradation of Organic Pollutants by Carbon Xerogel/Titania Composites," *Molecules*, vol. 27, no. 23, p. 8483, 2022.
- [146] O. Czakkel, K. Marthi, E. Geissler, and K. László, "Influence of drying on the morphology of resorcinol–formaldehyde-based carbon gels," *Microporous and Mesoporous Materials*, vol. 86, no. 1-3, pp. 124-133, 2005.
- [147] J. Ju *et al.*, "The stereoscopic honeycomb-like porous carbon nanofibers as a carrier of TiO₂ nanoparticles for high-performance Li-ion capacitor," *Journal of Alloys and Compounds*, vol. 791, pp. 1248-1256, 2019.
- [148] E. A. N. Simonetti, L. de Simone Cividanes, T. M. B. Campos, B. R. C. de Menezes, F. S. Brito, and G. P. Thim, "Carbon and TiO₂ synergistic effect on methylene blue adsorption," *Materials Chemistry and Physics*, vol. 177, pp. 330-338, 2016.
- [149] K. A. Cychosz and M. Thommes, "Progress in the physisorption characterization of nanoporous gas storage materials," *Engineering*, vol. 4, no. 4, pp. 559-566, 2018.
- [150] E. Martin, M. Prostredny, and A. Fletcher, "Investigating the Role of the Catalyst within Resorcinol–Formaldehyde Gel Synthesis," *Gels*, vol. 7, no. 3, p. 142, 2021.
- [151] P. I. Ravikovitch and A. V. Neimark, "Experimental confirmation of different mechanisms of evaporation from ink-bottle type pores: equilibrium, pore blocking, and cavitation," *Langmuir*, vol. 18, no. 25, pp. 9830-9837, 2002.

- [152] S. Ningaraju, A. G. Prakash, and H. Ravikumar, "Studies on free volume controlled electrical properties of PVA/NiO and PVA/TiO₂ polymer nanocomposites," *Solid State Ionics*, vol. 320, pp. 132-147, 2018.
- [153] J. Yu, T. Ma, G. Liu, and B. Cheng, "Enhanced photocatalytic activity of bimodal mesoporous titania powders by C 60 modification," *Dalton Transactions*, vol. 40, no. 25, pp. 6635-6644, 2011.
- [154] A. A. Ismail and D. W. Bahnemann, "Mesoporous titania photocatalysts: preparation, characterization and reaction mechanisms," *Journal of Materials Chemistry*, vol. 21, no. 32, pp. 11686-11707, 2011.
- [155] M. A. Khan, M. S. Akhtar, and O.-B. Yang, "Synthesis, characterization and application of sol-gel derived mesoporous TiO₂ nanoparticles for dye-sensitized solar cells," *Solar energy*, vol. 84, no. 12, pp. 2195-2201, 2010.
- [156] T. Ohno, K. Sarukawa, K. Tokieda, and M. Matsumura, "Morphology of a TiO₂ photocatalyst (Degussa, P-25) consisting of anatase and rutile crystalline phases," *Journal of Catalysis*, vol. 203, no. 1, pp. 82-86, 2001.
- [157] G. Socrates, *Infrared and Raman characteristic group frequencies: tables and charts*. John Wiley & Sons, 2004.
- [158] L. Lucarelli, V. Nadtchenko, and d. J. Kiwi, "Environmental photochemistry: quantitative adsorption and FTIR studies during the TiO₂-photocatalyzed degradation of orange II," *Langmuir*, vol. 16, no. 3, pp. 1102-1108, 2000.
- [159] A. Awadallah-F, A. M. Elkhatat, and S. A. Al-Muhtaseb, "Impact of synthesis conditions on meso-and macropore structures of resorcinol-formaldehyde xerogels," *Journal of materials science*, vol. 46, no. 24, pp. 7760-7769, 2011.
- [160] S. Shevlin and S. Woodley, "Electronic and optical properties of doped and undoped (TiO₂) n nanoparticles," *The Journal of Physical Chemistry C*, vol. 114, no. 41, pp. 17333-17343, 2010.
- [161] N. M. Mahmoodi, M. Arami, and J. Zhang, "Preparation and photocatalytic activity of immobilized composite photocatalyst (titania nanoparticle/activated carbon)," *Journal of Alloys and Compounds*, vol. 509, no. 14, pp. 4754-4764, 2011.
- [162] N. Wang, L. Zhu, Y. Huang, Y. She, Y. Yu, and H. Tang, "Drastically enhanced visible-light photocatalytic degradation of colorless aromatic pollutants over TiO₂ via a charge-transfer-complex path: A correlation between chemical structure and degradation rate of the pollutants," *Journal of Catalysis*, vol. 266, no. 2, pp. 199-206, 2009.
- [163] Y. Jiang *et al.*, "Effective TiO₂ hybrid heterostructure fabricated on nano mesoporous phenolic resol for visible-light photocatalysis," *Journal of Materials Chemistry*, vol. 22, no. 44, pp. 23642-23649, 2012.
- [164] Y. Shiraishi *et al.*, "Resorcinol-formaldehyde resins as metal-free semiconductor photocatalysts for solar-to-hydrogen peroxide energy conversion," *Nature materials*, vol. 18, no. 9, pp. 985-993, 2019.

- [165] G. Zhang and W. Choi, "A low-cost sensitizer based on a phenolic resin for charge-transfer type photocatalysts working under visible light," *Chemical Communications*, vol. 48, no. 86, pp. 10621-10623, 2012.
- [166] G. Zhang, C. Ni, L. Liu, G. Zhao, F. Fina, and J. T. Irvine, "Macro-mesoporous resorcinol-formaldehyde polymer resins as amorphous metal-free visible light photocatalysts," *Journal of Materials Chemistry A*, vol. 3, no. 30, pp. 15413-15419, 2015.
- [167] M. Abdolkarimi-Mahabadi, A. Bayat, and A. Mohammadi, "Use of UV-Vis Spectrophotometry for Characterization of Carbon Nanostructures: A Review," *Theoretical and Experimental Chemistry*, vol. 57, pp. 191-198, 2021.
- [168] D. Tahir, S. Ilyas, B. Abdullah, B. Armynah, and H. J. Kang, "Electronic properties of composite iron (II, III) oxide (Fe₃O₄) carbonaceous absorber materials by electron spectroscopy," *Journal of Electron Spectroscopy and Related Phenomena*, vol. 229, pp. 47-51, 2018.
- [169] M. A. A. Zaini, S. Yoshida, T. Mori, and S. R. Mukai, "Preliminary evaluation of resorcinol-formaldehyde carbon gels for water pollutants removal," *Acta chimica slovacca*, vol. 10, no. 1, pp. 54-60, 2017.
- [170] J. Biener *et al.*, "Advanced carbon aerogels for energy applications," *Energy & Environmental Science*, vol. 4, no. 3, pp. 656-667, 2011.
- [171] S. Higashimoto *et al.*, "Synthesis, characterization and photocatalytic properties of robust resorcinol-formaldehyde polymer fine particles," *Applied Catalysis A: General*, vol. 623, p. 118240, 2021.
- [172] S. Kim *et al.*, "Bacterial inactivation in water, DNA strand breaking, and membrane damage induced by ultraviolet-assisted titanium dioxide photocatalysis," *Water research*, vol. 47, no. 13, pp. 4403-4411, 2013.
- [173] J. Cornelisse and E. Havinga, "Photosubstitution reactions of aromatic compounds," *Chemical Reviews*, vol. 75, no. 4, pp. 353-388, 1975.
- [174] J.-i. Fujisawa, S. Matsumura, and M. Hanaya, "A single TiOC linkage induces interfacial charge-transfer transitions between TiO₂ and a π -conjugated molecule," *Chemical Physics Letters*, vol. 657, pp. 172-176, 2016.
- [175] L. Yuan, C. Zhang, J. Wang, C. Liu, and C. Yu, "Mesoporous resin nanobowls with optimized donor-acceptor conjugation for highly efficient photocatalytic hydrogen peroxide production," *Nano Research*, vol. 14, no. 9, pp. 3267-3273, 2021.
- [176] M. Rafatullah, O. Sulaiman, R. Hashim, and A. Ahmad, "Adsorption of methylene blue on low-cost adsorbents: a review," *Journal of hazardous materials*, vol. 177, no. 1-3, pp. 70-80, 2010.
- [177] X. Chen and S. S. Mao, "Titanium dioxide nanomaterials: synthesis, properties, modifications, and applications," *Chemical reviews*, vol. 107, no. 7, pp. 2891-2959, 2007.
- [178] W. Wei, C. Yu, Q. Zhao, G. Li, and Y. Wan, "Improvement of the Visible-Light Photocatalytic Performance of TiO₂ by Carbon Mesostructures," *Chemistry—A European Journal*, vol. 19, no. 2, pp. 566-577, 2013.

- [179] J.-L. Shi, H. Hao, and X. Lang, "Phenol-TiO₂ complex photocatalysis: visible light-driven selective oxidation of amines into imines in air," *Sustainable Energy & Fuels*, vol. 3, no. 2, pp. 488-498, 2019.
- [180] M. Xiong, S. Zhou, B. You, and L. Wu, "Trialkoxysilane-capped acrylic resin/titania organic-inorganic hybrid optical films prepared by the sol-gel process," *Journal of Polymer Science Part B: Polymer Physics*, vol. 43, no. 6, pp. 637-649, 2005.
- [181] C. Guan, C. L. Lü, Y. F. Liu, and B. Yang, "Preparation and characterization of high refractive index thin films of TiO₂/epoxy resin nanocomposites," *Journal of applied polymer science*, vol. 102, no. 2, pp. 1631-1636, 2006.
- [182] J. Bouajila, G. Raffin, S. Alamerçery, H. Waton, C. Sanglar, and M.-F. Grenier-Loustalot, "Phenolic resins (IV). Thermal degradation of crosslinked resins in controlled atmospheres," *Polymers and Polymer Composites*, vol. 11, no. 5, pp. 345-357, 2003.
- [183] K. A. Trick and T. E. Saliba, "Mechanisms of the pyrolysis of phenolic resin in a carbon/phenolic composite," *Carbon*, vol. 33, no. 11, pp. 1509-1515, 1995.
- [184] C. Chang and J. R. Tackett, "Characterization of phenolic resins with thermogravimetry-mass spectrometry," *Thermochimica Acta*, vol. 192, pp. 181-190, 1991.
- [185] T. L. Cottrell, *The strengths of chemical bonds*. Butterworths Scientific Publications, 1958.
- [186] C. Liu, K. Li, H. Li, S. Zhang, and Y. Zhang, "The effect of zirconium incorporation on the thermal stability and carbonized product of phenol-formaldehyde resin," *Polymer degradation and stability*, vol. 102, pp. 180-185, 2014.
- [187] K. Chrissafis and D. Bikiaris, "Can nanoparticles really enhance thermal stability of polymers? Part I: An overview on thermal decomposition of addition polymers," *Thermochimica Acta*, vol. 523, no. 1-2, pp. 1-24, 2011.
- [188] Y. Zhang, S. Shen, and Y. Liu, "The effect of titanium incorporation on the thermal stability of phenol-formaldehyde resin and its carbonization microstructure," *Polymer Degradation and Stability*, vol. 98, no. 2, pp. 514-518, 2013.
- [189] C. Leyva-Porras *et al.*, "Low-temperature synthesis and characterization of anatase TiO₂ nanoparticles by an acid assisted sol-gel method," *Journal of Alloys and Compounds*, vol. 647, pp. 627-636, 2015.
- [190] X. Nie, S. Zhuo, G. Maeng, and K. Sohlberg, "Doping of TiO₂ polymorphs for altered optical and photocatalytic properties," *International Journal of Photoenergy*, vol. 2009, 2009.
- [191] E. Santoso, R. Ediati, Y. Kusumawati, H. Bahruji, D. Sulistiono, and D. Prasetyoko, "Review on recent advances of carbon based adsorbent for methylene blue removal from waste water," *Materials Today Chemistry*, vol. 16, p. 100233, 2020.

- [192] J. A. Mattson, H. B. Mark Jr, M. D. Malbin, W. J. Weber Jr, and J. C. Crittenden, "Surface chemistry of active carbon: specific adsorption of phenols," *Journal of Colloid and Interface Science*, vol. 31, no. 1, pp. 116-130, 1969.
- [193] H. N. Tran, S.-J. You, and H.-P. Chao, "Fast and efficient adsorption of methylene green 5 on activated carbon prepared from new chemical activation method," *Journal of Environmental Management*, vol. 188, pp. 322-336, 2017.
- [194] S. Azizian, "Kinetic models of sorption: a theoretical analysis," *Journal of colloid and Interface Science*, vol. 276, no. 1, pp. 47-52, 2004.
- [195] W. Rudzinski and W. Plazinski, "Kinetics of solute adsorption at solid/solution interfaces: on the special features of the initial adsorption kinetics," *Langmuir*, vol. 24, no. 13, pp. 6738-6744, 2008.
- [196] Y.-S. Ho and G. McKay, "Kinetic models for the sorption of dye from aqueous solution by wood," *Process Safety and Environmental Protection*, vol. 76, no. 2, pp. 183-191, 1998.
- [197] E. Bailón-García, A. Elmouwahidi, M. A. Álvarez, F. Carrasco-Marín, A. F. Pérez-Cadenas, and F. J. Maldonado-Hódar, "New carbon xerogel-TiO₂ composites with high performance as visible-light photocatalysts for dye mineralization," *Applied Catalysis B: Environmental*, vol. 201, pp. 29-40, 2017.
- [198] J. A. Arcibar-Orozco, J. R. Rangel-Mendez, and T. J. Bandosz, "Reactive adsorption of SO₂ on activated carbons with deposited iron nanoparticles," *Journal of Hazardous Materials*, vol. 246, pp. 300-309, 2013.
- [199] S. Altenor, B. Carene, E. Emmanuel, J. Lambert, J.-J. Ehrhardt, and S. Gaspard, "Adsorption studies of methylene blue and phenol onto vetiver roots activated carbon prepared by chemical activation," *Journal of Hazardous Materials*, vol. 165, no. 1-3, pp. 1029-1039, 2009.
- [200] F. Dalto *et al.*, "Solar light-induced methylene blue removal over TiO₂/AC composites and photocatalytic regeneration," *Nanomaterials*, vol. 11, no. 11, p. 3016, 2021.
- [201] N. Jahan *et al.*, "A comparative study on sorption behavior of graphene oxide and reduced graphene oxide towards methylene blue," *Case Studies in Chemical and Environmental Engineering*, vol. 6, p. 100239, 2022.
- [202] A. N. Ebelegi, N. Ayawei, and D. Wankasi, "Interpretation of adsorption thermodynamics and kinetics," *Open Journal of Physical Chemistry*, vol. 10, no. 03, p. 166, 2020.
- [203] N. Ayawei, A. N. Ebelegi, and D. Wankasi, "Modelling and interpretation of adsorption isotherms," *Journal of chemistry*, vol. 2017, 2017.
- [204] Z. Uddin Ahmad, Q. Lian, M. E. Zappi, P. R. Buchireddy, and D. D. Gang, "Adsorptive removal of resorcinol onto surface modified ordered mesoporous carbon: kinetics and equilibrium study," *Environmental Progress & Sustainable Energy*, vol. 38, no. s1, pp. S386-S397, 2019.
- [205] F.-C. Wu, R.-L. Tseng, and R.-S. Juang, "Characteristics of Elovich equation used for the analysis of adsorption kinetics in dye-chitosan systems," *Chemical Engineering Journal*, vol. 150, no. 2-3, pp. 366-373, 2009.

- [206] M. Haghghi and A. Khoshfetrat, "Au-O-MWCNTs and TiO₂-O-MWCNTs as Efficient Nanocarriers for Dexamethasone: Adsorption Isotherms and Kinetic Studies," *International Journal of Chemical Engineering*, vol. 2021, 2021.
- [207] Y. Yu *et al.*, "Enhancement of photocatalytic activity of mesoporous TiO₂ by using carbon nanotubes," *Applied Catalysis A: General*, vol. 289, no. 2, pp. 186-196, 2005.
- [208] S. Sheshmani and M. Nayebi, "Modification of TiO₂ with graphene oxide and reduced graphene oxide; enhancing photocatalytic activity of TiO₂ for removal of remazol Black B," *Polymer Composites*, vol. 40, no. 1, pp. 210-216, 2019.
- [209] L. Li, X. Li, H. Duan, X. Wang, and C. Luo, "Removal of Congo Red by magnetic mesoporous titanium dioxide–graphene oxide core–shell microspheres for water purification," *Dalton Transactions*, vol. 43, no. 22, pp. 8431-8438, 2014.
- [210] X. Zheng *et al.*, "Adsorption properties of granular activated carbon-supported titanium dioxide particles for dyes and copper ions," *Scientific reports*, vol. 8, no. 1, pp. 1-9, 2018.
- [211] K. Tan and B. Hameed, "Insight into the adsorption kinetics models for the removal of contaminants from aqueous solutions," *Journal of the Taiwan Institute of Chemical Engineers*, vol. 74, pp. 25-48, 2017.
- [212] M. Riaz, R. Nadeem, M. A. Hanif, and T. M. Ansari, "Pb (II) biosorption from hazardous aqueous streams using *Gossypium hirsutum* (Cotton) waste biomass," *Journal of Hazardous Materials*, vol. 161, no. 1, pp. 88-94, 2009.
- [213] A. Safri, A. Fletcher, E. Abdel-Halim, M. Ismail, and A. Hashem, "Calligonum crinitum as a novel sorbent for sorption of Pb (II) from aqueous solutions: thermodynamics, kinetics, and isotherms," *Journal of Polymers and the Environment*, vol. 29, no. 5, pp. 1505-1515, 2021.
- [214] V. H. Uc, J. R. Alvarez-Idaboy, A. Galano, and A. Vivier-Bunge, "Theoretical explanation of nonexponential OH decay in reactions with benzene and toluene under pseudo-first-order conditions," *The Journal of Physical Chemistry A*, vol. 112, no. 33, pp. 7608-7615, 2008.
- [215] B. Hameed and M. El-Khaiary, "Batch removal of malachite green from aqueous solutions by adsorption on oil palm trunk fibre: equilibrium isotherms and kinetic studies," *Journal of hazardous materials*, vol. 154, no. 1-3, pp. 237-244, 2008.
- [216] A. B. Hamissa, F. Brouers, M. Ncibi, and M. Seffen, "Kinetic modeling study on methylene blue sorption onto *Agave americana* fibers: fractal kinetics and regeneration studies," *Separation Science and Technology*, vol. 48, no. 18, pp. 2834-2842, 2013.
- [217] Z. Gholamvand, "Development of novel integrated photocatalytic adsorbents (IPCA) for organics removal from water & wastewater," Dublin City University, 2016.
- [218] F. Dalanta and T. D. Kusworo, "Synergistic adsorption and photocatalytic properties of AC/TiO₂/CeO₂ composite for phenol and ammonia–nitrogen

- compound degradations from petroleum refinery wastewater," *Chemical Engineering Journal*, vol. 434, p. 134687, 2022.
- [219] A. S. Thajeel, "Isotherm, kinetic and thermodynamic of adsorption of heavy metal ions onto local activated carbon," *Aquatic Science and Technology*, vol. 1, no. 2, pp. 53-77, 2013.
- [220] D. C. Tsang, J. Hu, M. Y. Liu, W. Zhang, K. C. Lai, and I. M. Lo, "Activated carbon produced from waste wood pallets: adsorption of three classes of dyes," *Water, air, and soil pollution*, vol. 184, no. 1, pp. 141-155, 2007.
- [221] S. Kalam, S. A. Abu-Khamsin, M. S. Kamal, and S. Patil, "Surfactant adsorption isotherms: a review," *ACS omega*, vol. 6, no. 48, pp. 32342-32348, 2021.
- [222] T. S. Anirudhan and P. Suchithra, "Equilibrium, kinetic and thermodynamic modeling for the adsorption of heavy metals onto chemically modified hydrotalcite," 2010.
- [223] J. Zhou, Y. Wang, J. Wang, W. Qiao, D. Long, and L. Ling, "Effective removal of hexavalent chromium from aqueous solutions by adsorption on mesoporous carbon microspheres," *Journal of colloid and interface science*, vol. 462, pp. 200-207, 2016.
- [224] S. Karaca, A. Gürses, M. Açıkyıldız, and M. Ejder, "Adsorption of cationic dye from aqueous solutions by activated carbon," *Microporous and Mesoporous materials*, vol. 115, no. 3, pp. 376-382, 2008.
- [225] T. Kopac, K. Bozgeyik, and J. Yener, "Effect of pH and temperature on the adsorption of bovine serum albumin onto titanium dioxide," *Colloids and Surfaces A: Physicochemical and Engineering Aspects*, vol. 322, no. 1-3, pp. 19-28, 2008.
- [226] M. Horsfall Jnr and A. I. Spiff, "Effects of temperature on the sorption of Pb²⁺ and Cd²⁺ from aqueous solution by *Caladium bicolor* (Wild Cocoyam) biomass," *Electronic Journal of Biotechnology*, vol. 8, no. 2, pp. 43-50, 2005.
- [227] C. Goel, H. Bhunia, and P. K. Bajpai, "Resorcinol–formaldehyde based nanostructured carbons for CO₂ adsorption: kinetics, isotherm and thermodynamic studies," *RSC advances*, vol. 5, no. 113, pp. 93563-93578, 2015.
- [228] I. Ghanmi, W. Sassi, P. Oulego, S. Collado, A. Ghorbal, and M. Díaz, "Optimization and comparison study of adsorption and phosorption processes of mesoporous nano-TiO₂ during discoloration of Indigo Carmine dye," *Microporous and Mesoporous Materials*, p. 112138, 2022.
- [229] L. Abramian and H. El-Rassy, "Adsorption kinetics and thermodynamics of azo-dye Orange II onto highly porous titania aerogel," *Chemical Engineering Journal*, vol. 150, no. 2-3, pp. 403-410, 2009.
- [230] N. Somsesta, V. Srichaenchaikul, and D. Aht-Ong, "Adsorption removal of methylene blue onto activated carbon/cellulose biocomposite films: equilibrium and kinetic studies," *Materials chemistry and physics*, vol. 240, p. 122221, 2020.

- [231] K.-Y. A. Lin and C.-H. Wu, "Efficient and recyclable removal of imidazolium ionic liquids from water using resorcinol–formaldehyde polymer resin," *RSC advances*, vol. 6, no. 72, pp. 68111-68119, 2016.
- [232] E. Oyedoh A and M. Ekwonu C, "Experimental investigation on chromiumvi removal from aqueous solution using activated carbon resorcinol formaldehyde xerogels," 2016.
- [233] N. Tabrizi and M. Yavari, "Methylene blue removal by carbon nanotube-based aerogels," *Chemical Engineering Research and Design*, vol. 94, pp. 516-523, 2015.
- [234] I. Mobasherpour, E. Salahi, and M. Ebrahimi, "Thermodynamics and kinetics of adsorption of Cu (II) from aqueous solutions onto multi-walled carbon nanotubes," *Journal of Saudi Chemical Society*, vol. 18, no. 6, pp. 792-801, 2014.
- [235] S. Fan, Y. Wang, Z. Wang, J. Tang, J. Tang, and X. Li, "Removal of methylene blue from aqueous solution by sewage sludge-derived biochar: Adsorption kinetics, equilibrium, thermodynamics and mechanism," *Journal of Environmental Chemical Engineering*, vol. 5, no. 1, pp. 601-611, 2017.
- [236] L. Kong and M. Zhang, "Adsorption of Methylene Blue on Chestnut Shell-Based Activated Carbon: Calculation of Thermodynamic Parameters for Solid–Liquid Interface Adsorption," *Catalysts*, vol. 12, no. 8, p. 813, 2022.
- [237] L. L. Tan, S. P. Chai, and A. R. Mohamed, "Synthesis and applications of graphene-based TiO₂ photocatalysts," *ChemSusChem*, vol. 5, no. 10, pp. 1868-1882, 2012.
- [238] A. Houas, H. Lachheb, M. Ksibi, E. Elaloui, C. Guillard, and J.-M. Herrmann, "Photocatalytic degradation pathway of methylene blue in water," *Applied Catalysis B: Environmental*, vol. 31, no. 2, pp. 145-157, 2001.
- [239] F. Xu, "Review of analytical studies on TiO₂ nanoparticles and particle aggregation, coagulation, flocculation, sedimentation, stabilization," *Chemosphere*, vol. 212, pp. 662-677, 2018.
- [240] R. T. Noble, D. F. Moore, M. K. Leecaster, C. D. McGee, and S. B. Weisberg, "Comparison of total coliform, fecal coliform, and enterococcus bacterial indicator response for ocean recreational water quality testing," *Water research*, vol. 37, no. 7, pp. 1637-1643, 2003.
- [241] G. K. Elmund, M. J. Allen, and E. W. Rice, "Comparison of Escherichia coli, total coliform, and fecal coliform populations as indicators of wastewater treatment efficiency," *Water Environment Research*, vol. 71, no. 3, pp. 332-339, 1999.
- [242] H. Li, D. Wang, H. Fan, P. Wang, T. Jiang, and T. Xie, "Synthesis of highly efficient C-doped TiO₂ photocatalyst and its photo-generated charge-transfer properties," *Journal of Colloid and Interface Science*, vol. 354, no. 1, pp. 175-180, 2011.

- [243] X. Wang, S. Meng, X. Zhang, H. Wang, W. Zhong, and Q. Du, "Multi-type carbon doping of TiO₂ photocatalyst," *Chemical Physics Letters*, vol. 444, no. 4-6, pp. 292-296, 2007.
- [244] C. L. de Dicastillo, M. G. Correa, F. B. Martínez, C. Streitt, and M. J. Galotto, "Antimicrobial effect of titanium dioxide nanoparticles," *Antimicrobial Resistance-A One Health Perspective*, 2020.
- [245] S. Albukhaty, L. Al-Bayati, H. Al-Karagoly, and S. Al-Musawi, "Preparation and characterization of titanium dioxide nanoparticles and in vitro investigation of their cytotoxicity and antibacterial activity against *Staphylococcus aureus* and *Escherichia coli*," *Animal Biotechnology*, pp. 1-7, 2020.
- [246] S. Stankic, S. Suman, F. Haque, and J. Vidic, "Pure and multi metal oxide nanoparticles: synthesis, antibacterial and cytotoxic properties," *Journal of nanobiotechnology*, vol. 14, no. 1, pp. 1-20, 2016.
- [247] Y. Liao, J. Wang, X. Song, G. Zhang, and B. Chen, "Low-cost and large mass producible phenolic resin for water disinfection and antibacterial coating under weak visible light LED or sunlight irradiation," *Applied Catalysis B: Environmental*, vol. 292, p. 120189, 2021.
- [248] P. Liu, W. Duan, Q. Wang, and X. Li, "The damage of outer membrane of *Escherichia coli* in the presence of TiO₂ combined with UV light," *Colloids and Surfaces B: Biointerfaces*, vol. 78, no. 2, pp. 171-176, 2010.
- [249] Y. Yan *et al.*, "Carbon quantum dot-decorated TiO₂ for fast and sustainable antibacterial properties under visible-light," *Journal of Alloys and Compounds*, vol. 777, pp. 234-243, 2019.
- [250] N. Abbas *et al.*, "Inexpensive sol-gel synthesis of multiwalled carbon nanotube-TiO₂ hybrids for high performance antibacterial materials," *Materials Science and Engineering: C*, vol. 68, pp. 780-788, 2016.
- [251] A. A. Ashkarran, H. Hamidinezhad, H. Haddadi, and M. Mahmoudi, "Double-doped TiO₂ nanoparticles as an efficient visible-light-active photocatalyst and antibacterial agent under solar simulated light," *Applied Surface Science*, vol. 301, pp. 338-345, 2014.
- [252] L. M. Hamming, R. Qiao, P. B. Messersmith, and L. C. Brinson, "Effects of dispersion and interfacial modification on the macroscale properties of TiO₂ polymer-matrix nanocomposites," *Composites science and technology*, vol. 69, no. 11-12, pp. 1880-1886, 2009.
- [253] M. Šupová, G. S. Martynková, and K. Barabaszová, "Effect of nanofillers dispersion in polymer matrices: a review," *Science of advanced materials*, vol. 3, no. 1, pp. 1-25, 2011.
- [254] A. Azari, R. Nabizadeh, S. Nasser, A. H. Mahvi, and A. R. Mesdaghinia, "Comprehensive systematic review and meta-analysis of dyes adsorption by carbon-based adsorbent materials: Classification and analysis of last decade studies," *Chemosphere*, vol. 250, p. 126238, 2020.
- [255] D. C. Ko, D. H. Tsang, J. F. Porter, and G. McKay, "Applications of multipore model for the mechanism identification during the adsorption of dye on

- activated carbon and bagasse pith," *Langmuir*, vol. 19, no. 3, pp. 722-730, 2003.
- [256] A. N. Mohd Faizal and M. A. Ahmad Zaini, "Dyes adsorption properties of KOH-activated resorcinol-formaldehyde carbon gels-kinetic, isotherm and dynamic studies," *Toxin Reviews*, vol. 41, no. 1, pp. 186-197, 2022.
- [257] P. V. Samant, F. Gonçalves, M. M. A. Freitas, M. F. R. Pereira, and J. L. Figueiredo, "Surface activation of a polymer based carbon," *Carbon*, vol. 42, no. 7, pp. 1321-1325, 2004.
- [258] W. Ahlawat, N. Kataria, N. Dilbaghi, A. A. Hassan, S. Kumar, and K.-H. Kim, "Carbonaceous nanomaterials as effective and efficient platforms for removal of dyes from aqueous systems," *Environmental research*, vol. 181, p. 108904, 2020.
- [259] J. Matos, J.-M. Chovelon, T. Cordero, and C. Ferronato, "Influence of surface properties of activated carbon on photocatalytic activity of TiO₂ in 4-chlorophenol degradation," *The Open Environmental Engineering Journal*, vol. 2, no. 1, 2009.
- [260] J. Matos, A. Garcia, J.-M. Chovelon, and C. Ferronato, "Combination of adsorption on activated carbon and oxidative photocatalysis on TiO₂ for gaseous toluene remediation," *The Open Materials Science Journal*, vol. 4, no. 1, 2010.
- [261] H. Atout *et al.*, "Integration of Adsorption and Photocatalytic Degradation of Methylene Blue Using TiO₂ Supported on Granular Activated Carbon," *Arabian Journal for Science and Engineering*, vol. 42, no. 4, pp. 1475-1486, 2017.
- [262] M. Samy, M. Mossad, and H. K. El-Etriby, "Synthesized nano titanium for methylene blue removal under various operational conditions," *Desalin. Water Treat.*, vol. 165, pp. 374-381, 2019.
- [263] F. Azeez *et al.*, "The effect of surface charge on photocatalytic degradation of methylene blue dye using chargeable titania nanoparticles," *Scientific reports*, vol. 8, no. 1, pp. 1-9, 2018.
- [264] A. Hassan, A. Abdel-Mohsen, and M. M. Fouda, "Comparative study of calcium alginate, activated carbon, and their composite beads on methylene blue adsorption," *Carbohydrate polymers*, vol. 102, pp. 192-198, 2014.
- [265] P. Manoj Kumar Reddy, K. Krushnamurthy, S. Mahammadunnisa, A. Dayamani, and C. Subrahmanyam, "Preparation of activated carbons from bio-waste: effect of surface functional groups on methylene blue adsorption," *International Journal of Environmental Science and Technology*, vol. 12, no. 4, pp. 1363-1372, 2015.
- [266] S. Koner, A. Pal, and A. Adak, "Cationic surfactant adsorption on silica gel and its application for wastewater treatment," *Desalination and Water Treatment*, vol. 22, no. 1-3, pp. 1-8, 2010.

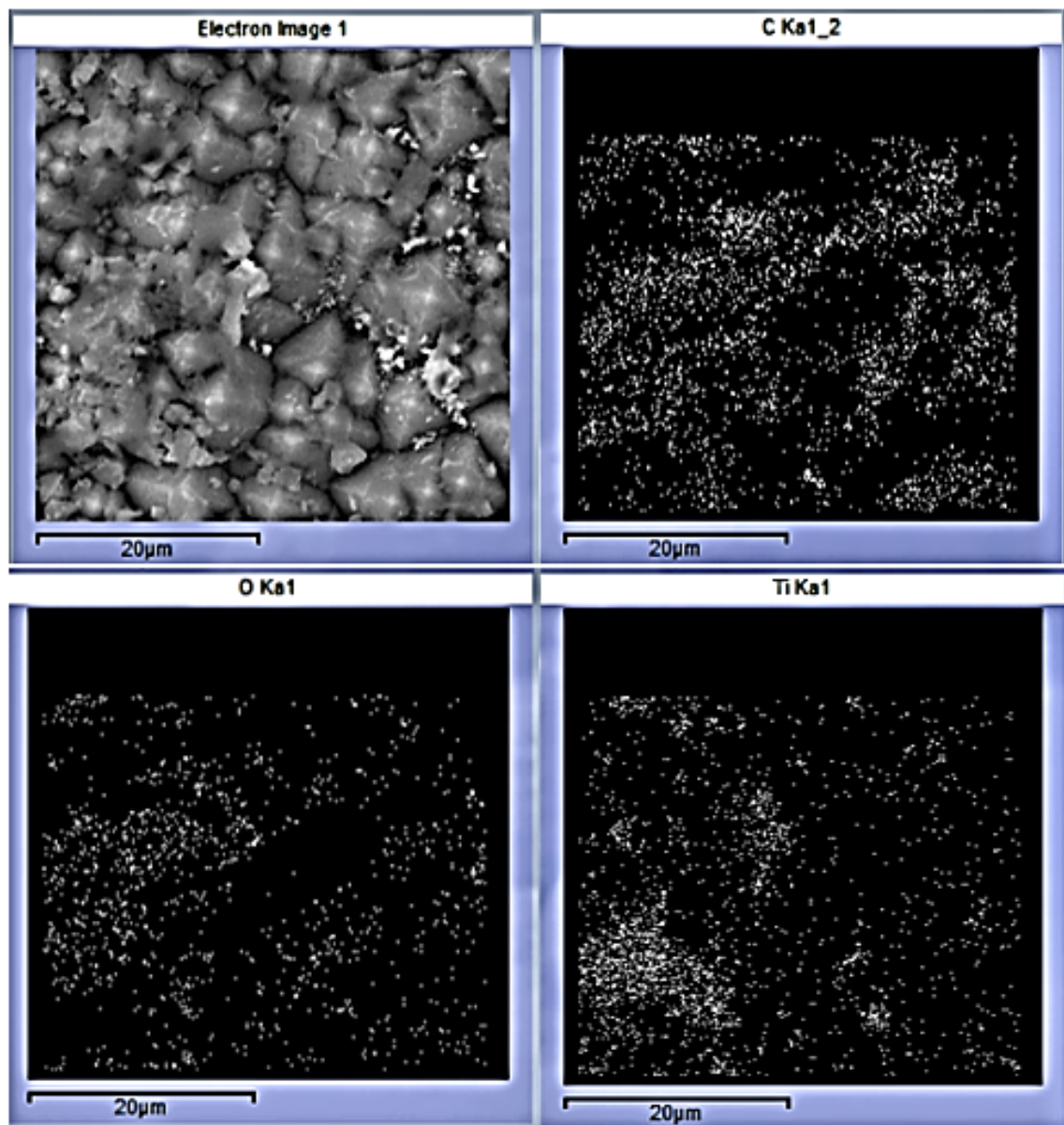
Appendices

Appendix A- Experimental

Table A1: Initial compositions of reagents.

Sample	Resorcinol (g)	Formaldehyde (g)	Catalyst (g)	Titania (g)
RF	7.7500	4.2301	0.02480	-
RFTi10	6.9810	3.8001	0.02014	1.50
RFTi20	6.2005	3.3816	0.01791	2.40
RFTi30	5.4254	2.9589	0.01572	3.60
RFTi40	4.6504	2.5362	0.01344	4.80
RFTi50	3.8756	2.1135	0.0112	6.00
RFTi60	3.10024	1.6908	0.00895	7.20
RFTi70	2.3252	1.2681	0.00670	8.40
RFTi80	1.5501	0.8454	0.00448	9.60
RFTi90	0.7750	0.4227	0.00224	10.8

Appendix B- EDX Analysis

Figure B 1 Distribution of TiO₂ nanoparticles in RF for sample RFTi40.

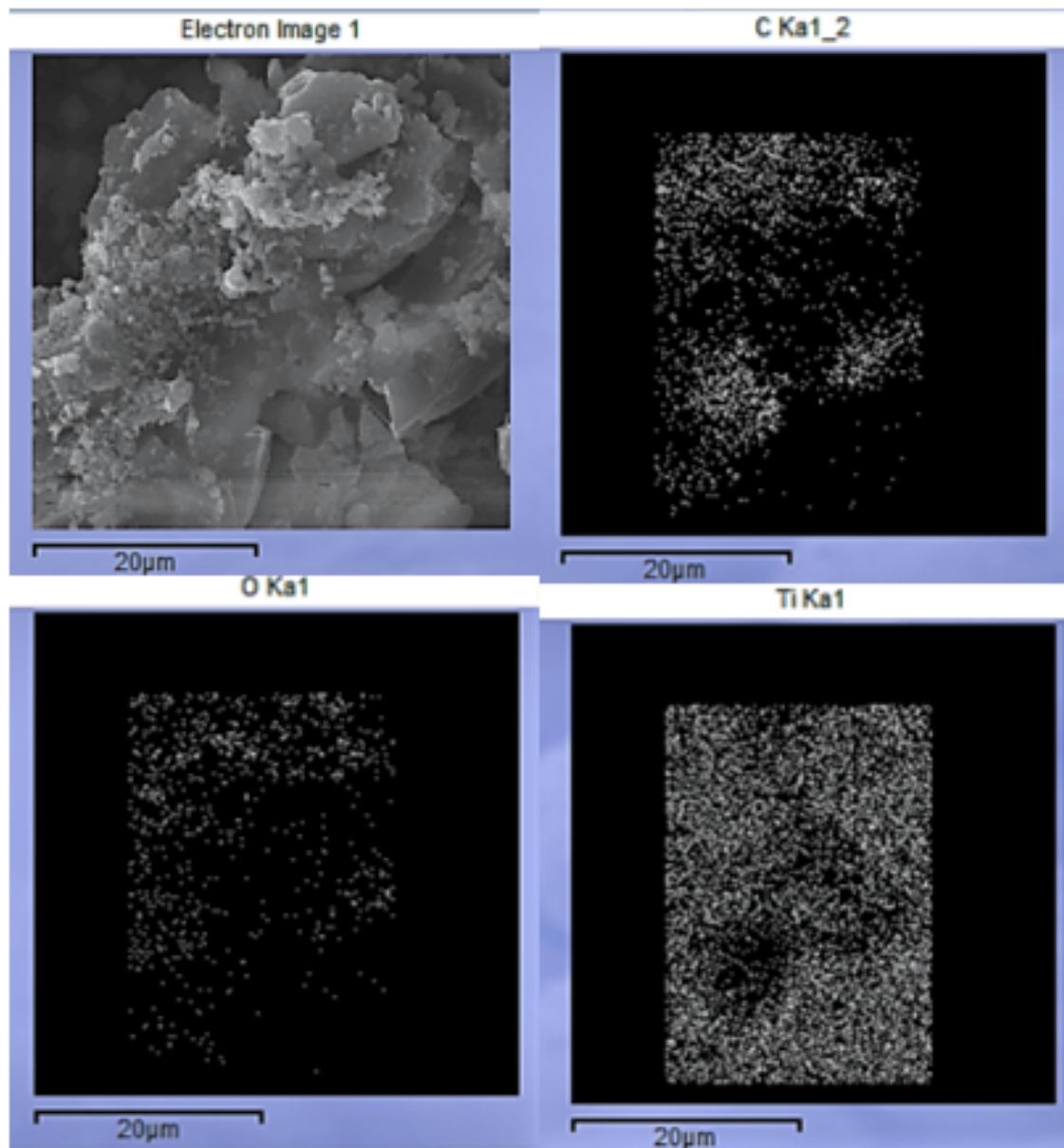


Figure B 2 Distribution of TiO₂ nanoparticles in RF for sample RFTi90.

Appendix C- X-Ray Diffraction Patterns

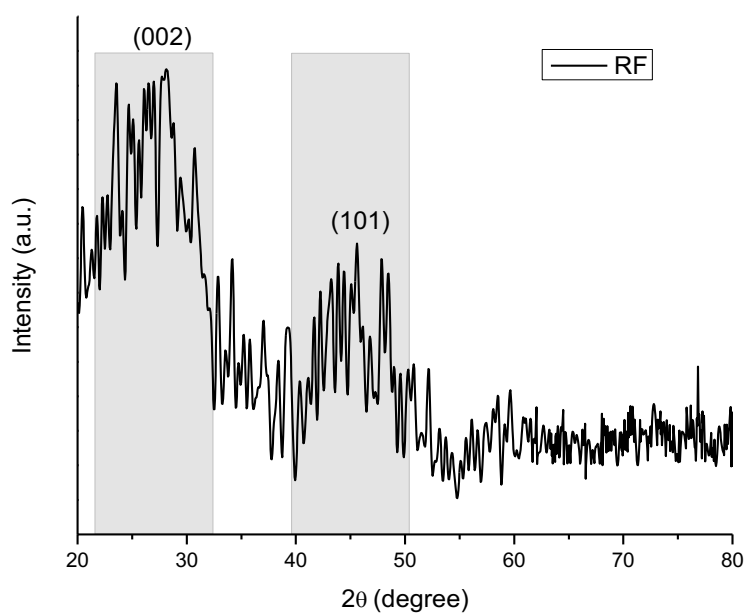


Figure C 1 X-ray diffraction (XRD) spectrum of RF sample indicating two broad diffraction peaks of RF at $2\theta=24^\circ$ and $2\theta=44^\circ$, represented by highlighted region in light grey. These findings are similar to previously described XRD pattern obtained for carbon derived from resorcinol-formaldehyde [261, 262].

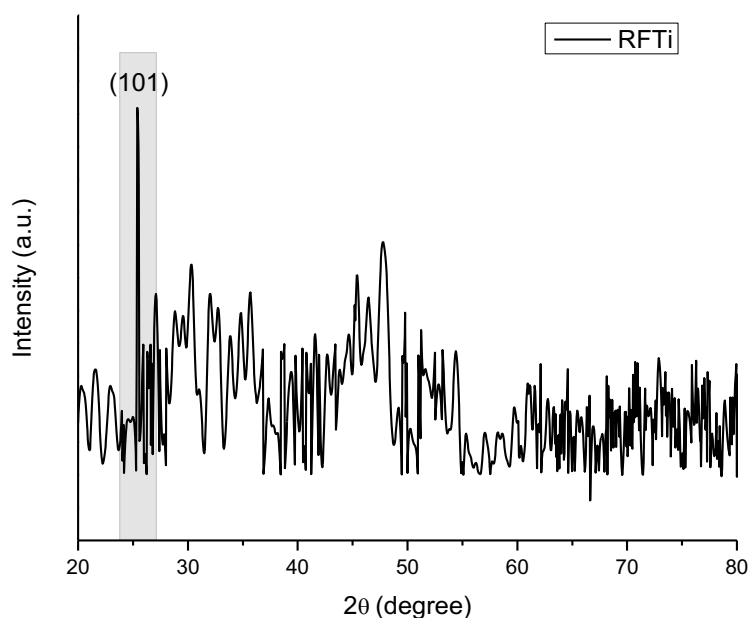


Figure C 2 X-ray diffraction spectrum RFTi indicating the presence of anatase phase at $2\theta=25^\circ$, represented by highlighted region light grey. These findings are similar to previously described carbon/titania systems [263].

Appendix D- Experimental Evaluation of Point of Zero Charge

The pH of an aqueous dye solution is an important parameter, which determines the adsorption capacity, since it controls the electrostatic interactions between the adsorbent and the adsorbate. It is important to understand the surface charge of the adsorbent, since the adsorbent may have a large surface area but could be ineffective if the surface charges repel the adsorptive, due to similar charges. Therefore, it is crucial to determine the pH conditions that exhibit the best adsorption capacity. The influence of pH on the adsorption capacity of synthesised samples was evaluated between pH 2-12 against the reduction of methylene blue (MB) cationic dye. To explain the effect of pH on the adsorption phenomenon, it is necessary to determine the pH at which the surface charge of the material is zero (pH at which contribution of cations and anions are equal) in the aqueous media or in other words the pH_{pzc} (pH point of zero charge) of the adsorbent material [254]. A general rule for pH_{pzc} is (i) pH > pH_{pzc} will favour cationic dye adsorption due to the presence of negatively charged functional groups, such as OH⁻, and (ii) pH < pH_{pzc} will favour anionic dye adsorption due to the presence of positively charge surface functional groups. The adsorbent surface charges (acidity and basicity) can be understood by the following equations, proposed by Ko *et al.* [255], the first resulting in surface acidity and the latter in surface basicity:

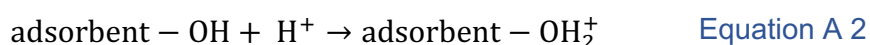
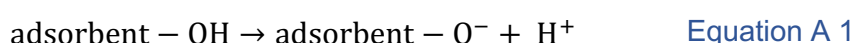


Figure D1 a-d show the percentage removal of MB as a function of initial pH. The evaluated pH_{pzc} is marked with a line of reference in the corresponding plot. The results for all synthesised samples show that MB removal increases with increasing initial pH. At low pH, in the acidic conditions (pH range 2 to 5), the removal capacity of synthesised samples increases minimally. The percentage removal drastically increases around neutral pH and there is a constant increase in removal capacity in the alkaline conditions (pH range 8 to 12); attainment of plateau was observed in some cases. The values of pH_{pzc} evaluated for all synthesised samples were in the range 5.5 to 6.5. These values were close to pH_{pzc} values previously reported for carbon

gels derived from RF [256, 257] and RFTi samples [95, 258-261]. Likewise, in this study, the pH_{pzc} values of samples with large amount of TiO₂ integrated with carbon, for example RFTi90 or pure TiO₂ (marked in Figure D1, respectively), are in agreement with values found in literature (i.e., pH 5.6 to 6.4 [262, 263]). The effect of pH on the surface charge on TiO₂ can be described by the Equations A3, where pH < pH_{pzc}, and A4, where pH > pH_{pzc}:

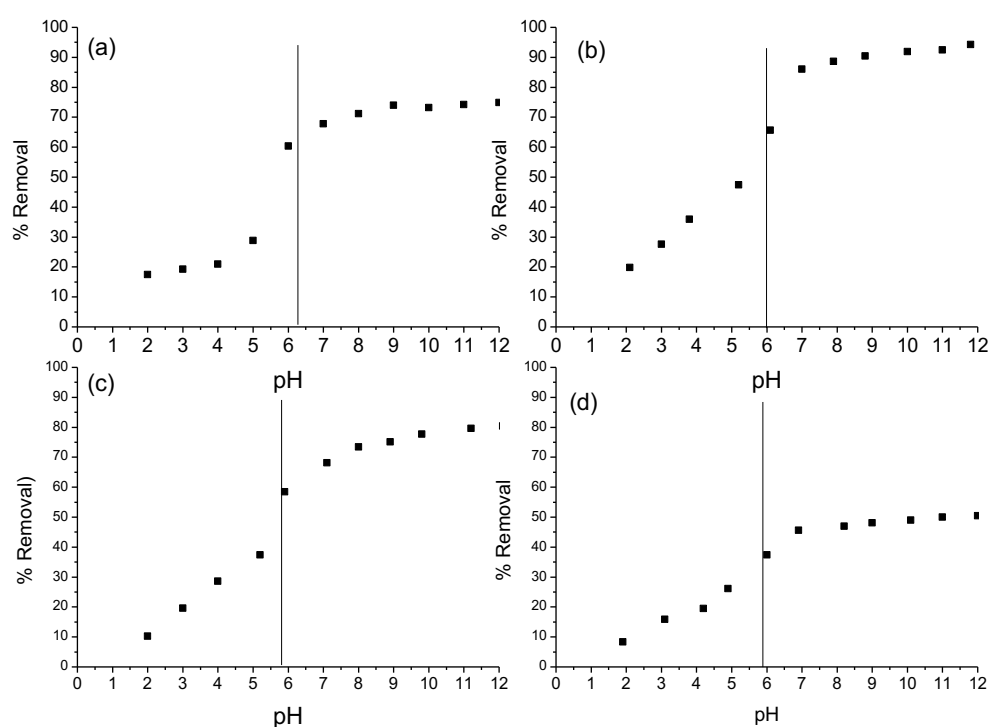
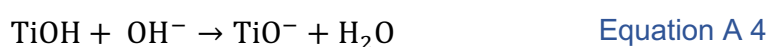


Figure D 1 Methylene blue removal percentage as a function of initial pH at T = 23°C, adsorbent dose 0.01 g, C₀ = 100 mg L⁻¹, volume 25 mL. pH_{pzc} values are marked with a straight line on each plot. (a) RFTi10, (b) RFTi30, (c) RFTi60 and (d) RFTi90

Considering the evaluated pH_{pzc} values of all synthesised samples, it is evident that, at pH values lower than the pH_{pzc}, the surface of the samples was positively charged, which hinders interactions with the cationic dye, due to the fact that the surface charges on the adsorbate and adsorbent are same. Reports within the literature show

that low adsorption of cations at low pH values has been attributed to various factors (or combination of these factors), such as: (i) repulsion between positive charges on the adsorbent and adsorbate [224], (ii) competition between H^+ adsorbent surface and adsorbate for the surface-binding sites [264], (iii) reduced interactions with cationic dye due to protonated surface functional groups of adsorbent. Hence when $pH < pHpzc$, the adsorption capacity observed was low for all samples. By contrast, when $pH > pHpzc$, the surface of the sample becomes deprotonated and electrostatic attraction is facilitated, due to the anionic nature of adsorbent, which in this case is mainly due to OH^- functional groups present on the sample surface, resulting in effective interactions with positively charged MB species. Thus, higher adsorption capacity is observed in an alkaline pH range. Similar pH influence has previously been reported for other adsorbents of amphoteric nature, where acidic sites are usually responsible for the adsorption of MB species [265, 266]. These studies demonstrate the same pH response toward the adsorption of cationic dyes i.e., the electrostatic interactions at low pH are ineffective due to the negatively charged adsorbent surface and cationic dye species. Hence, other mechanisms, such as pore filling, or $\pi-\pi$ interactions, may be beneficial for adsorption occurring at low pH. Whereas increased pH results in increased adsorption capacity due to increasing OH^- , whereby MB^+ are effectively adsorbed via electrostatic interactions.

Appendix E- Van't Hoff's Plots

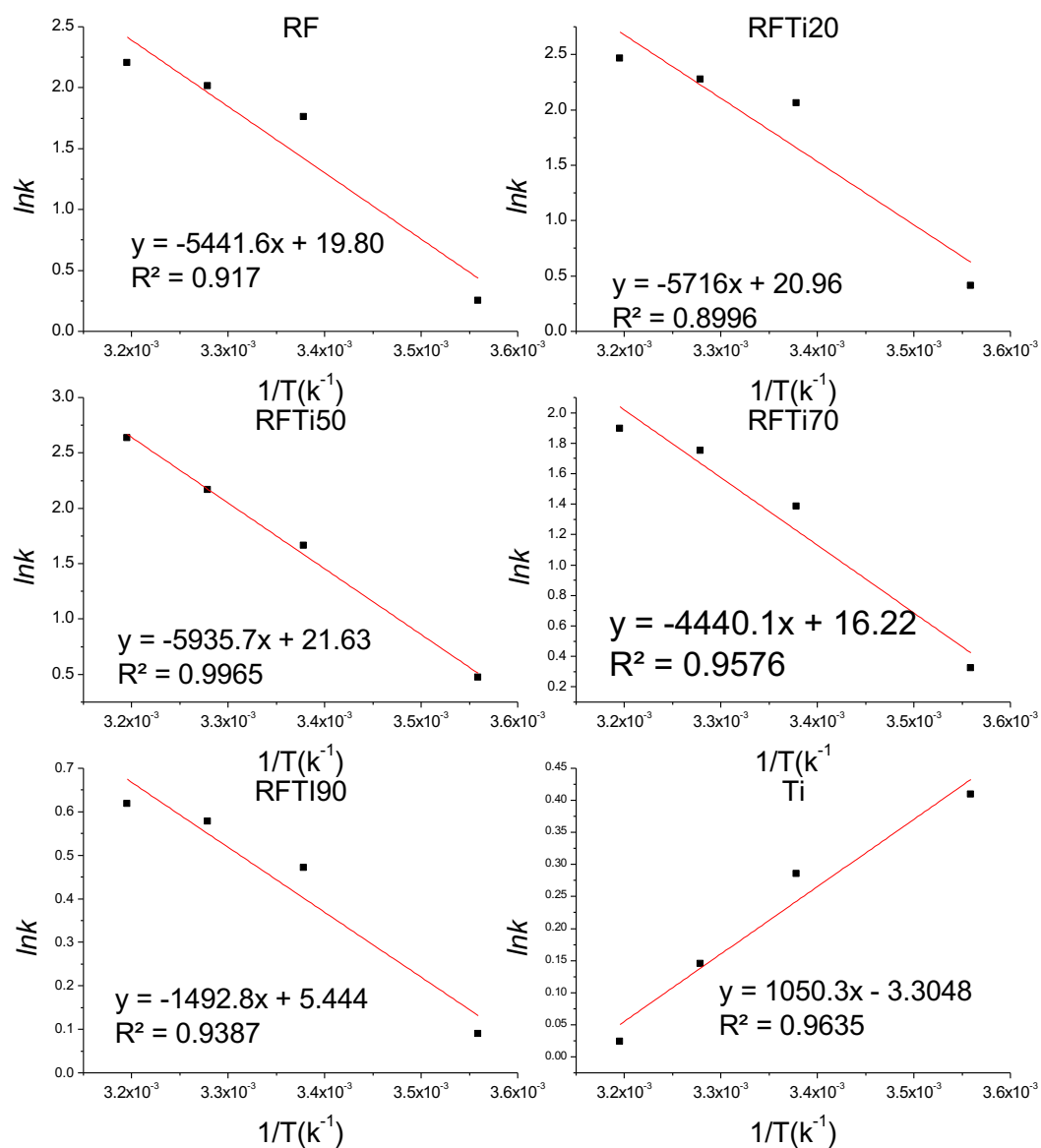


Figure E 1 Van't Hoff plots of $\ln k$ vs $1/T$ for calculation of thermodynamic parameters for RFTi20, RFTi50, RFTi70, RFTi90, RF and TiO_2 gel adsorbents at 281, 296, 305 and 313 K.

Appendix F- Antimicrobial Activity

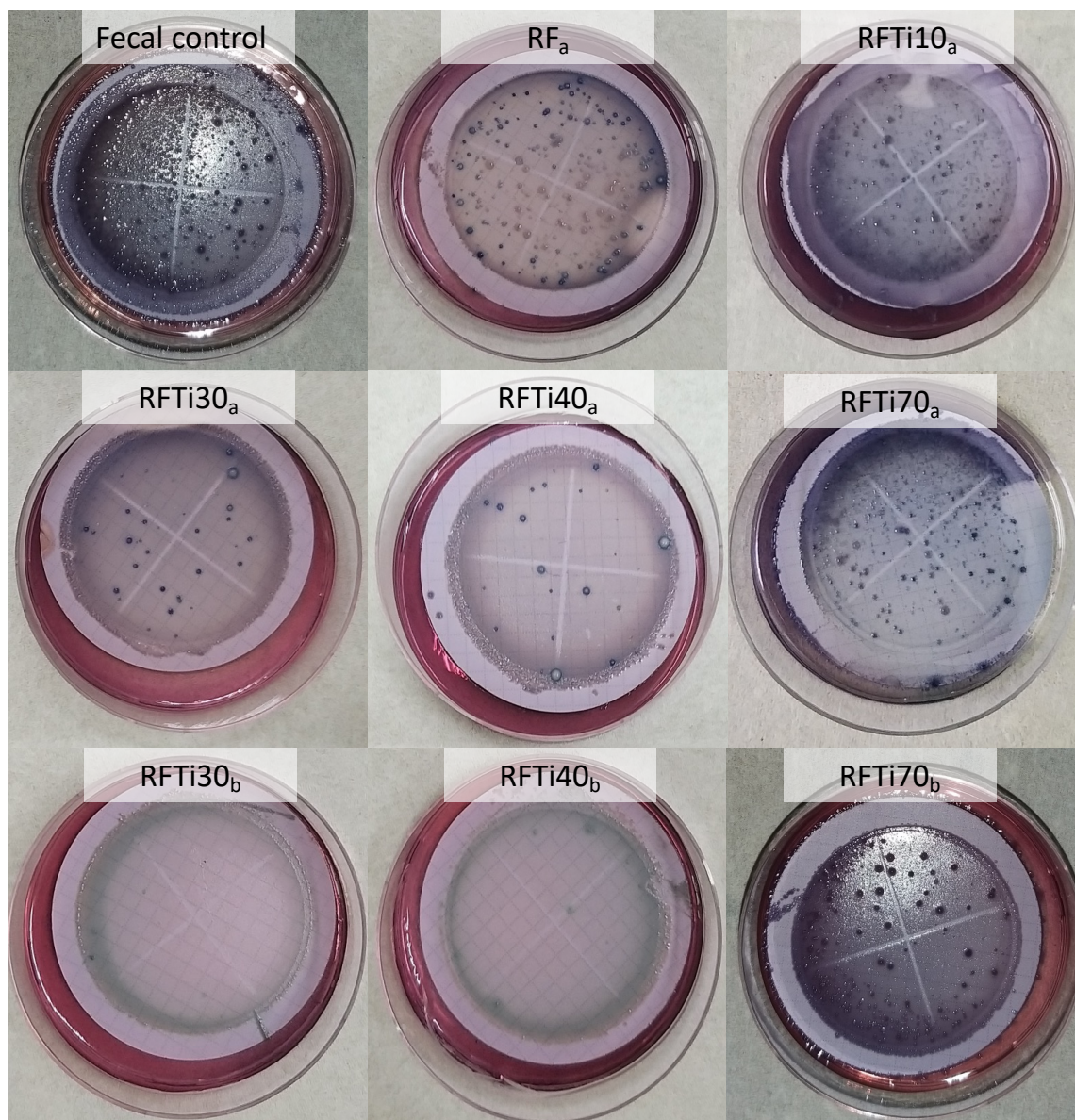


Figure F 1 Pictures of petri plates for detection of faecal coliforms following 24 h incubation at 44.5 °C before water treatment (labelled as faecal control) and after water treatment with the synthesised samples. Only blue colonies are counted, which are considered matter coliform colonies. E. coli form dark blue flat colonies, the subscript a and b denote 0.05 g and 0.1 g of sample dose, respectively.

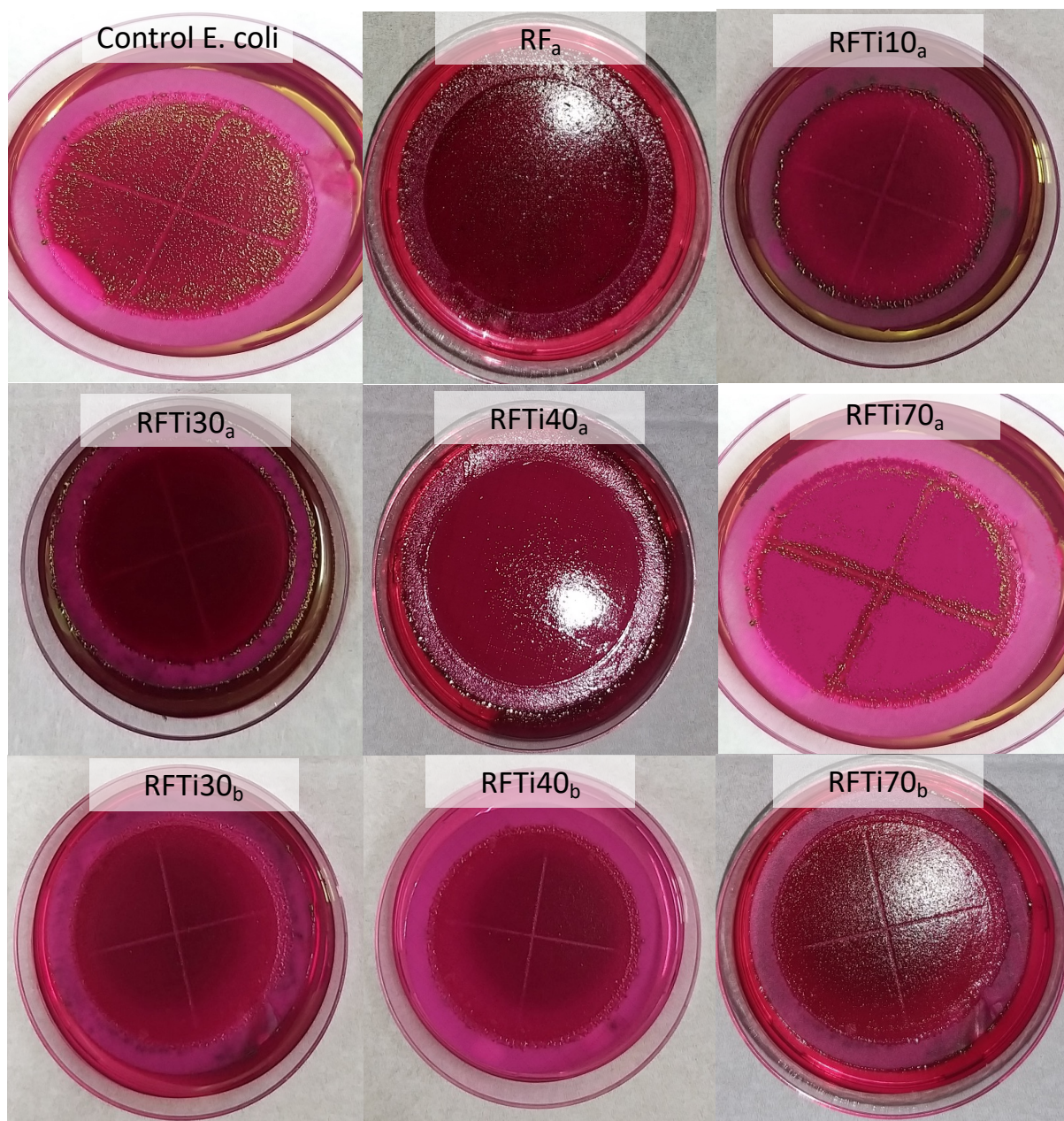


Figure F 2 Pictures of petri plates for detection of total coliforms following 24 h incubation at 35 °C before water treatment (petri plate labelled as control *E. coli*) after water treatment with synthesised samples. The colonies that were dark red, mucoidal and had dark centres were counted. Dark centres that produce metallic sheen are considered total coliform colonies. Metallic green colonies indicate the presence of *E. coli* in a water sample, the subscript a and b denote 0.05 g and 0.1 g of sample dose, respectively.

Appendix G- Error Analysis

Table G 1 List of error functions [203].

Error Function	Equation
Average Relative Error (ARE)	$ARE = \sum_{i=1}^n \left \frac{(q_e)_{\text{exp.}} - (q_e)_{\text{calc.}}}{(q_e)_{\text{exp.}}} \right $
Average Percentage Error (APE)	$APE\% = \frac{\sum_{i=1}^N [(q_e)_{\text{exp.}} - (q_e)_{\text{calc.}} / q_{\text{exp.}}]}{N} \times 100$
Sum Squares Error (ERRSQ/SSE)	$ERRSQ = \sum_{i=1}^n [(q_e)_{\text{calc.}} - (q_e)_{\text{exp.}}]^2$
Hybrid Fraction Error Function (Hybrid)	$Hybrid = \frac{100}{n-p} \sum_{i=1}^n \left[\frac{((q_e)_{\text{exp.}} - (q_e)_{\text{calc.}})^2}{(q_e)_{\text{exp.}}} \right]_i$
Marquardt's Percent Standard Deviation MPSD	$MPSD = \left(100 \sqrt{\frac{1}{n-p} \sum_{i=1}^n \left[\frac{((q_e)_{\text{exp.}} - (q_e)_{\text{calc.}})^2}{(q_e)_{\text{exp.}}} \right]} \right)^2$
Nonlinear chi-square test (χ^2)	$\chi^2 = \sum \frac{(q_{e,\text{exp}} - q_{e,\text{theoretical}})^2}{q_{e,\text{theoretical}}}$
Coefficient of determination (R^2)	$R^2 = \frac{\sum_{i=1}^n (q_{e,\text{calc}} - \overline{q_{e,\text{exp}}})^2}{\sum_{i=1}^n (q_{e,\text{calc}} - \overline{q_{e,\text{exp}}})^2 + \sum_{i=1}^n (q_{e,\text{calc}} - q_{e,\text{exp}})^2}$

Appendix H- Publications

Article

Effective Carbon/TiO₂ Gel for Enhanced Adsorption and Demonstrable Visible Light Driven Photocatalytic Performance

Anam Safri  and Ashleigh Jane Fletcher * 

Department of Chemical and Process Engineering, University of Strathclyde, Glasgow G1 1XJ, UK; anam.safri@strath.ac.uk

* Correspondence: ashleigh.fletcher@strath.ac.uk; Tel.: +44-141-5482-431

Abstract: A new strategy to synthesise carbon/TiO₂ gel by a sol–gel method is proposed. Textural, morphological, and chemical properties were characterised in detail and the synthesised material was proven to be an active adsorbent, as well as a visible light photocatalyst. Homogeneously distributed TiO₂ is mesoporous with high surface area and, hence, exhibited a high adsorption capacity. The adsorption equilibrium experimental data were well explained by the Sips isotherm model. Kinetic experiments demonstrated that experimental data fitted a pseudo second order model. The modification in electronic structure of TiO₂ resulted in a reduced bandgap compared to commercial P25. The absorption edge studied through UV-Vis shifted to the visible region, hence, daylight photocatalytic activity was efficient against degradation of MB dye, as an example pollutant molecule. The material was easily removed post treatment, demonstrating potential for employment in industrial water treatment processes.

Keywords: adsorption; carbon/TiO₂ gels; resorcinol formaldehyde RF/TiO₂ gels; photocatalysis; adsorption kinetics; methylene blue dye degradation



Citation: Safri, A.; Fletcher, A.J. Effective Carbon/TiO₂ Gel for Enhanced Adsorption and Demonstrable Visible Light Driven Photocatalytic Performance. *Gels* **2022**, *8*, 215. <https://doi.org/10.3390/gels8040215>

Academic Editors: Hiroyuki Takeno and Avinash J. Patil

Received: 11 February 2022

Accepted: 29 March 2022

Published: 1 April 2022

Publisher's Note: MDPI stays neutral with regard to jurisdictional claims in published maps and institutional affiliations.



Copyright: © 2022 by the authors. Licensee MDPI, Basel, Switzerland. This article is an open access article distributed under the terms and conditions of the Creative Commons Attribution (CC BY) license (<https://creativecommons.org/licenses/by/4.0/>).

1. Introduction

Adsorption of carbon is perhaps the most widely used water treatment technique. However, there is an ongoing effort to develop efficient adsorbents with reduced regeneration costs. Currently, the combination of carbon and titanium dioxide (TiO₂) appears to offer a promising route to obtain an adsorbent with self-regeneration properties. Additionally, the synergistic effect of both carbon and TiO₂ enhances the degradation process due to respective adsorptive and photocatalytic properties. Literature reports several studies to address the synergy of adsorption and photodegradation by experimental demonstration of various carbon/TiO₂ composite materials [1,2]. However, there is still a need to better understand the phenomenon of pollutant-adsorbent interactions in order to have a good knowledge to design an efficient water treatment process. Additionally, the improvement in design involves the type of materials and synthesis process employed to attain maximum efficiency of the system.

Previously, carbon has been combined with TiO₂ through various approaches, in different forms, such as carbon nanotubes [3–5], graphene [6–8], and activated carbon [9,10]. Lately, focus has been shifted to highly porous carbon materials as support matrix for industrial applications, due to the high surface area and tuneable porosity. Ideally, well-developed mesoporous structures with large pore volumes and uniform pore size distributions are preferred, due to enhanced accessible surface sites contributing to superior adsorption capacity of pollutants from the aqueous phase. However, the preparation process of these mesoporous carbons is costly and complicated, usually resulting in materials with moderate or low surface area. The efficiency of the material is also limited, since most TiO₂ nanoparticles incorporated in the pores of the carbon are unavailable for photocatalysis [11].

Amongst mesoporous carbon materials, carbon gels are a new type of nanocarbon with potential applications in photocatalysis [2,12,13]. Carbon gels produced by polycondensation of resorcinol (R) with formaldehyde (F) are highly porous and have flexible properties. A comprehensive review of sol–gel synthesis of RF gel reveals that the material can be easily tailored to attain desired properties, mainly tuneable porosity, and acts as a support for metals [14]. Hence, RF gels can be promising materials for water treatment applications, mainly due to their stability, owing to aromatic resorcinol rings and their overall interconnected mesoporous carbon structure. For industrial applications where a continuous process system is often required, carbon derived from RF gels can be more efficient and cost-effective than commercial adsorbents, which are in the form of granules or powders and are unsuitable for use in continuous systems.

The aim of this study is to synthesize an adsorbent with visible light driven photocatalytic activity by incorporating TiO₂ nanoparticles into RF gels. A typical synthesis route of an RF gel [15] is modulated in this study to integrate TiO₂ nanoparticles by formulating a twostep synthesis scheme. In addition to enhancement in textural properties of this newly synthesised adsorbent, improvement in photocatalytic properties is expected by (i) modification in electronic structure of TiO₂, due to the presence of RF gel as a carbon source, shifting the absorption edge to the visible light region, hence, enabling TiO₂ to activate under visible light irradiation; (ii) the carbon phase can entrap the photogenerated electron and hole pairs, which would otherwise recombine and dissipate heat energy; and (iii) the porous RF gel helps facilitate dispersion of TiO₂ and easy post treatment removal of the adsorbent/photocatalyst.

Here, we report a study of the textural and optical characteristics of the adsorbent/photocatalyst. Detailed adsorption experiments were carried out to study the effect of several parameters on adsorption capacity. Additionally, the interaction behaviour between potential pollutants and the material were investigated, using methylene blue (MB) as a model adsorptive. Equilibrium sorption data were modelled using Langmuir, Freundlich, Sips, and Toth isotherm models. Kinetic analyses were carried out by comparing the experimental data with pseudo first order and pseudo second order expressions, as well as a diffusion model to better understand the transfer behaviour of the adsorbate species. Further, photocatalytic application tests were performed under visible light irradiation and the data were modelled to study the kinetics of photocatalysis.

2. Results and Discussion

2.1. Morphology

The morphology of sample, studied using FESEM, is shown in Figure 1. Figure 1a shows a heterogenous nature of synthesised RF/TiO₂ with homogenously distributed TiO₂, as represented in Figure 1b. The overall structure shows the nanospheres connected to form a three-dimensional porous network, as represented in Figure 1c [14]. The heterogenous surface is more evident in Figure 1d where organic and inorganic phases can be differentiated. The diameter of microspheres ranged around 0.76–1.66 μm, indicating that the size of the primary particles was slightly larger than pristine RF, which generally is in the nanometre range [16]. Energy dispersive X-ray (EDX) spectra of the microspheres is shown in Figure 1e, (EDX zone shown in supplementary information, Figure S1) which evidently corresponds to the recorded spectra.

2.2. FTIR Analysis

The IR absorption bands of RF/TiO₂ overall resembled those of the pristine RF gel, as also observed through FESEM images with clear uniform spheres illustrating a porous network and the retention of the gel structure even after addition of TiO₂. Typical characteristic peaks, such as the previously reported C=C stretching, CH₂, and C-O-C of aromatic rings, methylene bridges, and methylene ether bridges [17,18], were observed. The broad peak at 3300 cm⁻¹ is characteristic of stretching vibrations associated with phenolic OH groups. Weak vibrations in the range of 2000–1700 cm⁻¹ are attributed to CH bending of

aromatic compounds. The absorption bands at 1605 and 1473 cm^{-1} correspond to aromatic ether bridges, attributed to condensation of resorcinol to form the RF gel network. A strong IR peak, expected in the range 1740–1700 cm^{-1} , associated with C=O stretching of aldehyde, was not observed, which confirms that the sol–gel reaction was complete. In comparison to a spectrum of pristine RF, a few additional peaks were observed that verify the chemical linkages between RF and TiO_2 , as marked in Figure 2. It has been established that the oxygenated surface groups of carbon materials support the attachment of TiO_2 . [19]. Here, crosslinking of TiO_2 with RF, via the hydroxyl groups, can be observed through the peaks in the vicinity of 1400 cm^{-1} , attributed to OH groups of RF, which appeared weak in the spectrum of RF/ TiO_2 , signifying the reaction of OH and TiO_2 . Meanwhile, new signals observed at 1200 and 1084 cm^{-1} suggest formation of Ti-O-C functionalities. Similar crosslinking has previously been reported in TiO_2 /phenol resol hybrid structures, where chemical interactions between TiO_2 and phenol resol form Ti-O-C complexes. This hetero-junction is responsive to visible light due to formation of a charge complex between the interface of TiO_2 and mesoporous phenol resol producing new electronic interactions [20]. Hence, it can be concluded that the interactions between RF and TiO_2 are chemical in nature. Additional signals below 1000 cm^{-1} , such as bands at 963 and 880 cm^{-1} , are associated with titanium ethoxide functional groups. Additionally, the broad band observed in the range of 600 cm^{-1} corresponds to the vibration of Ti-O-Ti bonds [21].

2.3. Surface Area Analysis

A nitrogen sorption isotherm was measured to determine the specific surface area and pore volume of RF/ TiO_2 . Figure 3 shows N_2 sorption isotherm and pore size distribution (inset Figure 3). As can be seen, the isotherm of RF/ TiO_2 is of Type IV classification [22] with a sharp capillary condensation at $P/P_0 = 0.4\text{--}0.9$ and a well-defined hysteresis loop of Type H1, associated with open ended pores whilst suggesting a mesoporous structure [16]. Pore filling occurs at low relative pressure and the calculated mesoporosity in the structure was ~94%. The S_{BET} , corresponding pore size and total pore volume of as prepared RF/ TiO_2 is 439 $\text{m}^2 \text{g}^{-1}$, 9.4 nm and 0.71 $\text{cm}^3 \text{g}^{-1}$, respectively. The S_{BET} value of pristine RF gel obtained in this study is 588 $\text{m}^2 \text{g}^{-1}$. The reason in reduced S_{BET} value for RF/ TiO_2 is attributed to blockage of pores of RF gel matrix with inclusion of TiO_2 nanoparticles. Meanwhile, in comparison with pristine TiO_2 , the S_{BET} value is significantly higher for the synthesised RF/ TiO_2 . Additionally, noteworthy S_{BET} value for pristine TiO_2 (i.e., 111 $\text{m}^2 \text{g}^{-1}$) is obtained in this study, contrary to commercial P25 with S_{BET} value of 57 $\text{m}^2 \text{g}^{-1}$.

2.4. Effect of pH

The influence of MB sorption was studied by varying the solution pH from 2–12 (25 mL, 100 mg L^{-1} , 0.01 g of adsorbent). The adsorption capacities at different pH values are shown in Figure 4. The efficiency of uptake increases from 47.24 to 65.96 mg g^{-1} when the pH increases from 2–5. Thereafter, a sharp increase in adsorption capacity is observed at $\text{pH} \geq 6$. The variation in adsorption behaviour of MB on RF/ TiO_2 can be explained by considering the structure of MB and evaluated point of zero charge (pzc). The pHpzc value for RF/ TiO_2 is determined to be 7.2 (Figure S2).

RF/ TiO_2 can be amphoteric having both positively and negatively charged surface sites in aqueous solution due to the varying amount and nature of surface oxygen [23]. At pH lower than the pHpzc , the surface of RF/ TiO_2 is positively charged, which repels the cationic dye (MB), and resultant interactions are hindered in acidic media due to electrostatic repulsion between the competing H^+ ions on the surface of adsorbent and MB dye molecules. As the pH increases, the surface of RF/ TiO_2 becomes deprotonated and the adsorption sites available for interaction with cationic species increase, therefore, increased adsorption capacity is observed. This suggests that the electrostatic forces of attraction between MB and the surface of RF/ TiO_2 increases due to increased ion density and positive

charges on the surface. Further, the OH groups on the surface of RF/TiO₂ can also attract MB dye molecules under higher pH conditions.

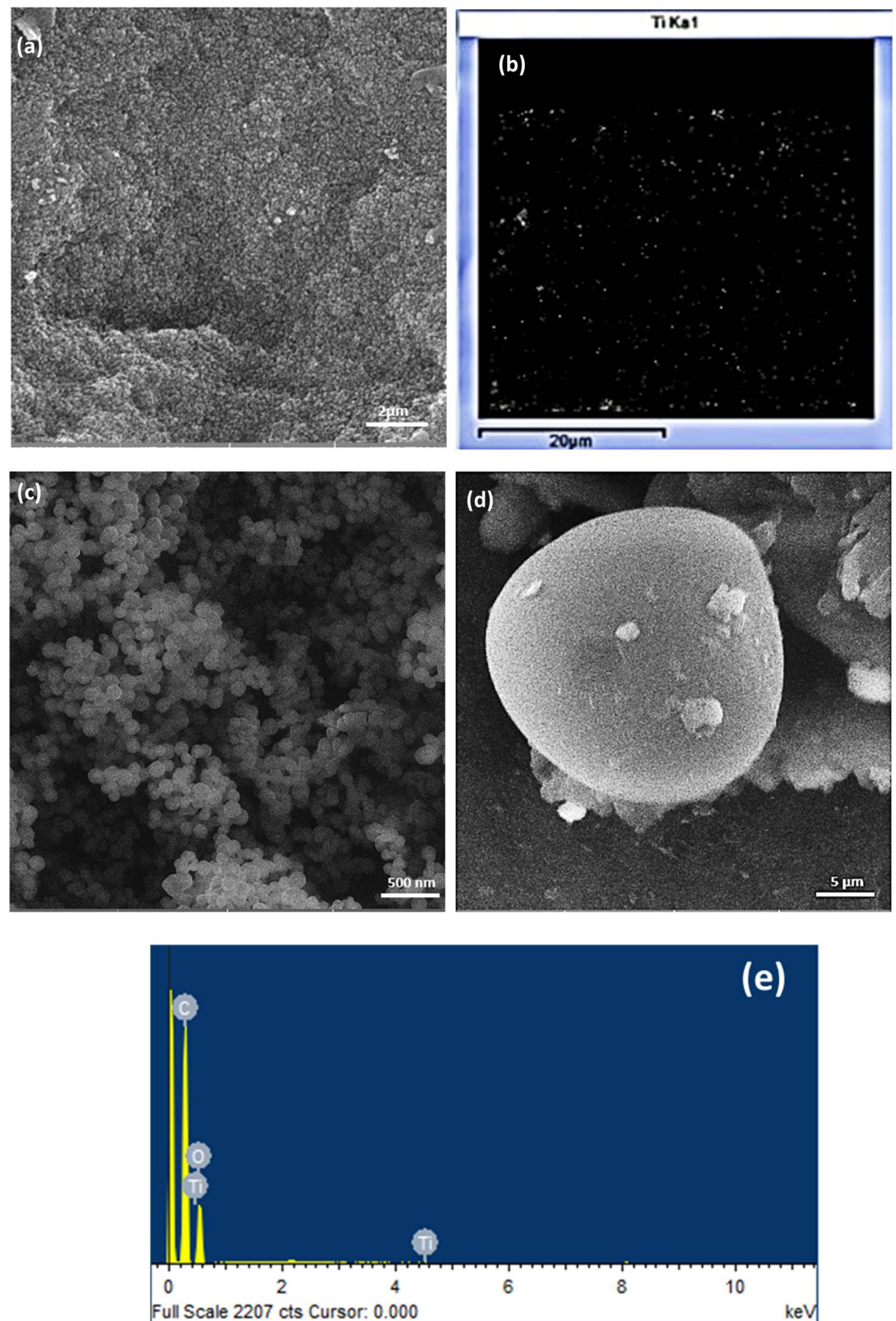


Figure 1. Morphology of RF/TiO₂ sample (a) FESEM image of RF/TiO₂, (b) TiO₂ distribution determined by EDX on the sample, (c) distinct appearance of micro/nanospheres, (d) isolated microsphere with differentiation between organic–inorganic phase, and (e) corresponding EDX spectra.

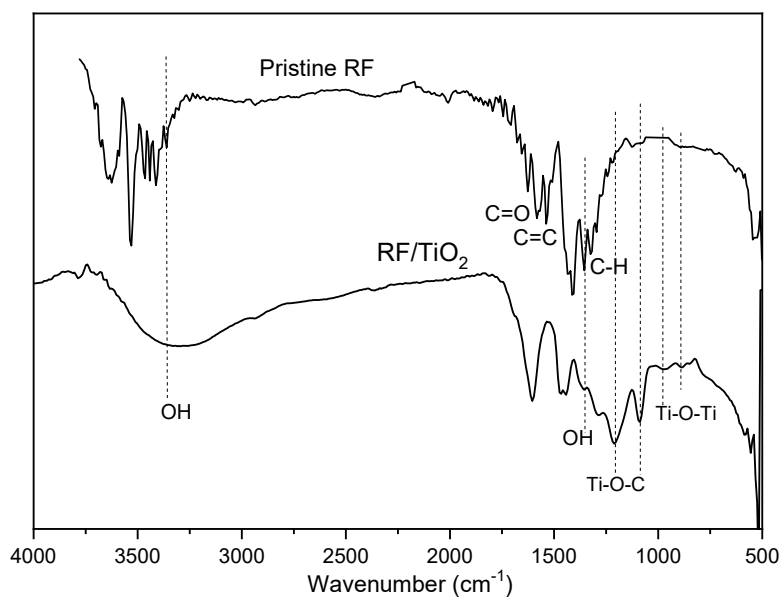


Figure 2. FTIR spectra of synthesised RF/TiO₂ gel compared to pristine RF gel.

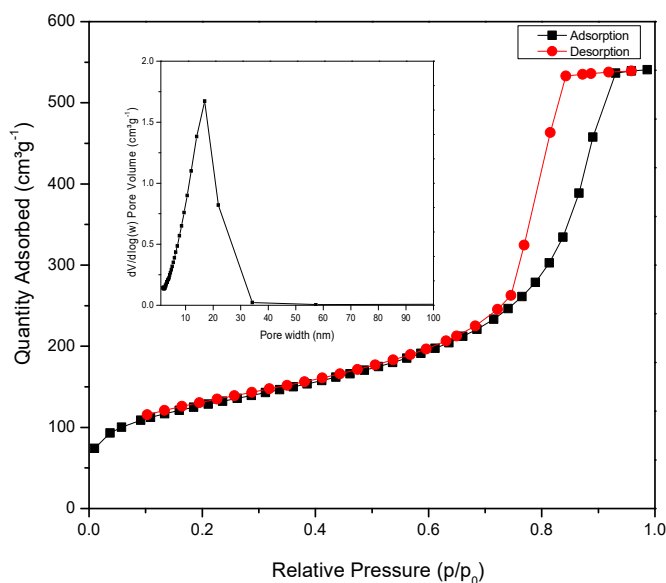


Figure 3. Nitrogen sorption isotherms and pore size distribution of synthesised RF/TiO₂ gel.

Overall, a good adsorption capacity for MB is observed at pH higher than the pH_{pzc} due to an increased number of negative sites in the higher pH range. This is in good agreement with the fact that, due to the presence of COO^- and OH^- functional groups, MB dye adsorption is favoured at $pH > pH_{pzc}$ [24]. The same trend has been observed in previous studies with activated carbon and TiO₂ composites where reduced activity was observed at acidic pH and maximum activity was observed in the pH range 6–10 [25–27].

2.5. Effect of Contact Time

Figure 5 shows the effect of contact time on the amount of MB molecules adsorbed by RF/TiO₂ gel under different initial MB concentrations. As shown, the adsorption capacity increases with increase in initial concentration. The equilibrium adsorption capacity increases from 102 mg g^{-1} to 207 mg g^{-1} by increasing the initial concentration of MB from 50 mg L^{-1} to 200 mg L^{-1} . Initially, the adsorption capacity overall is rapid for timeframes up to 30 min. This trend is expected, due to the greater driving force of MB dye molecules and immediate availability of vacant adsorption sites, hence resulting

in increased in frequency of collisions between MB dye molecules and the RF/TiO₂ gel. Additionally, mesoporosity throughout the RF/TiO₂ gel structure provides a high surface area for greater adsorption of MB molecules. It is noteworthy that at higher MB concentration the adsorption rate is greater and adsorption capacity attains equilibrium faster than at low concentration. The reason is attributed to immediate occupancy of available active sites by a large amount of adsorbate molecules. This rapid occurrence of sorption is due to the presence of mesoporosity within the RF/TiO₂ gel, which corresponds to a large portion of the adsorption sites. In this case, the mesoporous structure provides a large surface area to solution volume within the porous network of the adsorbent gel. Additionally, within the mesopores, MB dye molecules are confined to be in close proximity to the surface. Such observations have been reported in previous research, particularly for activated carbons [28]. Over time, saturation of active sites occurs, and adsorption becomes difficult on the fewer available active sites due to repulsive forces between the MB molecules and the RF/TiO₂ gel surface. Additionally, the blockage of pores and charge repulsion of MB dye species may decelerate the adsorption progress. Similar phenomena have been explained for porous TiO₂ and other carbon/TiO₂ porous composite materials, where it may have taken longer for the adsorbate to diffuse deeper in the fine pores [29]. Thereafter, the adsorption capacity increases gradually until 90 min, and equilibrium is attained for the entire concentration range. Thus, equilibrium time was considered as 90 min which was considered sufficient for removal of MB ions by RF/TiO₂ gel. Hence, the contact time was set to 90 min in the remaining experiments to ensure equilibrium was achieved.

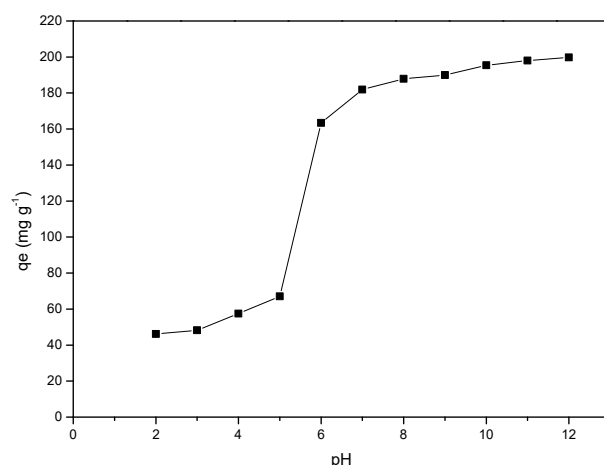


Figure 4. Effect of pH on the adsorption of MB dye by RF/TiO₂ gel.

2.6. Effect of Sorbent Dose

The percentage removal of MB dye increased with increase in the adsorbent dose from 0.005 to 0.01 g but remained almost constant with further increase in the dose range 0.01 to 0.1 g, as represented in Figure 6. Percentage removal was calculated using Equation (2), and showed an increase with increase in adsorbent dose, due to greater availability of vacant active sites, a large surface area, and a greater number of adsorptive sites present on the surface of RF/TiO₂. With further increase in adsorbent dose (>0.01 g), the rate of MB removal becomes low, as the concentrations at the surface and solution reach equilibrium. The resultant reduction in adsorption rate is attributed to unoccupied adsorbent sites, as well as overcrowding or aggregation of adsorbent particles [30]. Hence, the surface area available for MB adsorption per unit mass of the adsorbent reduces, whereby percentage removal was not significantly enhanced with further increase adsorbent dose.

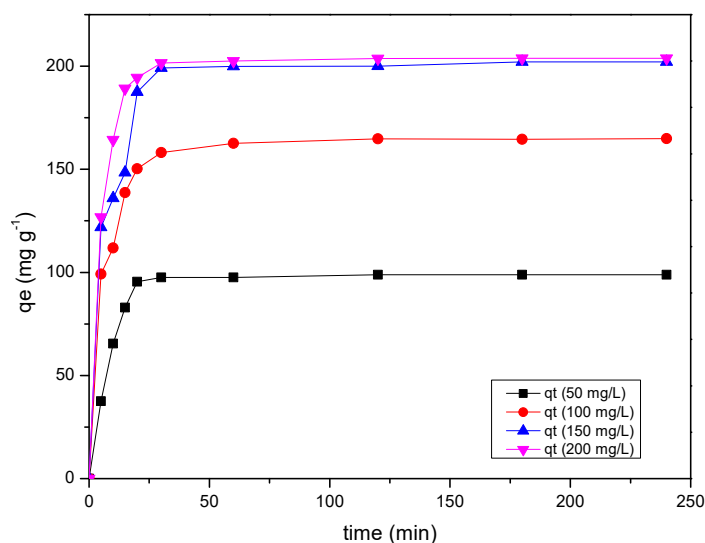


Figure 5. Effect of adsorption on contact time and initial concentration of MB dye by RF/TiO₂ gel.

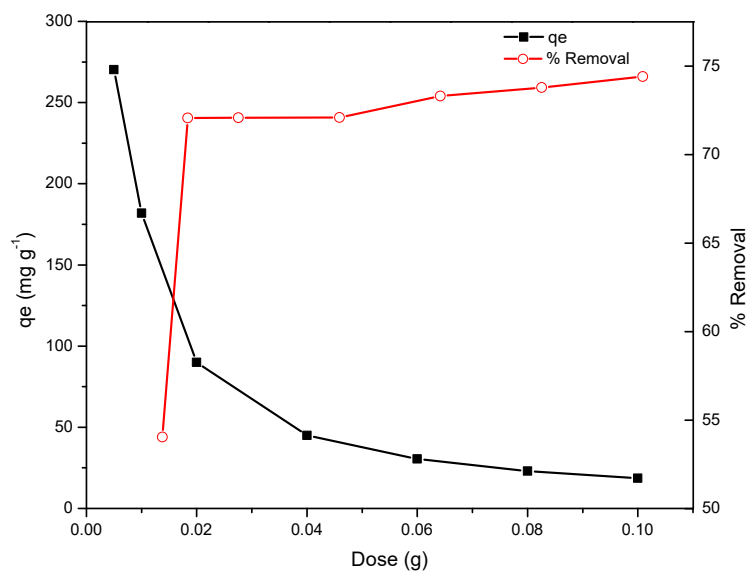


Figure 6. Effect of adsorbent dose on the removal and adsorption of MB dye by RF/TiO₂ gel.

2.7. Adsorption Kinetics

The adsorption kinetics were studied using a contact time of 240 min in the concentration range 50–200 mg L⁻¹. The experimental data obtained for MB dye adsorption capacity vs. time (t) were fitted with PFO and PSO, as presented in Figure 7a–d. The parameters determined, including measured equilibrium adsorption capacity q_e (experimental), theoretical equilibrium adsorption capacity q_e (calculated), first order rate constant K_1 , second order rate constant K_2 , and regression coefficient R^2 , are presented in Table 1.

As observed from the data, the correlation factor R^2 deviates significantly from 1 for PFO and, therefore, pseudo first order model does not exhibit good compliance with the experimental data for the entire concentration range. This implies that the adsorption reaction is not inclined towards physisorption, and the MB dye molecules adsorb to specific sites on the surface of RF/TiO₂ gel. The argument regarding the failure of the pseudo first order model suggests that several other interactions are responsible for the sorption mechanism. Hence, the correlation coefficients R^2 of the pseudo second order model were compared with pseudo first order parameters. R^2 values for pseudo second order behaviour are approximately 0.99 for the entire concentration range, indicating that the system is more appropriately described by the pseudo second order equation. The dependence on

initial concentration of MB dye is verified by good compliance of the experimental data with the pseudo second order equation, where the adsorption capacity is affected by the initial MB dye concentration, subsequent surface-active sites, and adsorption rate (Other error analyses are represented in Table S1).

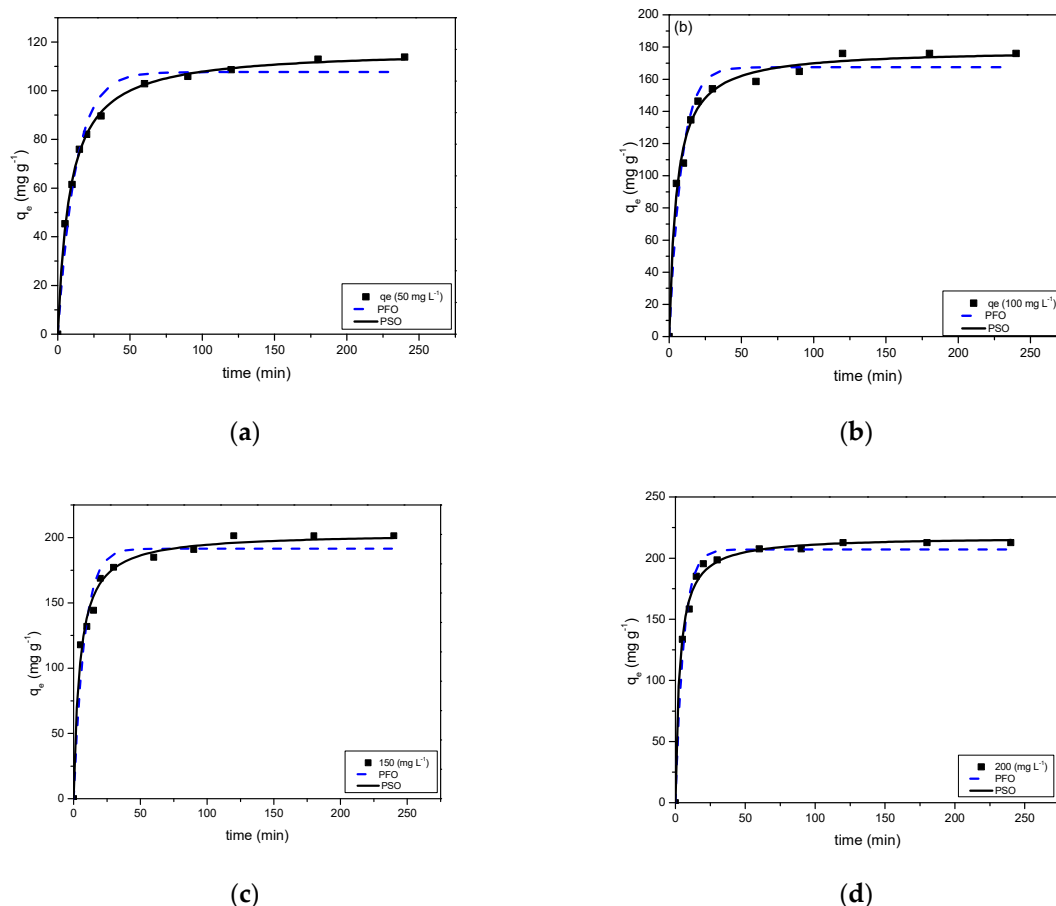


Figure 7. MB uptakes on RF/TiO₂ gel at (a) 50 mg L⁻¹, (b) 100 mg L⁻¹, (c) 150 mg L⁻¹, (d) 200 mg L⁻¹, and fitted data for pseudo first order and pseudo second order kinetic models.

Table 1. Kinetic parameters obtained by fitting kinetic data for MB adsorption to RF/TiO₂.

Model	50 mg L ⁻¹	100 mg L ⁻¹	150 mg L ⁻¹	200 mg L ⁻¹
q _e experimental (mg g ⁻¹)	112.75	175.98	201.46	212.56
<i>Pseudo first order</i>				
q _e , mg g ⁻¹	107.65	167.45	183.10	206.99
K ₁ (min ⁻¹)	0.08087	0.11886	0.1261	0.17078
R ²	0.9758	0.9632	0.948	0.985
<i>Pseudo second order</i>				
q _e , mg g ⁻¹	116.97	178.54	203.58	217.59
K ₂ (×10 ⁻³ g mg ⁻¹ min ⁻¹)	1.01	1.10	1.06	1.48
R ²	0.998	0.989	0.987	0.996

The equilibrium sorption capacity increased from 116.97 to 217.59 mg g⁻¹ when initial dye concentration was increased from 50 to 200 mg g⁻¹ confirming that MB dye removal is dependent on initial concentration, where the rate limiting step is determined by both adsorbate (MB) and adsorbent (RF/TiO₂) concentration. This signifies that the sorption mechanism is chemisorption. Previous studies have explained theoretically that if

diffusion is not the rate limiting factor, then higher adsorbate concentrations would give a good pseudo first order fit whereas, for low concentrations, pseudo second order better represents the kinetics of sorption, analogous to the observations made here [31]. Previously, the adsorption processes of MB on TiO₂/carbon composites have also exhibited strong dependencies of pseudo second order fitting parameters on initial concentrations [27].

Figure 8 shows a plot of MB dye uptake (q_e) on synthesised RF/TiO₂ against $(\text{time})^{0.5}$. The plots exhibit multi-linearity, rather than two straight lines, indicating that the adsorption process is influenced by several steps. The initial segment of the plots shows that diffusion across the boundary of the adsorbent only lasts for a short time in comparison to the whole adsorption process. This second section is attributed to diffusion into the mesopores of the adsorbent, i.e., the MB dye molecules enter less accessible pore sites. Resultantly, the diffusion resistance increases, and the diffusion rate decreases. This stage is a slow and gradual stage of the adsorption process. The third segment represents the final equilibrium stage where intra-particle diffusion slows down to an extremely low rate due to the remaining concentration of the MB dye molecules in the solution. This implies a slow transport rate of MB dye molecules from the solution (through the gel–dye solution interface) to available sites. Here, the surface of the RF/TiO₂ gel, and micropores, may be responsible for the uptake of MB dye molecules.

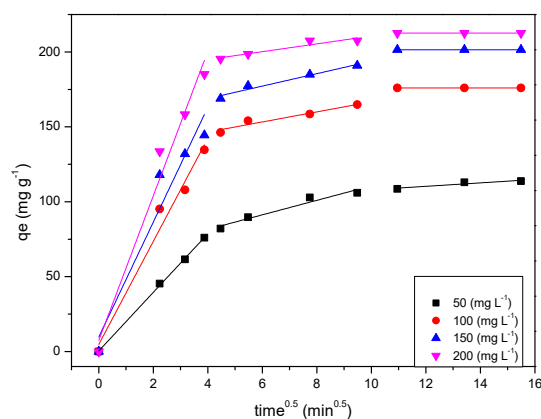


Figure 8. Intra-particle diffusion kinetics of MB dye adsorption on RF/TiO₂.

2.8. Adsorption Isotherms

The equilibrium data were analysed using Langmuir, Freundlich, Sips, and Toth isotherm equations to obtain the best fit. The isotherm data plots, and fitting model parameters are shown in Figure 9 and Table 2, respectively. Comparison of the correlation factor R^2 indicates that $q_{e,\text{exp}}$ fitted well to the Sips model with the lowest χ^2 value. The $q_{e,\text{cal}}$ value, calculated using the Sips model, is closest to $q_{e,\text{exp}}$ with R^2 closest to 1. The Sips model is a combination of the Langmuir and Freundlich adsorption isotherms, hence, the model suggests both monolayer and multilayer adsorption. At low MB dye concentrations, the model predicts Freundlich adsorption isotherms as a heterogeneous adsorption system and localised adsorption without adsorbate–adsorbate interactions, whereas at high concentrations the model predicts monolayer adsorption as in Langmuir isotherm [32,33]. In the present study, the value of constant n_s from Equation (11), the heterogeneity factor, is greater than 1 (i.e., $n_s = 1.91$), hence, the adsorption system is predicted to be heterogeneous [33]. Further, the Toth isotherm model validates multilayer and heterogeneous adsorption, where the factor n_T determines heterogeneity. Here, again the value of n_T is greater than 1, and, therefore, the system confirms heterogeneity. It is evident that the equilibrium uptakes follow the Sips model according to the correlation factor R^2 (other error analyses are represented in Table S2) and the isotherm models fit the data in the order Sips > Toth > Langmuir > Freundlich.

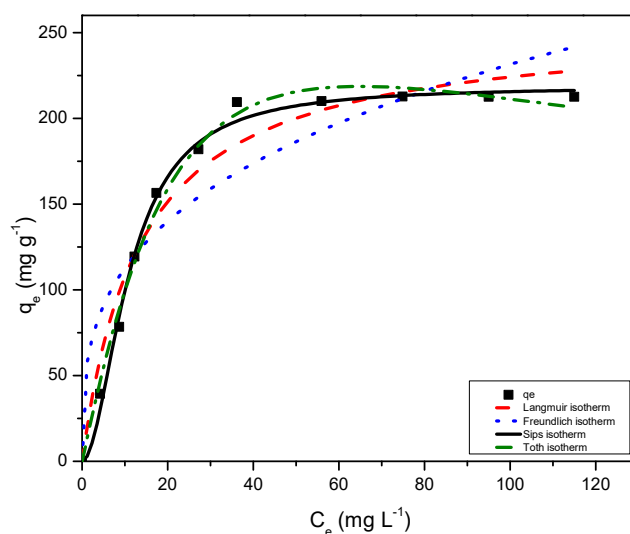


Figure 9. Adsorption data for RF/TiO₂ onto MB dye corresponding fits to Langmuir, Freundlich, Sips, and Toth equation.

Table 2. Isotherm parameters obtained by fitting MB adsorption data for RF/TiO₂ to the Langmuir, Freundlich, Sips, and Toth equations.

Langmuir	q_m (mg g ⁻¹)	254.65
	K_L (L mg ⁻¹)	0.0732
	R^2	0.960
Freundlich	K_F mg g ⁻¹ (L mg ⁻¹) ^{1/n}	54.85
	n_F	3.1993
	R^2	0.865
Sips	q_s (mg g ⁻¹)	218.71
	K_S	0.010
	n_s	1.913
Toth	R^2	0.994
	q_m (mg g ⁻¹)	558.47
	K_T	0.0295
	n_T	1.403
	R^2	0.991

2.9. Thermodynamic Study

Thermodynamic parameters for the adsorption system are recorded in Table 3. Negative values of free energy changes are evident from the data, which signifies the spontaneous adsorption of MB dye molecules on the sample for the studied temperature range. Adsorption capacity increases with an increase in temperature and a positive ΔH^0 (Table 3) suggests that the adsorption is endothermic in nature. Positive ΔS^0 indicates some structural changes in the MB dye and RF/TiO₂ gel causing an increase in the degree of freedom of the MB dye species and consequently increased randomness at the adsorbent–adsorbate interface. At high temperature, the release of high-energy desolvated water molecules from the MB dye molecules and/or aggregates arise after adsorption on RF/TiO₂ gel, which relates to a positive ΔS^0 [34]. Before sorption begins, the MB ions are surrounded by highly ordered water clusters strongly bound via hydrogen bonding. Once MB ions come in close contact with the surface of RF/TiO₂, the interaction results in agitation of the ordered water molecules, subsequently increasing the randomness of the system. Although, the adsorption of MB dye onto RF/TiO₂ gel may reduce the freedom of the system, the entropy increase in water molecules is much higher than the entropy decrease in MB ions. Therefore, the driving force for the adsorption of MB on RF/TiO₂ is controlled by an entropic effect rather than an enthalpic change. Similar phenomena have previously been reported

in order to explain the fact that thermodynamic parameters are not only related to the properties of the adsorbate but also to the properties of other solid particles [35,36].

Table 3. Thermodynamic data for MB adsorption onto RF/TiO₂ at various temperatures.

T (K)	lnk	ΔG^0 (KJ/mol)	ΔS^0 (J/mol)	112
281	1.29	−3.01	ΔH^0 (KJ/mol)	28.2
296	2.20	−5.41		
305	2.40	−6.09		
313	2.50	−6.51		

3. Photocatalytic Tests

Photocatalytic activity was determined by testing the efficiency of RF/TiO₂ against degradation of methylene blue (MB) under visible light irradiation. The maximum absorbance vs. wavelength spectra (in the range of 550–700 nm) were collected and subsequent activity, after 30 min, intervals was recorded, as shown in Figure 10.

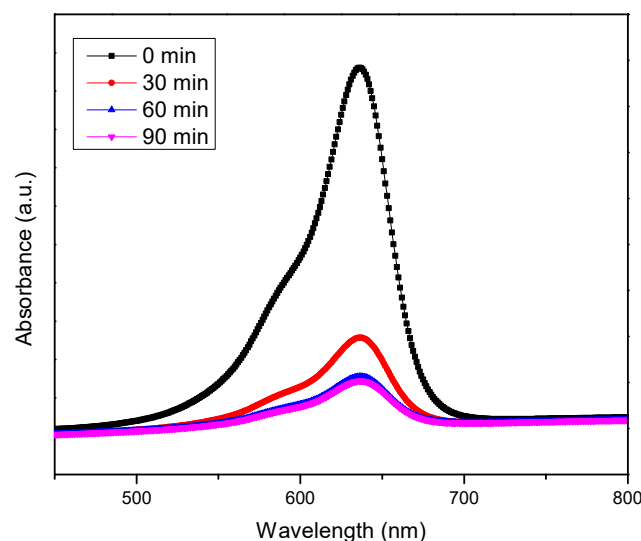


Figure 10. UV-Vis spectra of MB dye degradation using RF/TiO₂ gel.

Within the studied systems, no photodegradation activity (reduction in concentration and decolourisation of MB dye) was observed in the absence of adsorbent/catalyst, as well as in the presence of pristine RF, indicating that the properties of MB are more stable. Additionally, RF solely may not be recommended for photocatalysis due to slow charge transfer properties, which has also been proven by the study carried out by Zang, Ni, and Liu, where the researchers employed pristine RF resins for visible light photocatalysis [37]. Slight photodegradation is observed in the presence of pristine TiO₂, which may be attributed to the potential absorbance of UV-Vis light from the surroundings confirming that the process of MB degradation is light driven. Although the TiO₂ obtained for use in this study has a high surface area, which may possess good adsorption properties to exhibit efficient adsorption of MB dye, since TiO₂ only activates upon UV light irradiation (~280 nm), it does not produce enough reactive oxide species (ROS) to be an effective photodegradation system [38].

The dye degradation data obtained after treatment with RF/TiO₂ showed ~73% MB dye removal after 90 min. This is attributed to the synergy of RF and TiO₂, enabling an absorption shift to a higher wavelength, as λ_{max} is detected at 410 nm (Figure 11). Further analysis indicates modification in the electronic structure and a subsequent reduction in bandgap occurs due to doping of TiO₂ similar to when combined with carbon [39]. The calculated band gap energy is 2.97 eV, as shown in Figure 11 (inset). The value achieved is

significantly lower than pristine TiO₂ (i.e., 3.2 eV [21]), indicating photodegradation of MB dye under visible light irradiation. The RF matrix enables entrapment of a photogenerated electron and hole pairs and, therefore, rapid generation of ROS is possible for efficient degradation of the MB dye. These findings are comparable to other carbon/TiO₂ systems where synergistic effects have substantially enhanced the performance of the system due to improved optical properties of the material [1,40,41].

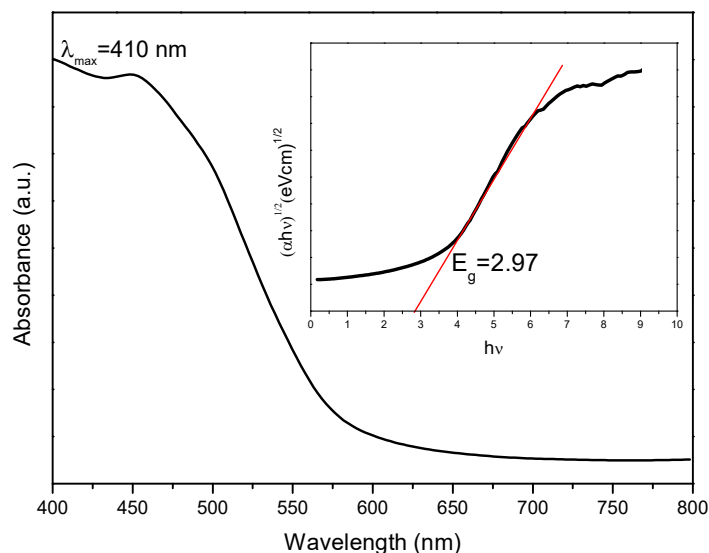


Figure 11. Absorption vs. wavelength spectrum of RF/TiO₂ dispersed in ethanol measured through UV-Vis spectrophotometer, inset shows calculated band gap of synthesised RF/TiO₂.

The photodegradation of MB dye, that is, the reduction in concentration with time is recorded in Figure 12 and the recorded data is modelled using pseudo first order kinetics, shown in Figure 12a,b. The data are fitted to the first order kinetic equation ($\ln(C_0/C_e) = kt$) to evaluate the value of the rate constant by slope of plot $\ln(C_0/C_e)$ vs. time (t) in minutes, where C_0 and C_e is the initial at $t = 0$ and final concentration at given time of MB concentration, respectively. The value of k here is the measure of photocatalytic performance, as it defines the concentration of reacting substances, that is, photogenerated reactive oxide species, therefore, a higher value of k signifies higher photocatalytic efficiency. As compared to no catalyst ($k = 2.43 \times 10^{-6} \text{ min}^{-1}$) pristine TiO₂ ($k = 1.74 \times 10^{-3} \text{ min}^{-1}$) and pristine RF ($k = 6.89 \times 10^{-4} \text{ min}^{-1}$), the rate of RF/TiO₂ was the highest ($k = 1.27 \times 10^{-2} \text{ min}^{-1}$). Clearly, the rate constant obtained for photodegradation of MB using RF/TiO₂ was the highest. Mainly, improved optical property was the most important advancement in forming RF/TiO₂ gel which is photocatalytically active under visible light (410 nm) irradiation.

The RF/TiO₂ material created in this study exhibits excellent photoactivity under visible light, which can further be explained by the mechanism of MB photodegradation represented in Equations (1)–(8). The system activates when RF/TiO₂ absorbs light with photon energy ($h\nu$) and generates conduction band (CB) electron (e^-) and valence band (VB) hole (h^+) pairs upon under visible light irradiation. The holes interact with moisture on the surface of the adsorbent gel yielding hydroxy free radicals or reactive oxide species (H^+ or OH^\bullet), which are oxidation agents that can mineralise a wide range of organic pollutants, ultimately producing CO₂ and H₂O as end products. The reaction sequence below represents the photodegradation of MB, showing a simplified mechanism of photoactivation by a photocatalyst (Equations (1)–(4)) [19]. For the mechanism of photoactivation of MB in the presence of RF/TiO₂, hydroxy free radicals or reactive oxide species (H^+ or OH^\bullet) attack the aromatic ring of the MB structure, degrading it into a single ring structure product, which then finally degrades to CO₂ and H₂O (Equations (5)–(8)) [42,43].

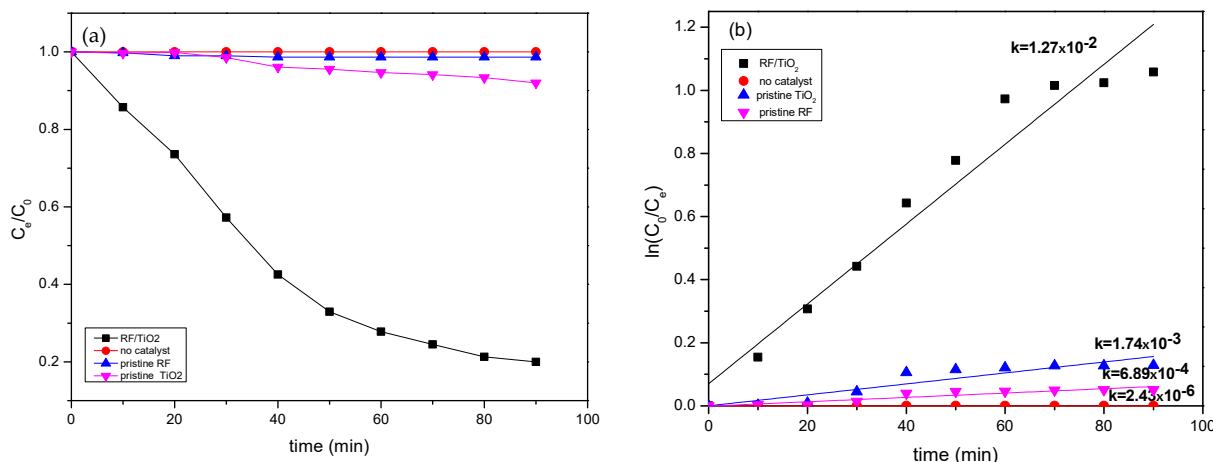
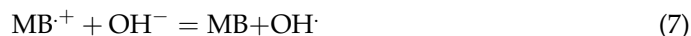
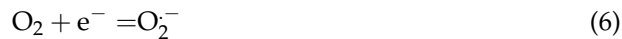
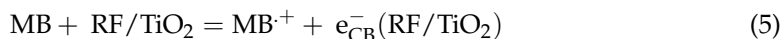


Figure 12. (a) Photocatalytic performance regarding MB dye degradation without catalyst, and with pristine RF, pristine TiO₂ and RF/TiO₂ gel (b) First-order kinetics of photoactivity without catalyst, and with pristine RF, pristine TiO₂, and RF/TiO₂ gel.



4. Conclusions

An RF/TiO₂ gel was successfully synthesised using sol-gel techniques via a straightforward route. The synergy of RF and TiO₂ exhibited excellent adsorption-photodegradation activity due to the corresponding characteristics, mainly mesoporosity and photocatalysis. The synergy of contributing materials allowed modification in the electronic structure of TiO₂ by formation of Ti-O-C chemical linkages, responsible for a reduction in the band gap of TiO₂ for photodegradation upon visible light irradiation. Kinetic studies revealed a pseudo second order reaction, signifying chemisorption phenomenon is involved in the adsorption mechanism. The adsorption isotherm study showed that the system was heterogeneous following the Sips model equation. The spontaneity of the process was validated via thermodynamic studies, which signified an entropically driven adsorption mechanism. Effective photodegradation results were observed due to the high adsorption capacity and improved optical properties of the material, enabling significant MB dye degradation within 90 min. Overall, the material possesses properties that have potential to effectively reduce/eliminate a wide range of pollutants and, therefore, can be employed as a low-cost photocatalytic adsorbent for water treatment Especially in the industrial applications where post treatment separation and recovery of the adsorbent is difficult, employing this material can reduce the costs since in this case the adsorbent precipitates and easy separation is possible just by filtration or even decantation.

5. Material and Methods

5.1. Synthesis

Synthesis of RF and TiO₂ precursors was carried out in two separate systems, which were integrated and processed further in order to obtain the final gel.

System 1: Preparation of Titania Sol

For preparation of the titania sol, 1.78 g of titanium precursor: titanium isopropoxide (TTIP) (98+%, ACROS Organics™, Geel, Belgium) was dissolved in ethanol and stirred for 30 min. A mixture of water and HCl was added dropwise to the titania/EtOH solution under constant stirring, at room temperature, to begin hydrolysis. After 2 h, a homogenous solution was obtained. The molar ratios for these parameters were 1 TTIP:10 EtOH:0.3 HCl:0.1 H₂O.

System 2: Preparation of RF sol

In total, 7.74 g of resorcinol (SigmaAldrich, ReagentPlus, 99%, Poole, UK) was added to 50 mL of deionised water until completely dissolved. 0.0249 g of sodium carbonate (Na₂CO₃, Sigma-Aldrich, anhydrous, ≥99.5%), as a catalyst, and 4.23 g of formaldehyde (37wt%) were added to the dissolved resorcinol under continuous stirring, at room temperature.

Finally, the prepared titania sol (system 1) was gradually transferred to the RF sol (from system 2) under constant stirring, at room temperature. The resulting sol was stirred at room temperature for 2 h after which the sol mixture was aged at 85 °C for 72 h.

After aging, the process of solvent exchange and drying the RF/TiO₂ gel, first involved cutting the gel into smaller pieces. These pieces were then immersed in acetone for 72 h to facilitate solvent exchange prior to drying, followed by vacuum drying at 110 °C for 48 h to obtain the final RF/TiO₂ adsorbent gel. In this way, the final gel corresponded to 10 wt% TiO₂ (theoretical percentage) incorporated in the RF gel matrix.

5.2. Adsorbent Characterisation

Morphology of the synthesised sample was studied by field emission electron scanning microscope (FESEM) TESCAN-MIRA. The functional groups on the surface of synthesised RF/TiO₂, and the chemical linkages between the constituent RF and TiO₂ components, were verified using Fourier Transform Infrared Spectroscopy (FTIR) (MB3000 series, scan range 4000–400 nm). BET surface area measurements were carried out using a Micromeritics ASAP 2420 to obtain N₂ adsorption isotherm at 77 K and pore size was determined via BJH theory [22]. A UV-Vis Spectrophotometer (Varian Cary 5000 UV-Vis NIR Spectrophotometer Hellma Analytics) was used to collect absorption spectra and the data used to interpret the change in electronic structure of RF/TiO₂ [44]. The data were manipulated to calculate the band gap energy values through the Tauc method described in previous studies [44].

6. Adsorption Experiments

6.1. Effect of pH

The effect of pH on the sorption of methylene blue (MB) dye was investigated with 0.01 g of sample by adjusting the pH of solution (25 mL, 100 mg L⁻¹ MB) between 2 and 12, at 23 °C. The pH was adjusted using 0.01 M HCl and 0.01 M NaOH. After 2 h of agitation, the solution was centrifuged for 15 min and the supernatant solution was collected via syringe. The initial and final concentrations were measured using a UV-Vis spectrophotometer (Varian Cary 5000 UV-Vis NIR Spectrophotometer, Agilent, UK) and onward calculations were performed.

6.2. Effect of Sorbent Dose

The amount of sorbent dose was gradually increased from 0.005 to 0.01 g to study the effect of sorbent dose on the adsorption capacity. pH and temperature were maintained at 7.0 and 23 °C, respectively, against 25 mL of 100 mg L⁻¹ MB concentrated solution. The pH was adjusted using 0.01 M HCl and 0.01 M NaOH. After 2 h of agitation, the solution was centrifuged for 15 min and the supernatant solution was collected via syringe. The initial and final concentrations were measured using a UV-Vis spectrophotometer (Varian

Cary 5000 UV-Vis NIR Spectrophotometer Hellma Analytics) and onward calculations were performed.

6.3. Effect of Initial Concentration

All adsorption experiments were performed at 23 °C in 125 mL conical flasks, using a shaker (VWR 3500 Analog orbital shaker) set to 125 rpm. The first experiment was conducted to study the isothermal equilibrium and the effect of initial MB concentration. Standard solutions of MB were prepared using distilled water, with initial concentrations in the range of 20–200 mg L⁻¹. Then, 25 mL aliquots were distributed into each flask, and 0.01 g of the adsorbent gel was added individually to each flask. The pH values of all solutions were recorded and adjusted to 7.0, if required, using 1 M HCl and 1 M NaOH. After 2 h of agitation, the solution was centrifuged for 15 min and the supernatant solution was collected via syringe. The initial and final concentrations were measured using UV-Vis spectrophotometer (Varian Cary 5000 UV-Vis NIR Spectrophotometer Hellma Analytics).

The equilibrium adsorption capacity, q_e (mg g⁻¹), was calculated using:

$$q_e = \frac{(C_o - C_e) \times V(l)}{W} \quad (9)$$

while the respective percentage removal of MB was calculated as:

$$\text{Removal \%} = \frac{C_o - C_e}{C_o} \times 100\% \quad (10)$$

where C_o and C_e are the initial MB and final concentration, respectively. W is the weight (g) of the adsorbent and V is the volume (L) of MB solution.

6.4. Effect of Contact Time

The effect of contact time was studied by adding MB solution (pH 7.0, 25 mL, 100 mg L⁻¹) and 0.01 g adsorbent gel into a flask, which was then agitated for a pre-determined contact time between 5 min and 4 h. The samples were prepared and treated as described in Section 2.5 and the amount of adsorption was calculated using Equation (11):

$$q_t = \frac{(C_o - C_t) \times V}{W} \quad (11)$$

where C_t is the equilibrium MB concentration at a given time, and C_o , V , and W are as previously defined. Equilibrium concentration was determined by plotting q_t versus time of aliquots collected at different time intervals. Adsorption-photodegradation (absorption) changes of MB dye with time were also recorded via UV-Vis spectrophotometry.

6.5. Effect of Temperature

The effect of temperature on the removal of MB (pH 7.0, 25 mL, 20–200 mg L⁻¹) was investigated by adding a known concentration MB solution and 0.01 g adsorbent gel to a flask. A hot plate with a stirrer (120 rpm) was used to maintain a constant temperature of 8, 23, 32, and 40 °C, under stirring, for 120 min after which the absorbance versus wavelength spectra were recorded to measure the final concentration, and subsequent adsorption was calculated using Equation (9).

6.6. Kinetic Models

The kinetic-based models: pseudo first order (PFO) and pseudo second order (PSO) were applied to study the adsorption kinetics and to explain the mode of sorption of MB onto the synthesised RF/TiO₂. The PFO model [33] has been frequently used to describe kinetic processes under non-equilibrium conditions. PFO is based on the assumption that the rate of adsorption is proportional to the driving force, that is, the difference between

the equilibrium concentration and solid phase concentration, presented as a differential Equation (12):

$$\frac{dq_t}{dt} = k_1(q_e - q_t) \quad (12)$$

Integrating Equation (13) with the initial condition of $q_t = 0$ at $t = 0$, the PFO model can be rewritten, in a linear form, as:

$$q_t = q_e(1 - e^{-k_1 t}) \quad (13)$$

Several studies have also reported the use of PSO [45] to interpret data obtained for the sorption of contaminants from water, including dyes, organic molecules, and metal ions. The PSO model assumes that the overall adsorption rate is proportional to the square of the driving force and can be expressed as Equation (14):

$$\frac{dq_t}{dt} = k_1(q_e - q_t)^2 \quad (14)$$

Integrating Equation (14) with the initial condition of $q_t = 0$ at $t = 0$, and $q_t = t$ at $t = t$, the PSO model can be rewritten as:

$$q_t = \frac{k_2 t q_e^2}{1 + k_2 t q_e} \quad (15)$$

In Equations (13)–(15), q_t (mg g^{-1}) and q_e (mg g^{-1}) are the adsorption capacities of MB dye molecules at time t and at equilibrium, respectively. k_1 ($\text{mg g}^{-1} \text{min}^{-1}$) and k_2 ($\text{mg g}^{-1} \text{min}^{-1}$) are the PFO and PSO rate constants, respectively.

6.7. Sorption Isotherm Models

The equilibrium data for the sorption of MB on RF/TiO₂ adsorbent gel as a function of equilibrium concentration (C_e mg L^{-1}) was analysed in terms of Langmuir, Freundlich, Sips, and Toth isotherm models [2]. The nonlinear form of Langmuir's isotherm model is represented as:

$$q_e = \frac{q_m K_L C_e}{1 + C_e K_L} \quad (16)$$

where q_e (mg g^{-1}) is the MB uptake at equilibrium, C_e (mg L^{-1}) is the equilibrium concentration, q_m (mg g^{-1}) is the amount of adsorbate at complete monolayer coverage, and K_L is the Langmuir constant.

The Freundlich equation can be expressed as follows:

$$q_e = K_F C_e^{1/n} \quad (17)$$

where q_e and C_e are as defined in the Langmuir equation, adsorption affinity is related to the adsorption constant K_F , and n indicates the magnitude of the adsorption driving force and the distribution of energy sites on the adsorbent surface, if $n < 1$, then adsorption is a chemical process, whereas if $n > 1$, then adsorption maybe dependent on distribution of the surface sites. Generally, n values within 1–10 represents good adsorption [46].

The Sips isotherm model is a combination of the Langmuir and Freundlich isotherms and is represented as:

$$q_e = \frac{q_s K_s C_e^{ns}}{1 + K_s C_e^{ns}} \quad (18)$$

where q_e and C_e are as defined for Equation (16), K_s is the Sips isotherm model constant (L g^{-1}), and ns ; is the Sips isotherm exponent.

The Toth model also describes heterogeneous systems, considering both low- and high-end concentrations. The Toth expression is as follows:

$$q_e = \frac{q_m K_T C_e}{[1 + (K_T C_e)^t]^{1/t}} \quad (19)$$

where q_e and C_e are as defined for Equation (16), q_m is the maximum adsorption capacity, t is the surface heterogeneity, and K_T is the surface affinity.

6.8. Photodegradation Procedure

Photocatalytic performance of as prepared RF/TiO₂ was investigated through MB dye degradation, by recording the dye degradation spectra with time using UV-Vis Spectrophotometry. 0.01 g of the adsorbent dose were used against 25 mL of 100 mg L⁻¹ dye concentration at pH ~7 and a temperature of 23 °C and light intensity of 111 Wm⁻². For comparison, the measurements were also recorded in the absence of catalyst, as well as pristine RF and TiO₂. All suspensions were stirred in the dark for 60 min to establish sorption equilibrium before exposure to visible light.

Supplementary Materials: The following supporting information can be downloaded at: <https://www.mdpi.com/article/10.3390/gels8040215/s1>, Figure S1: Zone of Energy dispersive x-ray (EDX) spectra; Figure S2: Point of zero charge (pHpzc) on the surface of RF/TiO₂; Table S1: Kinetic parameters obtained by fitting kinetic data for MB adsorption to RF/TiO₂; Table S2: Isotherm parameters obtained by fitting MB adsorption data for RF/TiO₂ to the Langmuir, Freundlich, SIPS and Toth equations.

Author Contributions: Methodology, A.S.; formal analysis, A.S. and A.J.F.; resources, A.J.F.; writing—original draft preparation, A.S.; writing—review and editing, A.J.F.; supervision, A.J.F.; project administration, A.J.F.; funding acquisition, A.J.F. All authors have read and agreed to the published version of the manuscript.

Funding: This research received no external funding.

Acknowledgments: Anam Safri thanks Ashleigh Fletcher and the Chemical and Process Engineering Department at the University of Strathclyde for funding this work. The authors gratefully acknowledge the Materials Science and Engineering Department at Institute of Space Technology, Islamabad, for providing support and facilities to conduct the morphological analysis.

Conflicts of Interest: The authors declare no conflict of interest.

References



- Xue, G.; Liu, H.; Chen, Q.; Hills, C.; Tyrer, M.; Innocent, F. Synergy between surface adsorption and photocatalysis during degradation of humic acid on TiO₂/activated carbon composites. *J. Hazard. Mater.* **2011**, *186*, 765–772. [[CrossRef](#)] [[PubMed](#)]
- Ajiboye, T.O.; Oyewo, O.A.; Onwudiwe, D.C. Adsorption and photocatalytic removal of Rhodamine B from wastewater using carbon-based materials. *FlatChem* **2021**, *29*, 100277. [[CrossRef](#)]
- Quyen, N.D.V.; Khieu, D.Q.; Tuyen, T.N.; Tin, D.X.; Diem, B.T.H.; Dung, H.T.T. Highly effective photocatalyst of TiO₂ nanoparticles dispersed on carbon nanotubes for methylene blue degradation in aqueous solution. *Vietnam. J. Chem.* **2021**, *59*, 167–178.
- Sampaio, M.J.; Silva, C.G.; Marques, R.R.; Silva, A.M.; Faria, J.L. Carbon nanotube—TiO₂ thin films for photocatalytic applications. *Catal. Today* **2011**, *161*, 91–96. [[CrossRef](#)]
- Murgolo, S.; Petronella, F.; Ciannarella, R.; Comparelli, R.; Agostiano, A.; Curri, M.L.; Mascolo, G. UV and solar-based photocatalytic degradation of organic pollutants by nano-sized TiO₂ grown on carbon nanotubes. *Catal. Today* **2015**, *240*, 114–124. [[CrossRef](#)]
- Morawski, A.W.; Kusiak-Nejman, E.; Wanag, A.; Narkiewicz, U.; Edelmánová, M.; Reli, M.; Kočí, K. Influence of the calcination of TiO₂-reduced graphite hybrid for the photocatalytic reduction of carbon dioxide. *Catal. Today* **2021**, *380*, 32–40. [[CrossRef](#)]
- Minella, M.; Sordello, F.; Minero, C. Photocatalytic process in TiO₂/graphene hybrid materials. Evidence of charge separation by electron transfer from reduced graphene oxide to TiO₂. *Catal. Today* **2017**, *281*, 29–37. [[CrossRef](#)]
- Faraldos, M.; Bahamonde, A. Environmental applications of titania-graphene photocatalysts. *Catal. Today* **2017**, *285*, 13–28. [[CrossRef](#)]

9. Zeng, G.; You, H.; Du, M.; Zhang, Y.; Ding, Y.; Xu, C.; Liu, B.; Chen, B.; Pan, X. Enhancement of photocatalytic activity of TiO₂ by immobilization on activated carbon for degradation of aquatic naphthalene under sunlight irradiation. *Chem. Eng. J.* **2021**, *412*, 128498. [[CrossRef](#)]
10. Paušová, M.; Riva, M.; Baudys, M.; Krýsa, J.; Barbieriková, Z.; Brezová, V. Composite materials based on active carbon/TiO₂ for photocatalytic water purification. *Catal. Today* **2019**, *328*, 178–182. [[CrossRef](#)]
11. Khalid, N.; Majid, A.; Tahir, M.B.; Niaz, N.; Khalid, S. Carbonaceous-TiO₂ nanomaterials for photocatalytic degradation of pollutants: A review. *Ceram. Int.* **2017**, *43*, 14552–14571. [[CrossRef](#)]
12. Biener, J.; Stadermann, M.; Suss, M.; Worsley, M.A.; Biener, M.M.; Rose, K.A.; Baumann, T.F. Advanced carbon aerogels for energy applications. *Energy Environ. Sci.* **2011**, *4*, 656–667. [[CrossRef](#)]
13. Faria, J.L.; Wang, W. *13 Carbon Materials in Photocatalysis*; John Wiley & Sons: Hoboken, NJ, USA, 2009; p. 481.
14. Al-Muhtaseb, S.; Ritter, J. Preparation and Properties of Resorcinol-Formaldehyde Organic and Carbon Gels. *Adv. Mater.* **2003**, *15*, 101–114. [[CrossRef](#)]
15. Prostředný, M.; Abduljalil, M.G.; Mulheran, P.A.; Fletcher, A.J. Process variable optimization in the manufacture of resorcinol-formaldehyde gel materials. *Gels* **2018**, *4*, 36. [[CrossRef](#)] [[PubMed](#)]
16. Awadallah-F, A.; Al-Muhtaseb, S.A. Nanofeatures of resorcinol-formaldehyde carbon microspheres. *Mater. Lett.* **2012**, *87*, 31–34. [[CrossRef](#)]
17. Awadallah-F, A.; Elkhatat, A.M.; Al-Muhtaseb, S.A. Impact of synthesis conditions on meso- and macropore structures of resorcinol-formaldehyde xerogels. *J. Mater. Sci.* **2011**, *46*, 7760–7769. [[CrossRef](#)]
18. Principe, I.A.; Fletcher, A.J. Parametric study of factors affecting melamine-resorcinol-formaldehyde xerogels properties. *Mater. Today Chem.* **2018**, *7*, 5–14. [[CrossRef](#)]
19. Shevlin, S.A.; Woodley, S.M. Electronic and Optical Properties of Doped and Undoped (TiO₂)_n Nanoparticles. *J. Phys. Chem. C* **2010**, *114*, 17333–17343. [[CrossRef](#)]
20. Jiang, Y.; Meng, L.; Mu, X.; Li, X.; Wang, H.; Chen, X.; Wang, X.; Wang, W.; Wu, F.; Wang, X. Effective TiO₂ hybrid heterostructure fabricated on nano mesoporous phenolic resol for visible-light photocatalysis. *J. Mater. Chem.* **2012**, *22*, 23642–23649. [[CrossRef](#)]
21. Zaleska, A. Doped-TiO₂: A review. *Recent Pat. Eng.* **2008**, *2*, 157–164. [[CrossRef](#)]
22. Aranovich, G.L.; Donohue, M.D. Adsorption isotherms for microporous adsorbents. *Carbon* **1995**, *33*, 1369–1375. [[CrossRef](#)]
23. Wang, S.; Zhu, Z.H.; Coomes, A.; Haghseresht, F.; Lu, G.Q. The physical and surface chemical characteristics of activated carbons and the adsorption of methylene blue from wastewater. *J. Colloid Interface Sci.* **2005**, *284*, 440–446. [[CrossRef](#)] [[PubMed](#)]
24. Chham, A.; Khouya, E.; Oumam, M.; Abourriche, A.; Gmouh, S.; Mansouri, S.; Elhammoudi, N.; Hanafi, N.; Hannache, H. The use of insoluble mater of Moroccan oil shale for removal of dyes from aqueous solution. *Chem. Int.* **2018**, *4*, 67–77.
25. Atout, H.; Bouguettoucha, A.; Chebli, D.; Gatica, J.M.; Vidal, H.; Yeste, M.P.; Amrane, A. Integration of Adsorption and Photocatalytic Degradation of Methylene Blue Using TiO₂ Supported on Granular Activated Carbon. *Arab. J. Sci. Eng.* **2017**, *42*, 1475–1486. [[CrossRef](#)]
26. Matos, J. *Hybrid TiO₂-C Composites for the Photodegradation of Methylene Blue Under Visible Light*; Bol Grupo Español Carbón: Zaragoza, Spain, 2013.
27. Natarajan, T.S.; Bajaj, H.C.; Tayade, R.J. Preferential adsorption behavior of methylene blue dye onto surface hydroxyl group enriched TiO₂ nanotube and its photocatalytic regeneration. *J. Colloid Interface Sci.* **2014**, *433*, 104–114. [[CrossRef](#)] [[PubMed](#)]
28. Baker, F.S.; Miller, C.E.; Repik, A.J.; Tolles, E.D. Activated carbon. In *Kirk-Othmer Encyclopedia of Chemical Technology*; Interscience Publishers: Geneva, Switzerland, 2000.
29. Zhang, X.; Zhang, F.; Chan, K.-Y. Synthesis of titania-silica mixed oxide mesoporous materials, characterization and photocatalytic properties. *Appl. Catal. A Gen.* **2005**, *284*, 193–198. [[CrossRef](#)]
30. Ashraf, M.A.; Peng, W.; Zare, Y.; Rhee, K.Y. Effects of Size and Aggregation/Agglomeration of Nanoparticles on the Interfacial/Interphase Properties and Tensile Strength of Polymer Nanocomposites. *Nanoscale Res. Lett.* **2018**, *13*, 1–7. [[CrossRef](#)] [[PubMed](#)]
31. Azizian, S. Kinetic models of sorption: A theoretical analysis. *J. Colloid Interface Sci.* **2004**, *276*, 47–52. [[CrossRef](#)]
32. Foo, K.Y.; Hameed, B.H. Insights into the modeling of adsorption isotherm systems. *Chem. Eng. J.* **2010**, *156*, 2–10. [[CrossRef](#)]
33. Ayawei, N.; Ebelegi, A.N.; Wankasi, D. Modelling and Interpretation of Adsorption Isotherms. *J. Chem.* **2017**, *2017*, 3039817. [[CrossRef](#)]
34. Tan, Y.; Kilduff, J.E. Factors affecting selectivity during dissolved organic matter removal by anion-exchange resins. *Water Res.* **2007**, *41*, 4211–4221. [[CrossRef](#)] [[PubMed](#)]
35. Li, J.; Zhang, S.; Chen, C.; Zhao, G.; Yang, X.; Li, J.; Wang, X. Removal of Cu(II) and Fulvic Acid by Graphene Oxide Nanosheets Decorated with Fe₃O₄ Nanoparticles. *ACS Appl. Mater. Interfaces* **2012**, *4*, 4991–5000. [[CrossRef](#)] [[PubMed](#)]
36. Shao, D.D.; Fan, Q.H.; Li, J.X.; Niu, Z.W.; Wu, W.S.; Chen, Y.X.; Wang, X.K. Removal of Eu(III) from aqueous solution using ZSM-5 zeolite. *Microporous Mesoporous Mater.* **2009**, *123*, 1–9. [[CrossRef](#)]
37. Zhang, G.; Ni, C.; Liu, L.; Zhao, G.; Fina, F.; Irvine, J.T.S. Macro-mesoporous resorcinol-formaldehyde polymer resins as amorphous metal-free visible light photocatalysts. *J. Mater. Chem. A* **2015**, *3*, 15413–15419. [[CrossRef](#)]
38. Chen, X.; Mao, S.S. Titanium dioxide nanomaterials: Synthesis, properties, modifications, and applications. *Chem. Rev.* **2007**, *107*, 2891–2959. [[CrossRef](#)]

39. Huang, X.; Yang, W.; Zhang, G.; Yan, L.; Zhang, Y.; Jiang, A.; Xu, H.; Zhou, M.; Liu, Z.; Tang, H.; et al. Alternative synthesis of nitrogen and carbon co-doped TiO₂ for removing fluoroquinolone antibiotics in water under visible light. *Catal. Today* **2019**, *361*, 11–16. [[CrossRef](#)]
40. Simonetti, E.A.N.; de Simone Cividanes, L.; Campos, T.M.B.; de Menezes, B.R.C.; Brito, F.S.; Thim, G.P. Carbon and TiO₂ synergistic effect on methylene blue adsorption. *Mater. Chem. Phys.* **2016**, *177*, 330–338. [[CrossRef](#)]
41. Wu, C.H.; Kuo, C.Y.; Chen, S.T. Synergistic effects between TiO₂ and carbon nanotubes (CNTs) in a TiO₂/CNTs system under visible light irradiation. *Environ. Technol.* **2013**, *34*, 2513–2519. [[CrossRef](#)]
42. Houas, A.; Lachheb, H.; Ksibi, M.; Elaloui, E.; Guillard, C.; Herrmann, J.M. Photocatalytic degradation pathway of methylene blue in water. *Appl. Catal. B: Environ.* **2001**, *31*, 145–157. [[CrossRef](#)]
43. Lakshmi, S.; Renganathan, R.; Fujita, S. Study on TiO₂-mediated photocatalytic degradation of methylene blue. *J. Photochem. Photobiol. A Chem.* **1995**, *88*, 163–167. [[CrossRef](#)]
44. Makuła, P.; Pacia, M.; Macyk, W. How To Correctly Determine the Band Gap Energy of Modified Semiconductor Photocatalysts Based on UV–Vis Spectra. *J. Phys. Chem. Lett.* **2018**, *9*, 6814–6817. [[CrossRef](#)] [[PubMed](#)]
45. Ho, Y.S.; McKay, G. Pseudo-second order model for sorption processes. *Process Biochem.* **1999**, *34*, 451–465. [[CrossRef](#)]
46. Sahoo, T.R.; Prelot, B. Adsorption processes for the removal of contaminants from wastewater: The perspective role of nano-materials and nanotechnology. In *Nanomaterials for the Detection and Removal of Wastewater Pollutants*; Elsevier: Amsterdam, The Netherlands, 2020; pp. 161–222.

Article

Integrated Adsorption–Photodegradation of Organic Pollutants by Carbon Xerogel/Titania Composites

Anam Safri ¹, Ashleigh Jane Fletcher ^{1,*}, Ramsha Safri ² and Hifza Rasheed ³¹ Department of Chemical and Process Engineering, University of Strathclyde, Glasgow G1 1XJ, UK² College of Medicine and Surgery, The Shaheed Zulfiqar Ali Bhutto Medical University Islamabad, Islamabad 44000, Pakistan³ Pakistan Council of Research in Water Resources (PCRWR), Islamabad 44000, Pakistan

* Correspondence: ashleigh.fletcher@strath.ac.uk; Tel.: +44-141-5482-431

Abstract: Recent studies on the removal of pollutants via adsorption include the use of carbon-based adsorbents, due to their high porosity and large surface area; however, such materials lack photoactive properties. This study evaluates the synergistic effect of integrated mesoporous carbon xerogel (derived from resorcinol formaldehyde) and titanium dioxide (TiO₂) for combined adsorption and photodegradation application. The complex formed between carbon xerogel and TiO₂ phase was investigated through FTIR, proving the presence of a Ti–O–C chemical linkage. The physicochemical properties of the synthesised adsorbent–photocatalyst were probed using FESEM, BET analysis and UV–Vis analysis. The kinetics, equilibrium adsorption, effect of pH, and effect of adsorbent dosage were investigated. The expansion of the absorbance range to the visible range was verified, and the corresponding band gap evaluated. These properties enabled a visible light response when the system was exposed to visible light post adsorption. Hence, an assistive adsorption–photodegradation phenomenon was successfully executed. The adsorption performance exhibited 85% dye degradation which improved to 99% following photodegradation. Further experiments showed the reduction of microorganisms under visible light, where no microbial colonies were observed after treatment, indicating the potential application of these composite materials.

Keywords: carbon xerogel; TiO₂ photocatalysis; adsorption–photodegradation; dye degradation; adsorption isotherm; adsorption kinetics; microbial degradation



Citation: Safri, A.; Fletcher, A.J.; Safri, R.; Rasheed, H. Integrated Adsorption–Photodegradation of Organic Pollutants by Carbon Xerogel/Titania Composites. *Molecules* **2022**, *27*, 8483. <https://doi.org/10.3390/molecules27238483>

Academic Editor: Oualid Hamdaoui

Received: 1 November 2022

Accepted: 28 November 2022

Published: 2 December 2022

Publisher's Note: MDPI stays neutral with regard to jurisdictional claims in published maps and institutional affiliations.



Copyright: © 2022 by the authors. Licensee MDPI, Basel, Switzerland. This article is an open access article distributed under the terms and conditions of the Creative Commons Attribution (CC BY) license (<https://creativecommons.org/licenses/by/4.0/>).

1. Introduction

Amongst several conventional water treatment techniques, adsorption is recognised as one of the most simple, reliable, and effective methods. New techniques use nano adsorbents, of which one of the main groups for wastewater treatment are carbon-based adsorbents [1]. Generally, carbon is preferred, due to its high effectiveness, abundant availability, and low cost. However, adsorption using basic carbon materials is restricted by slow kinetics, while advanced adsorbents, for example, zeolites or metal-based nano-adsorbents are expensive, and experience a loss of adsorption sites during the desorption process, resulting in pollution during the application process and requiring high energy for their regeneration [2].

Photodegradation techniques use light irradiance for the activation of a photocatalyst, upon which they generate charge carriers which transfer to the surface and undergo a series of chemical reactions to generate reactive oxide species or hydroxyl radicals. These species target the pollutant surface and chemically decompose it into harmless substances [3]. Titanium dioxide (TiO₂) is widely studied in this regard, due to its non-toxicity, cost efficiency and ability to oxidise organic pollutants and eventually convert them to carbon dioxide and water [4]. The major limitations encountered by TiO₂, which restricts the process efficiency, include agglomeration, wide band gap and rapid recombination of

photogenerated charge carriers. Nevertheless, the adsorption capacity on the surface of TiO_2 is poor; therefore, the degradation process is restricted. The use of carbon as a support matrix can not only enhance the adsorption capacity, but also solve the problem of charge recombination [5]. Additionally, chemical functionalisation can modify the bandgap of TiO_2 ; hence, enhanced performance of an integrated system under visible light is possible.

As a consequence of the likelihood of improved performance through composite development, several studies have reported on the functional crosslinking of carbon and TiO_2 through a wide range of synthesis procedures [6]. Sol–gel is commonly employed, as the synthesis process can be controlled to achieve strong chemical bonding and dispersibility of TiO_2 nanoparticles. Other methods are expensive, time-consuming and difficult to implement, due to stringent control of factors [7]. With regard to material properties, studies related to chemical interactions between carbon and TiO_2 are limited. Not many studies report on the complex formation between functional moieties of carbon and TiO_2 , which is theoretically responsible for the modification of the electronic structure and thus enables visible light response [8]. In this study, we have integrated TiO_2 in a nano mesoporous carbon xerogel (CX) to obtain a visible light-activated adsorbent–photocatalyst. CX was derived from the polycondensation of resorcinol and formaldehyde in the presence of a base catalyst. Resorcinol formaldehyde gels have been utilised for several applications including thermal insulation [9], electrical conductivity [10], adsorption, and gas storage [11]. However, less attention has been paid to studying their application in the water treatment sector, particularly for visible light photocatalysis. Our reasons for choosing resorcinol–formaldehyde as a carbon source to produce CX were (i) it is composed of a unique structure (aromatic rings and OH groups), which can bind with TiO_2 to produce new electronic interactions between CX and TiO_2 and activate visible light response; and (ii) the materials are generally highly mesoporous structures, possessing large surface areas for effective adsorption of pollutants. Within the nanostructure, homogeneously distributed TiO_2 forms a heterojunction with the carbon substrate, due to the chemical interaction between CX and TiO_2 , resulting in complex formation at the interface of the material. Remarkably, such structures can absorb visible light and exhibit photoactivity under visible light irradiation.

This indicates that integrated CX and TiO_2 may be an effective adsorbent–photocatalyst to target a wide range of pollutants in contaminated water, including dyes and microbes. Thus, a combined photocatalytic adsorbent, CXTi, was synthesised to exploit the synergistic effect of both adsorption and photocatalysis. The ratios of CX and TiO_2 were carefully selected to optimise the physicochemical and optical properties imperative to maximise adsorbent–adsorbate interactions and utilisation of a wide fraction of the electromagnetic spectrum. The synthesised CXTi was tested against adsorption and photodegradation of methylene blue (MB) from aqueous solutions, and the acquired data analysed using kinetic and isothermal analysis. Additionally, antimicrobial tests were performed against the reduction of an indicator microorganism, i.e., total faecal coliform.

2. Results and Discussion

2.1. Structural Properties of CXTi

Figure 1a–c show micrographs of synthesised CXTi at different magnifications, which confirm that the carbons phase developed as a spherical form, as previously reported for carbons derived from the polycondensation and subsequent pyrolysis of resorcinol and formaldehyde gels [12]. The micrographs reveal uniform microclusters of interconnected microspheres with diameters in the range 1.2–1.5 μm . The surface heterogeneity/roughness observed in a section of the micrograph in Figure 1c, marked by red arrows, denotes carbon xerogel spheres engulfed by TiO_2 nanoparticles. The yellow arrows show the porosity in the CXTi structure. The chemical bonding between carbon and TiO_2 was confirmed by the recorded FTIR spectrum, shown in Figure 1d, where characteristic peaks of a typical resorcinol–formaldehyde-derived carbon were observed, including signals from C–H, C=C, C–O–C of aromatic rings and methylene bridges [13]. The broad peak at 3300 cm^{-1} is

associated with OH of the phenolic groups. The vibrations in the range 2000–1700 are ascribed to C-H bending of aromatic moieties. The aromatic ether bridges formed during the polycondensation of resorcinol (R) and formaldehyde (F) result in the absorption bands observed at 1605 and 1473 cm^{-1} . These observations are in agreement with those reported by Awadallah et al., for the mesoporous RF xerogels [14]. The chemical bonding between the carbon xerogel and TiO_2 was confirmed by Ti-O-C functionalities in the range 1200–1000 cm^{-1} [15], indicating that the surface moieties of carbon xerogel support the attachment of TiO_2 . This heterojunction has been reported as a charge-transfer complex, which promotes electronic interactions and enhances the visible light response of the integrated carbon and TiO_2 material [16,17]. Furthermore, signals below 1000 cm^{-1} are attributed to functional groups of titanium ethoxide and Ti-O-Ti linkages [18].

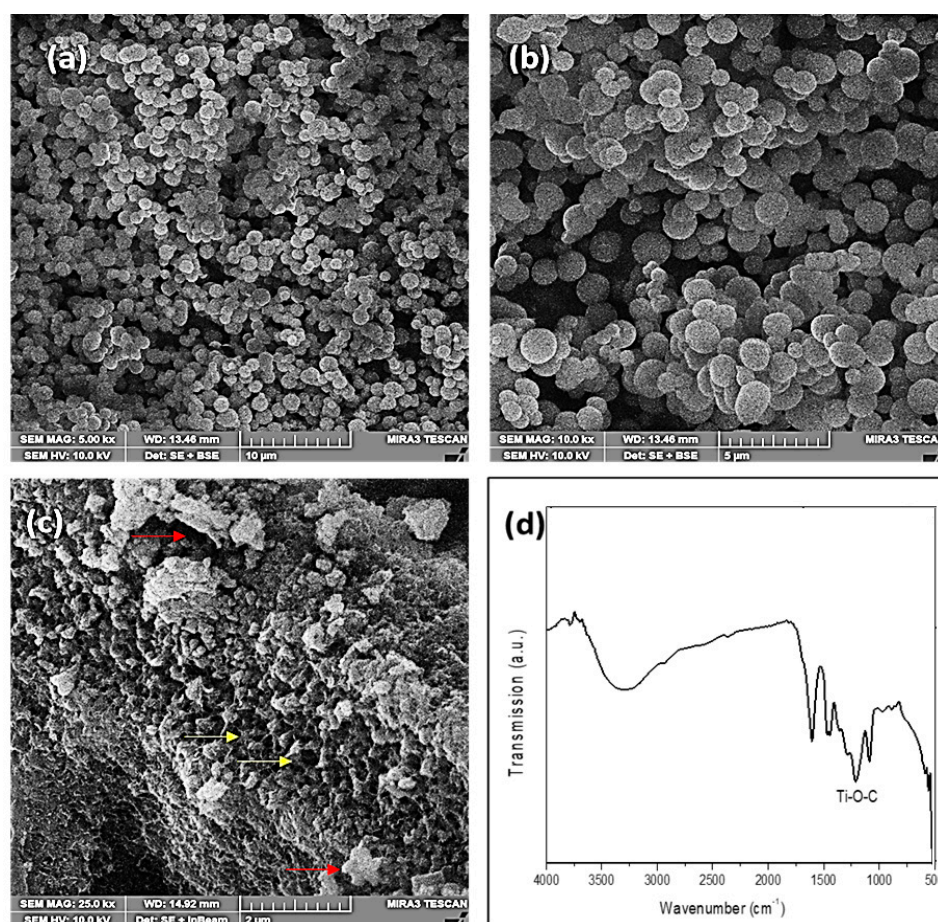


Figure 1. (a–c) FESEM micrographs (contrast altered) at different magnifications and (d) FTIR spectrum of CXTi synthesised in this study.

The surface area and porosity of synthesised CXTi were obtained using nitrogen sorption isotherms and subsequent BJH analysis to determine the pore size distributions [19], as shown in Figure 2. The isotherm shows that the characteristics of a typical mesoporous carbon xerogel derived from resorcinol–formaldehyde are retained [12]. The BET surface area and pore volume were calculated to be 384 $\text{m}^2 \text{g}^{-1}$ and 0.8 $\text{cm}^3 \text{g}^{-1}$, respectively. A narrow pore size distribution was observed, and the average pore width was calculated to be ~9 nm, as represented in the inset of Figure 2. It is evident that the shape of the isotherm is Type IV with a distinct hysteresis loop of Type H1 [20]. These findings suggest the presence of ordered mesopores with a uniform cylindrical shaped, open-ended three-dimensional pore network [20]. The calculated mesoporosity in the structure was 93%. These textural properties, comprising high surface area and well-developed mesoporous structure, are expected to facilitate the adsorption process and enhance the photocatalytic activity.

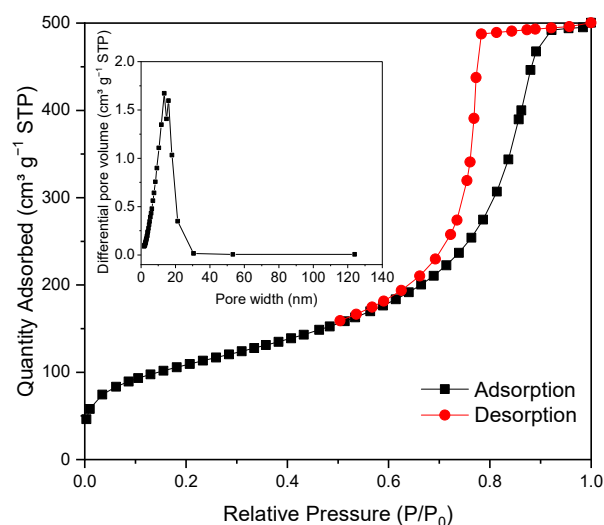


Figure 2. Nitrogen adsorption/desorption isotherm of CXTi synthesised in this study.

High adsorbent loading appears to reduce adsorption performance, while low adsorbent loading results in fewer pollutant molecules interacting with the active sites on the adsorbent; hence, the amount of adsorbent used is crucial in determining the ultimate adsorption performance. The study of the effect of dosage rate of CXTi on adsorption performance was performed at an initial concentration of 100 mg L^{-1} of MB (Figure 3a). It was observed that the amount of MB adsorbed increased rapidly with increasing adsorbent dose, from 0.005 to 0.01 g, tested against 25 mL of MB solution. This is attributed to the large surface area, mesoporous character and availability of vacant adsorptive sites associated with the CXTi sorbent. Further increase in adsorbent dose, up to 0.10 g, showed no significant increase in removal of MB. At this point, the concentration of adsorbate on the surface of the adsorbent, and the adsorptive in solution, reach equilibrium. Accordingly, 0.01 g was chosen as the optimal amount of adsorbent per 25 mL to conduct the following adsorption experiments.

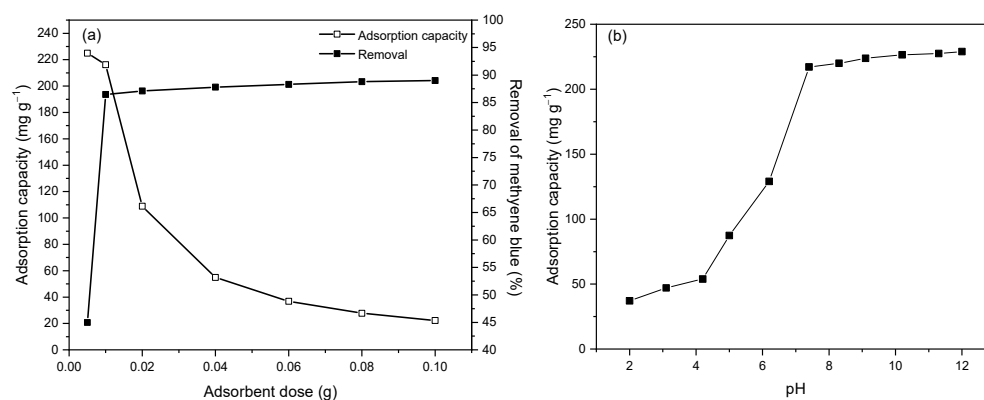


Figure 3. Effect of (a) adsorbent dosage and (b) pH on the adsorption capacity of methylene blue using CXTi synthesised in this study ($T = 23 \text{ }^{\circ}\text{C}$, adsorbent dose = 0.01 g, $C_0 = 100 \text{ mg L}^{-1}$).

Additionally, for optimum adsorption performance, it is important to determine a suitable operating pH, since this affects the surface charge and ionisation of pollutant molecules, while unfavourable adsorption, dissolution and decomposition lead to low adsorption uptakes [21]. Figure 3b shows the effect of pH on the adsorption of MB by CXTi, as a function of pH value. The adsorption capacity of MB at acidic pH (≤ 6) was low, which may be due to the positively charged sample surface repelling the cationic MB dye molecules. At higher pH values, i.e., more basic, in the range of 8–12, the interface of CXTi is negatively charged, which means it can favourably adsorb the cationic MB molecule;

hence, enhanced adsorption capacity is observed. Therefore, a pH of ~ 7.2 was maintained for all remaining adsorption experiments.

2.2. Adsorption Kinetics

Figure 4 shows the kinetic data obtained for MB adsorption on CXTi at different initial concentrations ($50\text{--}200\text{ mg L}^{-1}$) and contact times ($0\text{--}240\text{ min}$). It was observed that the adsorption capacity increases with increase in initial concentration, as time elapsed. This is attributed to increased frequency of collisions between MB molecules and the sample surface, which overcomes the resistance to mass transfer between the adsorbate and the adsorbent, and results in the immediate occupancy of available active sites [22]. Rapid attainment of equilibrium is attributed to the highly porous nature of the sample with abundant active sites. In this case, $\pi\text{-}\pi$ interactions between the MB dye molecules and the aromatic groups of the carbon xerogel, along with electrostatic interactions between the MB dye molecules and the hydroxyl groups of TiO_2 , are predominant binding strengths between the adsorbent and adsorbate. The adsorption process slows after this initial phase and eventually attains equilibrium at 90 min, as the mass transfer rate slows down due to saturation of the active sites, thus making it difficult for the MB molecules to further adsorb on the sample surface. In addition to this, higher initial concentrations of the adsorptive may result in aggregation of MB or charge repulsion of MB dye species, thereby decelerating the adsorption process [23]; thus, it takes longer for the adsorptive to diffuse deeper into the pores of the adsorbent.

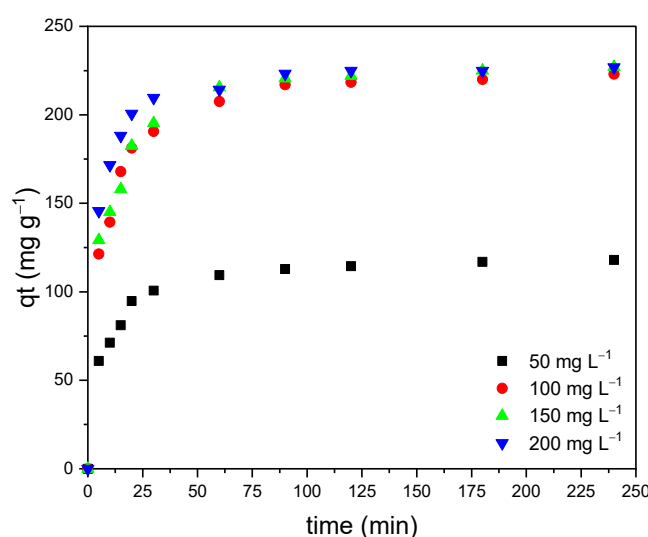


Figure 4. Effect of contact time ($0\text{--}240\text{ min}$) on MB adsorption on CXTi synthesised in this study, at initial concentrations of $50, 100, 150$ and 200 mg L^{-1} . Note: Error bars are negligibly small, hence the overlap of the limits.

To gain a better understanding of the kinetic and diffusion behaviour of the adsorptive–adsorbent system, the experimental data were analysed by models including Pseudo First Order (PFO), Pseudo Second Order (PSO), Elovich, and Intra-Particle Diffusion (IPD) [24]. The PFO model has frequently been used to describe kinetic processes under non-equilibrium conditions. PFO assumes that the rate of adsorption is proportional to the driving force, i.e., the difference between equilibrium concentration and solid phase concentration. The integrated form of the PFO model is given in Equation (1):

$$q_t = q_e \left(1 - e^{-k_1 t}\right) \quad (1)$$

By contrast, the PSO equation assumes that the overall adsorption rate is proportional to the square of the driving force. The integrated form of PSO model is given in Equation (2):

$$q_t = \frac{k_2 t q_e^2}{1 + k_2 t q_e} \quad (2)$$

In both Equations (1) and (2), q_t (mg g^{-1}) and q_e (mg g^{-1}) are the concentrations of MB dye molecules at time t and at equilibrium, respectively. k_1 ($\text{g mg}^{-1} \text{min}^{-1}$) and k_2 ($\text{g}^{-1} \text{mg min}^{-1}$) are the PFO and PSO rate constants, respectively.

Figure 5 shows the experimentally determined adsorption (q_{exp}) data fitted to the PFO and PSO models. The evaluated parameters, including q_{exp} , q_t (adsorption calculated at given time), first order rate constant k_1 , second order rate constant k_2 , and regression coefficient, are presented in Table 1. It was observed that PFO is incompatible with the experimental data, as the regression coefficient deviates from 1 throughout the concentration range; hence, physisorption is less likely to be the primary adsorption phenomenon.

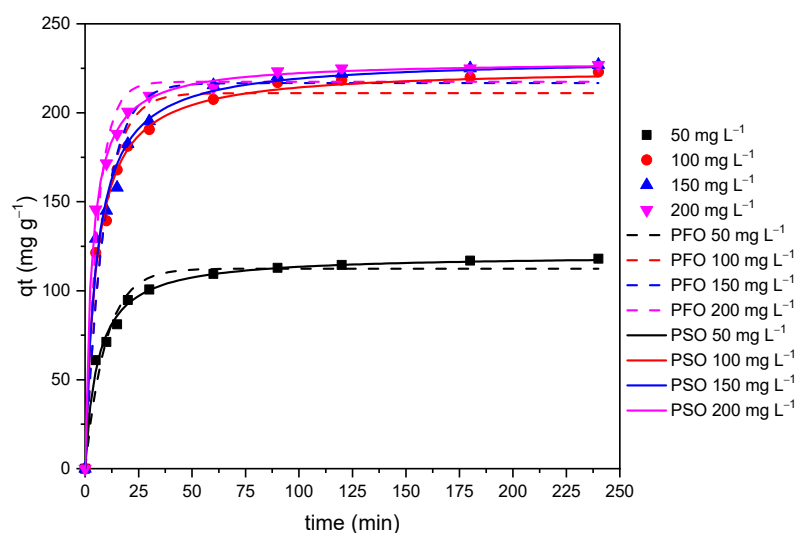


Figure 5. Pseudo first order and pseudo second order model fittings to experimental data for adsorption of MB on CXTi synthesised in this study, at initial concentrations of 50, 100, 150 and 200 mg L^{-1} ($T = 23\text{ }^{\circ}\text{C}$, dose = 0.01 g mL^{-1}).

Table 1. Kinetic constants for MB adsorption by CXTi; q_{exp} is the experimental amount adsorbed at equilibrium.

	50 mg L^{-1}	100 mg L^{-1}	150 mg L^{-1}	200 mg L^{-1}
q_{exp}	113	217	220	221
Pseudo first order				
$q_t \text{ mg g}^{-1}$	112	211	216	217
$k_1 \text{ min}^{-1}$	0.104	0.119	0.114	0.177
R^2	0.963	0.959	0.947	0.975
Pseudo second order				
$q_t \text{ mg g}^{-1}$	120	225	230	229
$k_2 (10^{-3}) \text{ g mg}^{-1} \text{ min}^{-1}$	1.40	0.875	0.839	1.43
R^2	0.993	0.993	0.990	0.999
Elovich				
R^2	0.976	0.977	0.979	0.979

By contrast, the regression coefficient values obtained for PSO are much closer to 1, indicating a better fit to the experimental data, and the calculated adsorption capacities through PSO equation closely match with the experimentally determined adsorption capacities (q_{exp}), as shown in Table 1. Hence, the system can be best interpreted by the PSO model, and thus it can be concluded that the interaction between the surface of CXTi and MB is chemical in nature, and MB is mainly removed by a chemisorption phenomenon [25].

To further verify the chemisorption phenomenon of adsorption, the kinetic data was fitted to the Elovich equation, as shown in Equation (3) [24].

$$q_t = \frac{1}{B} \ln(AB) + \frac{1}{B} \ln(t) \quad (3)$$

where A ($\text{mg g}^{-1} \text{min}^{-1}$) and B (g mg^{-1}) are the initial rate constant of adsorption and desorption, respectively. This equation has been applied to wastewater treatment systems and is useful in describing chemisorption processes, which involve valence forces through sharing or exchange between the adsorbate and the adsorbent. The equation also signifies that the removal efficiency decreases with time because of the coverage of active sites [24]. The fit of the experimental data to the Elovich model is shown in Figure 6, and the obtained fits are good ($R^2 > 0.97$), therefore verifying chemisorption within the adsorption process [26]. In addition, FTIR spectra of the adsorbent were recorded after adsorption treatment to confirm that the functional groups on CXTi are responsible for the observed adsorption activity. As shown in Figure 7, the change in spectra before and after adsorption of MB is evident, where the peaks associated with C-H, C=C and C-O-C vibrations appeared intense in comparison with CXTi before adsorption. Thus, it can be concluded that the adsorption of MB onto CXTi occurred predominantly via π - π interactions due to the aromatic rings of carbon xerogel [27].

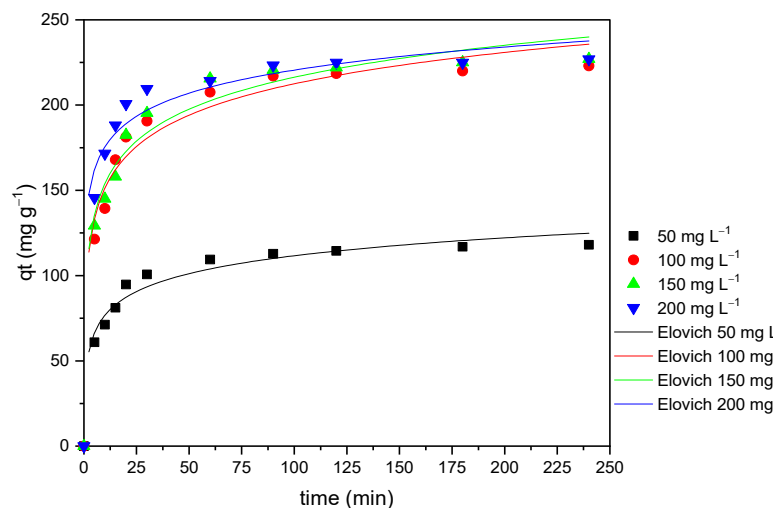


Figure 6. Elovich model fitting to experimental data for adsorption of MB on CXTi synthesised in this study, at initial concentrations of 50, 100, 150 and 200 mg L^{-1} ($T = 23\text{ }^{\circ}\text{C}$, dose = 0.01 g mL^{-1}).

To further understand the internal diffusion mechanism within the adsorbate–adsorbent system, the IPD model was applied to the experimental data. The IPD model is commonly applied to study the rate limiting step during the adsorption process, which is defined by either mass transfer or the diffusion of adsorbate and pore diffusion. IPD is studied by fitting the data to Equation (4) [24].

$$q_t = k_{ip}t^{0.5} + C \quad (4)$$

k_{ip} is the rate constant ($\text{mg}^{-1} \text{g min}^{0.5}$) and the intercept C is the boundary layer thickness. The value of C defines the boundary layer effect. A plot of q_t vs. $t^{0.5}$ gives a linear function;

if the line passes through the origin, IP diffusion controls the adsorption process. If the line does not pass through origin and shows multiple linear segments, these segments correspond to different mechanisms that control the adsorption process [24].

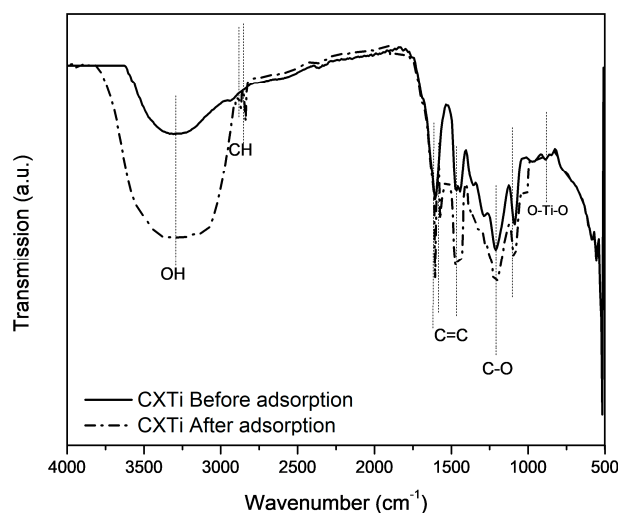


Figure 7. FTIR spectra of CXTi recorded before and after the adsorption treatment.

Figure 8 shows the plot of MB adsorption onto CXTi fitted to the IPD equation plotted against $t^{0.5}$. The multistep adsorption process is evident through the multi-linearity of the data (marked as stages 1, 2 and 3), which indicates that intra-particle diffusion was not rate limiting, and other adsorption mechanisms were also involved [25]. This means that the adsorption process, stage 1, began with rapid diffusion of MB from the bulk phase to the external surface of the sample, adsorbing swiftly due to the immediate availability of a large proportion of adsorption sites. The second stage was slower due to the boundary layer effect causing slow diffusion of the adsorptive into the porous structure of the sample. The third stage suggests an equilibrium stage, where intra-particle diffusion starts to slow down due to low adsorptive concentration or saturation of the active sites, preventing surface reactions from occurring [24,25]. The calculated parameters obtained by piecewise fitting are shown in Supplementary Materials, Table S1.

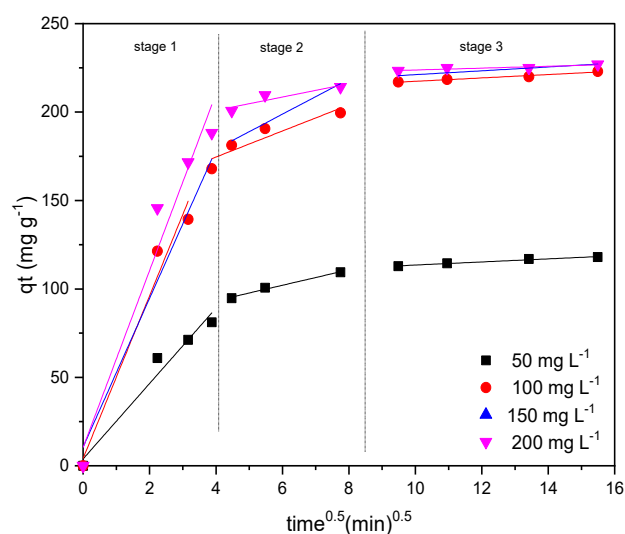


Figure 8. The intra-particle diffusion model linearly fitted to experimental data for adsorption of MB onto CXTi synthesised in this study, at initial concentrations of 50, 100, 150 and 200 mg L⁻¹ (T = 23 °C, dose = 0.01 g mL⁻¹).

2.3. Adsorption Isotherm Study

The maximum equilibrium adsorption capacity was determined over the concentration range 0–200 mg L⁻¹, recorded at intervals of 20 mg L⁻¹. It can be observed that the adsorption capacity of CXTi increased with the increase in initial concentration of MB. A rapid increase in adsorption capacity was observed at low concentration, suggesting that CXTi has abundant active sites. With increasing MB concentration, the adsorption capacity reached a saturation plateau, indicating that the active sites were completely occupied by MB dye molecules. To understand the interactions between the adsorbent and adsorbate at equilibrium, adsorption isotherms obtained in this study were analysed according to the nonlinear form of Langmuir, Freundlich, and Sips isotherm models, and values of the associated model parameters were determined. The model showing the best fit to the experimental data, based on determination of the regression coefficient (R²), was selected for adsorption interpretation. The Langmuir isotherm model is relevant for the prediction of monolayer adsorption on energetically uniform homogenous adsorption sites, whereas the Freundlich isotherm model predicts multilayer adsorption [28]. Langmuir and Freundlich models are expressed in Equations (5) and (7), respectively.

$$q_e = \frac{q_L K_L C_e}{1 + C_e K_L} \quad (5)$$

where q_e (mg g⁻¹) is the MB uptake at equilibrium, C_e (mg L⁻¹) is the equilibrium concentration, q_L (mg g⁻¹) is the amount of adsorbate at complete monolayer coverage, and K_L is the Langmuir constant related to the energy of adsorption, which can be used to determine the extent of adsorbate–adsorbent interaction. Furthermore, adsorption favourability can be determined by a dimensionless constant called the separation factor, R_L , expressed in Equation (6):

$$R_L = \frac{1}{(1 + K_L C_0)} \quad (6)$$

where, C_0 refers to the initial concentration of the adsorbate in (mg L⁻¹), and K_L is Langmuir constant related to the adsorption capacity. If the value of $R_L > 1$, the adsorption is unfavourable, and favourable when $0 < R_L < 1$. The Freundlich isotherm model is represented by:

$$q_e = K_F C_e^{1/n_F} \quad (7)$$

where q_e (mg g⁻¹) and C_e (mg L⁻¹) are as defined in the Langmuir equation, adsorption affinity is related to the adsorption constant K_F , and n_F indicates the magnitude of the adsorption driving force and is used to evaluate the adsorption favourability. When $1/n_F$ is greater than 0 ($0 < 1/n_F < 1$), adsorption is favourable; whereas, when $1/n_F$ is greater than 1, the adsorption process is unfavourable. Moreover, the adsorption intensity or surface heterogeneity and the energy distribution, as well as the adsorbate site heterogeneity, is indicated by $1/n_F$. A value of n_F between 2 and 10 represents good adsorption, indicating a high adsorption capacity, while values between 1 and 2 indicate moderate adsorption capacity, and values less than 1 indicate a small adsorption capacity.

Sips, a three-parameter model, is a combination of Langmuir and Freundlich adsorption isotherm models. It is stated that the Sips model predicts characteristics of the Langmuir isotherm at higher concentrations, while predicting Freundlich isotherm behaviour at lower concentrations [29]. The Sips model is expressed in Equation (8):

$$q_e = \frac{q_s K_s C_e^{n_s}}{1 + K_s C_e^{n_s}} \quad (8)$$

where q_e (mg g⁻¹) and C_e (mg L⁻¹) are as defined in the Langmuir and Freundlich equations, K_s is the Sips isotherm model constant (L g⁻¹), and n_s is the Sips isotherm exponent, which is related to the heterogeneity factor that represents the deviation of the linearity of adsorption. The heterogeneity of adsorbents in the equation is illustrated by

$1/n_s$; if $1/n_s < 1$, the adsorbent surface is heterogeneous, and if $1/n_s \sim 1$, the surface can be described as homogenous [29].

The fittings of the Langmuir, Freundlich and Sips isotherm models to adsorption data obtained for MB on CXTi are presented in Figure 9, and the calculated parameters are shown in Table 2. The fitting results based on regression coefficient values indicate that the Sips isotherm model exhibits the best fit to the experimentally obtained adsorption equilibrium data. The maximum adsorption capacity obtained from the Sips model ($q_s = 217 \text{ mg g}^{-1}$) was closest to the experimentally determined value ($q_e = 218 \text{ mg g}^{-1}$). The heterogeneity factor, n_s , is greater than 1; therefore, the suggestion is that the adsorption surface is heterogeneous. The evaluated parameters from the Freundlich model also validate the heterogeneous nature of the sorbent, since the value of n_F is greater than 1. Additionally, the separation factor, R_L is less than 1, which indicates favourable adsorption. The isotherm models fit most appropriately in the order Sips > Langmuir > Freundlich.

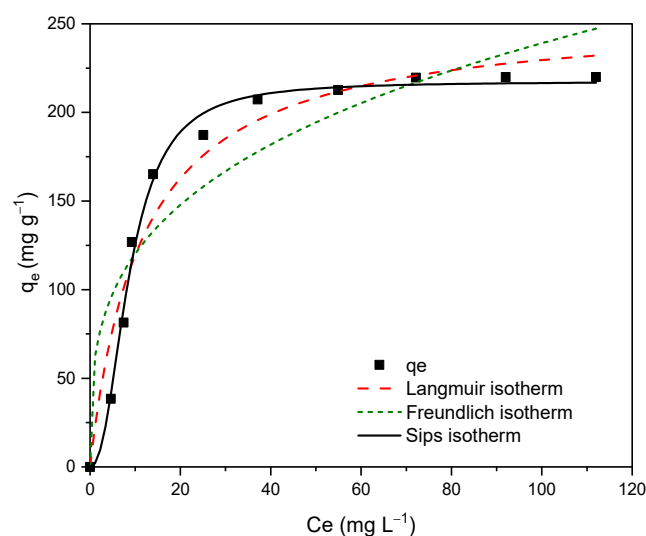


Figure 9. Adsorption isotherm fittings for Langmuir, Freundlich and Sips isotherm models for MB adsorption on CXTi synthesised in this study.

Table 2. Parameters for MB adsorption at equilibrium computed from Langmuir, Freundlich and Sips isotherm model equations.

Isotherm Model	Parameters	
Experimental	$q_e \text{ (mg g}^{-1}\text{)}$	218
	$q_L \text{ (mg g}^{-1}\text{)}$	255
Langmuir	$K_L \text{ (L mg}^{-1}\text{)}$	0.087
	R_L	0.103
	R^2	0.951
Freundlich	$K_F \text{ mg g}^{-1} \text{ (L mg}^{-1}\text{)}^{1/n}$	60.5
	n_F	3.35
	R^2	0.861
Sips	$q_s \text{ (mg g}^{-1}\text{)}$	217
	$K_s \text{ (L mg}^{-1}\text{)}$	0.007
	n_s	2.28
	R^2	0.992

2.4. Photocatalytic Study

As reflected in Figure 10a, absorption extends broadly to the visible region of the electromagnetic spectrum, with maximum absorption observed at 509 nm. The corresponding band gap calculated through the Tauc method was 2.24 eV [30]; meaning that CXTi can absorb and activate under visible light irradiation. This point was proven by performing

further experiments post adsorption to observe decolourisation of MB under visible light. Figure 10c validates the reduction of MB, with a flattened curve observed after 30 min of exposure to light irradiation. Consequent reduction in MB concentration by combined adsorption–photocatalysis is shown in Figure 10d. It was observed that the MB removal capacity of CXTi increased from ~85 to 99% upon light irradiation. As can be seen in Table 3, these results are more efficient than those of similar systems. The photocatalytic activity in this work arises from the synergy of CX and TiO₂. The chemical linkage between CX and TiO₂ forms a surface complex via a hydroxyl group, where a single oxygen atom separates the phenolic ligand from the TiO₂ surface [16]. This binding phenomenon is similar to that previously described for aromatic compounds with phenolic hydroxyl groups, which can chemically bind with functional groups of TiO₂ [31]. Binding through the hydroxyl group enables strong coupling due to ligand–metal charge transfer (LMCT). The formation of LMCT complexes modifies the overall electronic structure and creates a new absorption band in the visible light [31,32], as illustrated in Scheme 1. The visible light photocatalytic activity occurs when light falls on the surface of CXTi, resulting in generation of photoexcited charge carriers (electron and hole pairs). These charge carriers transfer from the highest occupied molecular orbital (HOMO) of the CX to the conduction band of TiO₂, similar to other chemically combined carbon/TiO₂ systems [33]. Charge carriers successfully transferred to the surface of the photocatalyst take part in redox reactions and produce reactive oxide species (ROS), including hydroxy radicals (\bullet OH) and superoxide radicals ($O_2^{\bullet-}$) that can efficiently decompose adsorbed MB species [23,34].

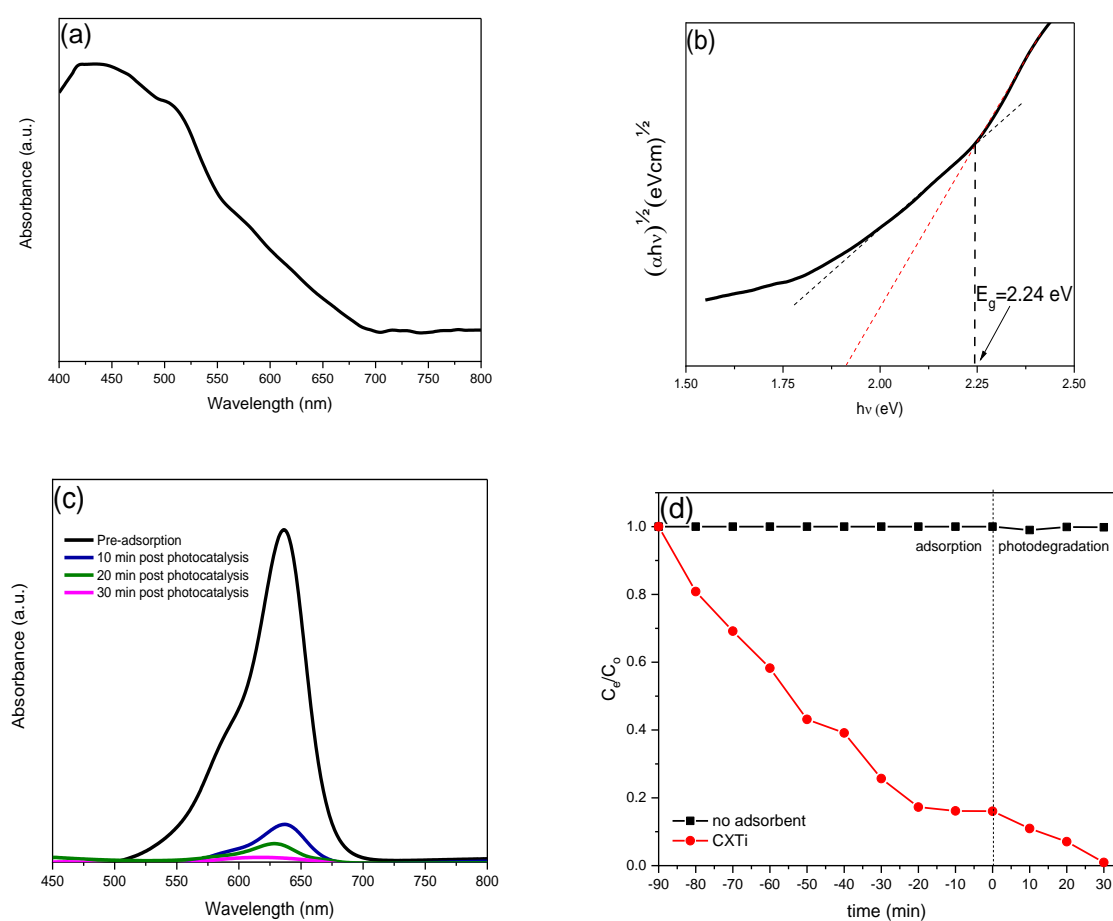
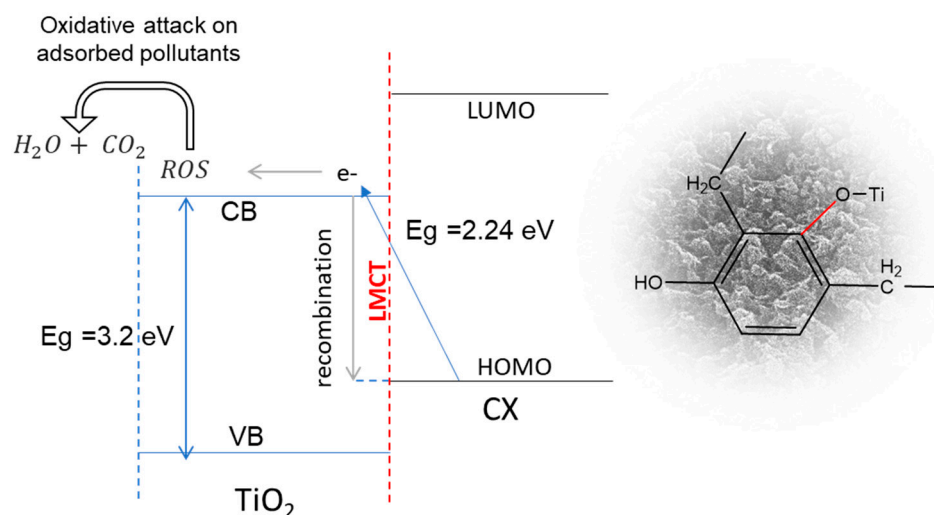


Figure 10. (a) UV-Vis absorption spectrum of CXTi synthesised in this study, (b) Tauc plot of CXTi, (c) post adsorption photocatalytic performance of CXTi under visible light irradiation and (d) kinetics of combined adsorption and photodegradation of MB on CXTi.

Table 3. Characteristics and degradation performance of comparable systems.

Material	Procedure	Inorganic Content	Surface Area $\text{m}^2 \text{g}^{-1}$	Band gap (eV)	Pollutant	Removal Efficiency	Ref.
Magnet photocatalyst based on Carbon Xerogels/ TiO_2	Photoinactivation under UV irradiation	$\text{Fe}_3\text{O}_4/\text{SiO}_2/\text{N-CXTi} = 70\%$ $\text{Fe}_3\text{O}_4/\text{N-CXTi} = 67\%$	$\text{Fe}_3\text{O}_4/\text{SiO}_2/\text{N-CXTi} = 388$ $\text{Fe}_3\text{O}_4/\text{N-CXTi} = 212$	$\text{Fe}_3\text{O}_4/\text{SiO}_2/\text{N-CXTi} = 3.22$ $\text{Fe}_3\text{O}_4/\text{SiO}_2/\text{N-CXTi} = 3.10$	Acetaminophen	$\text{Fe}_3\text{O}_4/\text{SiO}_2/\text{N-CXTi} = 98\%$ $\text{Fe}_3\text{O}_4/\text{SiO}_2/\text{N-CXTi} = 85\%$	[35]
Carbon/ TiO_2 gels	Adsorption–Photodegradation under UV–Vis irradiation	10%	588	2.97	Methylene blue, microbes	74%	[17]
Carbon Xerogel/Ti	Simultaneous adsorption–photodegradation	38%	650	2.68	Acetaminophen	96%	[36]
Carbon Xerogel/ TiO_2 composite	Adsorption–photodegradation	33%	401	2.60	Orange G	70%	[37]
TiO_2 /Carbon Aerogel composite	Photoinactivation under UV irradiation	85%	124	-	Dimethyl phthalate (DMP)	83%	[38]
Carbon Xerogel/Titania	Adsorption–photodegradation	30%	384	2.24	Methylene blue, Indicator microorganisms	99%	This work

**Scheme 1.** Proposed photocatalytic mechanism of CXTi under visible light irradiation.

The change in structure of MB after photodegradation was confirmed by recording FTIR spectra shown in Figure 11 before (a) and after (b) photocatalytic activity. The differences in both the spectra clearly validate the change in structure of the MB dye molecule post treatment, and are in agreement with the previous studies [39,40]. The main functional moiety associated with MB was detected at $\sim 2900 \text{ cm}^{-1}$ for methylene asymmetric stretching (C-H). The other functional moieties are observed for overlapped OH and NH at 3350 cm^{-1} , CH=N at 1645 cm^{-1} , C=C side rings in the range of 1500 to 1400 cm^{-1} , CH₃ or CH₂ stretching in the range of 1400 to 1300 cm^{-1} , C-N stretching absorption peaks at 1252 cm^{-1} , C-H at 1176 cm^{-1} , C-N at 1146 and C-S-C at 1060 cm^{-1} , and C-H out plane bending observed in the range of 800 cm^{-1} . After photodegradation of MB by ROS produced by CXTi under visible light, most of the characteristic absorption peaks linked with MB weakened or disappeared, which suggests the breakdown of the MB molecule at the interface of the CXTi. The main decomposed peaks were observed at 3338 and 1637 cm^{-1} for H-OH, 1470 for N-H and 2930 and 2850 cm^{-1} for C-H, which suggests successful degradation of MB by CXTi under visible light irradiation.

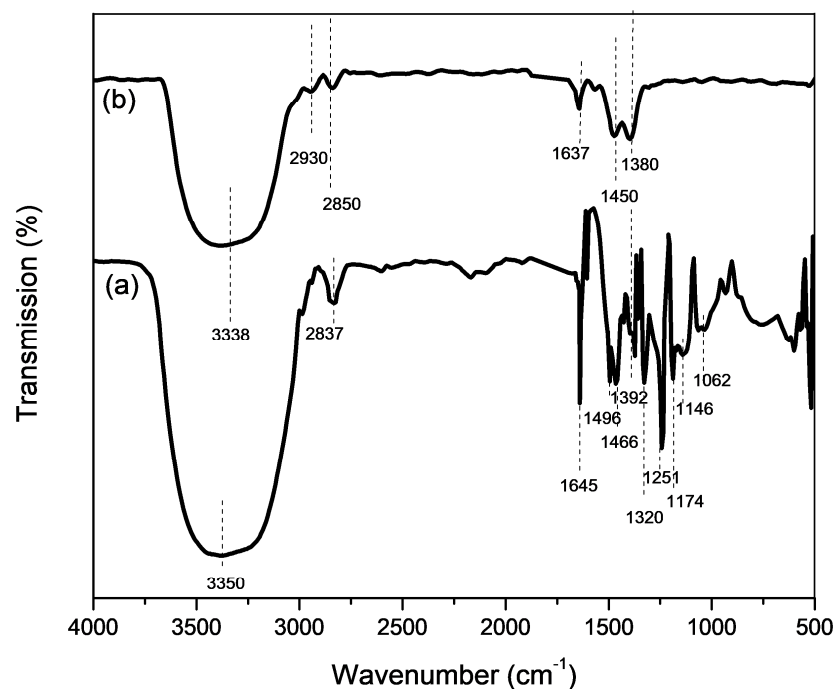


Figure 11. FTIR of (a) pure MB (b) MB after photodegradation.

Photogenerated ROS have been reported to kill bacteria by attacking the cell wall, leading to cell rupture, reduction in growth and ultimately cell death [34]. It has been reported that the usual first target of ROS is the cell wall; e.g., in *E. coli*, the cell wall is composed of lipopolysaccharide, peptidoglycan and phosphatidyl-ethanolamine, which have been reported to be affected by ROS [41]. Secondly, the rupture of the cell membrane occurs, leading to leakage of cellular matter and the ultimate breakdown of the cell [42]. Thirdly, cell lysis progresses by inhibiting the respiratory chain, followed by damage to DNA [43]. The antimicrobial performance of CXTi was studied by conducting tests using a membrane filtration procedure according to a standard method (9222 membrane filter technique for members of the coliform group [44]). The performance was tested against the reduction in total and faecal coliform bacteria and *E. coli*. After treating contaminated water with CXTi, the calculation of bacteria was performed by counting the number of colonies, colony forming units (CFU per 100 mL) and developed post incubation colonies grown on the grid after 24 h. Pictures of petri plates before (control) and after (surviving bacteria) treatment are shown in Figures 12 and 13, and numerical data is presented in Table 4. The reduction in colonies signifies complete eradication of almost all surviving bacteria. Remarkable antimicrobial activity is attributed to the production of a sufficient amount of ROS to attack the bacterial cell wall for complete destruction.

Table 4. Antimicrobial results after performing tests against reduction in total and faecal coliform and *E. coli* in control conditions and treatment using CXTi synthesised in this study.

	Total Coliform	Faecal Coliform	<i>E. coli</i>
Control	210	180	176
Post Treatment with CXTi	<1	<1	<1

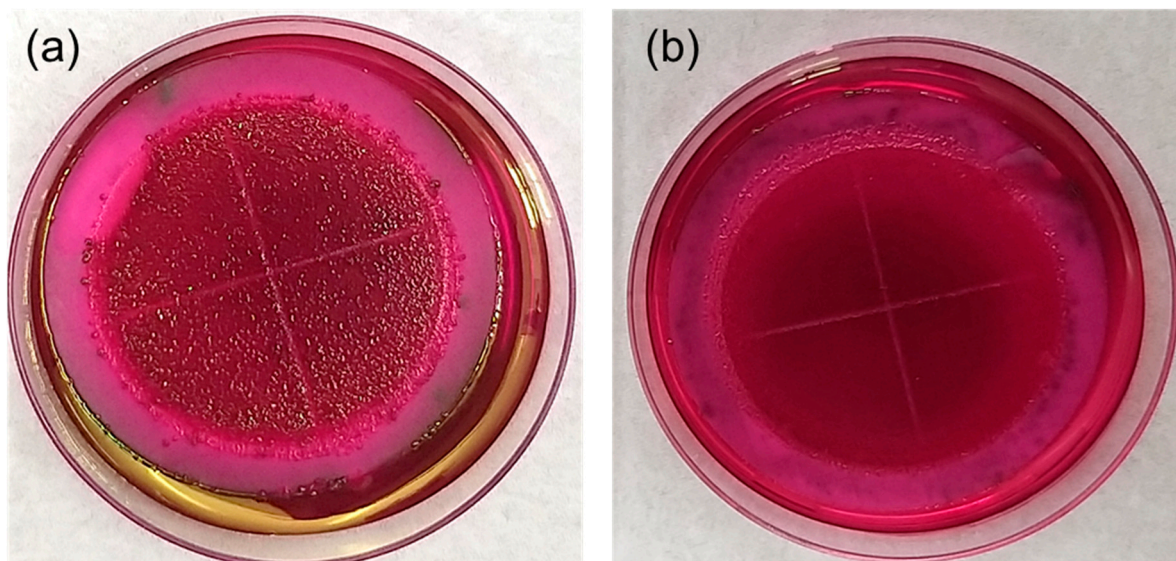


Figure 12. Pictures of petri plates for detection of total coliforms following 24 h incubation at 35 °C (a) before water treatment and (b) after water treatment with CXTi. The colonies that were dark red, mucoidal and had dark centres were counted. Dark centres that produce metallic sheen are considered to be total coliform colonies. Metallic green colonies indicate the presence of *E. coli* in a water sample.

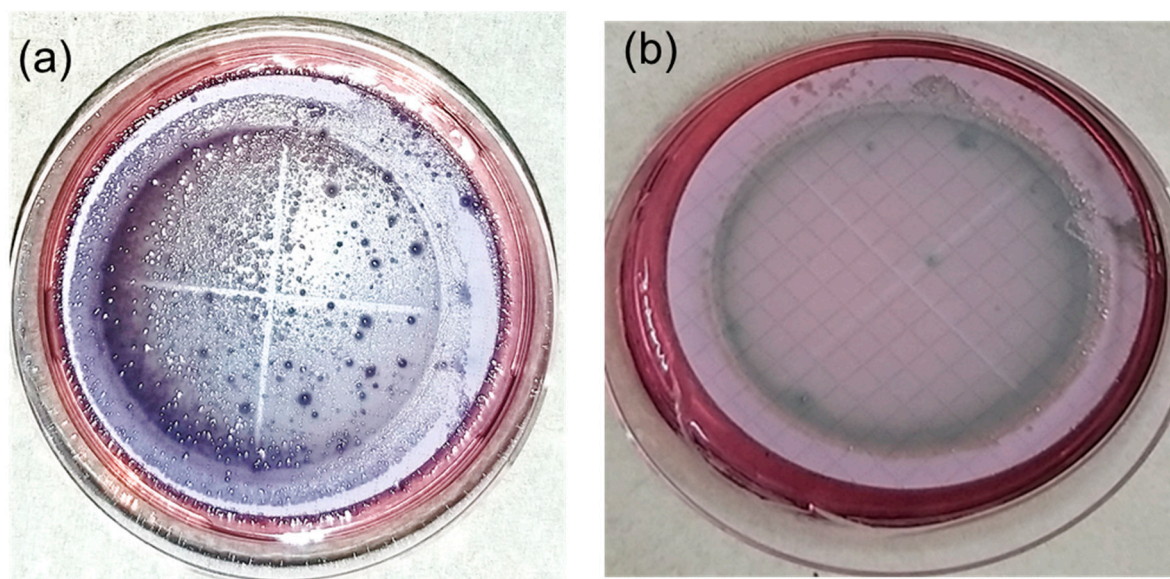


Figure 13. Pictures of petri plates for detection of faecal coliforms following 24 h incubation at 44.5 °C (a) before water treatment and (b) after water treatment with CXTi. Only blue colonies are counted, which are considered to be faecal coliform colonies. *E. coli* form dark blue flat colonies.

3. Materials and Method

3.1. Synthesis of CXTi

CX and TiO_2 were combined using a sol–gel process. 5.43 g of resorcinol (SigmaAldrich, ReagentPlus, 99%, Poole, UK) was completely dissolved in 50 mL of deionised water. 0.02 g of catalyst, sodium carbonate (Na_2CO_3 , Sigma-Aldrich, anhydrous, $\geq 99.5\%$) and 2.96 g of formaldehyde (37 wt%) were added to the resorcinol solution under continuous stirring, at room temperature. The pH recorded at this point was 7.4. A titania sol* was obtained using a conventional method described elsewhere [45], and added dropwise to the system. The integrated system was stirred at 23 °C for 2 h, after which the sol mixture was aged at 85 °C

for 72 h. Aging was followed by solvent exchange through immersion of wet monolithic CXTi in acetone. After 72 h, CX Ti was dried in a vacuum oven (Townson and Mercer 1425 Digital Vacuum Oven) at 110 °C for 48 h, and the ultimate CXTi was obtained with 30 wt% TiO₂ (theoretical percentage).

*Briefly, 3.6 g of precursor, titanium isopropoxide (TTIP) (98+%, ACROS Organics™, Geel, Belgium), was mixed with ethanol, followed by dropwise addition of HCl and water solution in the following molar ratio: 1 TTIP:10 EtOH:0.3 HCl:0.1 H₂O. The mixture was stirred at room temperature for the hydrolysis reaction to occur, and a homogenous solution was obtained after 2 h of agitation. The anatase phase of TiO₂ deposited was confirmed by X-ray diffraction spectrum [46–48] (displayed in Figure S2, Supplementary Materials).

3.2. Structural Characterisation

Morphology of the materials was studied using micrograph images obtained via field emission electron scanning microscopy (FESEM) TESCAN-MIRA. The chemical linkages were investigated through Fourier Transform Infrared (FTIR) Spectroscopy (MB3000 series, scanned in the range 4000–400 nm, at an interval 4 cm⁻¹, over 16 scans). Surface area was studied by obtaining N₂ adsorption isotherms at –196 °C (Micromeritics ASAP 2420) and using BET analysis; pore size was estimated using BJH theory [20]. Absorption vs. wavelength spectra were obtained using UV-Vis Spectrophotometry (Varian Cary 5000 UV-Vis NIR Spectrophotometer Hellma Analytics).

3.3. Adsorption and Photocatalytic Performance

The adsorption experiments were conducted by adding 0.01 g of CXTi to 25 mL of prepared concentrations of MB solution in the range 20–200 mg L⁻¹. The pH of the solutions was adjusted if required using 1M HCl and 1M NaOH. The adsorption equilibria were established by agitating the systems using an orbital shaker (VWR 3500 Analog Orbital Shaker unit), set to 125 rpm at 23 °C, in the dark. After a given time, the solution was centrifuged for 15 min and the supernatant was collected for measurement. The concentration of the treated solution was determined using UV-Vis spectrophotometry (Varian Cary 5000 UV-Vis NIR Spectrophotometer Hellma Analytics). Likewise, post adsorption, the concentration after photocatalytic treatment was determined at given time intervals of exposure to visible light (irradiance 111 W m⁻²).

The equilibrium adsorption capacity, q_e (mg g⁻¹), was calculated using

$$q_e = \frac{(C_o - C_e) \cdot V(l)}{W} \quad (9)$$

The corresponding percentage removal of MB was calculated by

$$\text{Removal \%} = \frac{C_o - C_e}{C_o} \times 100\% \quad (10)$$

where C_o and C_e are the initial MB and final concentration, respectively. W is the weight (g) of the adsorbent and V is the volume (L) of MB solution.

The effect of contact time was determined using aliquots of MB solution (25 mL, 100 mg L⁻¹) and 0.01 g adsorbent gel, added into flasks and agitated for contact times in the range 5 min to 4 h. The samples were prepared and treated as above, and the amount of adsorption was calculated using Equation (11).

$$q_t = \frac{(C_o - C_t) \cdot V}{W} \quad (11)$$

where C_o and C_t are the initial MB and equilibrium concentration at a given time, respectively, V is the volume of solution (L), and W is the mass of adsorbent sample in (g). Equilibrium concentration was determined by plotting q_t versus time of aliquots collected, at different time intervals.

3.4. Antimicrobial Performance

A stock solution of lab-cultivated bacteria was prepared with volume ratio 1:100. For the detection of bacteria, mEndo and mFC agars were prepared, and a membrane filtration procedure (MF) was performed according to 9222 standard methods for the examination of water and wastewater using the membrane filter (MF) technique for members of the coliform group [44].

Briefly, 250 mL transparent sterile water bottles were filled with 200 mL of contaminated water. According to standard microbiological examination (9000), the suggested sample volume to be filtered using membrane filtration for coliform or *E. coli* testing in drinking water is 100 mL. Therefore, 100 mL of each treated sample was measured twice, once for detection of *E. coli*, and the remaining 100 mL for detection of faecal coliform. The bottles were labelled with the respective sample codes and 0.1 g of CXTi was added to the contents of the bottle. After preparation, sample bottles were placed on an orbital shaker (VRN 360 Gemmy, Taipei, Taiwan) at 200 rpm for 90 min, to establish equilibrium. The bottles were then exposed to visible light. CXTi was filtered out and the membrane filtration procedure was carried out. 100 mL of each treated water sample was filtered twice using microfiltered paper, which was placed on mEndo and mFC agar petri plates. These plates were incubated for 24 h, at 35 °C for mEndo and at 44 °C for mFC agar plates. mEndo (pink plates) form a dark red, mucoid or dark centre without metallic sheen. *E. coli* will form colonies with a metallic sheen. mFC (blue plates) are for the detection of faecal coliform. Faecal coliforms form blue colonies on this medium, and *E. coli* will form flat dark blue colonies. The grown bacterial colonies were counted according to the standard counting procedure. The cell density of the original sample was calculated and compared with the cell density of water treated with CXTi. The counts were reported as coliform colony units (CFU/100 mL).

4. Conclusions

The CXTi adsorbent–photocatalyst was successfully synthesised within this study, using a sol–gel method to combine a resorcinol–formaldehyde xerogel (CX) with titanium dioxide (TiO₂). As expected, the integration of TiO₂ into the carbon xerogel material modified the electronic structure of TiO₂, which enabled visible light response, and the CXTi sample demonstrated efficient adsorbent–photocatalyst behaviour for the removal of MB under given conditions. The formation of a heterojunction between TiO₂ and the CX material was confirmed using spectroscopic methods. The kinetics of MB adsorption revealed that agitation for 90 min was sufficient to attain equilibrium, and the kinetic profiles better fitted a pseudo second order model, indicating chemical processes are involved within MB removal. The equilibrium adsorption data were best described by the Sips model, suggesting heterogeneity of the sample surface, which is fully in line with the mixed material composite produce here. Additionally, the mesoporous carbon phase provides a high surface area for optimised adsorption, and photocatalysis is enabled by the inclusion of TiO₂, resulting in the complete eradication of microbes under given conditions. The excellent adsorption–photodegradation abilities exhibited by CXTi, achieved through the synergistic effects of combining CX and titania, present an economically viable option for water treatment, as they can be effectively recovered and reused. Recycling efficiency tests, against the reduction in MB, demonstrated a minimal loss (~5%) in dye degradation efficiency by the fourth repeated cycle (Figure 14), suggesting good reusability of over 90% efficiency with repeated use. Thus, CXTi is a promising candidate for efficient removal of a wide range of synthetic azo dyes, as well as microbes, from industrial effluents.

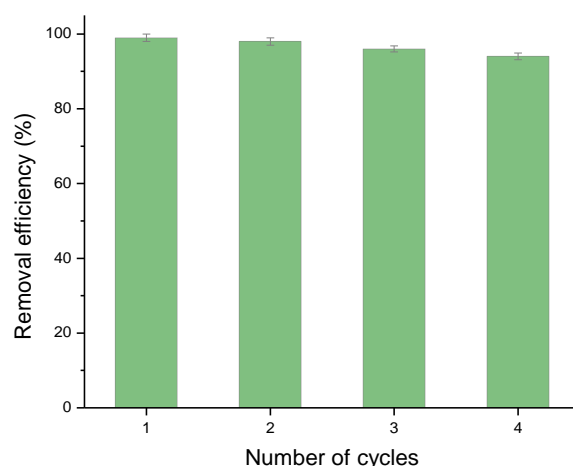


Figure 14. CXTi reusability after testing against degradation of MB dye ($C_0 = 100 \text{ mg L}^{-1}$, $T = 23 \text{ }^\circ\text{C}$, dose = 0.01 g mL^{-1} , total treatment time 120 min).

Supplementary Materials: The following supporting information can be downloaded at: <https://www.mdpi.com/article/10.3390/molecules27238483/s1>, Table S1: Parameters calculated from piecewise linear fittings to Intra-particle diffusion model, corresponding to Figure 7. Figure S1: X-ray diffraction (XRD) spectrum of Carbon Xerogel (CX) indicating two broad diffraction peaks of CX at $2\theta = 24^\circ$ and $2\theta = 44^\circ$, represented by highlighted region in light grey. These findings are similar to previously described XRD pattern obtained for CX derived from resorcinol-formaldehyde [46,47]. Figure S2: X-ray diffraction spectrum of Carbon Xerogel/TiO₂ (CXTi) indicating the presence of anatase phase at $2\theta = 25^\circ$, represented by highlighted region light grey. These findings are similar to previously described carbon/titania systems [48].

Author Contributions: Methodology, A.S. and A.J.F.; formal analysis, A.S. and A.J.F.; resources, A.J.F.; data curation, A.S. and R.S.; writing—original draft preparation, A.S.; writing—review and editing, A.J.F.; supervision, A.J.F.; project administration, A.J.F. and H.R.; funding acquisition, A.J.F. and H.R. All authors have read and agreed to the published version of the manuscript.

Funding: This research received no external funding.

Institutional Review Board Statement: Not applicable.

Informed Consent Statement: Not applicable.

Data Availability Statement: Not applicable.

Acknowledgments: Anam Safri thanks Ashleigh Fletcher and the department of Chemical and Process Engineering, University of Strathclyde, for funding this work. The authors gratefully acknowledge the administrative and technical support in conducting microbial analysis at PCRWR.

Conflicts of Interest: The authors declare no conflict of interest.

References

1. Manikandan, S.; Karmegam, N.; Subbaiya, R.; Devi, G.K.; Arulvel, R.; Ravindran, B.; Awasthi, M.K. Emerging nano-structured innovative materials as adsorbents in wastewater treatment. *Bioresour. Technol.* **2021**, *320*, 124394. [[CrossRef](#)] [[PubMed](#)]
2. Zhang, G.; Song, A.; Duan, Y.; Zheng, S. Enhanced photocatalytic activity of TiO₂/zeolite composite for abatement of pollutants. *Microporous Mesoporous Mater.* **2018**, *255*, 61–68. [[CrossRef](#)]
3. Lakshmi, S.; Renganathan, R.; Fujita, S. Study on TiO₂-mediated photocatalytic degradation of methylene blue. *J. Photochem. Photobiol. A Chem.* **1995**, *88*, 163–167. [[CrossRef](#)]
4. Kumari, P.; Alam, M.; Siddiqi, W.A. Usage of nanoparticles as adsorbents for waste water treatment: An emerging trend. *Sustain. Mater. Technol.* **2019**, *22*, e00128. [[CrossRef](#)]
5. Wang, H.; Lewis, J. Second-generation photocatalytic materials: Anion-doped TiO₂. *J. Phys. Condens. Matter* **2005**, *18*, 421. [[CrossRef](#)]
6. Khalid, N.; Majid, A.; Tahir, M.B.; Niaz, N.; Khalid, S. Carbonaceous-TiO₂ nanomaterials for photocatalytic degradation of pollutants: A review. *Ceram. Int.* **2017**, *43*, 14552–14571. [[CrossRef](#)]

7. Malekshahi Byranvand, M.; Nemati Kharat, A.; Fatholahi, L.; Malekshahi Beiranvand, Z. A review on synthesis of nano-TiO₂ via different methods. *J. Nanostructures* **2013**, *3*, 1–9.
8. Mehta, A.; Mishra, A.; Basu, S.; Shetti, N.P.; Reddy, K.R.; Saleh, T.A.; Aminabhavi, T.M. Band gap tuning and surface modification of carbon dots for sustainable environmental remediation and photocatalytic hydrogen production—A review. *J. Environ. Manag.* **2019**, *250*, 109486. [[CrossRef](#)]
9. Thapliyal, P.C.; Singh, K. Aerogels as promising thermal insulating materials: An overview. *J. Mater.* **2014**. [[CrossRef](#)]
10. Xu, P.; Drewes, J.E.; Heil, D.; Wang, G. Treatment of brackish produced water using carbon aerogel-based capacitive deionization technology. *Water Res.* **2008**, *42*, 2605–2617. [[CrossRef](#)]
11. Das, S.; Heasman, P.; Ben, T.; Qiu, S. Porous organic materials: Strategic design and structure–function correlation. *Chem. Rev.* **2017**, *117*, 1515–1563. [[CrossRef](#)] [[PubMed](#)]
12. Awadallah-F, A.; Al-Muhtaseb, S.A. Nanofeatures of resorcinol–formaldehyde carbon microspheres. *Mater. Lett.* **2012**, *87*, 31–34. [[CrossRef](#)]
13. Wang, Y.; Chang, B.; Guan, D.; Dong, X. Mesoporous activated carbon spheres derived from resorcinol-formaldehyde resin with high performance for supercapacitors. *J. Solid State Electrochem.* **2015**, *19*, 1783–1791. [[CrossRef](#)]
14. Awadallah-F, A.; Elkhatat, A.M.; Al-Muhtaseb, S.A. Impact of synthesis conditions on meso- and macropore structures of resorcinol–formaldehyde xerogels. *J. Mater. Sci.* **2011**, *46*, 7760–7769. [[CrossRef](#)]
15. Chen, Y.; Gao, H.; Xiang, J.; Dong, X.; Cao, Y. Enhanced photocatalytic activities of TiO₂-reduced graphene oxide nanocomposites controlled by TiOC interfacial chemical bond. *Mater. Res. Bull.* **2018**, *99*, 29–36. [[CrossRef](#)]
16. Jiang, Y.; Meng, L.; Mu, X.; Li, X.; Wang, H.; Chen, X.; Wang, X.; Wang, W.; Wu, F.; Wang, X. Effective TiO₂ hybrid heterostructure fabricated on nano mesoporous phenolic resol for visible-light photocatalysis. *J. Mater. Chem.* **2012**, *22*, 23642–23649. [[CrossRef](#)]
17. Safri, A.; Fletcher, A.J. Effective carbon/TiO₂ gel for enhanced adsorption and demonstrable visible light driven photocatalytic performance. *Gels* **2022**, *8*, 215. [[CrossRef](#)]
18. Zaleska, A. Doped-TiO₂: A review. *Recent Pat. Eng.* **2008**, *2*, 157–164. [[CrossRef](#)]
19. Bardestani, R.; Patience, G.S.; Kaliaguine, S. Experimental methods in chemical engineering: Specific surface area and pore size distribution measurements—BET, BJH, and DFT. *Can. J. Chem. Eng.* **2019**, *97*, 2781–2791. [[CrossRef](#)]
20. Aranovich, G.L.; Donohue, M.D. Adsorption isotherms for microporous adsorbents. *Carbon* **1995**, *33*, 1369–1375. [[CrossRef](#)]
21. Azeez, F.; Al-Hetlani, E.; Arafa, M.; Abdelmonem, Y.; Nazeer, A.A.; Amin, M.O.; Madkour, M. The effect of surface charge on photocatalytic degradation of methylene blue dye using chargeable titania nanoparticles. *Sci. Rep.* **2018**, *8*, 1–9. [[CrossRef](#)] [[PubMed](#)]
22. Azizian, S. Kinetic models of sorption: A theoretical analysis. *J. Colloid Interface Sci.* **2004**, *276*, 47–52. [[CrossRef](#)] [[PubMed](#)]
23. Rafatullah, M.; Sulaiman, O.; Hashim, R.; Ahmad, A. Adsorption of methylene blue on low-cost adsorbents: A review. *J. Hazard. Mater.* **2010**, *177*, 70–80. [[CrossRef](#)] [[PubMed](#)]
24. Ebelegi, A.N.; Ayawei, N.; Wankasi, D. Interpretation of adsorption thermodynamics and kinetics. *Open J. Phys. Chem.* **2020**, *10*, 166. [[CrossRef](#)]
25. Tan, K.; Hameed, B. Insight into the adsorption kinetics models for the removal of contaminants from aqueous solutions. *J. Taiwan Inst. Chem. Eng.* **2017**, *74*, 25–48. [[CrossRef](#)]
26. Wang, J.; Guo, X. Adsorption kinetic models: Physical meanings, applications, and solving methods. *J. Hazard. Mater.* **2020**, *390*, 122156. [[CrossRef](#)]
27. Tran, H.N.; Wang, Y.-F.; You, S.-J.; Chao, H.-P. Insights into the mechanism of cationic dye adsorption on activated charcoal: The importance of π - π interactions. *Proc. Saf. Environ. Prot.* **2017**, *107*, 168–180. [[CrossRef](#)]
28. Ayawei, N.; Ebelegi, A.N.; Wankasi, D. Modelling and interpretation of adsorption isotherms. *J. Chem.* **2017**. [[CrossRef](#)]
29. Al-Ghouti, M.A.; Da'ana, D.A. Guidelines for the use and interpretation of adsorption isotherm models: A review. *J. Hazard. Mater.* **2020**, *393*, 122383. [[CrossRef](#)]
30. Makuła, P.; Pacia, M.; Macyk, W. How to correctly determine the band gap energy of modified semiconductor photocatalysts based on UV-Vis spectra. *J. Phys. Chem. Lett.* **2018**, *9*, 6814–6817. [[CrossRef](#)]
31. Wang, N.; Zhu, L.; Huang, Y.; She, Y.; Yu, Y.; Tang, H. Drastically enhanced visible-light photocatalytic degradation of colorless aromatic pollutants over TiO₂ via a charge-transfer-complex path: A correlation between chemical structure and degradation rate of the pollutants. *J. Catal.* **2009**, *266*, 199–206. [[CrossRef](#)]
32. Fujisawa, J.-i.; Matsumura, S.; Hanaya, M. A single TiOC linkage induces interfacial charge-transfer transitions between TiO₂ and a π -conjugated molecule. *Chem. Phys. Lett.* **2016**, *657*, 172–176. [[CrossRef](#)]
33. Zhang, G.; Choi, W. A low-cost sensitizer based on a phenolic resin for charge-transfer type photocatalysts working under visible light. *Chem. Commun.* **2012**, *48*, 10621–10623. [[CrossRef](#)] [[PubMed](#)]
34. Kim, S.; Ghafoor, K.; Lee, J.; Feng, M.; Hong, J.; Lee, D.-U.; Park, J. Bacterial inactivation in water, DNA strand breaking, and membrane damage induced by ultraviolet-assisted titanium dioxide photocatalysis. *Water Res.* **2013**, *47*, 4403–4411. [[CrossRef](#)]
35. do Carmo Batista, W.V.F.; da Cunha, R.; dos Santos, A.C.; dos Reis, P.M.; Furtado, C.A.; Silva, M.C.; de Fátima Gorgulho, H. Synthesis of a reusable magnetic photocatalyst based on carbon xerogel/TiO₂ composites and its application on acetaminophen degradation. *Ceram. Int.* **2022**, *48*, 34395–34404. [[CrossRef](#)]

36. da Cunha, R.; do Carmo Batista, W.V.F.; de Oliveira, H.L.; dos Santos, A.C.; dos Reis, P.M.; Borges, K.B.; Martelli, P.B.; Furtado, C.A.; de Fátima Gorgulho, H. Carbon Xerogel/TiO₂ composites as photocatalysts for acetaminophen degradation. *J. Photochem. Photobiol. A Chem.* **2021**, *412*, 113248. [[CrossRef](#)]
37. Bailón-García, E.; Elmouwahidi, A.; Álvarez, M.A.; Carrasco-Marín, F.; Pérez-Cadenas, A.F.; Maldonado-Hódar, F.J. New carbon xerogel-TiO₂ composites with high performance as visible-light photocatalysts for dye mineralization. *Appl. Catal. B Environ.* **2017**, *201*, 29–40. [[CrossRef](#)]
38. Liang, Z.; Zhang, J.; Liu, H.; Shi, J. Enhancement of the photocatalytic activity of a TiO₂/carbon aerogel based on a hydrophilic secondary pore structure. *RSC Adv.* **2016**, *6*, 68416–68423.
39. Houas, A.; Lachheb, H.; Ksibi, M.; Elaloui, E.; Guillard, C.; Herrmann, J.-M. Photocatalytic degradation pathway of methylene blue in water. *Appl. Catal. B Environ.* **2001**, *31*, 145–157. [[CrossRef](#)]
40. Barışçi, S.; Turkyay, O.; Dimoglo, A. Review on greywater treatment and dye removal from aqueous solution by ferrate (VI). In *Ferrites and Ferrates: Chemistry and Applications in Sustainable Energy and Environmental Remediation*; ACS Symposium Series; ACS Publications: Washington, DC, USA, 2016; Volume 1238, pp. 349–409. [[CrossRef](#)]
41. de Dicastillo, C.L.; Correa, M.G.; Martínez, F.B.; Streitt, C.; Galotto, M.J. Antimicrobial effect of titanium dioxide nanoparticles. In *Antimicrobial Resistance: A One Health Perspective*; BoD—Books on Demand: Norderstedt, Germany, 2020. [[CrossRef](#)]
42. Albukhaty, S.; Al-Bayati, L.; Al-Karagoly, H.; Al-Musawi, S. Preparation and characterization of titanium dioxide nanoparticles and in vitro investigation of their cytotoxicity and antibacterial activity against *Staphylococcus aureus* and *Escherichia coli*. *Anim. Biotechnol.* **2022**, *33*, 864–870. [[CrossRef](#)] [[PubMed](#)]
43. Stankic, S.; Suman, S.; Haque, F.; Vidic, J. Pure and multi metal oxide nanoparticles: Synthesis, antibacterial and cytotoxic properties. *J. Nanobiotechnology* **2016**, *14*, 1–20. [[CrossRef](#)]
44. American Public Health Association. 9222 Membrane filter technique for members of the coliform group. In *Standard Methods For the Examination of Water and Wastewater*; American Public Health Association: Washington, DC, USA, 2018; Volume 27. [[CrossRef](#)]
45. Khan, M.A.; Akhtar, M.S.; Yang, O.-B. Synthesis, characterization and application of sol-gel derived mesoporous TiO₂ nanoparticles for dye-sensitized solar cells. *Sol. Energy* **2010**, *84*, 2195–2201. [[CrossRef](#)]
46. Lin, C.; Ritter, J. Effect of synthesis pH on the structure of carbon xerogels. *Carbon* **1997**, *35*, 1271–1278. [[CrossRef](#)]
47. Fonseca-Correa, R.A.; Giraldo, L.; Moreno-Piraján, J.C. Dataset of xerogel synthesis in basic medium at different resorcinol/catalyst ratios. *Data Brief* **2018**, *17*, 1056–1061. [[CrossRef](#)]
48. Singh, S.; Bhatnagar, A.; Dixit, V.; Shukla, V.; Shaz, M.; Sinha, A.; Srivastava, O.; Sekkar, V. Synthesis, characterization and hydrogen storage characteristics of ambient pressure dried carbon aerogel. *Int. J. Hydrog. Energy* **2016**, *41*, 3561–3570. [[CrossRef](#)]